Title

Optimizing the utility of diffusion imaging for discovering genetic and environmental influences on neural development, degeneration, and disease

Author

Jahanshad, Neda

Publication Date

2012

Peer reviewed|Thesis/dissertation

University of California
Los Angeles

Optimizing the utility of diffusion imaging for discovering genetic and environmental influences on neural development, degeneration, and disease

A dissertation submitted in partial satisfaction
of the requirements for the degree
Doctor of Philosophy in Biomedical Engineering

by

Neda Jahanshad

2012

Abstract of the Dissertation

Optimizing the utility of diffusion imaging for discovering genetic and environmental influences on neural development, degeneration, and disease

by

Neda Jahanshad

Doctor of Philosophy in Biomedical Engineering

University of California, Los Angeles, 2012

Professor Paul M. Thompson, Co-chair

Professor Ricky K. Taira, Co-chair

The complex interplay of nature and nurture make each individual unique in several ways; however, certain combinations of genetic and environmental factors lend themselves to devastating neurological diseases, whose mechanistic pathways are not fully understood. Many of these disorders damage and deteriorate the white matter neural connections within the brain. Non-invasive imaging techniques have recently been used to map structural variation in the living human brain; yet now, with the growing advances in diffusion-based magnetic resonance imaging (dMRI) techniques and its wide scale availability, we are able to uncover more about the interworking connections of the brain than ever before. In the work presented in this thesis, the utility of dMRI is explored. First, we examine the stability and reliability of diffusion imaging protocols – these acquisition protocols are often limited by a clinical time constraint and therefore trade-offs are made, which may compromise directional or spatial resolution and can affect signal-to-noise or reproducibility in brain maps. Next, we explore the degree to which genetic interpretations from the same individuals can be affected by the choice of imaging protocol. A preliminary investigation into different methods of population-based analyses lends itself to a large heritability study of brain fiber asymmetry. Knowledge of the genetic influence on brain fiber integrity motivates a study of the most pressing global nutritional deficiency, iron, and its genetic correlates, on the

healthy human brain structure. Methods presented are then carried forward on genetic and environmental fiber mapping experiments independently, studying the microstructural effect of a single Alzheimer's disease risk gene on healthy young adults and also cerebrovascular confounds in HIV patients. Finally, the brain's network and organization is visualized as a matrix describing the degree of physical connections between functional cortical regions through tractography and cortical parcellation. The degree of genetic and environmental influence on the "human connectome" is then estimated. These works mark only the beginning of this line of research, which will be further expanded with studies of connectivity biomarkers, viral and gene interactions, and global efforts in combining data to expand the search for genes influencing brain microstructure.

The dissertation of Neda Jahanshad is approved.

Arthur W. Toga

Luminita A. Vese

Ricky K. Taira, Committee Co-chair

Paul M. Thompson, Committee Co-chair

University of California, Los Angeles

2012

Table of Contents

1 Introduction **1**

1.1 White matter of the human brain 1

1.2 Structural brain mapping 1

1.2.1 Mapping of normal variation and development 2

1.2.2 Mapping of neurological disease 3

1.3 Imaging white matter with diffusion MRI 3

1.3.1 Diffusion tensor imaging 3

1.3.2 High angular resolution diffusion imaging 4

1.4 Brain mapping with diffusion MRI 5

1.4.1 Pointwise mapping of fiber integrity 5

1.4.2 Mapping the human connectome 6

1.4.3 Imaging protocol dependencies, artifacts, and biases 6

1.5 Heritability and genetic studies 8

1.6 Environmental influence on the brain 9

1.7 Organization of the dissertation 10

2 Optimizing diffusion protocols **12**

2.1 Trade-offs between directional and spatial resolution 13

2.2 Identifying protocol independent genetic associations 18

3 Fiber asymmetry **23**

3.1 Optimal template for asymmetry registration 24

3.2 Genetics of brain fiber asymmetry 33

4 Iron and white matter pathways 49

4.1 Transferrin and hemochromatosis gene association to brain structure 50

4.2 Is iron important in youth to prevent neurodegeneration? 60

5 DTI mapping of genes and environment 64

5.1 Alzheimer's risk gene mapped to white matter 65

5.2 Mapping HIV risk factors to the brain 73

6 Human brain connectivity 84

6.1 Mapping sex differences 85

6.2 Genetics of the connectome 91

7 Future works 96

7.1 Connectivity measures as biomarkers 96

7.1.1 The connectome as an endophenotype for disease 96

7.1.2 Biomarkers for disease progression 98

7.1.3 Defining new biomarkers 99

7.2 ENIGMA-DTI 103

7.2.1 Working group 105

7.2.2 Global expansion 106

7.3 LONI Pipeline updates 106

List of Figures

1.1 Constructing the connectome 7

7.1 Connectome genetics 97

7.2 Smallworldness parameters as biomarkers for degeneration 99

7.3 Discretized fibers 102

7.4 Matrix of path lengths 103

7.5 Illustration of interhemispheric path length 104

List of Tables

7.1 ENIGMA-DTI sites 106

Acknowledgments

To all my friends, family, collaborators, and mentors who have helped to guide and support me throughout my graduate career, *thank you*!!

First and foremost, I would like to thank my graduate mentor, Dr. Paul Thompson, whose dedication and expertise were unyielding sources of inspiration and encouragement. I will always be grateful to have had the opportunity to work under Paul's direction – his extraordinary leadership has laid the foundation upon which this work has been built, and his genuine kindness and round-the-clock advice has enabled me to make my passions and interests the basis for my career. I would not have had this chance without Dr. Ricky Taira, who convinced Paul to take me on as a student. Ricky's mentorship has always pushed me to think outside the box and his ability to intersperse humor throughout any discussion has made research never actually feel like work. I would also like to offer my most sincere thanks to the other members of my thesis committee, Dr. Luminita Vese and Dr. Arthur Toga whose thought-provoking scholarship and leadership have provided unlimited opportunities in this field.

To all the members of the Laboratory of Neuro Imaging and the Medical Imaging Informatics Group, thank you for creating the most amazing working environment I have ever been a part of – everyday has been a privilege. I am thankful to past and present LONI lab members – Eugenio Iglesias and Jason Stein for teaching me what it means to be a graduate student and for always being up for a good scientific debate; Priya Rajagopalan, Omid Kohannim, Liang Zhan, Derrek Hibar, Meredith Braskie, Gautam Prasad, and Emily Dennis for always being there with enthusiasm for research, and for their invaluable collaborations resulting in a continual stream of new and exciting research ideas; Jonathan Pierce for his systems support throughout the years; and to the late night team of researchers Talia Nir, Julio Villalon, and Marina Barysheva who were always there not only with connectivity ideas, neuroscience answers, medical expertise, but also with a great sense of humor and much more than scientific support. I am extremely grateful to have had the honor to work with Dr. Hooshang Kangarloo who was a great source of inspiration and always encouraged

me to do more. He will be sincerely missed. I am also very thankful to Dr. Alex Bui for his continual guidance, Dr. Deni Aberle for her support, Isabel Rippy for her friendship and help as I made my way through graduate school, Will Hsu, Emily Watt, Bill Speier, Lew Andrada and all other members of MII for teaching me all things informatics and reminding me to take a lunch break.

I am extremely thankful to all our collaborators, particularly those in Brisbane, Australia including Margie Wright, Greig de Zubicaray, Katie McMahon, Sarah Medland, John Whitfield and Nick Martin for their constant and continual advice, suggestions and encouragement on all things genetic. I would like to also thank Victor Valcour from UCSF for his enthusiasm and dedication in geriatric work; Peter Kochunov for all his hard work with DTI processing. Additionally, I am grateful to Guillermo Sapiro, Iman Aganj, and Christophe Lenglet from University of Minnesota for their support and brilliant ideas on HARDI. If it were not for my mentors and advisors at JHU early on, I would have never found my way to this incredible field, so thank you Susumu Mori, Jiangyang Zhang, Jerry Prince, Bennett Landman, Jack Rugh, Tilak Ratnanather, and Mike Miller for introducing me to my future career.

Thanks to Dr. Lauren Pinter-Brown and her warm and smiling team at 2020 Santa Monica Blvd. Finally, I would have never gotten through graduate school without the love and support of my friends and family, the Grischkan family, and of course, my own ever-growing family – my mom Yassi and father Khosrow, my grandmothers, my late grandfathers, my stepfather Bill, my brother Amir, my aunts Lily, Mina, Mitra and Minou, my uncles Ali and Hamid, all my cousins – particularly Shadi, Az and Kev – John, Tal, Adam and the four little ones.

Funding Agency Acknowledgements

The Australian twins study was supported by the National Institute of Child Health and Human Development (R01 HD050735), and the National Health and Medical Research Council (NHMRC 486682), Australia. Genotyping was supported by NHMRC (389875). Projects were also funded by the Alzheimer's Disease Neuroimaging Initiative (ADNI) (NIH Grant

U01 AG024904). ADNI is funded by the NIA, NIBIB, and through generous contributions from the following: Abbott, AstraZeneca AB, Bayer Schering Pharma AG, Bristol-Myers Squibb, Eisai Global Clinical Development, Elan Corporation, Genentech, GE Healthcare, GlaxoSmithKline, Innogenetics, Johnson and Johnson, Eli Lilly and Co., Medpace, Inc., Merck and Co., Inc., Novartis AG, Pfizer Inc, F. Hoffman-La Roche, Schering-Plough, Synarc, Inc., as well as non-profit partners the Alzheimer's Association and Alzheimer's Drug Discovery Foundation, with participation from the U.S. FDA. Private sector contributions to ADNI are facilitated by the Foundation for the National Institutes of Health (www.fnih.org). The grantee organization is the Northern California Institute for Research and Education, and the study is coordinated by the Alzheimer's Disease Cooperative Study at UCSD. ADNI data are disseminated by LONI. This research was also supported by NIH grants P30 AG010129, K01 AG030514, and the Dana Foundation. Algorithm development and data collection were also funded by the NIH - NIA, NIBIB, NICHD, NLM, NCRR AG040060, MH097268, MH089722, EB01651, LM05639, RR019771, EB008432, EB008281, and EB007813, to Paul Thompson. The research was also supported by the National Library of Medicine Grant T15 LM07356 to Professor Alex A.T. Bui, Department of Radiology, Training grant awarded to Neda Jahanshad.

Co-author Acknowledgements

As chapters 2 through 6 are the following articles, I would like to thank, and re-thank, all co-authors for their contributions:

Jahanshad N, Zhan L, Bernstein MA, Borowski B, Jack CR, Toga AW, Thompson PM (2010). Diffusion Tensor Imaging in Seven Minutes: Determining tradeoffs between spatial and directional resolution, International Symposium of Biomedical Imaging (ISBI) 2010, Rotterdam, The Netherlands, April 14-17, 2010

Jahanshad N, Kohannim O, Toga AW, McMahon KL, de Zubicaray GI, Martin NG, Wright MJ, and Thompson PM (2012). Diffusion imaging protocl effects on genetic associations. International Symposium of Biomedical Imaging (ISBI)

Barcelona, Spain, May 2-5 2012.

Jahanshad N, Lee AD, Leporé N, Chou YY, Brun CC, Barysheva M, Toga AW, McMahon KL, de Zubicaray GI, Wright MJ, Thompson PM (2009). Genetics of anisotropy asymmetry: registration and sample size effects. Med Image Comput Comput Assist Interv (MICCAI) London, England 2009; 12 (Pt 2): 498-505.

Jahanshad N, Lee AD, Barysheva M, McMahon KL, de Zubicaray GI, Martin NG, Wright MJ, Toga AW, Thompson PM. Genetic Influences on Brain Asymmetry: A DTI Study of 374 Twins and Siblings, NeuroImage, 2010 Aug 15;52(2):455-69.

Jahanshad N, Kohannim O, Hibar DP, Stein JL, Barysheva M, McMahon KL, de Zubicaray GI, Medland SE, Montgomery GW, Whitfield JB, Martin NG, Wright MJ, Toga AW, Thompson PM (2011). Brain structure in healthy young adults is related to serum transferrin and the H63D polymorphism in the *HFE* gene. PNAS Plus January 9, 2012.

Braskie MN,* **Jahanshad N***, Stein JL*, Barysheva M, McMahon KL, de Zubicaray GI, Martin NG, Wright MJ, Ringman JM, Toga AW, Thompson PM (2011). Common Alzheimer's disease risk variant within the *CLU* gene affects white matter microstructure in young adults, Journal of Neuroscience, 2011; 31 (18): 6764-70.

Nakamoto BK*, **Jahanshad N***, McMurtray A, Kallianpur KJ, Chow DC, Valcour VG, Paul RH, Thompson PM, Shikuma CM, Cerebrovascular Risk Factors and Brain Microstructural Changes on Diffusion Tensor Images in HIV-infected Individuals. J. Neurovirology In Press

Jahanshad N, Aganj I, Lenglet C, Jin Y, Joshi A, Barysheva M, McMahon KL, de Zubicaray GI, Martin NG, Wright MJ, Toga AW, Sapiro G, Thompson PM (2011). High angular resolution diffusion imaging (HARDI) tractography in 234 young adults reveals greater frontal lobe connectivity in women, International Symposium of Biomedical Imaging (ISBI) 2011.

Jahanshad N, Hibar DP, Ryles A, McMahon KL, de Zubicaray GI, Martin NG, Wright MJ, Toga AW, and Thompson PM (2012). Discovery of genes that affect the human brain connectivity: A genome-wide analysis of the connectome. International Symposium of Biomedical Imaging (ISBI) Barcelona, Spain, May 2-5 2012.

Vita

2004-6	Undergraduate researcher in imaging labs including the FM Kirby Center for Functional Brain Imaging, what is now the Center for Brain Imaging Science, and the Image Analysis and Communications Lab Johns Hopkins University, Baltimore, MD, USA
2006	B.S. Double Major (Biomedical Eng and Electrical Eng), Minor (Math), Johns Hopkins University, Baltimore, MD, USA
2007-2011	Doctoral Training Grant Awardee from the NLM, Bethesda, MD, USA
2009	Summer Trainee at the OHPCC(NLM) and STBB (NICHHD) NIH, Bethesda, MD, USA
2005–present	Co-author on 66 scientific abstracts presented at annual scientific conferences including the Society of Neuroscience, Organization of Human Brain Mapping, International Society of Magnetic Resonance in Medicine, etc.
2009–present	Co-author on 20 peer reviewed engineering conference papers presented at annual meetings including the International Symposium of Biomedical Imaging (ISBI), Medical Image Computing and Computer Assisted Intervention (MICCAI), and the Americal Medical Informatics Association (AMIA).
2009–present	Peer-Reviewer for Human Brain Mapping, Psychiatry Research, MICCAI, Proceedings of the National Academy of Sciences

Publications and Presentations

- **Jahanshad N**, et al. PNAS 2012.

- Thompson PM, **Jahanshad N**. Exp Rev Neurotheraputics. 2012
- Stein JL, et al. for the ENIGMA Consortium. Nature Genetics 2012
- Hibar DP, et al. Twin Research and Human Genetics 2012.
- Nakamoto BK* et al, J. Neurovir 2012
- Braskie MN, et al. J Neuroscience 2012.
- Kohannim O, et al. Neuropsychopharmocology 2012.
- Zhan L,et al. Human Brain Mapping 2012.
- Dennis EL et al. Brain Connectivity 2012.
- Duarte-Carvajalino JM, et al. Neuroimage 2011.
- Braskie MN* et al. J Neuroscience, 2011.
- Hibar DP, et al. Neuroimage, 2011.
- Aganj I, et al. Med Image Anal 2011.
- **Jahanshad N**, et al. Neuroimage, 2010.
- Zhan L, et al. Neuroimage 2010.
- Zhang J, et al. Neuroimage 2010.
- Hua J, et al. Circulation 2005.
- Taira RK, Iglesias JE, **Jahanshad N**. Ch 5 In Bui AAT, Taira RK eds, Medical Imaging Informatics. Springer, NY (2009).
- **Jahanshad N**.Guest Lecturer UCLA BME 226, April 2010-12.

CHAPTER 1

Introduction

Our every behavior, from each walking step or involuntary tremor, to every thought or forgotten memory, is governed by a complex interplay of genes and further shaped by our environment. Nowhere are these interactions more prevalent and yet, more mysterious, than in the connections and the organization of the human brain. These physical connections within the human brain can be visualized through in-vivo brain mapping studies of the brain's white matter using diffusion based imaging techniques and further applied to understand the genetic and environmental effects that independently and together combine to individually shape our brains and define who we are.

1.1 White matter of the human brain

Within the nervous system, the brains white matter is composed of highly myelinated axons, nerve fibers surrounded by an insulating sheath, together which transport information between various functioning gray matter structures and cortical regions. The fibers that comprise the white matter make up the structural network of the human brain and disruptions in these fibers can alter the way functional portions of the brain connect and communicate with each other.

1.2 Structural brain mapping

Mapping the structure of the brain using non-invasive *in-vivo* imaging techniques has been at the forefront of the research performed at the Laboratory of Neuro Imaging. The brain

mapping techniques developed here have allowed for population studies to identify trajectories in brain maturation in youth (Thompson *et al.* , 2000), significant differences in rates of anatomical degeneration in the cognitively impaired elderly (Thompson *et al.* , 2001a) and abnormalities in brain structure in states of psychological (Thompson *et al.* , 2001c) or immunological disease (Thompson *et al.* , 2005b; 2006). Differences in structural volumes in populations or cortical patterning using MRI based techniques can shed light onto the changes that occur in the living brain.

1.2.1 Mapping of normal variation and development

With standard MRI measurements, white matter structures have been shown to vary greatly throughout healthy development. For example, the corpus callosum, the primary white matter structure connecting the two hemispheres, shows various degrees of thickness across its development in childhood and adolescents as well as with respect to sex (Luders *et al.* , 2010). Comparing the normally developed white matter with those of disease allows us to better understand the pathways affected in the diseases and underlying causal structural mechanisms behind characteristic cognitive or behavior traits. Understanding these differences in normal variation can help better identify structural abnormalities and brain pathway involvement in developmental disorders such as autism (Vidal *et al.* , 2006) or psychopathic tendencies later in life (Raine *et al.* , 2003). Aberrant asymmetries, reported in several brain disorders, might indicate a derailment in processes that establish normal hemispheric specialization. Some mental illnesses, such as schizophrenia, are thought by some to arise due to a failure of normal functional lateralization (Crow, 1990, Hamilton *et al.* , 2007, Narr *et al.* , 2007) although such a view is not universally accepted. Altered asymmetries have been found in groups of patients with dyslexia (Beaton, 1997), Williams syndrome (Thompson *et al.* , 2005a, Eckert *et al.* , 2006), fetal alcohol syndrome (Sowell *et al.* , 2002), Huntington's disease (Muhlau *et al.* , 2007), and multiple sclerosis (Koziol *et al.* , 2005). Asymmetries in the rate of disease progression have also been reported in some studies of degenerative diseases such as Alzheimer's disease and mild cognitive impairment (Thompson *et al.* , 1998; 2003). Taken together, all these asymmetries heighten interest in possible differences in the vulnerability

of the two hemispheres to various types of neuropathology and age-related decline, and the genetic and environmental origins of these differences. Determining an understanding of the typically developing levels of asymmetry are therefore important in order to understand the derailments that can occur in these diseases, yet to obtain typical levels of variation within a population, generally large samples are needed. In one of the works described in this thesis, we map asymmetry in white matter microstructure in over 350 healthy individuals to obtain maps of normal levels of asymmetry (Jahanshad *et al.* , 2010).

1.2.2 Mapping of neurological disease

Not only do white matters structures such as the corpus callosum change during development as seen through MRI, but changes can also occur through a degenerative manner later in life (Thompson *et al.* , 2002). Mapping differences in the white matter, and relative rates of change, between healthy and disease allows for a better understanding of how the disease progresses and what neuroanatomical pathways are involved. While mapping healthy variations and disease alterations through macrostructural MRI imaging can lead us to better understanding human brain structure, mapping white matter microstructure can tell us more about neuroanatomy than shape and volume alone, as it can describe the makeup of the fiber connections within the human brain and their integrity. Newly developed diffusion based MRI acquisition and processing methodologies are being optimized for this very purpose.

1.3 Imaging white matter with diffusion MRI

1.3.1 Diffusion tensor imaging

Diffusion tensor imaging (DTI) and similarly more advanced diffusion imaging techniques such as high angular resolution diffusion imaging (HARDI) of the brain, are capable of capturing subtle changes in white matter make up, including intermixing of fibers, fiber directionality, and more generally, the integrity of fibers *in vivo* (Basser & Pierpaoli, 1996). Diffusion of water molecules attenuates the MR signal in direction r, according to the Stejskal-

Tanner equation: $S_k(r) = S_0(r)e^{-b_k D_k(r)}$. Here, $S_0(r)$ is the non-diffusion weighted baseline intensity in direction r, $D_k(r)$ is the apparent diffusion coefficient (ADC), and b_k is a constant depending on the gradient k. The fractional anisotropy of diffusion (FA) was computed from the tensor eigenvalues $(\lambda_1, \lambda_2, \lambda_3)$ at each voxel. FA is influenced by both axial diffusivity (DAX) (λ_1; a measure of diffusion along the axonal fibers) and radial diffusivity (DR) (the average of λ_2 and λ_3; a measure of diffusion orthogonal to the axonal fibers). Changes in white matter integrity, often measured through FA of the diffusion tensor, can reflect differences in the level of myelination, the compactness of the fibers, and their directional coherence (Klingberg *et al.* , 2000, Beaulieu, 2002).

1.3.2 High angular resolution diffusion imaging

While the standard diffusion tensor is used in many clinical settings, advancements in image acquisition and reconstructions can greatly reduce the shortcomings of DTI (Lenglet *et al.* , 2009), which can include artificial reduction in anisotropy and inflation of diffusion value in regions where fibers cross or intersect in the same voxel as a single tensor model is inherently incapable of resolving mixtures of multiple fiber orientations. Several high resolution lines of work including high angular resolution diffusion imaging (HARDI) (Tuch *et al.* , 2002), and DSI (Wedeen *et al.* , 2012) are able to reconstruct the multiple fiber patterns. For a good recent review of these topics, please see Assemlal *et al.* (2011). Resolving multiple fibers allows for more accurate tracing of fibers through HARDI based tractography (Aganj *et al.* , 2011). Using tractography methods better able to tract fibers through regions of crossings is ideal for more efficiently mapping fibers as they cross to reach and connect cortical regions, allowing reconstruction of the structural human connectome.

1.4 Brain mapping with diffusion MRI

1.4.1 Pointwise mapping of fiber integrity

As with other neuroimaging modalities, voxelwise images of scalar metrics, for example activity in fMRI, or gray matter volume in standard MRI, can be calculated and mapped for each individual in a study. However, to perform population based analyses and study differences in the population on a pointwise, or voxelwise level, all maps need to be put into a space of an atlas, or reference template through registration methods. Once this is performed, it is assumed that a single voxel represents the same anatomical location across all subjects. Then, subject scans can be compared at each anatomical point. However, when making upwards of hundreds and thousands of comparisons across the image when performing voxelwise analyses, there is a large inflation of the family-wise error rate, suggesting certain points will be more likely to be found to falsely reject the null hypotheses at any given threshold. Scalar measures derived from DTI or HARDI are no exception. With diffusion derived anatomical images, the choice of images to use as targets and maps to drive registration becomes of interest. One can choose to map higher resolution anatomical scans from MRI to align individual anatomy and apply registrations to diffusion based scans, or the choice of using the diffusion based anatomical scans directly is also common. For a good review of these voxel-based issues in imaging applications in general, see Kriegeskorte *et al.* (2010). In Section 2.1, we examine several choices of templates and registrations to examine effects of registration template on a FA based genetics of asymmetry study. We found using the DTI images was as effective, if not more so, than using MRI based T1 scans for picking up genetic correlations between twins. We carry this forward to use DTI-based images to drive registrations in other voxelwise studies of FA in subsequent sections. Mutual information based registrations were performed to avoid circularity in intensity based approaches when intensity (or FA value) was the variable of interest. Additionally, in our voxelbased analyses, to avoid unnecessary inflation of the family-wise error, we limited the search region to regions in the image space where the FA was higher than a particular threshold to focus our analyses on biologically relevant regions of the image less susceptible to paritial voluming.

Voxelwise points can also be labeled into regions of interest, or traced along tracts, which can serve as summary measures for a particular measure like FA.

1.4.2 Mapping the human connectome

Standard voxel based analyses are common and extremely descriptive ways of describing the mircostructural properties of white matter; however, the study of connectomics allows for avoiding issues with intersubject registration and within subject connections can be mapped into matrices of equal sizes and compared across populations. Anatomical brain MRI and high angular resolution diffusion imaging (HARDI) can be combined to map the cortical connectivity of the human brain network. Cortical regions can be delineates into areas of known structure and functionality (Desikan *et al.* , 2006) while also mapping white matter fiber pathways with high-resolution tractography. Although there are different definitions of connectivity maps, in this work, we defined connectivity maps as the proportion of the total number of fibers traced that intersect or inter-connect cortical regions within and across the brain hemispheres. Such maps of the structural connectome can be represented as graphs or matrices: here we use symmetric matrices, in which each matrix element (x, y) shows the proportion of fibers connecting regions x and y. An illustration of the pipeline to construct the connectome for a single subject is shown in Figure 1.1. These connectomes can be compared statistically across subjects either on an elementwise basis or using hierarchical graph theory measures (Duarte-Carvajalino *et al.* , 2012). The structural human connectome has already been found to be able to differentiate between the sexes (Jahanshad *et al.* , 2011), associate to developmental age (Gong *et al.* , 2009), and even relate to genetic risk for disease (Brown *et al.* , 2011, Braskie *et al.* , 2012), as well as being altered in disease states itself (Wen *et al.* , 2011).

1.4.3 Imaging protocol dependencies, artifacts, and biases

Despite its strong potential, determining subtle effects of development, genetics, or diseases on brain microstrucure using diffusion based images and tracts can be complicated by the

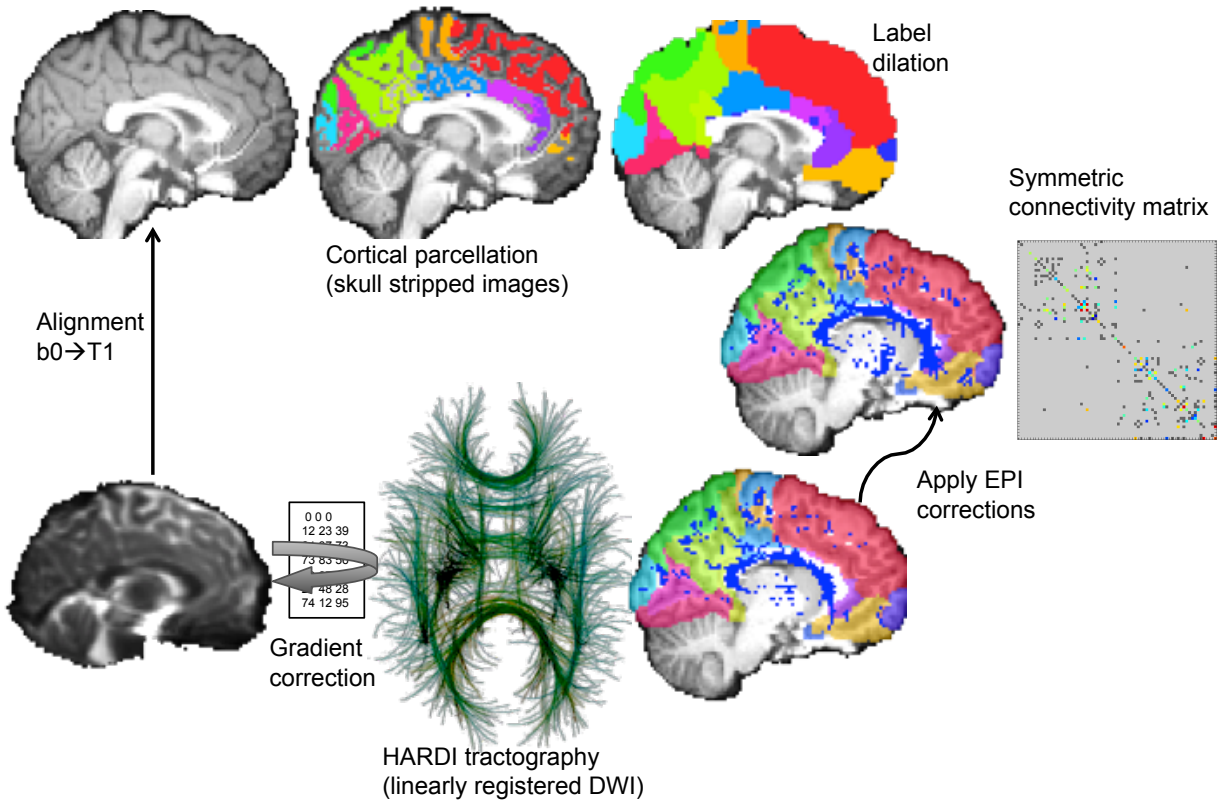

Figure 1.1: Cortical parcellation into N regions is performed on high resolution anatomical images while full brain tractography is performed using the DWI. Images are put in the same space and the proportion of fibers connecting various cortical regions are entered into an NxN matrix describing relative connections between cortical regions.

presence of imaging artifacts (Tournier *et al.* , 2011), and misalignment of small structures across individuals. Therefore, the potential of any imaging technique to identify specific anatomical properties is limited by the resolution of the image, and the signal-to-noise (SNR) level of the scan. DTI allows for the characterization of white matter microstructure on a voxelwise level and allows for the tracing of fiber bundles and white matter tracts throughout the brain. The higher the SNR, the more power the scans will have for estimating genetic influence on brain structure, and studying disease effects. However, as clinically appropriate scan times are kept fairly short to reduce patient discomfort, they therefore enforce limitations on the resolution of DTI. The resolution can be compromised in mainly two ways: 1) the spatial resolution is reduced such that the voxels are larger, or more anatomical mixing

(partial voluming) occurs at each point in the image (Alexander *et al.* , 2001), or 2) fewer directional gradients are imaged, resulting in a noisier reconstruction of the tensor at each voxel (Landman *et al.* , 2007, Zhan *et al.* , 2010). These reductions in resolution independently reduce SNR and power to pick up disease or genetic effects. Despite the fact that diffusion imaging has its limitations, with adequate optimization it becomes an increasingly powerful tool for deepening our understanding of human brain structure as influenced by genetics and environment. As described in the following chapter, we set out to determine temporally stable DTI protocols that are acceptable in a clinical acquisition time and also find imaging measures which are stable for genetic analyses regardless of protocol.

1.5 Heritability and genetic studies

Certain complex neurological diseases such as Alzheimer's disease and psychological disorders such as schizophrenia have been found, independently of brain imaging studies, to be influenced by several genetic risk factors. Heritability studies allow us to estimate the degree to which a particular trait is influenced by genetics and how much is due to environment. Monozygotic twins share all their genes while dizygotic twins share, on average, half. Estimates of the proportion of variance attributable to genes versus environment may be inferred by fitting structural equation models to data from both types of twins. Twin MRI studies have already found that genetic factors strongly influence several aspects of brain structure, such as cortical thickness, and gray and white matter volumes (Thompson *et al.* , 2001b, Hulshoff Pol *et al.* , 2006, Brun *et al.* , 2009, Chou *et al.* , 2009, Kochunov *et al.* , 2010). DTI studies in twins can be used to estimate levels of genetic and environmental effects on fiber architecture; this can help localize the highly genetically influenced regions of white matter. In this sense, neuroimaging markers can serve as intermediate phenotypes, or endophenotypes, for neurological diseases – lying between the genetic markers of interest and the disease outcome (Gottesman & Gould, 2003). Investigating the underlying genetic effect of these brain regions in diseased or disease-free populations with respect to specific candidate genes can be critical in understanding the risk and neurobiological pathways underlying the

progression of disease in the neural networks. Additionally, finding brain regions associated to disease that are also highly genetic will help us search the genome to find undiscovered markers relevant to the pathogenesis of the disease. By using one or several quantitative traits derived from the images as a trait, genome-wide associations studies (GWAS), can be performed to search the genome without any *a priori* expectations of the influence of any particular genes over the anatomy.

1.6 Environmental influence on the brain

While genetic influence on brain structure is strong, some neuroanatomical deficits are influenced heavily by environmental factors. For example, nutritional factors have been shown to greatly affect brain development and cognitive abilities. Iron is a key determinant of neural development and degeneration. Iron deficiency is the most common nutritional deficiency worldwide (CDC, 2002). Iron-deficient diets lead to poorer cognitive achievement in school-aged children (Halterman *et al.* , 2001). Iron deficiency also impairs dopamine metabolism in the brain, particularly in the caudate and putamen regions (Nelson *et al.* , 1997). Brain iron regulation is also disrupted in several neurodegenerative diseases. Neuroimaging methods reveal abnormally high brain iron concentrations in Alzheimers disease (Bartzokis *et al.* , 1994), Parkinson's disease (Bartzokis *et al.* , 1999), and Huntington's disease (Jurgens *et al.* , 2010). High iron concentrations may cause neuronal death (Ke & Ming Qian, 2003, Benarroch, 2009). Iron is transported throughout the body by the iron-binding protein, transferrin. It then enters the brain primarily when transferrin is transported through the blood-brain barrier (Pardridge *et al.* , 1987). Brain iron and transferrin levels are inversely related as iron deficiency promotes the liver to produce more transferrin molecules to better transport iron. Additionally, one of the strongest correlates to the clinical onset of Alzheimer's disease is a person's level of education (Stern *et al.* , 1994). Such degeneration may also be modulated by dietary intake (Raji *et al.* , 2011). Viral infections can also have a strong influence on white matter deterioration. A common Epstein-Barr virus may be critical in the pathogenesis of Multiple Sclerosis (Pender, 2011), a chronic demyelinating disease of

the central nervous system; and the human immunodeficiency virus, HIV, also has a strong influence on gray and white matter structure (Chiang *et al.* , 2007); we show in Section 5.2 that cerebrovascular risk factors can further effect the aberrations found with the infection.

1.7 Organization of the dissertation

All the works presented in this dissertation are performed in order to understand the degree of interplay of genes and environment on white matter integrity and organization within the human brain through the use of diffusion based MRI. Chapters 2-6 reflect published works that help shed light on these associations. Chapter 2 presents work on finding stable, high signal-to-noise measures from DTI. In Section 2.1, a comparison of three clinically acceptable DTI protocols of varying angular and spatial resolutions is made with respect to signal-to-noise and temporal stability. In Section 2.2, two drastically different protocols are compared across a large sample of twins to determine the effect of imaging protocol on heritability and genetic associations. In Chapter 3, the genetics of fiber asymmetry is explored by first determining optimal symmetric registration methods (Section 3.1), followed by the first large-scale voxelwise level study of fiber integrity asymmetry while exploring the relative genetic contributions. In Chapter 4 we explore the epigenetic relation between the common blood serum measure of iron stores, transferrin, and the white matter integrity of the brain to find not only specific regions of the brain to which levels are associated, but also attribute a portion of the epigenetics to a common iron-related genetic variant (in the *HFE* gene) with associations to AD. In Chapter 5, together with other researchers, we apply techniques presented previously to: firstly, map a common AD genetic risk variant in the *CLU* gene to the brain microstructure of young adults decades before typical onset of AD; secondly, we correlate microstructural abnormalities in subcortical structures to cerebrovascular risk factors in HIV infected individuals to find significant basal ganglia and hippocampal abnormalities. In Chapter 6, we utilize HARDI tractography methods to map out the neural connectivity network within healthy individuals and find sex differences in the population as well as specific genetic markers attributable to the variability within the connectome. Chap-

ter 7 describes future works in the field of connectivity by examining network disruptions in AD and HIV infection, as well as developing worldwide efforts for enhancing genetic analysis of white matter through meta analysis.

CHAPTER 2

Optimizing diffusion protocols

2.1 Trade-offs between directional and spatial resolution

The following section is adapted from:

Jahanshad N, Zhan L, Bernstein MA, Borowski B, Jack CR, Toga AW, Thompson PM (2010). Diffusion Tensor Imaging in Seven Minutes: Determining Trade-Offs Between Spatial and Directional Resolution, International Symposium of Biomedical Imaging (ISBI) 2010, Rotterdam, The Netherlands, April 14-17, 2010

DIFFUSION TENSOR IMAGING IN SEVEN MINUTES: DETERMINING TRADE-OFFS BETWEEN SPATIAL AND DIRECTIONAL RESOLUTION

Neda Jahanshad[1], Liang Zhan[1], Matt A. Bernstein[2], Bret J. Borowski[2], Clifford R. Jack Jr[2], Arthur W. Toga[1], Paul M. Thompson[1]

[1]Laboratory of Neuro Imaging, Dept. of Neurology, UCLA School of Medicine, Los Angeles, CA, USA
[2]Mayo Clinic, Rochester, MN, USA

ABSTRACT

Imaging protocols must obtain maximum information under tight time constraints, to minimize patient discomfort or attrition, and motion artifacts. As part of a pilot study optimizing DTI sequences for the Alzheimer's Disease Neuroimaging Initiative, we scanned 8 subjects with 3 DTI protocols of equal duration at two time-points (48 scans). If scan duration is fixed, collecting more diffusion-sensitized gradient directions can increase angular resolution at the expense of spatial. We compared 7-minute sequences with 3.0(48), 2.7(41), and 2.5(37) mm isotropic voxels (directions), to assess (1) SNR; (2) bias in estimating fiber anisotropy; (3) reproducibility over time; (4) intersubject variance--relevant for group comparisons. Statistical maps revealed that higher angular resolutions gave more reproducible estimates; FA depended on voxel size, with a steeper dependency in more heterogeneous regions. The intermediate resolution gave best SNR. 2mm DTI scans are common, but improved angular resolution may add temporal stability, and benefits for tractography.

Index Terms— Diffusion Tensor Imaging (DTI), spatial resolution, angular resolution, signal to noise, imaging protocols

1. INTRODUCTION

For all clinical applications, minimizing patient discomfort is vital. In non-invasive imaging, this mainly involves reducing the scan time as far as possible. Diffusion tensor imaging (DTI) is an MRI-based method to study water diffusion in tissue, and is particularly sensitive to neuronal myelination and white matter micro-architecture. It can also be used to study fiber connectivity in the brain. Various measures, most commonly fractional anisotropy (FA) and mean diffusivity (MD), may be computed from the local diffusion tensor. FA is often used as a measure of local fiber integrity, is correlated with cognitive performance [1], and is sensitive to brain maturation during development and degenerative processes in old age.

The diffusive properties of the anatomy are often modeled by tensors computed at every voxel [2]. Each diffusion tensor is mathematically represented by a 3x3 symmetric positive definite matrix, and may be visualized as an ellipsoid in space with varying levels of anisotropy. To estimate the elliptical tensors for DTI, at least 7 images are required, one with no diffusion sensitization, and 6 non-collinear gradient-encoded diffusion-weighted (DW) images. Due to the poor signal-to-noise in these images, it is often desirable to increase the angular resolution and obtain more than the minimal 7 images. SNR improvements level off as more gradient directions are collected, and SNR plateaus at different rates for different tensor-derived measures [3]. With more gradient directions, or more *q*-space samples at multiple *b*-values [4], one can calculate measures with greater angular and/or radial resolution, including the orientation distribution function (ODF) [5,6], the tensor distribution function (TDF) [7], or the full 3D diffusion propagator, to better characterize the fiber mixture in each voxel. Each DWI obtained takes a fixed amount of time, which depends on the protocol. The more refined the imaging grid, the longer the scan will take. Therefore, to increase the number of diffusion directions while maintaining scan time requires imaging on a coarser anatomical grid. It is therefore clinically useful to understand how trade-offs between angular and spatial resolution impact SNR, bias, and reproducibility, to use the available scan time efficiently.

Previous studies proposed optimal encoding schemes and *q*-space sampling strategies for diffusion tensor images. Many examined effects of applying different sets of gradients directions on diffusion measures [8,9] while others examined effects of spatial resolution [10]. Using 2 mm voxels at 4 Tesla, we recently found that SNR for FA and MD was near-maximal with 66 and 58 gradient directions, but for some ODF-derived measures, such as generalized fractional anisotropy (GFA), SNR still increased rapidly with even more gradient directions [3].

To the best of our knowledge, no study has evaluated the relative benefits of directional versus spatial resolution for ensuring that brain DTI measures are stable over time, given fixed scan time constraints.

Many studies describe procedures to boost SNR through lengthy imaging sessions or repeated scans that may be of value for research purposes [11]. However, long scans

978-1-4244-4126-6/10/$25.00 ©2010 IEEE

can be impractical when imaging children or subjects who are ill or elderly, especially in longitudinal studies where the added patient burden will lead to sample attrition. Methods to minimize noise have been proposed [12]. These procedures may also benefit from estimates of the reproducibility of various acquisitions.

Approaches have also been proposed to optimize the gradient encoding scheme depending on the orientation of the fibers of interest [13] by applying magnetic field gradients to particular locations around the unit sphere rather distributing them uniformly. However, this method may be problematic if the goal is to examine fiber orientations throughout the brain without bias.

Here we imaged 8 subjects with 3 scanning protocols at 2 time-points. Protocols were chosen such that they did not exceed 7 minutes while falling within standard clinical DTI acquisition parameters (2-3mm, > 26 gradients) and could easily be reproduced at multiple ADNI sites across the US. Our goal was to determine the longitudinal reproducibility, SNR, cross-subject variance, and biases, for clinically relevant DTI-derived features. We hope our efforts will help medical researchers decide among protocols when making trade-offs to stay within time constraints.

2. METHODS

2.1. Image Acquisition

We acquired diffusion tensor (DT) MRI scans from 8 control subjects (age: 32.0 +/- 3.9SD; 4 male, 7 right handed) using a GE 3T MRI scanner running 14.0 M5 software. To explore the trade-off between spatial and angular resolution, we used three separate acquisition protocols, each with the acquisition time held fixed at 7 min +/- 3 sec. For each series of images, there was an additional EPI calibration scan lasting approximately 1 min.

Contiguous axial slices were obtained with b = 1000 s/mm^2. To ensure whole-brain coverage, the field of view was fixed at 119 ± 1 mm in the S/I direction and 230.0 $\pm$ 0.4 mm A/P. The coverage in the R/L direction (i.e., the frequency encoded direction) exceeded 320 mm in all cases, so it easily covered the entire head. All imaging protocols acquired 4 b0 images, i.e., T2-weighted images without diffusion sensitization. To keep scan time fixed, TR was allowed to vary, as was the number of DTI angular gradient directions. The parameters are summarized in **Table 1.**

	R1	***R2***	***R3***
Isotropic (mm)	**3.0**	**2.7**	**2.5**
DTI gradient dirs.	**48**	**41**	**37**
TR (ms)	7750	9000	9825
Number of slices	40	44	48
FOV -S/I (mm)	120	118.8	120
FOV-A/P (mm)	230.4	230.1	230.4
FOV-R/L (mm)	384	350	320

Table 1: Different parameters used for each protocol.

Throughout this paper we will refer to these three resolutions by their isotropic voxel size. Each subject was imaged on two separate occasions, two weeks apart, with each protocol.

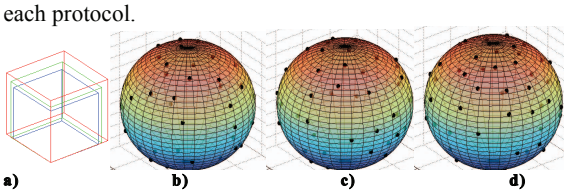

Figure 1: a): Three different voxel sizes were used. The smallest (blue cube) voxel size (2.5 mm) corresponds to the protocol with the *lowest* number of gradient directions. **(b-d)** show points on the unit sphere where diffusion-sensitized gradients were applied for each protocol; the number of gradient directions increases from left to right: 37 in (b), 41 in (c), and 48 in (d).

2.2. Preprocessing, Registration and Tensor Estimation

For all 48 sets of images (8 subjects, 3 protocols, 2 time points), diffusion-weighted images were corrected for motion and eddy current distortion using FSL (http://fsl.fmrib.ox.ac.uk/fsl). Tensors were created using MedINRIA(www.sop.inria.fr/asclepios/software/MedINRIA). Extra-cerebral matter was removed using FSL.

The first b0 image of all subjects, which was used as the reference image for motion and eddy current correction, was aligned to a common template. All subjects' images were linearly registered to a high-resolution single subject average scan, the Colin27 [14], using FSL's FLIRT software with 9-parameters (df) to avoid shearing. The corresponding transformation matrices were retained. To optimize registration, these linearly aligned images were then mapped to the template using a mutual information based elastic registration [15].

2.3. Anisotropy and Signal to Noise (SNR) Calculations

Linearly aligned tensors were used to obtain scalar maps of anisotropy. Eigen-values were extracted from the diffusion tensors. Fractional anisotropy (FA), and the mean diffusivity (MD) - were calculated as follows:

$$FA = \sqrt{\frac{3}{2}} \frac{\sqrt{(\lambda_1 - \bar{\lambda})^2 + (\lambda_2 - \bar{\lambda})^2 + (\lambda_3 - \bar{\lambda})^2}}{\sqrt{\lambda_1^2 + \lambda_3^2 + \lambda_3^2}}$$

$$MD = \bar{\lambda} = \frac{\lambda_1 + \lambda_3 + \lambda_3}{3}$$

Once scalar maps were calculated, the corresponding deformation fields from the nonlinear mappings were applied to align anatomy across protocols. SNR is reported as a ratio between the mean signal for all subjects over the standard deviation, in regions of interest selected for their anatomical homogeneity.

2.4. ROI Extraction and Statistical Analyses

To compare anisotropy measures in the subjects' anatomy across protocols, regions of interest (ROIs) were extracted from the template scan and applied to the individual

registered scans. Regions examined included the splenium of the corpus callosum, and the frontal lobe.

For statistical analyses, we used paired Student's *t*-tests to compare ROI and voxel-based anisotropy measures across time points and to compare various scanning protocols. As we expected noise to play a role in this analysis, we also examined protocol-dependent differences in the group variance of FA and MD values, using *F*-tests.

3. RESULTS

3.1. Anisotropy Averages

Figure 2 shows the mean and standard deviations for the FA and MD measures, for each scanning protocol (N=16). Qualitative differences are seen among the three different protocols.

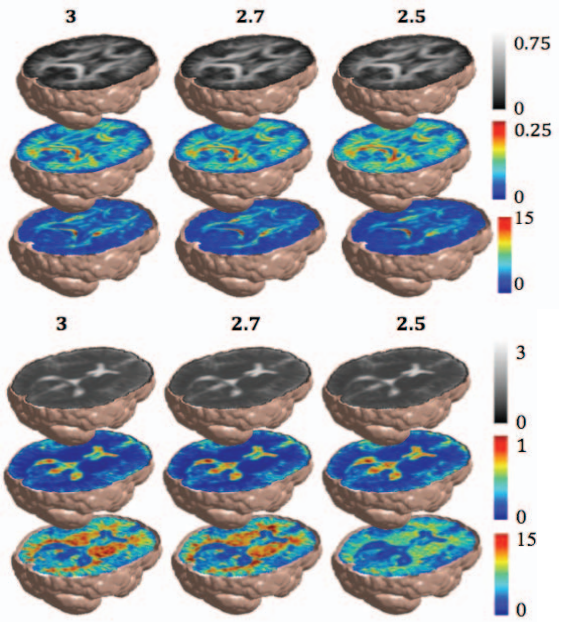

Figure 2: The μ (top), σ(mid), and SNR = (μ/σ) (bottom) for FA (**a**) and MD (**b**) are shown for all resolutions. 2.5mm scans give higher variance in caudate and optic radiations, resulting in a lower SNR.

3.2. Differences in Anisotropy Mean and Variance

Figure 3 shows significant differences in FA and MD values between the three different resolutions using one sided paired t-tests including every subject at a single time point (N=8). False Discovery Rate (FDR) analysis confirmed these differences after multiple comparison correction.

Figure 4 highlights regions where the group variance between the resolutions is significantly different, using one sided paired *F*-tests at every voxel. In general, sequences with large voxels and more gradient directions have less noise and variance across the subject sample.

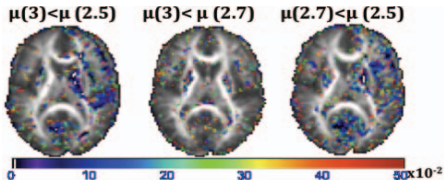

Figure 3: One-sided pairwise *t*-tests, comparing FA between protocols, highlight regions where the coarser spatial resolution image had systematically lower anisotropy, due a greater partial volume effect. No significant differences were detected for MD (*not shown*).

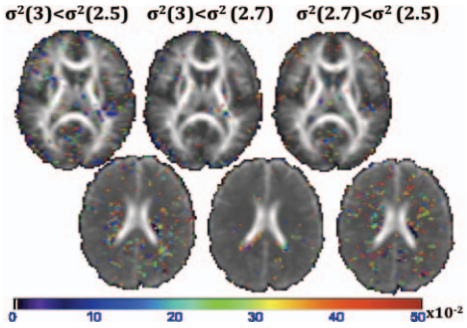

Figure 4: *F*-tests at every voxel highlight differences in sample (cross-subject) variances between protocols for FA (top) and MD (bottom). No significant difference is seen between 3mm and 2.7mm voxels. The 2.5mm protocol gives higher variance across the sample.

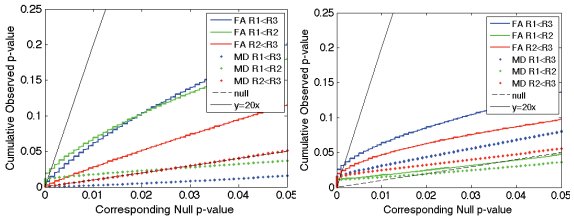

Figure 5: Multiple comparison correction was performed using the FDR procedure for *t*-tests (left) and *F*-tests (right). Significant differences exist in the means and variance of anisotropy for voxels of size 2.5 and 3mm.

3.3. ROI analysis and Consistency

Figure 5 shows average FA values in the frontal lobe and splenium, plotted against the number of gradient directions.

The average FA values in the ROIs were also measured at each time-point. The protocol using 3mm isotropic voxels

was most stable over time, but it gave artificially lower values for FA (**Figure 8**); this is a consequence of increased partial volume effects, in which voxels with more than one fiber direction appear more isotropic with large voxels.

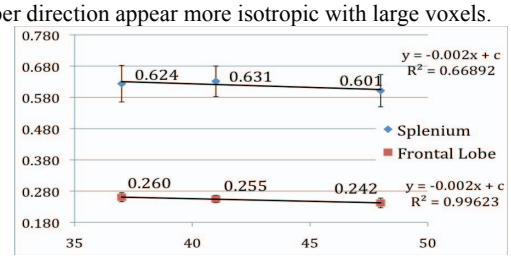

Figure 6: Mean FA values are shown (error bars denote standard deviations) for ROIs using various scan resolutions. Higher linear correlations with voxel size are found in the frontal lobe, which has more fiber crossing (partial volumed voxels) than the splenium. As expected, effects of voxel size on FA are less pronounced in regions where fiber coherence is high.

Figure 7 shows the average (N=8) absolute difference, and standard deviation of differences, between time points for FA at every resolution.

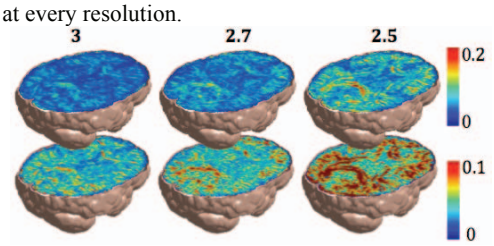

Figure 7: Maps of mean and standard deviation for the absolute FA difference in scans across time. Scans with larger voxels, but more gradient directions, give more reproducible measures.

4. CONCLUSIONS

Differences were clear between the two most extreme resolution protocols (3mm versus 2.5mm voxels). Scans with the largest voxel size and angular resolution were most stable over time, and had least variance for DTI-derived measures across the group of 8 subjects. Scans with smaller voxels and sparser angular sampling were less stable over time. The intermediate resolution scan had highest SNR, and intermediate stability and bias for FA estimation. Temporal stability alone is critical in clinical studies to allow detection of change overtime; instability can lead to false conclusions on the progression of dementia.

In future, we will examine specific tracts and compare images after DTI denoising and other types of cross-subject registration. We will also examine uncertainty in the principal eigenvector field, and in the directions of the ODF maxima, to understand how these protocols may affect reconstruction accuracy in tractography studies.

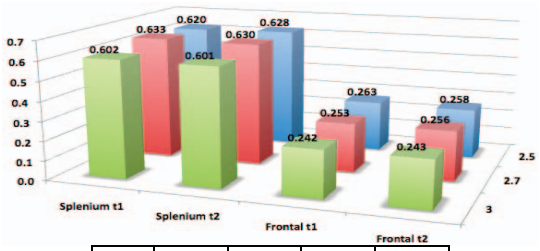

SNR	S t1	S t2	F t1	F t2
2.5	11.48	9.97	17.54	18.41
2.7	13.76	12.11	19.48	23.31
3	12.04	11.33	17.28	14.28

Figure 8: FA in the splenium and the frontal lobe plotted at 2 time points, t1 and t2. SNR (μ/σ) is consistently highest in scans with intermediate voxel size (*middle row*).

5. REFERENCES

[1] Chiang MC et al. Genetics of brain fiber architecture and intelligence. **J. Neuroscience**, Feb 18; 29(7):2212-24 (2009)

[2] Basser P et al. Estimation of the effective self-diffusion tensor from the NMR spin echo. **J Mag Res B** 103, 247-254 (1994)

[3] Zhan L et al. How does angular resolution affect diffusion imaging measures? **NeuroImage**, available online Sep. 2009, DOI: 10.1016/j.neuroimage.2009.09.057 (2009)

[4] Wedeen VJ et al. Mapping complex tissue architecture with diffusion spectrum magnetic resonance imaging, **MRM** 54(6):1377-1386 (2005)

[5] Tuch DS. Q-ball Imaging. **MRM** 52(6):1358-1372 (2004)

[6] Aganj I. ODF reconstruction in *q*-ball imaging with solid angle considerations. **Proc. IEEE ISBI** (2009)

[7] Leow AD et al. The tensor distribution function. **MRM** 61(1):205-214 (2008)

[8] Landman B et al. Effects of diffusion weighting schemes on the reproducibility of DTI-derived fractional anisotropy, mean diffusivity, and principal eigenvector measurements at 1.5T, **NeuroImage** 36(4): 1123-1138 (2007)

[9] Hasan KM et al. Comparison of Optimization Procedures for Diffusion Tensor Encoding Directions **Proc ISMRM** 8:792 (2000)

[10] Fujiwara S et al. Feasibility of 1.6mm isotropic voxel diffusion tensor tractography in depicting limbic fibers. **Diagnostic Neuroradiology** 50:131-136 (2008)

[11] Liu X et al. Optimization of in vivo high-resolution DTI of non-human primates on a 3T human scanner. **Methods** (2009)

[12] Hasan KM et al. Evaluation of SNR Performance and Utility of High Spatial and Angular Resolution Denoised 1mm^3 Isotropic DTI of Entire Human Brain at 3T. **Proc ISMRM** 14:334 (2006)

[13] Peng H, Arfanakis K. Diffusion tensor encoding schemes optimized for white matter fibers with selected orientations. **Mag Res Imaging** 25:147:153 (2007)

[14] Holmes CJ et al. Enhancement of MR images using registration for signal averaging. **JCAT** 22(2):324-33 (1998).

[15] Leow A et al. Statistical Properties of Jacobian Maps and the Realization of Unbiased Large-Deformation Nonlinear Image Registration, **IEEE TMI** 26(6):822-832(2007)

2.2 Identifying protocol independent genetic associations

The following section is adapted from:

Jahanshad N, Kohannim O, Toga AW, McMahon KL, de Zubicaray GI, Martin NG, Wright MJ, and Thompson PM (2012). Diffusion imaging protocl effects on genetic associations. International Symposium of Biomedical Imaging (ISBI) Barcelona, Spain, May 2-5 2012.

DIFFUSION IMAGING PROTOCOL EFFECTS ON GENETIC ASSOCIATIONS

Neda Jahanshad[1], Omid Kohannim[1], Arthur W. Toga[1], Katie L. McMahon[2], Greig I. de Zubicaray[3], Narelle K. Hansell[4], Grant W. Montgomery[4], Nicholas G. Martin[4], Margaret J. Wright[4], and Paul M. Thompson[1]

[1]Laboratory of Neuro Imaging, Department of Neurology, UCLA School of Medicine, Los Angeles, CA
[2]University of Queensland, Centre for Advanced Imaging, Brisbane, Australia
[3]University of Queensland, School of Psychology, Brisbane, Australia
[4]Queensland Institute of Medical Research, Brisbane, Australia

ABSTRACT

Large multi-site image-analysis studies have successfully discovered genetic variants that affect brain structure in tens of thousands of subjects scanned worldwide. Candidate genes have also associated with brain integrity, measured using fractional anisotropy in diffusion tensor images (DTI). To evaluate the heritability and robustness of DTI measures as a target for genetic analysis, we compared 417 twins and siblings scanned on the same day on the same high field scanner (4-Tesla) with two protocols: (1) 94-directions; 2mm-thick slices, (2) 27-directions; 5mm-thickness. Using mean FA in white matter ROIs and FA 'skeletons' derived using FSL, we (1) examined differences in voxelwise means, variances, and correlations among the measures; and (2) assessed heritability with structural equation models, using the classical twin design. FA measures from the *genu* of the corpus callosum were highly heritable, regardless of protocol. Genome-wide analysis of the genu mean FA revealed differences across protocols in the top associations.

Index Terms— imaging genetics, DTI protocol stability, corpus callosum, genome-wide association study, multi-site analysis

1. INTRODUCTION

Large-scale meta-analyses of brain images, such as the ENIGMA project ([1], http://enigma.loni.ucla.edu) reveal common variants on the human genome that are associated with measurable brain differences. Each of these variants individually explains less than 5% of the variance in the brain measures, so the quest to identify them has been empowered by multivariate models of the image and genome [2], as well as meta-analysis.

Large imaging genetics consortia, such as ENIGMA, have recently combined structural imaging measures and genome-wide scans (GWAS) from 20,800 individuals assessed at over 21 sites worldwide, and have identified robust gene effects not detectable in any single cohort but replicated by meta-analysis. These meta-analyses have identified common genetic variants associated with hippocampal volume and total brain volume [1]. In a multi-site study, any differences across sites in scanning protocols (different scanner field strengths, image resolutions) and in image analysis protocols (such as segmentation methods) may reduce power to find and replicate genetic associations. Segmentation programs, for example, do not always work well across all datasets [3]. Realizing that scanner effects may matter, some studies have recently compared 1.5 and 3 Tesla scans of the same subjects for detecting neurodegenerative changes with morphometric analysis [4].

Recently, DTI measures have shown promising associations with common genetic variants, such as those in the Alzheimer's disease risk gene, *CLU* [5] and the growth factor gene, *BDNF* [6]. However, the reproducibility and signal-to-noise ratio in DTI depends on the spatial and angular resolution (the number of directional diffusion-weighted gradients applied) [7]. Structural MRI images are typically acquired with ~1-mm^3 spatial resolution, but 2-5 mm voxels are common for diffusion-weighted scans. Additionally, the number of diffusion-weighted gradients applied may vary drastically, from the minimum needed to reconstruct a tensor (6), to high angular resolution (HARDI) scans with hundreds of diffusion-weighted scans.

To determine a stable DTI phenotype for genetic analysis, here we analyzed DTI scans from 417 genotyped twins and siblings scanned with two diffusion imaging protocols, differing in spatial (2mm vs 5mm slices) and angular resolution (27 vs 94 directions). Common voxelwise and region-of-interest analyses were performed on FA maps and on the FA 'skeletons' from the widely-used method, TBSS ('tract-based spatial statistics' from FSL [8]). Various levels of Gaussian smoothing were also applied to the FA images prior to analysis. As genetic associations are likely to be discovered only for traits that are heritable, a formal twin-based heritability analysis was performed using an A/C/E-type structural equation model on the mean FA of various regions defined by the JHU-DTI atlas. A region of the corpus callosum, with high heritability regardless of to the protocol, was then carried forward for genome-wide association analyses (GWAS) where the most significantly associated single nucleotide polymorphisms (SNPs) from different protocols and analyses were compared.

2. METHODS

2.1. Image Acquisition and Genotyping

Structural and diffusion-weighted whole-brain MRI scans were acquired for each of 620 genotyped subjects (on a 4T Bruker Medspec scanner in Brisbane, Australia). T1-weighted images were acquired with an inversion recovery rapid gradient echo sequence (TI/TR/TE = 700/1500/3.35 ms; flip angle=8°; slice thickness = 0.9 mm, with a 256^2 acquisition matrix). Diffusion-weighted images were acquired using single-shot echo planar imaging with a twice-refocused spin echo sequence to reduce eddy-current induced distortions.

The first imaging protocol consisted of a 3-minute, 30-image acquisition designed to optimize signal-to-noise ratio for diffusion tensor estimation [9]. Imaging parameters were: TR/TE=6090/91.7 ms, FOV=23 cm, with a 128x128 acquisition matrix. Each 3D volume consisted of 21 5-mm thick axial slices with a 0.5mm gap, and a 1.8x1.8 mm^2 in-plane resolution. 30 images were acquired

978-1-4577-1858-8/12/$26.00 ©2012 IEEE

per subject: 3 with no diffusion sensitization (i.e., T2-weighted b_0 images) and 27 diffusion-weighted (DW) images (b = 1132 s/mm^2) with gradient directions uniformly distributed on the hemisphere. We will refer to this protocol as DTI-30.

The second imaging protocol was used for 490 of the same subjects. It consisted of a 14.2-minute, 105-image acquisition. Imaging parameters were: TR/TE=6090/91.7 ms, FOV=23 cm, with a 128x128 acquisition matrix. Each 3D volume consisted of 55 2-mm thick axial slices with no gap and 1.8x1.8 mm^2 in-plane resolution. 105 images were acquired per subject: 11 with no diffusion sensitization (i.e., T2-weighted b_0 images) and 94 diffusion-weighted (DW) images (b = 1149 s/mm^2) with gradient directions uniformly distributed on the hemisphere. We refer to this protocol as DTI-105.

Genomic DNA was analyzed on the Human610-Quad BeadChip (Illumina) according to the manufacturers' protocols (Infinium HD Assay; Super Protocol Guide; Rev. A, May 2008).

2.2. Image Processing and Co-registration

Extracerebral tissues were removed from structural and diffusion-weighted images with ROBEX [3]and FSL's BET, respectively. All DW images were corrected for minor motion and eddy current distortions using FSL. Average b0 images were elastically registered [10] to T1-scans to adjust for EPI-induced distortions.

Using the high-resolution scans, a minimal deformation template (MDT) was created based on corrected FA maps from 32 (16M/16F) subjects. Template creation and subject coregistration of FA maps was performed as in [11]. Registered FA maps were also smoothed with different sized Gaussian filters (5- and 7-mm FWHM) to assess differences related to smoothing of the data.

Rigorous quality control (QC) excluded subjects with imaging artifacts in their raw scans including slice dropouts, excess movement, or a cropped FOV. All scans from both protocols were also assessed for the quality of their registration to the template image. This thorough QC filtering of scans left 417 subjects with usable scans for both DWI protocols.

TBSS [8] was performed using the registered images. We did not use the full TBSS pipeline including registration, to ensure that differences in registration methods did influence our analysis. TBSS was performed for all co-registered raw FA maps, as well as those smoothed at 5 and 7mm, for both the DTI-30 and DTI-105 scans. The suggested FA threshold of 0.2 was used.

12 sets of images were analyzed in total – 6 (3 variously smoothed DTI-30 and 3 DTI-105) images of the full WM in 3D (not just skeletons), and 6 corresponding TBSS skeletons.

2.3. Defining regions of interest

The FA image from the Johns Hopkins University DTI atlas [12] was registered to the MDT using the same registration pipeline used for co-registration. Deformations from this registration were applied to the atlas labels defining 50 regions of interest. 10 of these regions - including the lower part of the corticospinal tract and the cerebellar peduncles - fell mostly or partly outside the cerebral field of view and were excluded from analysis. **Table 1** lists the regions assessed.

Table 1 - Regions of interest evaluated from the JHU DTI atlas

3/4/5	G/B/SCC	*Genu*/body/*splenium* of corpus callosum
6	FX	Fornix (column and body of fornix)
15/16	CP	Cerebral peduncle L/R
17/18	ALIC	Anterior limb of internal capsule L/R
19/20	PLIC	Posterior limb of internal capsule L/R
21/22	RLIC	Retrolenticular part of internal capsule L/R
23/24	ACR	Anterior *corona radiata* L/R
25/26	SCR	Superior *corona radiata* L/R
27/28	PCR	Posterior *corona radiata* L/R
29/30	PTR	Posterior thalamic radiation L/R
31/32	SS	Sagittal stratum L/R
33/34	EC	External capsule left
35/36	CGC	Cingulum (cingulate gyrus) L/R
37/38	CGH	Cingulum (hippocampus) L/R
39/40	FX/ST	Fornix (*crus*) / *stria terminalis* L/R
41/42	SLF	Superior longitudinal fasciculus L/R
43/44	SFO	Superior fronto-occipital fasciculus L/R
45/6	IFO	Inferior fronto-occipital fasciculus L/R
47/8	UNC	Uncinate fasciculus L/R
49/50	TAP	*Tapetum* L/R

2.4. Voxelwise/ROI comparison maps

Images were analyzed on a voxelwise level by performing *t*-tests, *F*-tests, and correlations to assess differences between the DTI-30s and DTI-105s. We assessed differences in the means and standard deviations of the DTI-derived measures, as well as correlations between them. For this analysis, we assessed a subset of 266 unrelated subjects to avoid the kinship issue (correlated samples).

2.4. A/C/E Heritability Analysis

A covariance matrix S_g was obtained for every white matter ROI for all twins (identical and fraternal). A structural equation model (SEM) was fitted to compare the observed and expected covariances (under different degrees of heritability) to infer the proportion of the variance attributable to additive genetic (A), shared environmental (C) and unique environmental (E) components of variance [13]: $Z = Aa + Cc + Ee$. Z can be any quantitative phenotypic trait, in this case the mean FA for the particular ROI. A, C, and E are latent (unobserved) variables and a, c, e are each parameter's weights determined by optimizing S via full information maximum likelihood estimation (FIML). The variance components combine to create the total observed inter-individual variance, and sum to one: $a^2 + c^2 + e^2 = 1$

This SEM uses FIML: $FIML_g = N_g\left\{\ln|S_g| - \ln|\Sigma_g| + tr\left(S_g\Sigma_g^{-1}\right) - 2m\right\}$ with a χ^2 null distribution to estimate genetic versus environmental contributions to the observed variance, where m is the number of twin pairs per group (48 for MZ and 74 for DZ), S_g is the observed covariance matrix for each twin group g, and Σ_g is the expected covariance matrix for group g, with α=1 for the MZ group and α=0.5 for DZ: $\Sigma_g = \begin{bmatrix} a^2+c^2+e^2 & \alpha a^2+c^2 \\ \alpha a^2+c^2 & a^2+c^2+e^2 \end{bmatrix}$

In SEM, the χ^2 goodness of fit measure determines a p-value for all specified regions of interest (elements of the matrix) where the test was performed. This value indicates that the model fits the data well if p>0.05 (this is the opposite of the usual convention that rejects models or hypotheses).

OpenMX software [14] was implemented in R (http://www.r-project.org/) to calculate the A/C/E parameters. Subject sex was added to the model to control for the inclusion of mixed-sex dizygotic twin pairs.

2.3. Genome-wide associations across protocols

Genome-wide associations were performed for the mean FA in the *genu* of the corpus callosum - approximately the front third of the CC as defined by the JHU atlas. The mean FA was defined for regions-of-interest in the full FA map or the TBSS skeleton, by overlaying the co-registered, parcellated, JHU atlas on the individual data. To account for family structure, EmmaX [15] was used, with a kinship matrix specifying the relationships among family members, to fit a mixed effects model regression. As with the A/C/E model, MZ twins were coded with a kinship of 1 and dizygotic twins and siblings with 0.5. The kinship for unrelated individuals was set to 0. SNPs (single nucleotide polymorphisms) with a minor allele frequency (MAF) below 0.05 were excluded from the analysis, leaving a total of 500,628 SNPs. As no SNPs were found to be genome-wide significant ($5x10^{-8}$) across the GWASs, we set a threshold for suggestive significance of $5x10^{-5}$. GWAS results from protocols were compared in the following respects: 1) the number of SNPs found to be suggestively significant, 2) the number of those SNPs that were also significant between protocols (DTI-30 and DTI-105), 3) the number of those SNPs that are also suggestively significant in the other protocol, 4) the most significant (lowest) *p*-value for genetic association, and whether that same SNP was also significant in the corresponding matched protocol.

3. RESULTS

Voxelwise tests are shown in **Figures 1-2** for unsmoothed images overlaid on the JHU atlas ROIs. Paired *t*-tests between the DTI-30 and DTI-105 protocols (not shown) revealed that only sparsely distributed voxels on the borders of tracts appear to have similar values. This is expected as FA value is much lower in images with larger voxels (due to partial volume effects). **Figure 1** shows the results of *F*-tests between the DTI-30 and DTI-105 protocols. Even when mean values of FA differ (as seen through the *t*-tests), many WM regions do not significantly differ in variance structure ($p > 0.05$ from an *F*-test) despite differences in imaging protocols. This is an important consideration for imaging genetics studies, as the variance structure is decomposed to estimate the contributions of genetic and environmental factors to the observed variance. **Figure 2** shows Pearson's correlations between measures derived from the two protocols. The *genu* and longitudinal *fasciculi* show high correlations while the *splenium* shows lower correlation.

Results showing variance components from A/C/E analysis of the JHU ROIs are shown in **Figure 3** for the full FA maps and **Figure 4** for the TBSS analysis. Regions (including the *splenium* of the corpus callosum) were not shown if the A/C/E model did not fit the data well (in SEMs, this means that the *p*-value for the fit was *less* than 0.05). Genetic components (a^2) derived from A/C/E structural equation modeling of 48 pairs of monozygotic twins and 74 pairs of dizygotic twins in ROIs defined on TBSS skeletonized FA maps, although higher, were not as indifferent to smoothing or protocol as when using the full ROIs. The smoothing level did not influence results as much as the scanning protocol. More regions' mean FA values were more heritable when not skeletonized: the *genu* of the corpus callosum generally exhibited high heritability regardless of the protocol, level of smoothing, or the type of analysis (TBSS or otherwise). Therefore, we carried forward the mean genu FA as a target phenotype to run genome-wide associations.

Table 2 shows results from the various GWAS analyses. When using full ROIs as opposed to the TBSS skeletal ROIs, a single SNP was suggestively significant in both the DTI-30 and the DTI-105 protocols in all smoothing schemes. Interestingly, the *lower* resolution scans yielded more suggestively significant SNPs for both TBSS GWAS and otherwise. Surprisingly, most SNPs that were suggestive in one protocol were not so in the other, with some not even nominally significant ($p<0.05$) in the other protocol. Not skeletonizing the FA (i.e. averaging across the full ROI) resulted in roughly the same amount of suggestively associated SNPs. As evident by the 5mm smoothed results, some smoothing may be beneficial for finding more consistently associated SNPs.

Table 2 – Genome-wide associations for the different DTI protocols at different smoothing levels reveal varying numbers of suggestively associated SNPs. Little difference in protocol variation is seen between skeletonizing the FA maps and using the full ROI.

		# SNPs suggestively significant	# SNPs significant in matched protocol	# SNPs suggestive in matched protocol	Does the lowest *p*-value replicate? (yes/no)
TBSS-0mm	**105**	27	12	1	$4.9x10^{-6}$-N
	30	31	18	1	$2.3x10^{-6}$-N
fullROI-0mm	**105**	28	16	1	$5.4x10^{-6}$ -Y
	30	55	39	1	$5.6x10^{-7}$ -N
TBSS-5mm	**105**	30	21	2	$6.7x10^{-7}$-Y
	30	58	41	2	$3.5x10^{-7}$-Y
fullROI-5mm	**105**	27	18	2	$3.1x10^{-7}$-Y
	30	58	40	2	$4.7x10^{-7}$-Y
TBSS-7mm	**105**	29	22	1	$1.1x10^{-6}$-Y
	30	54	38	1	$4.5x10^{-7}$-N
fullROI-7mm	**105**	26	18	1	$1.1x10^{-6}$-Y
	30	62	36	1	$5.2x10^{-7}$-N

4. DISCUSSION

In this large DTI study of over 400 individuals, we compared two very different diffusion imaging protocols to determine a stable phenotype for genetic analysis. The *genu* of the corpus callosum showed high heritability, regardless of imaging protocol and the method used to define its mean FA. However, in GWAS analyses, the most significant SNPs from one protocol were not necessarily replicated in another, which suggests the critical need for meta-analysis and/or multivariate methods that simultaneously assess sets of locations on the genome and the image [2]. Amazingly, regardless of protocol, level of smoothing, skeletonization or not, one single SNP continuously showed suggestive significance.

One limitation of this study is that in order to ensure that different registration methods did not play a role in our comparisons, we did not use FSL registrations typically used for TBSS analysis; this will be assessed in future. Additionally, ROI analyses incur partial voluming effects, when the atlas is not perfectly aligned with the individual data. Fiber tractography and clustering may be useful to obtain improved ROIs in the future.

REFERENCES

[1]ENIGMA Consortium, "Genome-Wide Association Meta-Analysis of Hippocampal Volume: Results from the ENIGMA Consortium," in *Organization for Human Brain Mapping*, Quebec City, Canada, 2011.
[2]D. P. Hibar, *et al.*, "Multilocus genetic analysis of brain images," *Frontiers in Genetics,* vol. 2, October 21 2011.
[3]J. E. Iglesias, *et al.*, "Robust brain extraction across datasets and comparison with publicly available methods," *IEEE Trans Med Imaging,* vol. 30, pp. 1617-34, Sep 2011.
[4]A. J. Ho, *et al.*, "Comparing 3 T and 1.5 T MRI for tracking Alzheimer's disease progression with tensor-based morphometry," *Hum Brain Mapp,* vol. 31, pp. 499-514, Apr 2010.
[5]M. N. Braskie, *et al.*, "Common Alzheimer's Disease Risk Variant within the *CLU* Gene Affects White Matter Microstructure in Young Adults," *J Neurosci,* vol. 31, 2011.
[6]M. C. Chiang, *et al.*, "*BDNF* gene effects on brain circuitry replicated in 455 twins," *Neuroimage,* vol. 55, pp. 448-54, 2011.
[7]L. Zhan, *et al.*, "How does angular resolution affect diffusion imaging measures?," *NeuroImage,* vol. 49, pp. 1357-71, 2010.
[8]S. M. Smith, *et al.*, "Tract-based spatial statistics: voxelwise analysis of multi-subject diffusion data," *Neuroimage,* vol. 31, pp. 1487-505, Jul 15 2006.
[9]D. K. Jones, *et al.*, "Optimal strategies for measuring diffusion in anisotropic systems by magnetic resonance imaging," *Magn Reson Med,* vol. 42, pp. 515-25, Sep 1999.
[10]A. D. Leow, *et al.*, "Statistical properties of Jacobian maps and the realization of unbiased large-deformation nonlinear image registration," *IEEE Trans Med Imaging,* vol. 26, pp. 822-32, 2007.
[11]N. Jahanshad, *et al.*, "Genetic influences on brain asymmetry: a DTI study of 374 twins and siblings," *Neuroimage,* vol. 52, pp. 455-69, Aug 15 2010.
[12]S. Mori, *et al.*, "Stereotaxic white matter atlas based on diffusion tensor imaging in an ICBM template," *Neuroimage,* vol. 40, pp. 570-82, Apr 1 2008.
[13]F. V. Rijsdijk and P. C. Sham, "Analytic approaches to twin data using structural equation models," *Brief Bioinform,* vol. 3, pp. 119-33, Jun 2002.
[14]S. Boker, *et al.*, "OpenMx: An Open Source Extended Structural Equation Modeling Framework," *Psychometrika,* vol. 76, pp. 306-317, Apr 2011.
[15]H. M. Kang, *et al.*, "Variance component model to account for sample structure in genome-wide association studies," *Nat Genet,* vol. 42, pp. 348-54, Apr 2010.

ACKNOWLEDGMENTS

This work was supported by NIH grant R01 HD050735, NHMRC (Australia) grant 496682, R01 EB008281, and P41 RR013642.

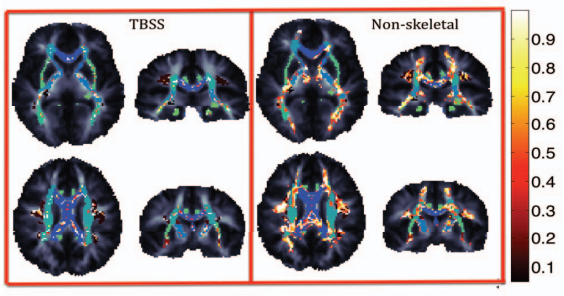

Figure 1 – Voxelwise *F*-tests between DTI-30 and DTI-105 protocols (in 266 independent subjects) to test the difference in FA variation (across the sample) at every voxel. Regions are highlighted if they are *not* significantly different (p>0.05). Green/blue regions represent ROIs from the JHU atlas.

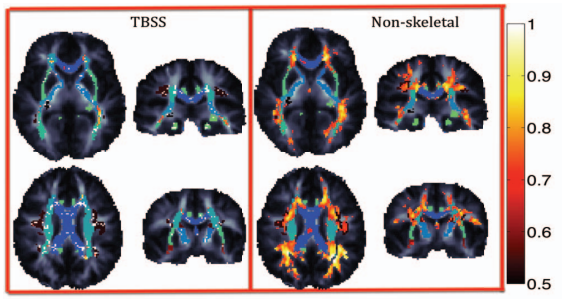

Figure 2 – Voxelwise Pearson's correlations between DTI-30 and DTI-105 protocols (in 266 independent subjects). In some regions is very strong (*hot colors* run from 0.5 to 1).

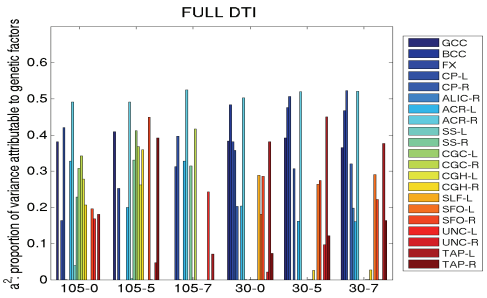

Figure 3 – The heritability of DTI measures (i.e., the genetic component of variance, a^2) derived from A/C/E structural equation modeling of 48 pairs of monozygotic twins and 74 pairs of dizygotic twins depends little on the smoothing level applied, but is highly dependent on imaging protocol. The *x*-axis shows the number of diffusion gradients followed by the level of smoothing applied (FWHM in mm)

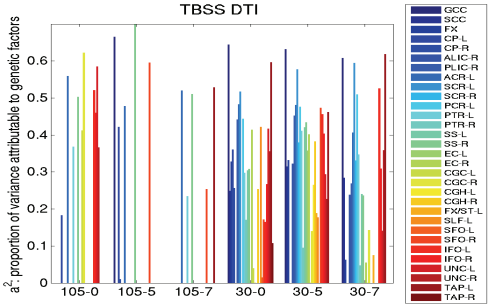

Figure 4 – Heritability (i.e., genetic component of variance, a^2) for ROIs defined on TBSS skeletonized FA maps is generally higher, but not as indifferent to smoothing or protocol used as when using the full ROIs to compute the mean FA.

CHAPTER 3

Fiber asymmetry

3.1 Optimal template for asymmetry registration

The following section is adapted from:

Jahanshad N, Lee AD, Lepor N, Chou YY, Brun CC, Barysheva M, Toga AW, McMahon KL, de Zubicaray GI, Wright MJ, Thompson PM (2009). Genetics of anisotropy asymmetry: registration and sample size effects. Med Image Comput Comput Assist Interv (MICCAI) London, England 2009; 12 (Pt 2): 498-505.

Genetics of Anisotropy Asymmetry: Registration and Sample Size Effects

Neda Jahanshad[1,2], Agatha D. Lee[1], Natasha Leporé[1], Yi-Yu Chou[1], Caroline C. Brun[1], Marina Barysheva[1], Arthur W. Toga[1], Katie L. McMahon[3], Greig I. de Zubicaray[3], Margaret J. Wright[4], and Paul M. Thompson[1]

[1] Laboratory of Neuro Imaging, Department of Neurology, UCLA, CA USA
[2] Medical Imaging Informatics Group, Department of Radiology, UCLA, CA USA
[3] University of Queensland, fMRI Laboratory, Centre for MR, Brisbane, Australia
[4] Queensland Institute of Medical Research, Brisbane, Australia

Abstract. Brain asymmetry has been a topic of interest for neuroscientists for many years. The advent of diffusion tensor imaging (DTI) allows researchers to extend the study of asymmetry to a microscopic scale by examining fiber integrity differences across hemispheres rather than the macroscopic differences in shape or structure volumes. Even so, the power to detect these microarchitectural differences depends on the sample size and how the brain images are registered and how many subjects are studied. We fluidly registered 4 Tesla DTI scans from 180 healthy adult twins (45 identical and fraternal pairs) to a geometrically-centered population mean template. We computed voxelwise maps of significant asymmetries (left/right hemisphere differences) for common fiber anisotropy indices (FA, GA). Quantitative genetic models revealed that 47-62% of the variance in asymmetry was due to genetic differences in the population. We studied how these heritability estimates varied with the type of registration target (T1- or T2-weighted) and with sample size. All methods consistently found that genetic factors strongly determined the lateralization of fiber anisotropy, facilitating the quest for specific genes that might influence brain asymmetry and fiber integrity.

1 Introduction

Asymmetries in brain structure and function have been the topic of neuroimaging studies for many years. Anatomical asymmetries may help to reveal the origins of lateralized cognitive functions or behavioral traits, such as language and handedness, that may arise from partially genetic hemispheric differences during development [1]. Studies of brain asymmetry can also inform clinical research, as aberrant asymmetries have been hypothesized or detected in disorders such as schizophrenia, dyslexia, or hemiparesis, which may arise from a derailment in processes that establish normal brain lateralization and hemispheric specialization. Deformation-based morphometry studies have used the theory of random Gaussian vector fields to detect statistical departures from the normal level of brain asymmetry [2].

G.-Z. Yang et al. (Eds.): MICCAI 2009, Part II, LNCS 5762, pp. 498–505, 2009.

Genetics of Anisotropy Asymmetry: Registration and Sample Size Effects

Many imaging studies have used MRI to study brain asymmetries, but very few have used DTI. In DTI, the MR signal attenuation due to water diffusion in direction k decreases according to the Stejskal-Tanner equation: $S_k(\mathbf{r}) = S_0(\mathbf{r})e^{-b_k D_k(\mathbf{r})}$ where $S_0(\mathbf{r})$ is the non-diffusion weighted baseline intensity, $D_k(\mathbf{r})$ is the apparent diffusion coefficient (ADC), and b_k is Le Bihan's factor; the fractional and geodesic anisotropy (FA and GA), calculated from a local tensor approximation for $D_k(\mathbf{r})$, are commonly used measures of fiber integrity; FA correlates highly with IQ (intelligence quotient) in normal subjects [3].

Previous DTI asymmetry studies have focused on specific tracts (e.g., the corticospinal tract [4], and the arcuate fasciculus involved in language processing [5,6]). Frontal and temporal white matter show left greater than right FA even in early infancy [7], suggesting greater myelination in the left hemisphere [7]. Frontal FA differences between the two hemispheres diminish as the brain develops, but temporal lobe asymmetries persist [8].

Studies of asymmetries in white matter characteristics may be confounded by the vast structural asymmetries present. In frontal and occipital regions, the natural petalia (torquing) of the brain shifts the right hemisphere structures anterior to their left hemisphere counterparts [1]. Men may have greater anatomical asymmetries than women [1], making it advantageous to reduce these pronounced macrostructural differences when gauging the level of microstructural asymmetry in a mixed-sex population.

Twin studies have long been used to determine genetically and environmentally influenced human traits. Monozygotic twins share all their genes while dizygotic twins share, on average, half. Estimates of the proportion of variance attributable to genes versus environment can be inferred by fitting structural equation models to data from both types of twins. Twin neuroimaging studies reveal that genetic factors strongly influence several aspects of brain structure, e.g., cortical thickness, and gray and white matter volumes [9], but twin studies using DTI are rare.

Here we created the first DTI-based maps of asymmetries (left/right hemisphere differences) in fiber characteristics (FA, GA) in a large twin population (N=180). We adjusted, as far as possible, for the known structural differences between hemispheres by aligning brains to a symmetrized minimal deformation target (MDT) created from all of the images.

The choice of registration target is known to affect the accuracy of region of interest (ROI) analyses [10], so we evaluated the effects of using different registration targets based on the separate structural MRI images, including (1) an MDT created by geometrically adjusting an individual subject's image, (2) a population-averaged MDT, and (3) a population-averaged MDT based on the non-diffusion-sensitized T2-weighted images collected as part of the DTI protocol. We then determined whether genetic factors influenced the residual asymmetries, and examined the stability of the estimates with respect to sample size and the choice of registration target.

2 Methods

2.1 Image Acquisition and Subject Information

Structural and diffusion tensor (DT) MRI scans were acquired from 180 subjects using a high magnetic field (4T) Bruker Medspec MRI scanner. T1-weighted images were collected using an inversion recovery rapid gradient echo sequence, with parameters: TI/TR/TE= 1500/2500/3.83 $msec$; flip angle=15 degrees; slice thickness = 0.9 mm, and 256x256x256 acquisition matrix. Diffusion-weighted images were also acquired using 30 gradients (27 diffusion-weighted images and 3 with no diffusion sensitization; i.e., T2- weighted images) with gradient directions uniformly distributed on the hemisphere. Parameters were: 23 cm FOV, TR/TE 6090/91.7ms, b-value =1132 s/mm^2, scan time: 3.05 minutes. Each 3D volume consisted of 21 5-mm thick axial slices with a 0.5mm gap and 1.8x1.8 mm^2 in-plane resolution. The subjects included 90 young adult monozygotic (MZ) twins and 90 dizygotic (DZ) same sex twins (45 pairs of each). All subjects were right-handed young adults (average age 24.37, stdev 1.936).

2.2 Creating Templates

To determine whether asymmetric differences are influenced by the template used for registration, several templates were created and compared. Three templates were created using the T1-weighted images to help adjust for the structural differences across subjects and hemispheres, and another template was created from the T2-weighted images acquired along with the diffusion weighted scans, which are in perfect register with the diffusion tensor data. T1-weighted structural MR images were edited to remove extracerebral tissues and were linearly registered to a symmetrical template. This symmetrical template was created by averaging a high-resolution single subject average scan, the Colin27 [11], with the same image reflected in the midsagittal plane. This centered each subjects midline within the image volume. All subjects images were linearly registered to the symmetrical template using FLIRT software `http://fsl.fmrib.ox.ac.uk/fsl/flirt` with 9-parameter registration and a correlation ratio cost function.

T1 Template 1(non-symmetric). One minimal deformation target (MDT) was created using only the original scan orientations, using non-linear fluid registration as described in [12,13]. This template was not symmetrical as all the images used to create it were of the original orientation. MDTs were created using the method proposed by Kochunov [14] (although alternative methods are possible): the N 3D vector fields fluidly registering a specific individual to all other subjects were averaged and applied to that subject, geometrically adjusting their anatomy, but retaining the image intensities and anatomical features of that specific subject. **T1 Template 2 (initial symmetrization).** Linearly aligned subject images were reflected over the midline to produce a mirrored set. Another MDT was then created from four independent (one per pair) monozygotic (MZ) twins and four independent dizygotic (DZ) twin image volumes randomly selected with their corresponding reflected images. These 16 image sets were

then used to generate an MDT using fluid registration as described in [12,13]. The flipped images of the same brains were included during MDT construction to make it symmetric.

T1 Template 3 (symmetric population averaged MDT). A population-averaged MDT was created to further reduce the structural asymmetries. 8 separate MDTs were constructed as described above, each formed from 6 subjects and their corresponding images flipped over the midline. For 4 of these MDTs, the initial template image was in the original orientation while for the other 4, the template was in the flipped orientation. All 8 MDTs were then averaged together to produce the population averaged MDT, incorporating T1 information from 50 independent subjects.

T2 Template (symmetric population averaged MDT). Another population averaged MDT was constructed from the T2-weighted images, in the same manner as for the T1-weighted population MDT, with the same set of subjects. All subjects' images were first linearly aligned to a single subject image. This image of the single subject was aligned such that the midsagittal plane of the brain was centered. Another image was created by mirroring the result in the midsagittal plane. This flipped image was averaged with its original to create a symmetric template to linearly align all the T2-weighted scans and their mirror images before creating the MDT.

Structural T1 images from 100 subjects (25 MZ, 25 DZ pairs) were then fluidly registered to each of the 3 T1-weighted MDTs using a 3D Navier-Stokes-based fluid warping technique enforcing diffeomorphic mappings, using least squares intensity differences as a cost function [12,13]. T2-weighted images for each of the 180 subjects were registered to the T2-weighted MDT with the same technique. 3D deformation fields for all mappings were retained.

2.3 Anisotropy Asymmetry Maps

Diffusion tensors were computed from the diffusion-weighted images using MedINRIA software `http://www.sop.inria.fr/asclepios/software/MedINRIA`.

Scalar images of anisotropy measures were created for each of the 180 subjects from the eigenvalues (λ_1, λ_2, λ_3) of the symmetric $3x3$ diffusion tensor. These included the fractional anisotropy (FA), geodesic anisotropy (GA) computed in the Log-Euclidean framework [15], hyperbolic tangent of the GA (tGA), to take values in the same range as FA, i.e., [0,1], and mean diffusivity (MD):

$$FA = \sqrt{\frac{3}{2}}\frac{\sqrt{(\lambda_1-\hat{\lambda})^2+(\lambda_2-\hat{\lambda})^2+(\lambda_3-\hat{\lambda})^2}}{\sqrt{\lambda_1^2+\lambda_2^2+\lambda_3^2}},\ \hat{\lambda}=MD=\frac{\lambda_1+\lambda_2+\lambda_3}{3} \quad (1)$$

$$GA(S)=\sqrt{Trace(\log S - <\log S> I)^2},\ <\log S>=\frac{Trace(\log S)}{3} \quad (2)$$

Extra-cerebral tissue was manually deleted from one directional component of the diffusion tensors (D_{xx}) creating a mask that was then applied to the scalar anisotropy maps created for each subject. Once masked, these anisotropy images

were then linearly aligned to the symmeterized templates and fluidly registered to each of the MDTs by applying the deformation fields described in Section 2.2.

Each aligned anisotropy map was then mirrored across midline, and the voxel-wise difference map between the original and flipped images was created. In this new map, the left side of the image represents the difference between the subjects right and left hemispheres; voxels on the other side of the image have the opposite sign. Maps were obtained of the percent difference between the resulting difference image and the average of the two mirror image orientations.

2.4 Calculating Genetic Contributions

Voxel-wise maps of the intra-class correlations (ICC) within MZ and DZ twins, r_{MZ} and r_{DZ} respectively, were derived as well as Falconer′s heritability estimate, $h^2 = 2(r_{MZ} - r_{DZ})$ [16] for the asymmetry in FA, GA, tGA and MD.

Average measures of the anisotropy difference were examined in certain regions of interest (ROIs). We determined the genetic contribution to the asymmetries in each lobe of the brain. ROIs were traced for the four lobes (frontal, parietal, temporal, and occipital) in one hemisphere of each MDT and were flipped to define the same ROI in the opposite hemisphere. This ensured consistency between hemispheres and reduced errors due to manual labeling. For each anisotropy measure, covariances for the average ROI values in pairs of MZ and DZ twins were entered into a univariate structural equation model to estimate additive genetic (A), shared environmental (C) and unique environmental (E) components of the variance in asymmetry [17]. Mx modeling software `http://www.vcu.edu/mx/` was used.

This form of structural equation modeling finds the maximum likelihood estimate (eq. 3) for Σ ($\alpha = 1$ for MZ and 0.5 for DZ) to estimate genetic versus environmental contributions to the variance, where S_g is the observed covariance matrix for each twin group g:

$$ML_g = N_g\left\{\ln|\Sigma_g| - ln|S_g| + tr(S_g\Sigma_g^{-1}) - 2m\right\}, \Sigma = \begin{bmatrix} a^2+c^2+e^2 & \alpha a^2+c^2 \\ \alpha a^2+c^2 & a^2+c^2+e^2 \end{bmatrix} \quad (3)$$

3 Results

Figure 1A shows the mean FA asymmetry as a percent difference between left and right hemispheres, relative to which genetic effects were determined. Frontal and temporal regions show high asymmetry ($\sim 25\%, p < 0.05$). Frontal FA is higher in the right hemisphere, while temporal FA is higher on the left. The asymmetries found in the temporal lobe correspond to language centers [1] consistent with [7,8]. The magnitude of the asymmetry difference is somewhat dependent on the number of subjects used in the study, but patterns are largely consistent. Figure 1B shows differences arising in ICC and Falconer's heritability estimates when using the T1-weighted population template for 100 subjects and the T2-weighted MDT for the different population sizes. Despite evidence for some subcortical effects, voxelwise maps are somewhat noisy even with N=180 subjects, partly

Genetics of Anisotropy Asymmetry: Registration and Sample Size Effects

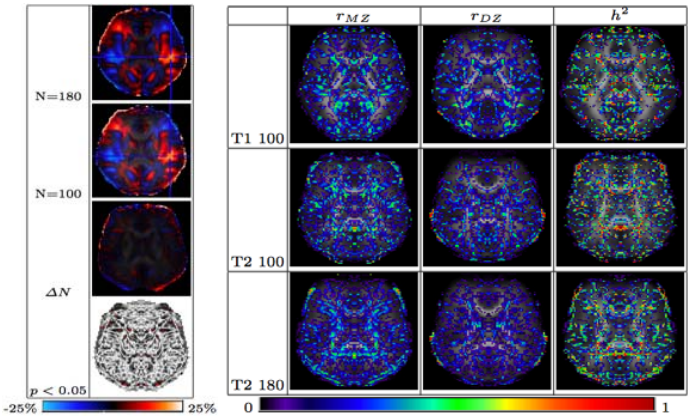

Fig. 1. A: The mean asymmetry in FA, in a sample of N=180 subjects, reaches 25% in frontal and temporal regions. The localization of results based on 180 vs only 100 subjects is largely consistent, as shown by the difference image and the image of the p-values. **B:** ICC and Falconer's h^2 maps for asymmetries in FA images. *Top:* FA results of 100 subjects mapped to the population-averaged T1 MDT; *Center:* results from 100 subjects mapped to population-averaged T2 MDT; *Bottom:* results from 180 subjects mapped to the T2 MDT

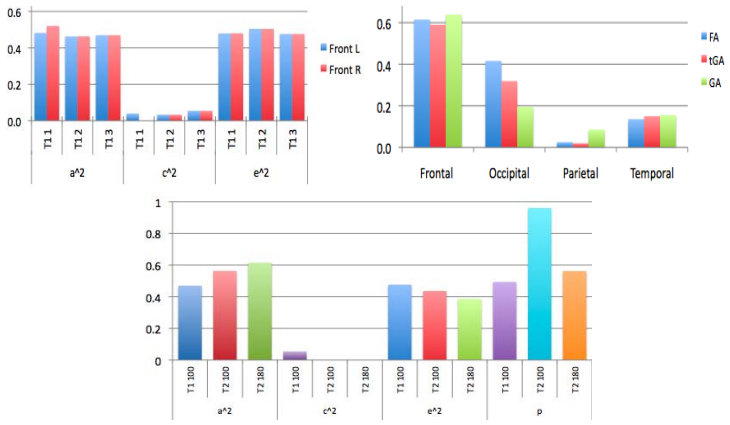

Fig. 2. A/C/E Genetic effects: *Top Left: Symmetrization Effects:*ACE results showing genetic and environmental contributions of template choice asymmetry in FA; *Top Right: Frontal Lobe FA* ACE results of using the population averaged T1 template (100 subjects) and T2 template (100 and 180 subjects) for FA asymmetry in the frontal lobe. p-values derived from χ^2 statistics show the ACE model fits well in all cases ($p > 0.05$); *Bottom:* $N = 180$ *Genetic Effects* genetic component of variance (A) determined from mapping 180 subjects to the T2-weighted MDT for all anisotropy measures, in each lobe. Genetic effects are greatest in lobes with the highest mean asymmetries (Fig. 1).

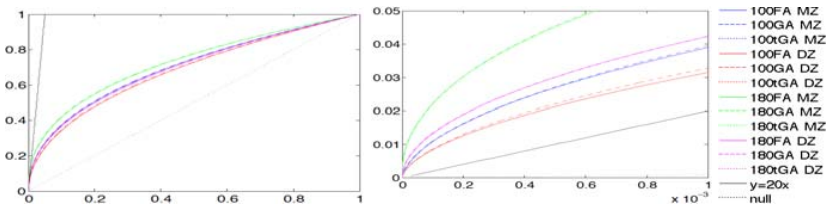

Fig. 3. CDF of significant p-values for anisotropy asymmetries mapped to the T2-weighted population MDT for 100 (left) and 180 subjects (right)

because h^2 is a difference in correlations. We therefore summarize FA asymmetry in lobar ROIs, to increase power for genetic analyses.

Figure 2 shows genetic (a^2) vs environmental (c^2, e^2) effects on FA asymmetry. Intriguingly, the asymmetry in frontal lobe mean FA was $\sim 50\%$ determined by genetic factors, with no evidence for a shared environmental effect ($c^2 \sim 0\%$). The e^2-term contains registration errors as well as unique effects, so there is some evidence that using 180 (vs 100) subjects, and using a T2 vs T1 template, more accurately captures the true genetic contributions to these asymmetries, as the e^2-term is slightly lower. In structural equation models, $p > 0.05$ denotes that the ACE model fits well. All models here yield a good fit.

Figure 3 plots the cumulative distribution function (cdf) of the p-values associated with the ICC against those that would be expected from a null distribution. As the cdf initially rises faster than 20 times the null, we are able to reasonably claim significance at the 5% level. For null distributions (i.e. no group difference detected), these are expected to fall along the x = y line, and larger deviations from that curve represent larger effect sizes.

4 Discussion

In this study, we examined the genetic and environmental contributions to the differences in fiber integrity across brain hemispheres. Genetic factors determined about half of the variance in these asymmetries, with greatest effects in the frontal and occipital lobes, where mean asymmetries were greatest (reaching 25%) (Fig. 1A). Interestingly, strong genetic effects (significant ACE models) were detectable for anisotropy indices (FA, GA). Results were stable when the images were fluidly registered to various different anatomical templates, including ones constructed to have hemispheric symmmetry. These results suggest that specific genetic factors determining hemispheric asymmetries in fiber architecture may be identifiable in very large samples.

Acknowledgments. Supported by grants from the NLM, NIH and NICHD.

Genetics of Anisotropy Asymmetry: Registration and Sample Size Effects

References

1. Toga, A., Thompson, P.: Mapping brain asymmetry. Nat. Rev. Neurosci. 4(1) (2003)
2. Thirion, J.P., Prima, S., Subsol, G., Roberts, N.: Statistical analysis of normal and abnormal dissymmetry in volumetric medical images. Med. Im. Analy. 4(2) (2000)
3. Chiang, M., Barysheva, M., Lee, A., Madsen, S., Klunder, A., Toga, A., McMahon, K., de Zubicaray, G., Wright, M., Srivastava, A., Balov, N., Thompson, P.: Genetics of brain fiber architecture and intelligence. Journal of Neuroscience (2009)
4. Westerhausen, R., Huster, R.J., Kreuder, F., Wittling, W., Schweiger, E.: Corticospinal tract asymmetries at the level of the internal capsule: Is there an association with handedness? Neuroimage 37(2), 379–386 (2007)
5. de Jong, L., Kovacs, S., Bamps, S., Calenbergh, F.V., Sunaert, S., van Loon, J.: The arcuate fasciculus: a comparison between diffusion tensor tractography and anatomy using the fiber dissection technique. Surgical Neurology 71(1) (2009)
6. Rodrigo, S., Naggara, O., Oppenheim, C., Golestani, N., Poupon, C., Cointepas, Y., Mangin, J.F., Le Bihan, D., Meder, J.F.: Human subinsular asymmetry studied by diffusion tensor imaging and fiber tracking. AJNR 28(8), 1526–1531 (2007)
7. Dubois, J., Hertz-Pannier, L., Cachia, A., Le Bihan, D., Dehaene-Lambertz, G.: Structural asymmetries in the infant language and sensori-motor networks. Cerebral Cortex 19(2), 414–423 (2008)
8. Barnea-Goraly, N., Menon, V., Eckert, M., Tamm, L., Bammer, R., Karchemskiy, A., Dant, C.C., Reiss, A.L.: White matter development during childhood and adolescence: A cross-sectional diffusion tensor imaging study. Cereb. Cortex 15(12), 1848–1854 (2005)
9. Pfefferbaum, A., Sulluvan, E.V., Carmelli, D.: Genetic regulation of regional microstructure of the corpus callosum in late life. Neuroreport 12(8), 1677–1681 (2001)
10. Wang, Q., Seghers, D., D'Agostino, E., Maes, F., Vandermeulen, D., Suetens, P., Hammers, A.: Construction and validation of mean shape atlas templates for atlas-based brain image segmentation. In: Christensen, G.E., Sonka, M. (eds.) IPMI 2005. LNCS, vol. 3565, pp. 689–700. Springer, Heidelberg (2005)
11. Holmes, C.J., Hoge, R., Collins, L., Woods, R., Toga, A.W., Evans, A.C.: Enhancement of MR images using registration for signal averaging. J. Comput. Assist. Tomogr. 22(2), 324–333 (1998)
12. Leporé, N., Brun, C., Pennec, X., Chou, Y.Y., Lopez, O., Aizenstein, H., Becker, J., Toga, A., Thompson, P.: Mean template for tensor-based morphometry using deformation tensors. In: Ayache, N., Ourselin, S., Maeder, A. (eds.) MICCAI 2007, Part II. LNCS, vol. 4792, pp. 826–833. Springer, Heidelberg (2007)
13. Leporé, N., Chou, Y.Y., Lopez, O.L., Aizenstein, H.J., Becker, J.T., Toga, A.W., Thompson, P.M.: Fast 3D fluid registration of brain magnetic resonance images, vol. 6916. SPIE, San Diego (2008)
14. Kochunov, P., Lancaster, J., Thompson, P., Toga, A., Brewer, P., Hardies, J., Fox, P.: An optimized individual target brain in the Talairach coordinate system. Neuroimage 17(2), 922–927 (2002)
15. Arsigny, V., Fillard, P., Pennec, X., Ayache, N.: Log-Euclidean metrics for fast and simple calculus on diffusion tensors. MRM 56(2), 411–421 (2006)
16. Falconer, D., Macka, T.F.: Introduction to Quantitative Genetics, 4th edn. Addison Wesley Longman, Amsterdam (1995) (Pearson Education)
17. Rijsdijk, F.V., Sham, P.C.: Analytic approaches to twin data using structural equation models. Briefings in Bioinformatics 3(2), 119–133 (2002)

3.2 Genetics of brain fiber asymmetry

The following section is adapted from:

Jahanshad N, Lee AD, Barysheva M, McMahon KL, de Zubicaray GI, Martin NG, Wright MJ, Toga AW, Thompson PM. Genetic Influences on Brain Asymmetry: A DTI Study of 374 Twins and Siblings, NeuroImage, 2010 Aug 15;52(2):455-69.

NeuroImage 52 (2010) 455–469

Contents lists available at ScienceDirect

NeuroImage

journal homepage: www.elsevier.com/locate/ynimg

Genetic influences on brain asymmetry: A DTI study of 374 twins and siblings

Neda Jahanshad [a,b], Agatha D. Lee [a], Marina Barysheva [a], Katie L. McMahon [d], Greig I. de Zubicaray [c], Nicholas G. Martin [d], Margaret J. Wright [d], Arthur W. Toga [a], Paul M. Thompson [a,*]

[a] Laboratory of Neuro Imaging, Department of Neurology, UCLA School of Medicine, Los Angeles, CA, USA
[b] Medical Imaging Informatics Group, Department of Radiology, UCLA School of Medicine, Los Angeles, CA, USA
[c] School of Psychology, University of Queensland, Brisbane, Australia
[d] Queensland Institute of Medical Research, Brisbane, Australia

ARTICLE INFO

Article history:
Received 4 November 2009
Revised 17 April 2010
Accepted 20 April 2010
Available online 27 April 2010

Keywords:
DTI
Brain asymmetry
Fractional anisotropy
Geodesic anisotropy
Structural equation model
Twins
Quantitative genetics
Path analysis

ABSTRACT

Brain asymmetry, or the structural and functional specialization of each brain hemisphere, has fascinated neuroscientists for over a century. Even so, genetic and environmental factors that influence brain asymmetry are largely unknown. Diffusion tensor imaging (DTI) now allows asymmetry to be studied at a microscopic scale by examining differences in fiber characteristics across hemispheres rather than differences in structure shapes and volumes. Here we analyzed 4 Tesla DTI scans from 374 healthy adults, including 60 monozygotic twin pairs, 45 same-sex dizygotic pairs, and 164 mixed-sex DZ twins and their siblings; mean age: 24.4 years ± 1.9 SD). All DTI scans were nonlinearly aligned to a geometrically-symmetric, population-based image template. We computed voxel-wise maps of significant asymmetries (left/right differences) for common diffusion measures that reflect fiber integrity (fractional and geodesic anisotropy; FA, GA and mean diffusivity, MD). In quantitative genetic models computed from all same-sex twin pairs ($N = 210$ subjects), genetic factors accounted for 33% of the variance in asymmetry for the inferior fronto-occipital fasciculus, 37% for the anterior thalamic radiation, and 20% for the forceps major and uncinate fasciculus (all L>R). Shared environmental factors accounted for around 15% of the variance in asymmetry for the cortico-spinal tract (R>L) and about 10% for the forceps minor (L>R). Sex differences in asymmetry (men>women) were significant, and were greatest in regions with prominent FA asymmetries. These maps identify heritable DTI-derived features, and may empower genome-wide searches for genetic polymorphisms that influence brain asymmetry.

Introduction

Asymmetries in brain structure and function have been studied for over a century. Anatomical asymmetries give evidence for the developmental and evolutionary origins of lateralized cognitive functions and behavioral traits, such as language and handedness (Lancaster et al., 2003; Toga and Thompson, 2003; Luders et al., 2005).

Structural brain asymmetries are influenced by both genetic and environmental factors throughout life. The degree of anatomical asymmetry depends to some extent on age (Sowell et al., 2002a), sex (Luders et al., 2003; Witelson et al., 1992), and handedness (Narr et al., 2007).

Aberrant asymmetries, reported in several brain disorders, may indicate a derailment in processes that establish normal hemispheric specialization. Some mental illnesses, such as schizophrenia, are thought by some to arise due to a failure of normal functional lateralization (Crow, 1990; Narr et al., 2007; Hamilton et al., 2007) although such a view is not universally accepted. Altered asymmetries have been found in groups of patients with dyslexia (Beaton, 1997), Williams syndrome (Thompson et al., 2005; Eckert et al., 2006), fetal alcohol syndrome (Sowell et al., 2002b), Huntington's disease (Mühlau et al., 2007), and multiple sclerosis (Koziol et al., 2005). Inherently lateralized pathologies, such as temporal lobe epilepsy (where the seizure focus is typically on one side of the brain only) may also be assessed by mapping the level of brain asymmetry (Lin et al., 2006).

Asymmetries in the rate of disease progression have reported in some, but not all, studies of degenerative diseases such as Alzheimer's disease and mild cognitive impairment (MCI; Thompson et al., 2003; Thompson et al., 1998; Morra et al., 2009). Taken together, all these asymmetries heighten interest in possible differences in the vulnerability of the two hemispheres to various types of neuropathology and age-related decline, and the origins of these differences.

Diffusion tensor imaging (DTI) offers a new opportunity to study hemispheric differences in microscopic fiber characteristics. DTI is a variant of magnetic resonance imaging, sensitive to directionally constrained water diffusion that occurs preferentially along myelinated axons (Basser and Pierpaoli, 1996). The fractional anisotropy (FA) of

* Corresponding author. Laboratory of Neuro Imaging, Department of Neurology, UCLA School of Medicine, 635 Charles E. Young Drive South, Suite 225E, Los Angeles, CA 90095-7332, USA. Fax: +1 310 206 5518.
E-mail address: thompson@loni.ucla.edu (P.M. Thompson).

1053-8119/$ – see front matter © 2010 Elsevier Inc. All rights reserved.
doi:10.1016/j.neuroimage.2010.04.236

N. Jahanshad et al. / NeuroImage 52 (2010) 455–469

diffusion tends to be higher when fiber tracts are more directionally coherent, or more heavily myelinated, and is a widely accepted index of the microstructural integrity of white matter (Klingberg et al., 2000; Beaulieu, 2002).

DTI studies in twins can be used to determine genetic and environmental effects on fiber architecture. Monozygotic twins share all their genes while dizygotic twins share, on average, half. Estimates of the proportion of variance attributable to genes versus environment may be inferred by fitting structural equation models to data from both types of twins. Twin MRI studies have already found that genetic factors strongly influence several aspects of brain structure, such as cortical thickness, and gray and white matter volumes (Thompson et al., 2001; Styner et al., 2005; Hulshoff Pol et al., 2006; Peper et al., 2007; Schmitt et al., 2008; Chou et al., 2009; Leporé et al., 2008b; Brun et al., 2009). Even so, twin studies using DTI are still quite rare (recent examples include Lee et al., 2009a,b; Kochunov et al., 2010; Chiang et al., 2009b).

Here we used a twin design to map the 3D pattern of asymmetries and to search for regions where these asymmetries are highly heritable. Honing in on heritable DTI-derived signals may empower genome-wide searches for specific contributing genes, by first isolating regions where differences are heritable. This may alleviate, to some degree, the enormous sample sizes and multiple comparisons corrections that frustrate efforts to detect and replicate single-gene effects on brain structure (Stein et al., 2010) and DTI (Chiang et al., 2009b).

We set out to create the first DTI-based maps of asymmetries (left/right hemisphere differences) for commonly-studied fiber characteristics (FA, GA, MD) in a large, mixed-sex twin population ($N = 374$). Studies of fiber-level asymmetries may be confounded by known asymmetries in brain shape, such as the natural petalias that make the right frontal lobe protrude beyond the left (Toga and Thompson, 2003). It makes sense to reduce these pronounced macrostructural differences across subjects before gauging the level of microstructural asymmetry, especially in a mixed-sex population, where sex differences in anatomy may also be found (Brun et al., 2009). We therefore adjusted, as far as possible, for the known structural differences between hemispheres by aligning brains to a "symmetrized" mean deformation target (MDT) created from the set of fractional anisotropy images in the study.

As well as assessing genetic influences on diffusion asymmetry, secondary (exploratory) analyses were also performed to assess any effects of sex and IQ.

Methods

Subjects and image acquisition

Structural and diffusion tensor (DT) whole-brain MRI scans were acquired from 374 subjects with a high magnetic field (4 T) Bruker Medspec MRI scanner. T1-weighted images were acquired with an inversion recovery rapid gradient echo sequence. Acquisition parameters were as follows: TI/TR/TE = 700/1500/3.35 ms; flip angle = 8°; slice thickness = 0.9 mm, with an acquisition matrix of $256 \times 256 \times 256$. Diffusion-weighted images were also acquired using single-shot echo planar imaging with a twice-refocused spin echo sequence to reduce eddy-current induced distortions. Acquisition parameters were optimized to provide the best signal-to-noise ratio for estimation of diffusion tensors (Jones et al., 1999). Imaging parameters were: 23 cm FOV, TR/TE 6090/91.7 ms, with a 128×128 acquisition matrix. Each 3D volume consisted of 55 2-mm thick axial slices with no gap and $1.79 \times 1.79\ mm^2$ in-plane resolution. 105 images were acquired per subject: 11 with no diffusion sensitization (i.e., T2-weighted b_0 images) and 94 diffusion-weighted (DW) images ($b = 1149\ s/mm^2$) with gradient directions evenly distributed on the hemisphere. Scan time was 14.2 min. The subjects included 120 young adult monozygotic (MZ) twins (60 pairs — 21 males, 39 females), 90 same-sex dizygotic (DZ) twins (45 pairs — 15 males, 30 females); and an additional 164 mixed-sex dizygotic twins (i.e., one male and female twin per pair) and any non-twin siblings for whom scans were available. No subjects reported a history of significant head injury, neurological or psychiatric illness, substance abuse or dependence, or had a first-degree relative with a psychiatric disorder. In addition, all subjects were screened, using a detailed neurocognitive evaluation (de Zubicaray et al., 2008) to exclude cases of pathology known to affect brain structure. In total, diffusion images from 374 (145 males, 229 females) right-handed young adults (mean age: 24.37 years, SD 1.94) were included in this study. Handedness was assessed in these subjects based on 12 items from Annett's Handedness Questionnaire (Annett, 1970).

Preprocessing and general overview

Each subject's T1-weighted MR and DWI images were edited to remove extracerebral tissues. All skull-stripped structural T1-weighted images were linearly aligned (with 9 degrees of freedom) to a standard template to ensure alignment in space. The raw diffusion weighted images were corrected for eddy-current induced distortions using the FSL tool, "eddy_correct". For each subject, the 11 eddy-corrected images with no diffusion sensitization, also called the b_0 images, were averaged. The average b_0 maps were then aligned and elastically registered to the subject's aligned T1-weighted structural scan using a mutual information cost function (Leow et al., 2005) to account for EPI induced susceptibility artifacts. Similar registrations have been shown to be useful for EPI distortion correction (Huang et al., 2008). The rest of the image processing steps, using the distortion corrected sets of diffusion weighted images, are summarized in Fig. 1. A mean deformation template image was created using fractional anisotropy (FA) maps derived from the diffusion-weighted data (detailed below). The FA images were registered directly to the target and the resulting deformation fields were applied to all the anisotropy maps to put them all into the same coordinate space. To further ensure alignment of white matter tracts, the registered FA maps were thresholded to include only those regions where FA>0.25. These images were then registered to the thresholded template, and the resulting deformation fields were reapplied to all the registered anisotropy maps. Left–right asymmetries in the anisotropy maps were calculated, and various group-wise statistical analyses were performed. Voxel-wise statistics were used, as in many prior DTI studies (Liu et al., 2009; Ardekani et al., 2007). These included quantitative genetic analyses to estimate genetic and environmental contributions to the observed differences. We expected genetic factors to play a substantial role in the lateralization of the fiber anisotropy in language association regions of the temporal lobe, including the arcuate fasciculus (de Jong et al., 2009; Rodrigo et al., 2007). We also predicted that the use of a symmetrized brain template as a registration target might somewhat reduce the level of observed asymmetry, by eliminating factors reflecting brain shape, such as the level of petalia, or torquing, of the brain.

Anisotropy calculation and registration

DTI was introduced by Basser et al. (1994) to characterize the anisotropy (directional preference) in the diffusion of water molecules in brain tissue. In DTI, the MR signal attenuation due to water diffusion in direction k decreases according to the Stejskal–Tanner equation, if a Gaussian distribution is assumed: $S_k(\mathbf{r}) = S_0(\mathbf{r})e^{-b_k D_k(r)}$. Here $S_0(\mathbf{r})$ is the non-diffusion weighted baseline intensity in direction r, $D_k(\mathbf{r})$ is the apparent diffusion coefficient (ADC), and b_k is a constant depending on the direction k. Two of the many popular scalar measures of fiber anisotropy include the fractional anisotropy and geodesic anisotropy. Fractional anisotropy (FA) is one of the most

N. Jahanshad et al. / NeuroImage 52 (2010) 455–469

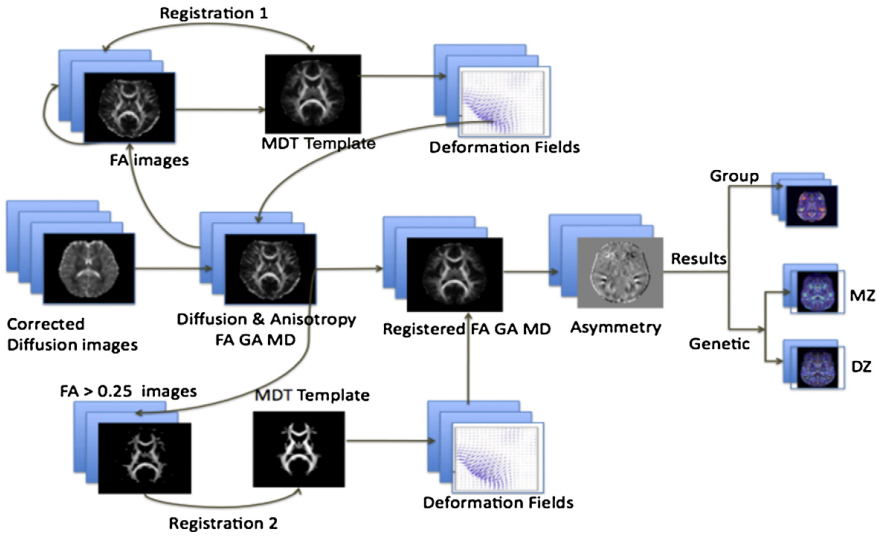

Fig. 1. Flow chart of steps used to analyze DTI asymmetries. FA maps from all subjects were used to make a group "average-shape" brain, or mean deformation template (MDT), and they were nonlinearly registered to this template. The deformation fields were also applied to maps of mean diffusivity (MD) and anisotropy (FA, GA) to align them all to the common template. Statistical maps were made to show the mean level of asymmetry in different brain regions. Genetic analysis of the variance in fiber characteristics was performed at each location in the brain.

widely used measures in DTI research. Geodesic anisotropy (GA) is a measure more recently advocated by several groups (Batchelor et al., 2005; Arsigny et al., 2006). Both measures are calculated from a local tensor (3D Gaussian) approximation for $D_k(\mathbf{r})$; GA assesses differences between tensors using a geodesic distance measure on the manifold on which the tensors lie (Arsigny et al., 2006; Fletcher and Joshi, 2004). Prior work on the genetics of fiber integrity suggested that GA was slightly better able to detect genetic influences on the DTI signal than FA (Lee et al., 2008, 2009a).

Diffusion tensors were computed from the 105-gradient diffusion-weighted images using the FSL software (http://fsl.fmrib.ox.ac.uk/fsl/). FA and GA scalar images of anisotropy, and mean (MD), axial (AD) and radial diffusivity (RD) measures were created for the 374 subjects from the eigenvalues (λ_1, λ_2, λ_3) of the symmetric 3×3 diffusion tensor (S). The hyperbolic tangent of the GA (tanh GA or tGA) was also computed, which takes values in the same range as FA, i.e., [0,1]:

$$\mathrm{FA} = \sqrt{\frac{3}{2}}\frac{\sqrt{(\lambda_1 - <\lambda>)^2 + (\lambda_2 - <\lambda>)^2 + (\lambda_3 - <\lambda>)^2}}{\sqrt{\lambda_1^2 + \lambda_2^2 + \lambda_3^2}} \in [0,1] \quad (1)$$

$$\mathrm{MD} = <\lambda> = \frac{\lambda_1 + \lambda_2 + \lambda_3}{3}$$

$$\mathrm{GA}(S) = \sqrt{Trace(\log S - \langle \log S \rangle I)^2} \quad (2)$$

$$\frac{\langle \log S \rangle = Trace(\log S)}{3}$$

$$tGA = \tanh GA \in [0,\ 1]. \quad (3)$$

Template creation and registration

To avoid misinterpreting any detected differences, it is helpful to reduce the pronounced macrostructural differences when gauging the level of microstructural asymmetry, especially in a mixed-sex population. We therefore adjusted, as far as possible, for the known structural differences between hemispheres by aligning brains to a symmetrized mean deformation target (MDT) created from the set of FA images. The choice of registration target is known to affect the accuracy of region of interest (ROI) analyses (Wang et al., 2005), so we created a symmetrical population-based (MDT) using nonlinear fluid registration, as described in (Leporé et al., 2006, 2008a,b). Several alternative methods to create an MDT have been proposed, but here we used the method proposed by (Kochunov et al., 2001, 2002): the N 3D vector fields fluidly registering a specific individual to all other N subjects were averaged and applied to that subject. This way, the anatomy was geometrically adjusted while the image intensities and anatomical features of that specific subject were retained.

To construct a symmetric, population-based MDT, a random selection of 32 (16 females/16 males) non-related subjects' fractional anisotropy images was used (calculated after b_0 susceptibility correction). This group was split into two subgroups of 16 (8 women in each). Within each subgroup, half the subjects (8 total, 4 women) were reflected across the midsagittal plane. All subjects in the subgroups were then fluidly registered to a single subject target within the group. In one group the target was selected to be a mirrored image, while in the other the target was in the original orientation. One group's target was female, the other male. In each group, 8 of the 15 images aligned to the target were of the opposite orientation to the target (original orientation or mirrored across the midsagittal) and the other 7 were in the same orientation (see Fig. 2). Once all images were registered to the designated target, the deformation fields from all registrations within the group were averaged and applied to the corresponding target to obtain the within-group (MDT). The 2 group MDTs were the co-registered, and averaged along with their mirror images to ensure a structurally symmetric template on both a macro and microstructural scale.

In our prior work (Jahanshad et al., 2009), we found that using T2-weighted images for registration purposes yields results similar to those

N. Jahanshad et al. / NeuroImage 52 (2010) 455–469

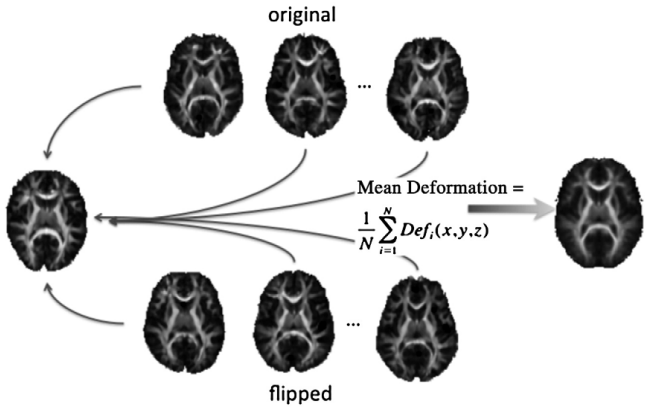

Fig. 2. To create an MDT that was symmetrical by design, deformation fields – mapping images in their original orientation and others in the flipped orientation to the template – were averaged and applied to the template.

obtained from using higher resolution T1-weighted images, with the advantage that they are inherently in register with the diffusion-weighted images from the same scanning session. To further ensure alignment of the white matter regions of interest, in this study, we decided to use a DTI-derived measure, the FA, to drive the registration. This should reduce the bias in examining microstructural asymmetry by greatly reducing the macroscopic misregistration of the white matter. Other groups have proposed the use of multiple diffusion tensor based channels may improve the process of template generation and reduce the misregistration bias (Park et al., 2003, 2004).

FA maps for each of the linearly aligned 374 subjects were registered to the final population averaged FA-based MDT using a 3D elastic warping technique. This elastic registration enforces diffeomorphic mappings and uses mutual information as a cost function (Leow et al., 2005). 3D deformation fields mapping each subject to the MDT were retained and applied to the original FA, tGA, and MD maps. To further ensure alignment of white matter regions of interest, the FA-MDT as well as all whole-brain registered FA maps were then thresholded to include only those regions where the FA was greater than 0.25. The individual thresholded FA maps were then re-registered to the thresholded MDT in the same way as the whole-brain registration. The resulting deformation fields were once again applied to the anisotropy maps. When transforming FA maps onto a common template, strictly speaking, the FA values cannot be absolutely preserved as they are trilinearly interpolated after they are transformed through a displacement field. As such they will be very slightly smoother than the raw data, but the smoothing will not vary in a spatially biased way. The warping of FA maps through a non-rigid transform will also slightly alter the relative volumes of different brain regions, although this spatial normalization is deliberate and is required for cross-subject averaging and comparisons. For region of interest analysis, the JHU DTI atlas (Mori et al., 2005; Wakana et al., 2007) was also mapped to the MDT using elastic registration. Tract probability maps were thresholded to include all regions that had a probability greater than 0.25 of being within a specific tract.

Creating asymmetry maps

Each aligned anisotropy map was mirrored across the midline (Fig. 3), and the voxel-wise difference map between the original and flipped images was created. In this new map, the left side of the image represents the difference between the subjects' right and left hemispheres; voxels on the other side of the image have the opposite sign.

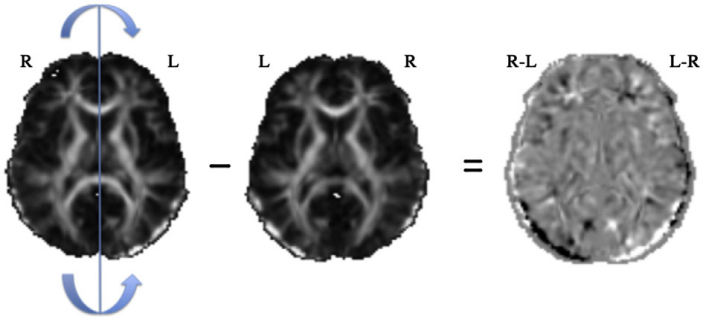

Fig. 3. Maps of anisotropy asymmetry were created by reflecting every axial slice in the original image across midline and subtracting the flipped image from the original. Dark regions represent negative values; brighter (e.g., white) regions represent positive values.

N. Jahanshad et al. / NeuroImage 52 (2010) 455–469

Estimating genetic contributions

To determine the magnitude of the genetic contributions to fiber asymmetry, three approaches were employed, each of which takes advantage of the fact that monozygotic twins share all of their genetic material while dizygotic twins share, on average, half. All genetic analyses were performed on a subset of 210 subjects: 60 pairs of monozygotic twins and 45 pairs of same-sex dizygotic twins.

First, voxel-wise maps were derived showing the intra-class correlations (ICC) within MZ and DZ twins, r_{MZ} and r_{DZ} respectively, to compute a simple measure of genetic effects: Falconer's heritability estimate, $h^2 = 2(r_{MZ} - r_{DZ})$ (Falconer and Mackay, 1995) for the asymmetry in FA, MD, and tGA. The intra-class correlations are general measures of resemblance defined as the difference between the mean squared estimates of the between-pair and within-pair variance divided by the sum of the two. Falconer's heritability measures differences between the correlations of the two types of twins as an initial index of any genetic contribution to the overall observed variance.

Next, average measures of the anisotropy difference were examined in certain regions of interest (ROIs). For region of interest analysis, the tract probability maps from the JHU DTI atlas (Mori et al., 2005; Wakana et al., 2007) were mapped using elastic registration to the symmetric MDT, and were thresholded to include regions where the probability for the tract occurring at that voxel was greater than 0.25. As these tracts were already mapped to our symmetric template, only portions of the tracts in one hemisphere were retained to accurately assess inter-hemispheric differences. The tracts included in the analysis were the anterior thalamic radiation, cortico-spinal tract, cingulate gyrus, hippocampus cingulum, forceps major, forceps minor, inferior fronto-occipital fasciculus, inferior longitudinal fasciculus, superior longitudinal fasciculus, uncinate fasciculus, and the temporal superior longitudinal fasciculus.

For each anisotropy measure, covariances for the average asymmetry in the ROI were computed between the pairs of MZ and DZ twins (Fig. 4). These were entered into a univariate structural equation model to estimate additive genetic (A), shared environmental (C) and unique environmental (E) components of the variance in asymmetry (Rijsdijk and Sham, 2002) using Mx modeling software (http://www.vcu.edu/mx/).

Finally, voxel-wise $A/C/E$ tests were computed for asymmetries in the anisotropy measures, after determining the covariance between the twin pairs using the same type of univariate structural equation model to specify locations of heritable effects on fiber asymmetry. The asymmetry was calculated for each subject and the covariance between the members of the twin pairs was measured for each type of twin (MZ and DZ) at every voxel, resulting in an observed covariance matrix S for every voxel. These observed covariance matrices may be computed for any variable (Z) modeled as in Eq. (4), and a structural equation model (SEM) may be fitted to compare the observed and expected covariances (Σ in Eq. (5)) to infer the proportion of the variance due to the A, C and E factors:

$$Z = aA + cC + eE \tag{4}$$

A, C, and E are latent (unobserved) variables and a, c, and e are the weights of each parameter determined through optimization of Σ using maximum likelihood fitting. The variance components combine to create the total observed inter-individual variance, so that $a^2 + c^2 + e^2 = 1$.

This form of SEM uses the maximum likelihood estimate (MLE; Eq. (5)) with a χ^2 null distribution to estimate genetic versus environmental contributions to the variance, where $m = 1$, the number of observed variables, N_g, is the number of twin pairs used, and S_g is the expected covariance matrix for group g, with $\alpha = 1$ for the MZ group and $\alpha = 0.5$ for the DZ group:

$$ML_g = N_g\{\ln|\Sigma_g| - \ln|S_g| + \mathrm{tr}\left(S_g\Sigma_g^{-1}\right) - 2m\} \tag{5}$$

$$\Sigma = \begin{bmatrix} a^2 + c^2 + e^2 & \alpha a^2 + c^2 \\ \alpha a^2 + c^2 & a^2 + c^2 + e^2 \end{bmatrix}.$$

In structural equation modeling, the χ^2 goodness-of-fit measure determines a p-value for all specified regions of interest where the test was performed, in this case either the lobar regions (for the regional summaries) or at every individual voxel. This value indicates that the model is a *good* fit to the data if $p > 0.05$. However, to determine the significance of a particular factor, such as A or C, the χ^2 goodness-of-fit values of the model may be compared to those for a model that does not include the factor (i.e., to a C/E model to determine the significance of the additional A factor, and to an A/E model to determine the significance of the C factor), giving:

$$\begin{aligned} p(A) &= \chi^{2^{-1}}_{1DF}\left[\chi^2(ACE) - \chi^2(CE)\right] \\ p(C) &= \chi^{2^{-1}}_{1DF}\left[\chi^2(ACE) - \chi^2(AE)\right] \end{aligned} \tag{6}$$

where ${\chi^2}_{1DF}{}^{-1}$ denotes the inverse of the cumulative distribution function for a chi-squared distributed variable with one degree of freedom. In this case, low p-values express significant improvements when adding a factor, which is consistent with the more standard convention for p-values, and allows the resulting uncorrected p-value maps to be assessed using false discovery rate analyses.

To account for the multiple comparison problem that arises when testing a statistical hypothesis at every voxel, non-parametric permutation tests were conducted based on the correlation values at each voxel. Non-parametric permutation tests are widely used in imaging (e.g., Nichols and Holmes, 2002). We also confirmed the reliability of our results by assessing whether statistical thresholding of the statistical maps could be used to control the false discovery rate (FDR) at the conventional 5% level (Benjamini and Hochberg, 1995; Genovese et al., 2002; Lawyer et al., 2009). To visualize effect sizes in the maps, the cumulative distribution function (CDF) of the p-values associated with the intra-class correlations was computed and graphed. The p-values were plotted against those p-values that would be expected from a null distribution, in a Q–Q plot. If the CDF initially rises faster than 20 times the null CDF, there is some non-zero statistical threshold that controls the FDR at the 5% level. For null distributions (where no group differences are detected), these plots are expected to fall approximately along the $y = x$ line. Larger deviations from this line represent larger effect sizes; curves that rise at a rate steeper than $y = 20x$, show that the corresponding maps are significant (in the sense of controlling the FDR) after stringent multiple comparison correction.

As the $A/C/E$ model is difficult to randomize to run permutation tests, the p-values for determining the significance of adding the A and C factors into the model were corrected for multiple comparisons by finding the highest p-value threshold that controlled the FDR in the map at 5%, where possible.

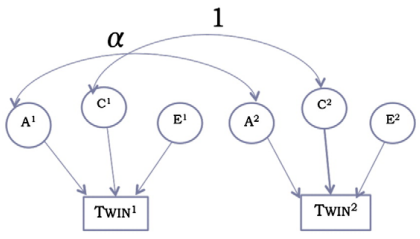

Fig. 4. Path diagram showing how various components in the structural equation model are related between twins in a pair. α values are the only parameters that differ for each type of twin: $\alpha = 1$ for the MZ group and $\alpha = 0.5$ for the DZ group. Registration and measurement errors are included as part of the E component.

Additional asymmetry analyses

In *post hoc* analyses, we examined whether the degree of asymmetry in the anisotropy measures was associated with the subject's sex or IQ.

Asymmetry differences between the sexes

To determine if there were sex differences in fiber integrity asymmetry, we compared fiber asymmetries in men versus women, based on using the largest possible sample of unrelated subjects. 126 female subjects and 81 male subjects were used for this comparison. Voxel-wise statistics of sex differences were calculated using Student's *t*-tests. The false discovery rate was also controlled at the 5% level to correct for multiple comparisons.

Correlations between asymmetry and IQ

Three measures of intelligence were obtained from each subject; the perceptual intelligence quotient (PIQ), the verbal intelligence quotient (VIQ), and the full scale IQ (FIQ).

Using asymmetry information from the entire group of subjects with IQ information ($N = 358$), statistics were computed at all voxels to correlate the fiber integrity difference across the hemispheres with

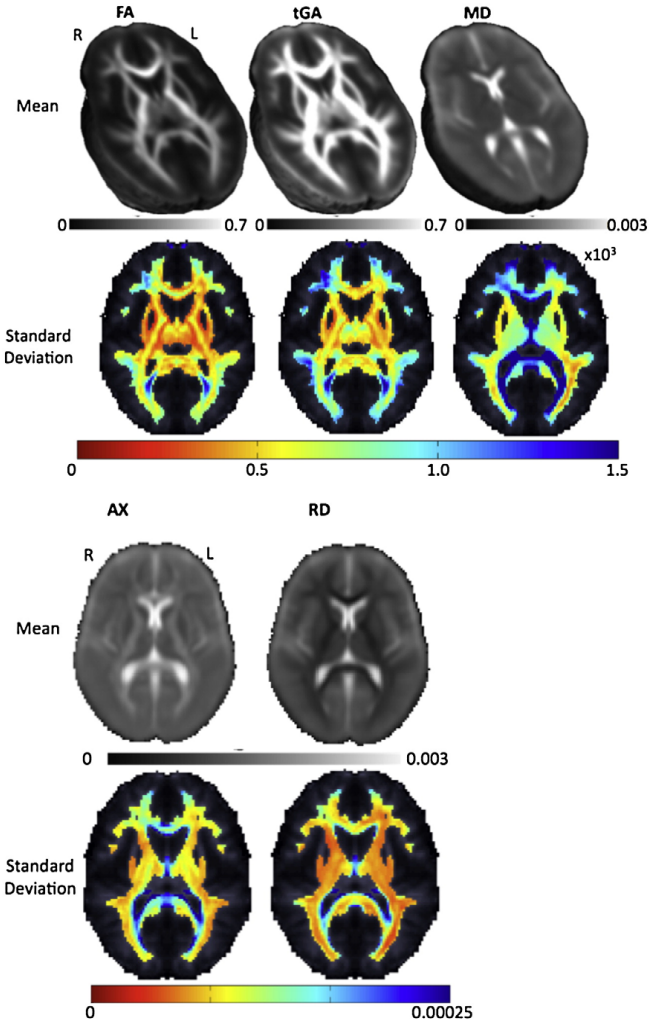

Fig. 5. Average and standard deviation maps for FA, tGA, MD, axial and radial diffusivity from the 207 independent subjects used in this analysis. In the FA and tGA maps, fiber anisotropy is higher, as expected, in the deep white matter tracts (*corpus callosum*, *internal capsule* and *corona radiata*), and the variance in the DTI-derived measures is higher in the same regions (blue colors). The notation $\times 10^3$ on the figure indicates that the range of the standard deviation color bar is 0 to 1.5×10^{-3}.

N. Jahanshad et al. / NeuroImage 52 (2010) 455–469

intellectual performance. We used a random mixed effects regression model for this analysis to account for the familial relation between subjects.

Results

Population-based average maps of diffusion and anisotropy

Fig. 5 shows average FA, tGA and MD maps for all 207 independent subjects used in this analysis.

Anisotropy asymmetry

Fig. 6 shows the average difference in anisotropy measures between hemispheres. Anisotropy differences exceeded 0.15 in frontal and temporal regions — this number is the difference in the mean FA between left and right hemisphere. FA values run from 0 to 1, so the difference reaches ~1/6 of the allowable range. Percent differences are not shown to avoid over-emphasizing differences in regions with low anisotropy. Significant asymmetries were detected after using FDR to correct for multiple comparisons, when comparing registered images in their original orientation to their reflected

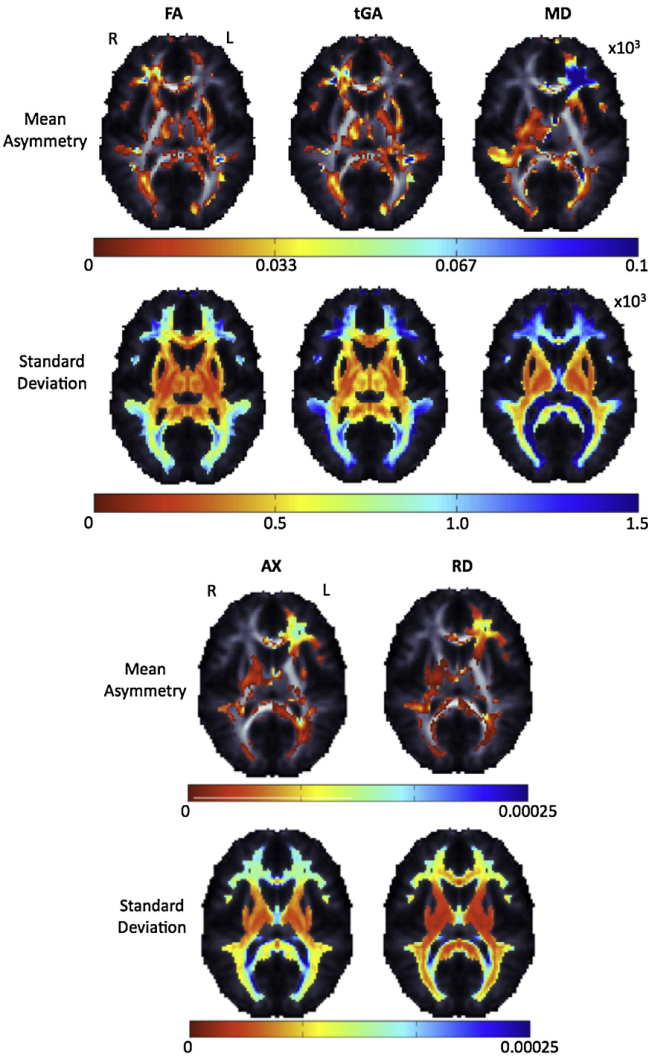

Fig. 6. Average and standard deviation for FA, tGA, mean, axial and radial diffusivity asymmetry (left–right difference) maps are shown for 207 unrelated subjects. Only one twin per pair was used to ensure independent sampling. The dorsolateral pre-frontal cortex (DLPFC) and Meyer's loop have strong asymmetries; also frontal lobe asymmetry is highly variable (bottom row — blue colors). The notation $\times 10^3$ on the figure indicates that the range of the top two color bars are 0 to 0.1×10^{-3}, and 0 to 1.5×10^{-3}.

Table 1
FDR was controlled at the 5% level, showing that the observed asymmetries survived a multiple comparison correction, when measured using any index above (FA, tGA, MD). Around half of the white matter (defined as voxels with FA>0.25) showed a detectable asymmetry.

	FA	tGA	MD
FDR corrected *p*-value	0.0238	0.0243	0.0283
% significant	47.69%	48.62%	56.68%

images. The percentage of voxels significant after FDR correction is shown in Table 1. In Fig. 7 the pairwise differences calculated from Student's *t*-test across hemispheres are shown as maps of the *t*-statistics and associated *p*-values.

Anisotropy asymmetry differences between sexes

Fig. 8 shows the average difference in fiber anisotropy across hemispheres in analyses split by sex. Asymmetry maps for the two sexes were compared, using a map of *t*-statistics. FDR confirmed sex differences, but very few voxels had sufficient effect sizes to pass the FDR threshold. The percentage of voxels within the brain found to be significant, while still keeping the FDR at 5%, is shown in Table 2, and is less than 1%. This result is formally significant, due to the large sample, but may not be relevant in practice.

In a *post hoc* exploratory analysis, we examined the significance of the *variance* in fiber asymmetry difference across the sexes using *F*-tests and found a much greater effect in white matter (FA>0.25) regions (Table 3).

Genetics of fiber asymmetry

Falconer's heritability maps were computed from the intra-class correlations of the monozygotic and dizygotic twin pairs (Fig. 9). This revealed regions of high heritability for asymmetry in some frontal and temporal lobe regions.

To account for multiple comparisons, non-parametric permutation tests were performed on a voxel by voxel level to avoid assuming parametric null distributions for the statistics. Cumulative distribution functions (CDFs) of the resulting significance values from the ICCs were plotted against their expected null distribution (Fig. 10). This reveals which results were significant overall when enforcing a false discovery rate at the 5% level.

Fig. 11 shows an $A/C/E$ analysis of variance components for mean fiber measures in various white matter regions of interest (ROIs). Asymmetries in the inferior fronto-occipital fasciculus and the anterior thalamic radiation are highly genetically influenced ($a^2=0.33$ and $a^2=0.37$ respectively for FA). Both the forceps major and the uncinate fasciculus showed genetic ($a^2=0.2$ and $a^2=0.2$, respectively for FA) and common environmental ($c^2=0.05$ and $c^2=0.11$, respectively for FA) components of variance contributing to asymmetries. In contrast, the cortico-spinal tract and the forceps minor showed larger proportions of asymmetry variance attributable to shared environmental factors.

When the goodness-of-fit probability for the ACE model is greater than $p=0.05$, it suggests a good fit (note that this is the opposite of the usual *p*-value convention). All models shown in Fig. 11 had a sufficient goodness-of-fit. For a few of the regions tested (not shown), the ACE model did not fit. These included: for FA, the cingulum ($p=0.02$) and the inferior longitudinal fasciculus ($p=0.04$) and for MD: the inferior fronto-occipital fasciculus ($p=0.02$), and the inferior longitudinal fasciculus ($p=1\times10^{-6}$). All tGA models fitted well.

Voxel-wise $A/C/E$ tests were also performed to estimate the genetic component of variance at each voxel. Voxels in temporal and frontal lobe subregions showed highest genetic influences. Results were similar for both anisotropy measures, although geodesic anisotropy measures gave slightly higher measures of genetic variance than FA (Fig. 12).

To account for multiple comparisons in the structural equation models that calculate additive genetic and shared environmental factors at every voxel, the model of the individual component of interest $p(A)$ and $p(C)$ was calculated and FDR was performed on the

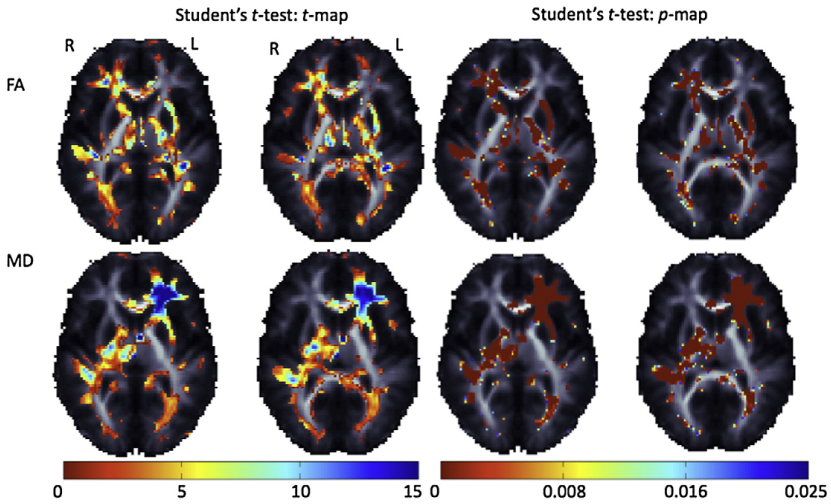

Fig. 7. Pairwise *t*-tests show regions with inter-hemispheric differences in FA and MD, based on comparing images in their original orientation with their reflected versions. These maps visualize the effect size for the asymmetry (high in the DLPFC and Meyer's loop). The *p*-values and absolute value of *t* are shown from this test — $|t|$ values are as high as 15. Over 50% of the brain's white matter (Table 1) shows detectable asymmetry.

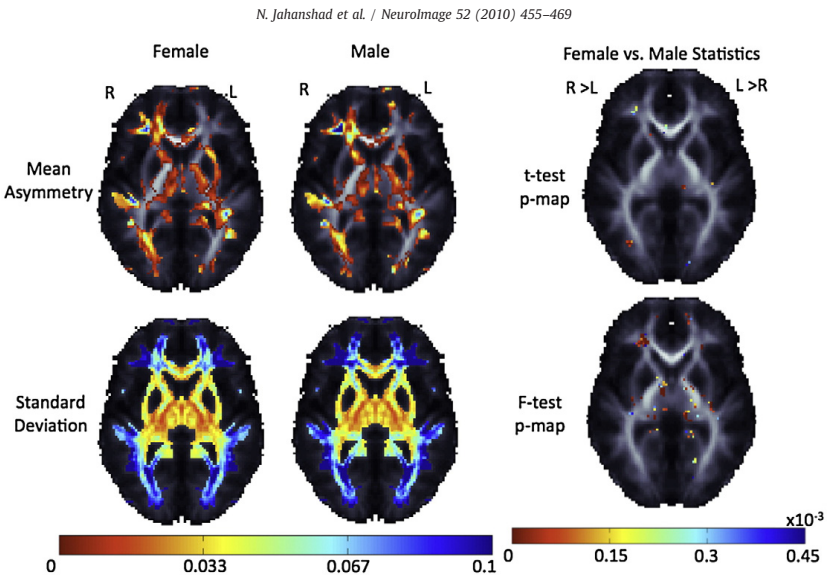

Fig. 8. Top row: Average FA asymmetry maps are shown for separate groups of 126 women and 81 men, all unrelated. One twin per pair was used, to ensure independent sampling and avoid including correlated observations. Sex differences (last column) were detected in the degree of fiber asymmetry. Men showed greater asymmetries than women, but these sex differences were detectable in <1% of the brain's white matter. Bottom row: The standard deviation for asymmetry in each sex is presented along with the resulting *p*-map after a test for differences in within-group variance. Group differences in the variance of asymmetry are minor, but are more pronounced than the differences in asymmetry intensity itself.

resulting model to yield the probabilities of significance seen in Table 5.

Fiber asymmetry and IQ correlations

As various measures of intelligence were obtained from all subjects, as a *post hoc* test we examined possible correlations between fiber FA asymmetry and IQ. For this exploratory test, we hypothesized that greater fiber asymmetry might be associated with higher performance IQ (and performance IQ in particular, which may depend on processing speed more than the linguistic skills involved in verbal IQ). ROI-based and voxel-wise random effects regression models were fitted to the data. We used the entire sample of subjects with available IQ information, fixed the effect of sex, and regressed out the random effects due to familial structure. However, after multiple comparisons correction using FDR in the entire white matter region, no overall correlations were detected across the entire group of 358 subjects. We consider this null finding worth reporting, as the sample size is large for a DTI study.

Discussion

Our analysis of DTI asymmetries, in this large population ($N = 374$ adults), had 3 main findings.

First, frontal and temporal regions had significant asymmetries in FA. Frontal lobe FA is greater in the right hemisphere, but left temporal lobe FA is greater than on the right. The mean difference in this large sample reached 0.15 (which is very high, considering that FA runs on a scale of 0 to 1). Second, in a regional analysis of FA asymmetry, genetic factors accounted for 33% of the variance in asymmetry in the inferior fronto-occipital fasciculus, 37% of the variance in the anterior thalamic radiation, and 20% of the variance in the forceps major and the uncinate fasciculus. Shared environmental factors accounted for ~15% of the variance in the cortico-spinal tract and ~10% of the variance in the forceps minor. Asymmetries are therefore influenced by both genetic and environmental factors. Results were similar regardless of the anisotropy measure used (FA versus tGA). Finally, the frontal lobe FA asymmetry had higher variance in men than in women, but only a small proportion of voxels showed sex differences in the average level of asymmetry.

As expected from twin studies of brain structure (Brun et al., 2009; Thompson et al., 2001), monozygotic twins showed higher similarities in the intra-class correlation maps than dizygotic twins suggesting that fiber asymmetries are genetically influenced. This is in line with a large body of work by Annett, who proposed that there might be a single "right-shift" gene influencing the degree of cerebral dominance and lateralized behavior such as handedness (Annett, 1998).

A preliminary map of heritability, based on Falconer's heritability formula (Fig. 9), crudely estimates the genetic proportion of variance as twice the difference between the monozygotic twin correlations and the dizygotic twin correlations. As this initial analysis detected

Table 2
Sex differences in asymmetry. FDR was controlled at the 5% level, as a multiple comparison correction. Even so, <1% of voxels fell below the statistical threshold required to control the FDR.

	FA	tGA	MD
FDR corrected *p*-value	3.232×10^{-6}	3.251×10^{-5}	3.844×10^{-4}
% significant	0.0079%	0.067%	0.781%

Table 3
These maps of differences in the variance of asymmetry between the sexes could be thresholded at the above critical *p*-values while controlling the FDR at the 5% level, as a multiple comparison correction. There were significant sex differences in the population variance associated with fiber asymmetry (with significantly greater asymmetry variance in men than women in the frontal lobe and in women than men in temporal–parietal regions, on average).

	FA	tGA	MD
FDR corrected *p*-value	0.0032	0.0030	0.012
% significant	6.39%	6.21%	25.49%

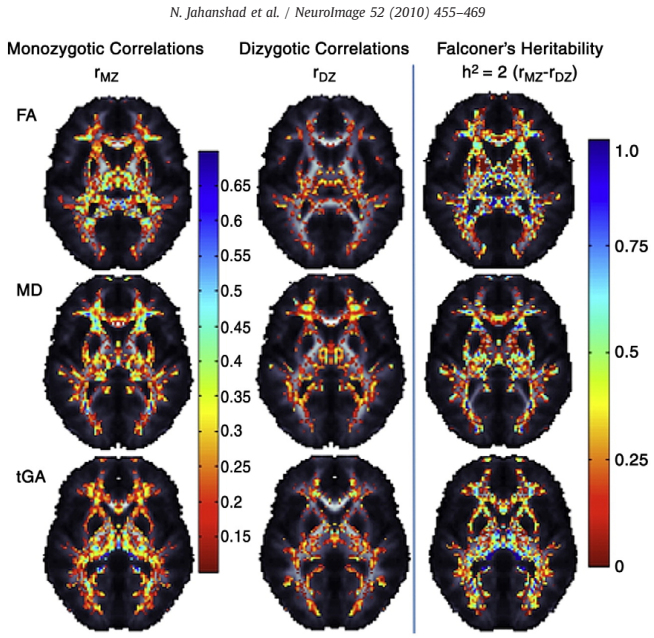

Fig. 9. Intra-class correlation maps for monozygotic and dizygotic twins along with Falconer's heritability maps for asymmetries in FA, and tGA. In general, monozygotic twins have higher intra-pair correlations than dizygotic twins.

genetic involvement in fiber asymmetry, we fitted structural equation models to data from ROIs (Table 4). Voxel-wise genetic models confirmed the genetic effects on the frontal lobe asymmetries, and also suggested high genetic contributions in some temporal lobe regions.

Regions with high genetic contributions to fiber asymmetry were also the regions where asymmetry is greatest. The finding that frontal lobe FA is greater in the right hemisphere, but greater on the left for the temporal lobes, confirm prior DTI reports of frontal and temporal white matter asymmetries. In general, prior studies focused on specific tracts, e.g., the cortico-spinal tract (Westerhausen et al., 2007) and the arcuate fasciculus, which is involved in language processing (de Jong et al., 2009; Rodrigo et al., 2007). A voxel-wise analysis (Buchel et al., 2004) suggested left greater than right FA white matter

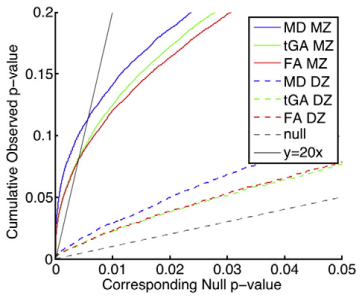

Fig. 10. CDF plots of the distribution of the *p*-values obtained after non-parametric permutation testing, to account for multiple comparisons. For all measures, MZ and DZ twins showed significant intra-class correlations after multiple comparison correction using FDR. The MZ twin effects were much greater as denoted by the higher FDR-controlling critical *p*-values (i.e., the highest non-zero *x*-coordinate where the CDF crosses the $y = 20x$ line). These probabilities were obtained from pre-selected brain regions with average FA>0.25, to avoid analyzing voxels with very low anisotropy.

asymmetries in the arcuate fasciculus and found asymmetries contralateral to the dominant hand (i.e., higher on the left in right-handers) in tracts innervating the precentral gyrus (as expected, given the crossing of the cortical motor circuitry). Frontal and temporal white matter already show left greater than right FA in early infancy (Dubois et al., 2008), suggesting greater myelination in the left hemisphere. Some developmental studies found that frontal FA differences between the two hemispheres diminish as the brain develops, but temporal lobe asymmetries persist (Barnea-Goraly et al., 2005). These asymmetries may relate to the functional lateralization of higher-level cognitive processes such as spatial association and language, but our regressions with global cognitive measures did not reveal any associations.

Early studies of anatomical asymmetry noted a natural *petalia* (torquing) of the brain, that shifts right hemisphere structures anterior to their left hemisphere counterparts (Kimura, 1973; Toga and Thompson, 2003). Post mortem studies found volumetric asymmetries in the *planum temporale*, part of a temporal lobe auditory and language processing area (Geschwind and Levitsky, 1968). More recently, a large MRI study of 142 young adults confirmed leftward volume asymmetries in posterior language areas, and rightward asymmetries in the cingulate gyrus and caudate nucleus (Watkins et al., 2001). Surface-based analysis methods that adjust for the effects of structural translocation in space (e.g., torquing) also found leftward asymmetries in the Heschl's gyrus and *planum temporale* (Lyttelton et al., 2009). Deformation-based morphometry studies have used the theory of random Gaussian vector fields to detect brain asymmetries, and have been used to detect statistical departures from the normal level of brain asymmetry (also termed "dissymmetry"; Thirion et al., 2000; Lancaster et al., 2003). In addition, some "apparently" lateralized effects in brain mapping may arise due to hemispheric differences in the statistical power to detect effects. This is inevitable, as the structures in the two hemispheres have different patterns of anatomical variability (Thompson et al., 1998; Fillard et al., 2007).

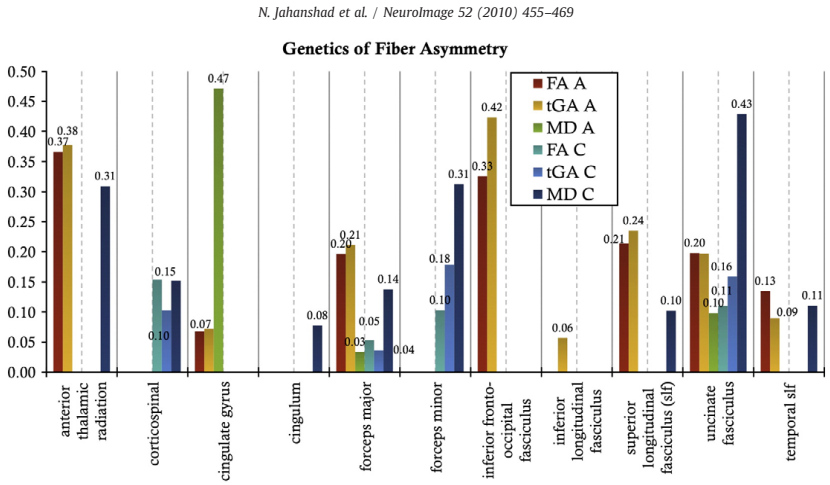

Fig. 11. *A*/*C*/*E* genetic results for fiber asymmetry per lobe. The proportion of variance (ranging from 0 to 1) due to each factor is shown for each region of interest. Both anisotropy measures show similar trends.

FA asymmetry had a higher variance in men than women, but there was only limited evidence for differences in the overall level of asymmetry (i.e., the sex difference formally passed the FDR criterion for significance but showed differences in less than 1% of the brain). Many studies report greater anatomical asymmetries in men than women (reviewed in Toga and Thompson, 2003). A voxel-based MRI study of 465 normal adults found sex differences in gray matter volumes and concentrations but no effects of handedness on the level of asymmetries (Good et al., 2001). In a small sample ($N=20$), Szeszko et al. (2003) reported that women had higher FA in the left frontal lobes compared to men, and a general leftward asymmetry of FA. No hemispheric asymmetry was detected in men. The level of leftward asymmetry in women was associated with better verbal comprehension and memory functioning. This result is surprising, given our finding of strong R>L asymmetry for FA; the magnitude of this effect is quite large in our much larger sample of subjects. Our finding of significant but limited sex differences could be due to our efforts to create a template that minimizes the structural differences between the hemispheres. This reduces the influence of "brain shape" on the asymmetries, which may have diminished any sex differences.

With fMRI, Shaywitz et al. (1995) found significant sex differences in the phonological processing of language. Brain activation in men was lateralized to the left inferior frontal gyrus, while women engaged more diffuse neural systems involving both the left and right inferior frontal gyri. Men and women also have brain regions in which regional volumes correlate with intelligence. Haier et al. (2005) found that women showed more white matter and fewer gray matter areas with volumes correlated with intelligence, when compared to men. IQ correlates with FA in normal subjects, and both IQ and FA are genetically influenced (Chiang et al., 2009a; Kochunov et al., 2009). Because of this, we also regressed FA asymmetry against IQ, but no correlations survived FDR correction. IQ may relate closely to FA in specific brain regions, but not so much to its asymmetry.

A premise of any voxel-wise analysis of brain asymmetry is that there is a structural homology between white matter structures in the left and right hemispheres. For the major white matter tracts, such as the corpus callosum, fornix, and optic radiations, this assumption is tenable. The registration methods proposed here are likely to adjust for any macroscopic shape differences that get in the way of pairing homologous anatomy, where it exists, on both sides of the brain. Even so, as in all studies mapping brain asymmetry, there will always be a set of structures – cortical U-fibers for example – with no obvious homologs in the other hemisphere. As such, differences in hemispheric anatomy near the cortex may reflect not just a signal difference from the same structure occurring in both hemispheres but a lack of homology. These cases may ultimately be distinguishable with tools that model and cluster each hemisphere's tracts as a graph, with known connectivity and topological relations; in that case, differences in tract composition between hemispheres would be easier to identify.

Table 4
ACE summaries: sub-models (AE and CE) are compared to the full (ACE) model to test whether dropping a parameter resulted in significant differences in the chi-squared goodness-of-fit value.

tGA	Correlation (95% CI)				Model fit: χ^2 (dχ^2 (df), p)					ACE estimates		
	MZ		DZ		ACE	AE		CE		a^2	c^2	e^2
Anterior thalamic radiation	0.44	(0.34:0.77)	0.00	(0:0.44)	6.34	6.34	(0(1);1.00)	10.15	(3.812(1);0.05)	0.38	0.00	0.62
Cortico-spinal tract	0.00	(0:0.37)	0.33	(0.08:0.72)	7.56	8.42	(0.854(1);0.36)	7.56	(0(1);1.00)	0.00	0.10	0.90
Cingulate gyrus	0.12	(0:0.53)	0.00	(0:0.38)	1.57	1.57	(0(1);1.00)	1.81	(0.242(1);0.62)	0.07	0.00	0.93
Cingulum	0.00	(0:0.21)	0.00	(0:0.39)	6.64	6.64	(0(1);1.00)	6.64	(0(1);1.00)	0.00	0.00	1.00
Forceps major	0.27	(0.05:0.66)	0.12	(0:0.57)	3.17	3.18	(0.009(1);0.92)	3.44	(0.263(1);0.61)	0.21	0.04	0.75
Forceps minor	0.12	(0:0.53)	0.23	(0:0.66)	10.93	11.62	(0.693(1);0.41)	10.93	(0(1);1.00)	0.00	0.18	0.82
Inferior fronto-occipital fasciculus	0.43	(0.33:0.76)	0.12	(0:0.57)	8.47	8.47	(0(1);1.00)	11.83	(3.364(1);0.07)	0.42	0.00	0.58
Inferior longitudinal fasciculus	0.11	(0:0.52)	0.00	(0:0.27)	11.75	11.75	(0(1);1.00)	11.97	(0.224(1);0.64)	0.06	0.00	0.94
Superior longitudinal fasciculus (slf)	0.29	(0.09:0.67)	0.00	(0:0.45)	6.51	6.51	(0(1);1.00)	7.31	(0.798(1);0.37)	0.24	0.00	0.77
Uncinate fasciculus	0.36	(0.22:0.72)	0.25	(0:0.67)	2.83	3.07	(0.242(1);0.62)	3.14	(0.312(1);0.58)	0.20	0.16	0.64
Temporal slf	0.12	(0:0.53)	0.00	(0:0.45)	3.54	3.54	(0(1);1.00)	3.72	(0.172(1);0.68)	0.09	0.00	0.91

Table 5
FDR was computed from the probability maps for the individual components, $p(A)$, $p(C)$ of the twin $A/C/E$ structural model. Genetic effects were confirmed; environmental effects were also detected.

	$p(A)$	$p(C)$
FDR corrected p-value for FA	0.000049	0.000048
FDR corrected p-value for tGA	0.000033	0.000037
FDR corrected p-value for MD	–	–

Methodological sources of variance in DTI data may also contribute to the level of asymmetries seen here. Magnetic susceptibility gradients occur at interfaces where tissue and air are in close proximity, and these are known to cause geometric distortions in the frontal and temporal poles. If severe, these distortions can cause a complete loss of signal, but in most cases they only lead to a geometrical warping of the data that can be corrected; here, we adjusted for it by using a mutual information based 3D elastic warping approach. In individual cases, this distortion could contribute to the level of asymmetry in the DTI signal, and to its variance, but it is unlikely to produce a systematic pattern of asymmetry that favors the left or the right side of the brain. Maps such as Fig. 8 (the mean asymmetry of FA) are unlikely to be affected much by susceptibility effects. These artifacts may contribute somewhat to the variance in asymmetry, slightly depleting the true biological correlations across members of a twin pair. Such artifacts would be lumped into the E-term of our structural equation model (which contains variance due to methodological error).

In addition, while the maps of DTI-derived measures (such as FA) were spatially normalized across subjects, no global intensity normalization was performed. We used each subject's raw FA measures and did not adjust them for overall differences in mean FA between subjects. In group analyses of PET scans, individual data

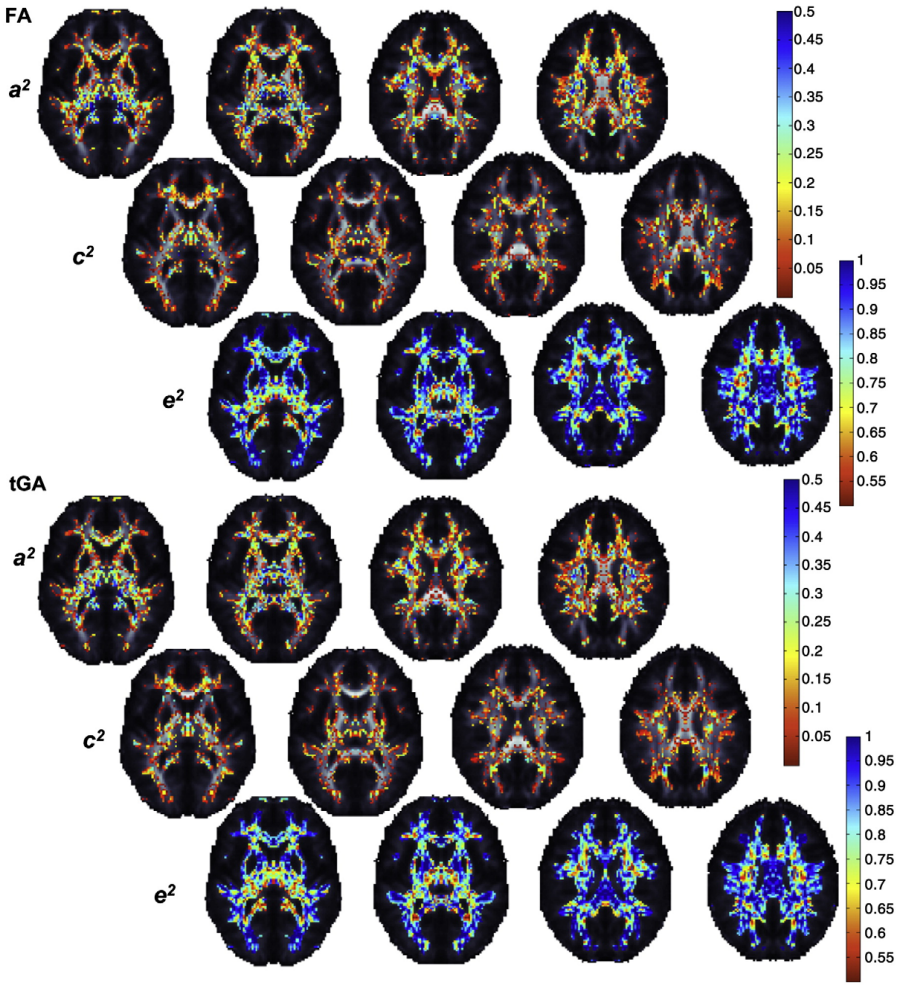

Fig. 12. Voxel-wise genetic analysis using the $A/C/E$ model shows that most of the asymmetry in fiber integrity is attributable to unique environmental influences, random differences, and measurement error; in some frontal and temporo-parietal regions, ~50% of the differences across hemispheres are due to genetic differences. Geodesic anisotropy measures may be marginally better for detecting genetic effects on fiber asymmetry, but maps for both DTI-derived indices were very similar.

are commonly adjusted for overall (global) levels of activation or ligand binding, but this is not typically done in DTI studies. It is assumed that the FA is an absolute measure of fiber coherence, that is associated with physiological parameters such as axonal conduction speed, and with cognitive measures such as IQ. As a result, global normalization is not usually applied and raw values are thought to provide a fundamental measure of fiber coherence. Even so, it is possible that local differences may, in part, reflect global differences in FA, or its asymmetry, across subjects.

Our study had 3 main limitations. First, we registered the FA images to a population averaged template created from the subjects' FA images. The same registrations, based on the FA images, were applied to all the DTI-derived maps, allowing us to structurally align all the images in the same way. Even so, there may be a slight bias in using a single anisotropy measure to drive the nonlinear registration, and other measures could be used, individually or in combination (Park et al., 2003, 2004). Several nonlinear registration algorithms have been proposed for DTI. Studholme (2008) used DTI-derived measures as constraints when aligning standard anatomical images. Chiang et al. (2008) and Li et al. (2009) used orientation and multivariate information in the full diffusion tensor to find correspondences between DTI images.

Second, in this paper, we used voxel-based statistical maps, focusing on highly anisotropic white matter regions. Other approaches may also be helpful for selecting regions with high anisotropy, such as the tract-based spatial statistics method (TBSS: Smith et al., 2006). In TBSS, a skeletonized (one pixel thick) map of the FA is created, and correspondences across subjects are based on distance, rather than by computing a correspondence field for the entire image. A third limitation of our study is that we do not fully exploit the angular information in the 105-direction diffusion-weighted images. Asymmetries in local diffusion geometry could also be examined by analyzing the local 3D diffusion profile, reconstructed using angular space deconvolution methods such as the tensor distribution function (Leow et al., 2008). This could further probe the sources of asymmetry after adjusting for confounds due to the partial voluming and fiber crossings — inherent limitations of scalar DTI-derived measures. One could then distinguish whether the right greater than left asymmetries are due to higher fiber integrity in the right hemisphere or whether the anisotropy levels on the left are reduced due to a higher level of fiber crossings.

Acknowledgments

This study was supported by grant number RO1 HD050735 from the National Institute of Child Health and Human Development, USA, T15 LM07356 from the NIH/National Library of Medicine, and Project Grant 496682 from the National Health and Medical Research Council, Australia. Additional support for algorithm development was provided by the NIA, NIBIB, and the National Center for Research Resources (EB008432, EB008281, EB007813, AG016570, and RR013642 to PT). Zygosity typing was supported by the Australian Research Council (A7960034, A79906588, A79801419, and DP0212016). We are extremely grateful to the twins for their participation, to the radiographer, Matt Meredith, Centre for Magnetic Resonance, University of Queensland, for image acquisition, and research nurses, Marlene Grace and Ann Eldridge, Queensland Institute of Medical Research, for twin recruitment.

References

Annett, M., 1998. Handedness and cerebral dominance: the right shift theory. J. Neuropsychiatry Clin. Neurosci. 10 (4), 459–469.
Annett, M., 1970. A classification of hand preference by association analysis. Br. J. Psychol. 61, 303–321.
Ardekani, S., Kumar, A., Bartzokis, G., Sinha, U., 2007. Exploratory voxel-based analysis of diffusion indices and hemispheric asymmetry in normal aging. Magn. Reson. Imaging 25 (2), 154–167.
Arsigny, V., Fillard, P., Pennec, X., Ayache, N., 2006. Log-Euclidean metrics for fast and simple calculus on diffusion tensors. Magn. Res. Med. 56 (2), 411–421.
Barnea-Goraly, N., Menon, V., Eckert, M., Tamm, L., Bammer, R., Karchemskiy, A., Dant, C.C., Reiss, A.L., 2005. White matter development during childhood and adolescence: a cross-sectional diffusion tensor imaging study. Cereb. Cortex 15 (12), 1848–1854.
Basser, P.J., Mattiello, J., Bihan, D.L., 1994. Estimation of the effective self-diffusion tensor from the NMR spin echo. J. Magn. Reson. B 103, 247–254.
Basser, P.J., Pierpaoli, C., 1996. Microstructural and physiological features of tissues elucidated by quantitative diffusion-tensor MRI. J. Magn. Reson. B 111, 209–219.
Batchelor, P., Moakher, M., Atkinson, D., Calamante, F., Connelly, A., 2005. A rigorous framework for diffusion tensor calculus. Magn. Reson. Med. 53, 221–226.
Beaton, A.A., 1997. The relation of planum temporale asymmetry and morphology of the corpus callosum to handedness, gender and dyslexia: a review of the evidence. Brain Lang. 60, 255–322.
Beaulieu, C., 2002. The basis of anisotropic water diffusion in the nervous system — a technical review. NMR Biomed. 15, 435–455.
Benjamini, Y., Hochberg, Y., 1995. Controlling the false discovery rate: a practical and powerful approach to multiple testing. J. R. Stat. Soc. Ser. B Methodol. 57 (1), 289–300.
Brun, C.C., Leporé, N., Pennec, X., Lee, A.D., Barysheva, M., Madsen, S.K., Avedissian, C., Chou, Y.Y., de Zubicaray, G.I., McMahon, K., Wright, M.J., Toga, A.W., Thompson, P.M., 2009. Mapping the regional influence of genetics on brain structure variability — a tensor-based morphometry study. NeuroImage. July 2009.
Buchel, C., Raedler, T., Sommer, M., Sach, M., Weiller, C., Koch, M., 2004. White matter asymmetry in the human brain: a diffusion tensor MRI study. Cereb. Cortex 14 (9), 945–951.
Chiang, M.C., Leow, A.D., Dutton, R.A., Barysheva, M., Rose, S., McMahon, K.L., de Zubicaray, G.I., Toga, A.W., Thompson, P.M., 2008. Fluid registration of diffusion tensor images using information theory. IEEE Trans. Med. Imaging 27 (4), 442–456 Apr.
Chiang, M.C., Barysheva, M., Lee, A.D., Madsen, S., Klunder, A., Toga, A.W., McMahon, K.L., de Zubicaray, G., Wright, M., Srivastava, A., Balov, N., Thompson, P.M., 2009a. Genetics of brain fiber architecture and intelligence. J. Neurosci. 29 (7), 2212–2224 Feb 18.
Chiang, M.C., Avedissian, C., Barysheva, M., Toga, A.W., McMahon, K.L., de Zubicaray, G.I., Wright, M.J., Thompson, P.M., 2009b. Extending genetic linkage analysis to diffusion tensor images to map single gene effects on brain fiber architecture. Medical Image Computing and Computer Assisted Intervention (MICCAI2009), pp. 506–513.
Chou, Y.Y., Lepore, N., Chiang, M.C., Avedissian, C., Barysheva, M., McMahon, K.L., de Zubicaray, G.I., Meredith, M., Wright, M.J., Toga, A.W., Thompson, P.M., 2009. Mapping genetic influences on ventricular structure in twins. Neuroimage 44, 1312–1323.
Crow, T.J., 1990. Temporal lobe asymmetries as the key to the etiology of schizophrenia. Schizophr. Bull. 16 (3), 433–443.
de Jong, L., Kovacs, S., Bamps, S., Calenbergh, F.V., Sunaert, S., van Loon, J., 2009. The arcuate fasciculus: a comparison between diffusion tensor tractography and anatomy using the fiber dissection technique. Surg. Neurol. 71 (1), 153-153.
de Zubicaray, G.I., Chiang, M.C., McMahon, K., Shattuck, D., Toga, A.W., Martin, N., Wright, M.J., Thompson, P.M., 2008. Meeting the challenges of neuroimaging genetics. Brain Imaging Behav. 2 (4), 258–263 12 2008.
Dubois, J., Hertz-Pannier, L., Cachia, A., Le Bihan, D.L., Dehaene-Lambertz, G., 2008. Structural asymmetries in the infant language and sensori-motor networks. Cereb. Cortex 19 (2), 414–423.
Eckert, M.A., Galaburda, A.M., Karchemskiy, A., Liang, A., Thompson, P.M., Dutton, R.A., Lee, A.D., Bellugi, U., Korenberg, J.R., Mills, D.L., Rose, F., Reiss, A.L., 2006. Anomalous Sylvian fissure morphology in Williams syndrome. NeuroImage 33 (1), 39–45 (Electronic publication ahead of print, 2006 Jul 28).
Falconer, D., Mackay, T.F., 1995. Introduction to Quantitative Genetics, 4th ed. Addison Wesley Longman (Pearson Education.
Fillard, P., Arsigny, W., Pennec, X., Hayashi, K.M., Thompson, P.M., Ayache, N., 2007. Measuring brain variability by extrapolating sparse tensor fields measured on sulcal lines. NeuroImage 34 (2), 639–650 (Electronic publication ahead of print, 2006 Nov 17).
Fillard, P., Arsigny, V., Pennec, X., Ayache, N., 2006. Clinical DT-MRI estimation, smoothing and fiber tracking with Log-Euclidean metrics. Biomedical Imaging: Nano to Macro, 2006: 3rd IEEE International Symposium on, pp. 786–789.
Fletcher, P.T., Joshi, S., 2004. Principal geodesic analysis on symmetric spaces: statistics of diffusion tensors. ECCV Workshops CVAMIA and MMBIA. Springer-Verlag, pp. 87–98.
Genovese, C.R., Lazar, N.A., Nichols, T., 2002. Thresholding of statistical maps in functional neuroimaging using the false discovery rate. NeuroImage 15 (4), 870–878.
Geschwind, N., Levitsky, W., 1968. Human brain: left–right asymmetries in temporal speech region. Science 161 (3837), 186–187.
Good, C.D., Johnsrude, I., Ashburner, J., Henson, R.N.A., Friston, K.J., Frackowiak, R.S.J., 2001. Cerebral asymmetry and the effects of sex and handedness on brain structure: a voxel-based morphometric analysis of 465 normal adult human brains. NeuroImage 14 (3), 685–700.
Hamilton, L.S., Narr, K.L., Luders, E., Szeszko, P.R., Thompson, P.M., Bilder, R.M., Toga, A.W., 2007. Asymmetries of cortical thickness: effects of handedness, sex, and schizophrenia. NeuroReport 18 (14), 1427–1431 Sep 17.
Haier, R.J., Jung, R.E., Yeo, R.A., Head, K., Alkire, M.T., 2005. The neuroanatomy of general intelligence: sex matters. NeuroImage 25 (1), 320–327.

Hulshoff Pol, H.E., Schnack, H.G., Posthuma, D., Mandl, R.C.W., Baare, W.F., Van Oel, C.J., Van Haren, N.E., Collins, D.L., Evans, A.C., Amunts, K., Burgel, U., Zilles, K., de Geus, E., Boomsma, D.I., Kahn, R.S., 2006. Genetic contributions to human brain morphology and intelligence. J. Neurosci. 26, 10235–10242.

Huang, H., Ceritoglu, C., Li, X., Qiu, A., Miller, M.I., van Zijl, P.C.M., Mori, S., 2008. Correction of B0 susceptibility induced distortion in diffusion-weighted images using large-deformation diffeomorphic metric mapping. Magn. Reson. Imaging 26 (9), 1294–1302.

Jahanshad, N., Lee, A.D., Chou, Y., Lepore, N., Brun, C., Barysheva, M., Toga, A.W., McMahon, K., de Zubicaray, G., Wright, M., Thompson, P.M., 2009. Genetics of anisotropy asymmetry: registration and sample size effects. Medical Image Computing and Computer-Assisted Intervention. MICCAI, pp. 498–505.

Jones, D.K., Horsfield, M.A., Simmons, A., 1999. Optimal strategies for measuring diffusion in anisotropic systems by magnetic resonance imaging. Magn. Reson. Med. 42 (3), 515–525 September.

Kimura, D., 1973. The asymmetry of the human brain. Sci. Am. 228 (3), 70–78.

Klingberg, T., Hedehus, M., Temple, E., Salz, T., Gabrieli, J.D., Moseley, M.E., Poldrack, R.A., 2000. Microstructure of temporo-parietal white matter as a basis for reading ability: evidence from diffusion tensor magnetic resonance imaging. Neuron 25, 493–500.

Kochunov, P., Glahn, D.C., Lancaster, J.L., Winkler, A.M., Smith, S., Thompson, P.M., Almasy, L., Duggirala, R., Fox, P.T., Blangero, J., 2010. Genetics of microstructure of cerebral white matter using diffusion tensor imaging. Neuroimage.

Kochunov, P., Lancaster, J.L., Thompson, P.M., Toga, A.W., Brewer, P., Hardies, J., Fox, P., 2002. An optimized individual target brain in the Talairach coordinate system. NeuroImage 17 (2), 922–927.

Kochunov, P., Lancaster, J.L., Thompson, P.M., Woods, R., Mazziotta, J., Hardies, J., Fox, P., 2001. Regional spatial normalization: toward an optimal target. J. Comput. Assist Tomogr. 25 (5), 805–816.

Koziol, J.A., Wagner, S., Sobel, D.F., Feng, A.C., Adams, H.P., 2005. Asymmetries in the spatial distributions of enhancing lesions and black holes in relapsing–remitting ms. J. Clin. Neurosci. 12 (8), 895–901.

Lancaster, J.L., Kochunov, P.V., Thompson, P.M., Toga, A.W., Fox, P.T., 2003. Asymmetry of the brain surface from deformation field analysis. Hum. Brain Mapp. 19 (2), 79–89 June.

Lawyer, G., Ferkingstad, E., Nesvag, R., Varnas, K., Agartz, I., 2009. Local and covariate-modulated false discovery rates applied in neuroimaging. NeuroImage 2009.03.047.

Lee, A.D., Leporé, N., Barysheva, M., Chou, Y.Y., Brun, C., Madsen, S.K., McMahon, K., de Zubicaray, G.I., Wright, M.J., Toga, A.W., Thompson, P.M., 2008. Gene effects mapped using fractional and geodesic anisotropy in diffusion tensor images of 92 monozygotic and dizygotic twins. MICCAI.

Lee, A.D., Lepore, N., Brun, C.C., Chou, Y.Y., Barysheva, M., Chiang, M.C., Madsen, S.K., de Zubicaray, G.I., McMahon, K.L., Wright, M.J., Toga, A.W., Thompson, P.M., 2009a. Tensor-based analysis of genetic influences on brain integrity using DTI in 100 twins. Medical Image Computing and Computer Assisted Intervention (MICCAI2009), pp. 967–974.

Lee, K., Yoshida, T., Kubicki, M., Bouix, S., Westin, C.F., Kindlmann, G., Niznikiewicz, M., Cohen, A., McCarley, R.W., Shenton, M.E., 2009b. Increased diffusivity in superior temporal gyrus in patients with schizophrenia: a diffusion tensor imaging study. Schizophr. Res. 108 (1–3), 33–40.

Leow, A.D., Zhu, S., Zhan, L., McMahon, K., de Zubicaray, G.I., Meredith, M., Wright, M.J., Toga, A.W., Thompson, P.M., 2008. The tensor distribution function. Magn. Reson. Med. 18 (61(1), 205–214.

Leow, A.D., Huang, S.C., Geng, A., Becker, J.T., Davis, S.W., Toga, A.W., Thompson, P.M., 2005. Inverse consistent mapping in 3D deformable image registration: its construction and statistical properties. IPMI 2005, 493–503.

Leporé, N., Brun, C., Chiang, M.C., Chou, Y.Y., Dutton, R., Hayashi, K., Lopez, O., Aizenstein, H., Toga, A.W., Becker, J., Thompson, P.M., 2006. Multivariate statistics of the Jacobian matrices in tensor based morphometry and their application to HIV/AIDS. Medical Image Computing and Computer-Assisted Intervention. MICCAI — 2006, pp. 191–198.

Leporé, N., Chou, Y.Y., Lopez, O.L., Aizenstein, H.J., Becker, J.T., Toga, A.W., Thompson, P. M., 2008a. Fast 3D fluid registration of brain magnetic resonance images. Medical Imaging 2008: Physiology, Function, and Structure from Medical Images, vol. 6916. SPIE, San Diego, CA, USA.

Leporé, N., Brun, C.C., Chou, Y.Y., Lee, A.D., Barysheva, M., de Zubicaray, G.I., Meredith, M., McMahon, K., Wright, M.J., Toga, A.W., Thompson, P.M., 2008b. Multi-atlas tensor-based morphometry and its application to a genetic study of 92 twins. MICCAI.

Li, H., Xue, Z., Guo, L., Wong, S.T., 2009. Simultaneous consideration of spatial deformation and tensor orientation in diffusion tensor image registration using local fast marching patterns. In: Prince, J.L., Pham, D.L., Myers, K.J. (Eds.), Proceedings of the 21st international Conference on information Processing in Medical Imaging (Williamsburg, Virginia, July 05–10, 2009); Lecture Notes In Computer Science, vol. 5636. Springer-Verlag, Berlin, Heidelberg, pp. 63–75.

Lin, J.J., Salamon, N., Lee, A.D., Dutton, R.A., Geaga, J.A., Hayashi, K.M., London, E.D., Luders, E., Toga, A.W., Engel, J., Thompson, P.M., 2006. Reduced neocortical thickness and complexity mapped in mesial temporal lobe epilepsy with hippocampal sclerosis. Cerebral Cortex 2006 Nov 6.

Liu, Z., Zhu, H., Marks, B.L., Katz, L.M., Goodlett, C.B., Gerig, G., Styner, M., 2009. Voxel-wise group analysis of DTI. Proceedings of the 6th IEEE International Symposium on Biomedical Imaging: from Nano to Macro, pp. 807–810.

Luders, E., Rex, D.E., Narr, K.L., Woods, R.P., Jancke, L., Thompson, P.M., Mazziotta, J.C., Toga, A.W., 2003. Relationships between sulcal asymmetries and corpus callosum size: gender and handedness effects. Cerebral Cortex 13 (10), 1084–1093 2003 Oct.

Luders, E., Narr, K.L., Thompson, P.M., Rex, D.E., DeLuca, H., Jancke, L., Toga, A.W., 2005. Hemispheric asymmetries in cortical thickness. Cereb. Cortex Nov. 2 2005.

Lyttelton, O.C., Karama, S., Ad-Dab'bagh, Y., Zatorre, R.J., Carbonell, F., Worsley, K., Evans, A.C., 2009. Positional and surface area asymmetry of the human cerebral cortex. NeuroImage.

Morra, J., Tu, Z., Apostolova, L.G., Green, A.E., Avedissian, C., Madsen, S.K., Parikshak, N., Hua, X., Toga, A.W., Jack, C.R., Schuff, N., Weiner, M.W., Thompson, P.M., 2009. Automated 3D mapping of hippocampal atrophy and its clinical correlates in 400 subjects with Alzheimer's disease, mild cognitive impairment, and elderly controls. Hum. Brain Mapp. 2009 Jan 26.

Mori, S., Wakana, S., Nagae-Poetscher, L.M., van Zijl, P.C.M., 2005. MRI Atlas of Human White Matter. Elsevier, Amsterdam, The Netherlands.

Mühlau, M., Gaser, C., Wohlschläger, A.M., Weindl, A., Städtler, M., Valet, M., Zimmer, C., Kassubek, J., Peinemann, A., 2007. Striatal gray matter loss in Huntington's disease is leftward biased. Mov. Disord. 22 (8), 1169–117310.1002/mds.21137.

Narr, K.L., Bilder, R.M., Luders, E., Thompson, P.M., Woods, R.P., Robinson, D., Szeszko, P., Dimtcheva, T., Gurbani, M., Toga, A.W., 2007. Asymmetries of cortical shape: effects of handedness, sex and schizophrenia. NeuroImage 34 (3), 939–948.

Nichols, T.E., Holmes, A.P., 2002. Nonparametric permutation tests for functional neuroimaging: a primer with examples. Hum. Brain Mapp. 15 (1), 1–2510.1002/hbm.1058.

Park, H.J., Westin, C.F., Kubicki, M., Maier, S.E., Niznikiewicz, M., Baer, A., Frumin, M., Kikinis, R., Jolesz, F.A., McCarley, R.W., Shenton, M.E., 2004. White matter hemisphere asymmetries in healthy subjects and in schizophrenia: a diffusion tensor MRI study. Neuroimage 23 (1), 213–223.

Park, H.J., Kubicki, M., Shenton, M.E., Guimond, A., McCarley, R.W., Maier, S.E., Kikinis, R., Jolesz, F.A., Westin, C.F., 2003. Spatial normalization of diffusion tensor MRI using multiple channels. Neuroimage 20 (4), 1995–2009.

Peper, J.S., Brouwer, R.M., Boomsma, D.I., Kahn, R.S., Hulshoff Pol, H.E., 2007. Genetic influences on human brain structure: a review of brain imaging studies in twins. Hum. Brain Mapp. 28, 464–473.

Rijsdijk, F.V., Sham, P.C., 2002. Analytic approaches to twin data using structural equation models. Brief. Bioinform. 3 (2), 119–133.

Rodrigo, S., Naggara, O., Oppenheim, C., Golestani, N., Poupon, C., Cointepas, Y., Mangin, J.F., Le Bihan, D.L., Meder, J.F., 2007. Human subinsular asymmetry studied by diffusion tensor imaging and fiber tracking. AJNR 28 (8), 1526–1531.

Schmitt, J.E., Lenroot, R.K., Wallace, G.L., Ordaz, S., Taylor, K.N., Kabani, N., Greenstein, D., Lerch, J.P., Kendler, K.S., Neale, M.C., Giedd, J.N., 2008. Identification of genetically mediated cortical networks: a multivariate study of pediatric twins and siblings. Cereb Cortex.

Shaywitz, B.A., Shaywltz, S.E., Pugh, K.R., Constable, R.T., Skudlarski, P., Fulbright, R.K., Bronen, R.A., Fletcher, J.M., Shankweiler, D.P., Katz, L., Gore, J.C., 1995. Sex differences in the functional organization of the brain for language. Nature 373 (6515), 607–609.

Smith, S.M., Jenkinson, M., Johansen-Berg, H., Rueckert, D., Nichols, T.E., Mackay, C.E., Watkins, K.E., Ciccarelli, O., Cader, M.Z., Matthews, P.M., Behrens, T.E., 2006. Tract-based spatial statistics: voxelwise analysis of multi-subject diffusion data. Neuroimage 31 (4), 1487–1505.

Sowell, E.R., Thompson, P.M., Rex, D.E., Kornsand, D.S., Jernigan, T.L., Toga, A.W., 2002a. Mapping sulcal pattern asymmetry and local cortical surface gray matter distribution in vivo: maturation in perisylvian cortices. Cereb. Cortex 12 (1), 17–26 Jan. 2002.

Sowell, E.R., Thompson, P.M., Peterson, B.S., Mattson, S.N., Welcome, S.E., Henkenius, A.L., Riley, E.P., Jernigan, T.L., Toga, A.W., 2002b. Mapping cortical gray matter asymmetry patterns in adolescents with heavy prenatal alcohol exposure. Neuroimage 17 (4), 1807–1819 Dec. 2002.

Stein, J.L., Hua, X., Morra, J., Lee, S., Ho, A.J., Leow, A., Toga, A.W., Sul, J., Kang, H., Eskin, E., Saykin, A., Shen, L., Foroud, T., Pankratz, N., Huentelman, M., Craig, D., Gerber, J., Allen, A., Corneveaux, J., Stephan, D., Webster, J., DeChairo, B., Potkin, S., Jack, C., Weiner, M., Thompson, P.M., 2010. Genome-wide association study of temporal lobe structure identifies novel quantitative trait loci for neurodegeneration in Alzheimer's disease. NeuroImage 51 (2), 542–554.

Stein, J.L., Hua, X., Lee, S., Ho, A.J., Leow, A.D., Toga, A.W., Saykin, A.J., Shen, L., Foroud, T., Pankratz, N., Huentelman, M.J., Craig, D.W., Gerber, J.D., Allen, A., Corneveaux, J., Stephan, D.A., Webster, J., DeChairo, B.M., Potkin, S.G., Jack, C.R., Weiner, M.W., Thompson, P.M., 2010. Voxelwise genome-wide association study (vGWAS), NeuroImage, Special issue on Imaging Genomics, March 2010.

Studholme, C., 2008. Dense feature deformation morphometry: incorporating DTI data into conventional MRI morphometry. Special issue on Information Processing in Medical Imaging 2007: Medical Image Analysis, vol. 12, pp. 742–751. Issue 6, December.

Styner, M., Lieberman, J.A., McClure, R., Weinberger, D., Jones, D., Gerig, G., 2005. Morphometric analysis of lateral ventricles in schizophrenia and healthy controls regarding genetic and disease-specific factors. Proc. Natl. Acad. Sci. 102, 4872–4877.

Szeszko, P.R., Vogel, J., Ashtari, M., Malhotra, A.K., Bates, J., Kane, J.M., Bilder, R.M., Frevert, T., Lim, K., 2003. Sex differences in frontal lobe white matter microstructure: a DTI study. NeuroReport 14 (18), 2469–2473.

Thirion, J.P., Prima, S., Subsol, G., Roberts, N., 2000. Statistical analysis of normal and abnormal dissymmetry in volumetric medical images. Med. Imaging Anal. 4 (2).

Thompson, P.M., Lee, A.D., Dutton, R.A., Geaga, J.A., Hayashi, K.M., Eckert, M.A., Bellugi, U., Galaburda, A.M., Korenberg, J.R., Mills, D.L., Toga, A.W., Reiss, A.L., 2005. Abnormal cortical complexity and thickness profiles mapped in Williams syndrome. Journal of Neuroscience 25 (18), 4146–4158 April 20, 2005.

Thompson, P.M., Hayashi, K.M., de Zubicaray, G., Janke, A.L., Rose, S.E., Semple, J., Herman, D., Hong, M.S., Dittmer, S., Doddrell, D.M., Toga, A.W., 2003. Dynamics of gray matter loss in Alzheimer's disease. J. Neurosci. 23 (3), 994–1005 Feb. 1 2003.

Thompson, P.M., Cannon, T.D., Narr, K.L., van Erp, T., Poutanen, V.P., Huttunen, M., Lonnqvist, J., Standertskjold-Nordenstam, G.G., Kaprio, J., Khaledy, M., Dail, R., Zoumalan, C.I., Toga, A. W., 2001. Genetic influences on brain structure. Nat. Neurosci. 4, 1253–1258.

Thompson, P.M., Moussai, J., Khan, A.A., Zohoori, S., Goldkorn, A., Mega, M.S., Small, G.W., Cummings, J.L., Toga, A.W., 1998. Cortical variability and asymmetry in normal aging and Alzheimer's disease. Cereb. Cortex 8 (6), 492–509 Sept.1998.

Toga, A.W., Thompson, P.M., 2003. Mapping brain asymmetry. Nat. Rev. Neurosci. 4 (1), 37–48.

Wakana, S., Caprihan, A., Panzenboeck, M.M., Fallon, J.H., Perry, M., Gollub, R.L., Hua, K., Zhang, J., Jiang, H., Dubey, P., Blitz, A., van Zijl, P.C.M., Mori, S., 2007. Reproducibility of quantitative tractography methods applied to cerebral white matter. NeuroImage 36, 630–644.

Wang, Q., Seghers, D., D'Agostino, E., Maes, F., Vandermeulen, D., Suetens, P., Hammers, A., 2005. Construction and validation of mean shape atlas templates for atlas-based brain image segmentation. IPMI., pp. 689–700.

Watkins, K., Paus, T., Lerch, J., Zijdenbos, A., Collins, D., Neelin, P., Taylor, J., Worsley, K., Evans, A., 2001. Structural asymmetries in the human brain: a voxel-based statistical analysis of 142 MRI scans. Cereb. Cortex 11 (9), 868–877.

Westerhausen, R., Huster, R.J., Kreuder, F., Wittling, W., Schweiger, E., 2007. Corticospinal tract asymmetries at the level of the internal capsule: is there an association with handedness? NeuroImage 37 (2), 379–386.

Witelson, S.F., Kigar, D.L., 1992. Sylvian fissure morphology and asymmetry in men and women: bilateral differences in relation to handedness in men. J. Comp. Neurol. 323, 326–340.

CHAPTER 4

Iron and white matter pathways

4.1 Transferrin and hemochromatosis gene association to brain structure

The following section is adapted from:

Jahanshad N, Kohannim O, Hibar DP, Stein JL, Barysheva M, McMahon KL, de Zubicaray GI, Medland SE, Montgomery GW, Whitfield JB, Martin NG, Wright MJ, Toga AW, Thompson PM (2011). Brain structure in healthy young adults is related to serum transferrin and the H63D polymorphism in the HFE gene. PNAS Plus January 9, 2012.

PNAS PLUS

Brain structure in healthy adults is related to serum transferrin and the H63D polymorphism in the *HFE* gene

Neda Jahanshad[a,b], Omid Kohannim[a], Derrek P. Hibar[a], Jason L. Stein[a], Katie L. McMahon[c], Greig I. de Zubicaray[d], Sarah E. Medland[e], Grant W. Montgomery[e], John B. Whitfield[e], Nicholas G. Martin[e], Margaret J. Wright[e], Arthur W. Toga[a], and Paul M. Thompson[a,1]

[a]Laboratory of NeuroImaging, Department of Neurology, University of California, Los Angeles, School of Medicine, Los Angeles, CA 90095; [b]Medical Imaging Informatics Group, Department of Radiology, University of California, Los Angeles, School of Medicine, Los Angeles, CA 90095; [c]Centre for Advanced Imaging, University of Queensland, Brisbane QLD 4072, Australia; [d]School of Psychology, University of Queensland, Brisbane QLD 4072, Australia; and [e]Queensland Institute of Medical Research, Herston QLD 4006, Australia

Edited by Marcus E. Raichle, Washington University, St. Louis, MO, and approved December 1, 2011 (received for review April 7, 2011)

Control of iron homeostasis is essential for healthy central nervous system function: iron deficiency is associated with cognitive impairment, yet iron overload is thought to promote neurodegenerative diseases. Specific genetic markers have been previously identified that influence levels of transferrin, the protein that transports iron throughout the body, in the blood and brain. Here, we discovered that transferrin levels are related to detectable differences in the macro- and microstructure of the living brain. We collected brain MRI scans from 615 healthy young adult twins and siblings, of whom 574 were also scanned with diffusion tensor imaging at 4 Tesla. Fiber integrity was assessed by using the diffusion tensor imaging-based measure of fractional anisotropy. In bivariate genetic models based on monozygotic and dizygotic twins, we discovered that partially overlapping additive genetic factors influenced transferrin levels and brain microstructure. We also examined common variants in genes associated with transferrin levels, *TF* and *HFE*, and found that a commonly carried polymorphism (H63D at rs1799945) in the hemochromatotic *HFE* gene was associated with white matter fiber integrity. This gene has a well documented association with iron overload. Our statistical maps reveal previously unknown influences of the same gene on brain microstructure and transferrin levels. This discovery may shed light on the neural mechanisms by which iron affects cognition, neurodevelopment, and neurodegeneration.

neuroimaging genetics | twin modeling | pathway analysis | tensor-based morphometry | voxel based analysis

Iron and the proteins that transport it are critically important for brain function. Iron deficiency (ID) is the most common nutritional deficiency worldwide (1). Iron-deficient diets lead to poorer cognitive achievement in school-aged children (2). In rural areas where ID anemia is prevalent, iron supplements can increase motor and language capabilities in children (3). ID also impairs dopamine metabolism in the brain, particularly in the caudate and putamen regions (4).

ID clearly has adverse effects on cognitive development, but iron overload in later life is also associated with damage to the brain. Brain iron regulation is disrupted in several neurodegenerative diseases. Neuroimaging methods reveal abnormally high brain iron concentrations in Alzheimer's disease (5), Parkinson disease (6), and Huntington disease (7). High iron concentrations may even cause neuronal death (8, 9).

As deficiency and excess of iron can negatively impact brain function, the regulation of iron transport to the brain is crucial for cognition. Iron is transported throughout the body by the iron-binding protein transferrin. The interaction between transferrin and the transferrin receptors appears to regulate iron transport (10). When iron levels are low, the liver produces more transferrin for increased iron transport. In humans, transferrin can increase in iron-deficient states, which may help to distinguish ID anemia from anemia of chronic disease (11). Dietary ID has also been shown in rats to elevate the concentration of transferrin in the brain (12), specifically in the hippocampus and striatum (13). Transferrin is also decreased in cases of iron overload (14).

The gold standard for determining accurate iron measures is obtained from invasive bone marrow or liver tests, which are impractical for general applications. Serum levels of iron fluctuate greatly (15) and depend on dietary factors such as vitamin C intake (16) and the time of blood collection (17). Transferrin is arguably a more reliable and reproducible index of the long-term availability of iron to the brain (18, 19). In fact, in a 2-y study of postmenopausal women (20), total iron-binding capacity (equivalent to transferrin concentration) was a more reliable measure of iron status [(0.60; 95% confidence interval (CI), 0.44–0.76)], whereas serum iron measures varied more (0.50; 95% CI, 0.22–0.65). Transferrin is therefore used as a more reproducible measure to infer iron availability to the neural pathways.

As iron is a key determinant of neural development and degeneration, we set out to investigate whether brain structure in healthy adults depends on serum transferrin levels. We scanned 615 young adult twins and siblings with standard MRI. A total of 574 of them were also scanned with diffusion tensor imaging (DTI) to assess volumetric and microstructural white matter differences potentially associated with variations in serum transferrin levels measured during adolescence.

The participants in our study were healthy young adults, in whom iron overload is unlikely. We instead expected that iron levels toward the lower end of the normal range might lead to a poorer developmental phenotype in the brain of these young adults.

The brain synthesizes transferrin itself, so serum transferrin is not necessarily indicative of the levels of brain transferrin. However, in healthy populations without iron overload or hemochromatosis, all iron in the plasma is bound to transferrin (10). Iron enters the brain primarily by transport through the blood–brain barrier (21), yet transport through the blood–cere-

Author contributions: N.J., O.K., and P.M.T. designed research; N.J. and P.M.T. performed research; K.L.M., G.I.d.Z., S.E.M., G.W.M., J.B.W., N.G.M., M.J.W., and A.W.T. contributed new reagents/analytic tools; N.J., O.K., D.P.H., J.L.S., and P.M.T. analyzed data; and N.J. and P.M.T. wrote the paper.

The authors declare no conflict of interest.

This article is a PNAS Direct Submission.

[1]To whom correspondence should be addressed. E-mail: thompson@loni.ucla.edu.

This article contains supporting information online at www.pnas.org/lookup/suppl/doi:10.1073/pnas.1105543109/-/DCSupplemental.

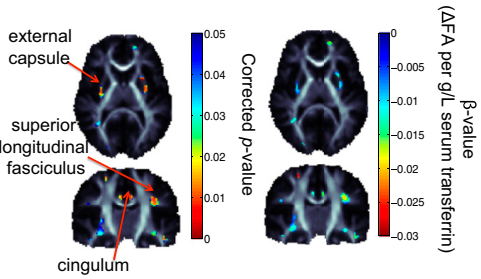

Fig. 1. Voxel-wise associations, between FA, a measure of white matter fiber integrity derived from the DW images, and serum transferrin levels in 574 subjects (five of whom had repeated scans). There are significant associations in the external capsule, superior longitudinal fasciculus, and the cingulum bilaterally. As transferrin levels increase, the diffusivity across the axons also tends to decrease by approximately 0.025 units for every g/L unit increase in the serum transferrin level. Significance was confirmed by enforcing a regional control over the FDR as described by Langers et al. (70) at the 5% level. Corrected *P* values of association are shown. Maps are adjusted for effects of age and sex; random-effects regression accounted for familial relatedness and the use of repeated scans. β-values shown represent the regression coefficient (or slope) of the transferrin level term, after accounting for covariates.

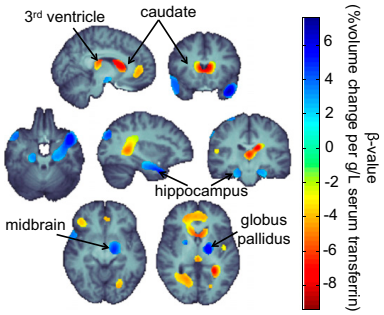

Fig. 2. Brain regions where there are detectable associations between serum transferrin levels and patterns of brain morphometry. Higher blood transferrin levels were associated with greater regional brain volumes in the hippocampus and basal ganglia, including the globus pallidus bilaterally and midbrain regions appearing to contain the substantia nigra. Shrinkage in structure volume is seen as transferrin levels increase bilaterally in the caudates, the third ventricle, as well as temporoparietal regions of white matter. Lower regional volumes are also observed in frontal gray matter in those with higher serum transferrin levels. The greatest regional brain volume deficit, per unit difference in transferrin levels, is seen in the caudate, whereas the greatest expansion is detected in the hippocampus and basal ganglia. All highlighted regions were significant after a multiple comparisons correction that enforces a regional control over the FDR at the 5% level as described by Langers et al. (70). Maps are adjusted for effects of age and sex; random-effects regression accounted for familial relatedness and the use of repeated scans (N = 652 scans, N = 615 subjects). All images are in radiological convention: the left side shown is the right hemisphere. The β-value corresponds to the unnormalized slope of the regression. Corrected *P* values range from 0.001 to 0.05; uncorrected values range from 2.6×10^{-6} to 0.04 for the thresholded regions shown.

brospinal fluid (CSF) and cellular–plasmalemma barriers have also been described (10). Upon binding to its receptor, transferrin is thought to be mostly released back into the blood stream (although some transcytosis of transferrin may occur). The iron can then bind to transferrin synthesized in the oligodendrocytes of white matter (22, 23).

Most of the brain's iron is found in oligodendrocytes, where it supports myelination (24). Oligodendrocytes also maintain iron homeostasis in the brain. Our primary hypothesis was that we might find poorer white matter integrity in adulthood in those who had lower iron levels available during development, as high transferrin levels are often a sign of the liver reacting to lower iron availability. We therefore framed our hypothesis by testing if serum transferrin levels in adolescence were related to fractional anisotropy (FA; measured later in adulthood from DTI scans of the brain). Lower FA can be a sign of less mature or poorer myelination.

We further hypothesized that brain structure volumes in iron-rich regions might be lower in people with high serum transferrin levels. Iron levels are highest in the basal ganglia and substantia nigra (25). By measuring brain volumes regionally with tensor-based morphometry (TBM), we predicted that we might find insufficiently developed (i.e., smaller) subcortical structures in those with higher transferrin levels. ID additionally alters dopamine metabolism in the caudate and putamen (4), so we predicted that people with high transferrin (and, by implication, lower brain iron) might have lower volumes for dopamine-containing structures, such as the caudate. Finally, we expected lower hippocampal volumes, as iron-deficient rats have lower iron concentrations in the hippocampus (13), a region vulnerable to neuronal loss in neurodegenerative disease (26).

Genetic factors explain 66% and 49% of the variance in serum transferrin levels in men and women, respectively (17). As such, if transferrin is found to be associated with neuroanatomical differences, we might expect that common genes influence both brain structure and transferrin levels. To understand such shared genetic contributions to brain variations and transferrin, we used a twin design. Many neuroimaging studies of identical and fraternal twins reveal substantial genetic contributions to brain structure (27–30) and function (31, 32). Cross-twin cross-trait designs can also discover overlapping (i.e., pleiotropic) genetic influences on very different biological traits, such as brain volume (33) or fiber integrity (34) with IQ.

After discovering a common genetic basis for transferrin levels and brain fiber integrity, we hypothesized that genes modulating transferrin also play a role in brain structure within the same regions. We performed exploratory tests on all SNPs within the two major transferrin related genes: the transferrin gene, *TF*, on chromosome 3, and the *HFE* gene on chromosome 6, where a handful of SNPs have been found to explain a remarkable 40% of the genetic variance in serum transferrin levels (35). We performed exploratory tests on all these SNPs and additional imputed ones (to HapMap2) within the same genes.*

Genes influencing transferrin are not the only cause of variation in iron levels measured in the blood serum. However, they do influence the limited amount of serum iron that becomes transported into the brain. Therefore, we expected genes that influence transferrin levels to show associations with brain structure. Some variants increase the risk for iron overload late in life, and these may also increase the availability of brain iron for developmental processes such as myelination. If high iron levels improve myelination, we might expect to see increased fiber integrity as measured through DTI.

*Our dataset included a genotype list that had been imputed (to HapMap2) whereas the Benyamin et al. (2008) paper (35) did not; the previous paper therefore did not analyze the H63D polymorphism at all.

Results

Serum transferrin levels for the 615 individuals in our study ranged from 1.89 to 5.18 g/L of serum (mean, 2.99 ± 0.37 g/L; median, 2.96 g/L). Regressions fitted to data at each voxel in the brain DTI and MRI scans revealed significant associations with microstructural variations in diffusion anisotropy (Fig. 1). There were also strong associations between transferrin levels and gross anatomical volume differences (Fig. 2), even after controlling for age and sex. As ID is known to reduce myelination, we had expected in advance, to find a negative association between transferrin and FA (36); this was in fact observed.

Transferrin Levels Relate to Neuroanatomical Structure. As noted, cross-twin cross-trait models can determine whether a partially overlapping set of genes contributes to two traits of interest, such as fiber integrity (assessed by using FA) and transferrin levels. If this is the case, common genetic influences mediate the observed correlation between the two measures. Before examining the full cross-twin cross-trait model, we independently assessed these correlations within each group of twins; if the variables correlate more strongly for monozygotic (MZ) than for dizygotic (DZ) twin pairs, then we can infer the greater difference is a result of additive genetic factors. Fig. 3 shows the correlations between FA and transferrin levels in MZ twins and DZ twins separately, highlighting the higher magnitude of the correlations for MZ than DZ pairs.

Cross-Twin Cross-Trait Analysis of Shared Genetic Determination. We performed cross-twin cross-trait heritability analysis starting from the full bivariate model as described in *Methods*, where the ACE structural equation model was used to fit the additive genetic (A), shared environmental (C), and unique environmental (E) components of variance for the brain measures and transferrin levels. We removed individual components one by one to determine the best fitting model. For both MRI- and DTI-based bivariate ACE models, the AE model fitted the best for transferrin and the full ACE model fitted best for the imaging measures. This means that genetic effects were detected in both cases, and the effects of common rearing environment were also detectable for the imaging measures. The path diagram for the best fitting model is shown in Fig. 4.

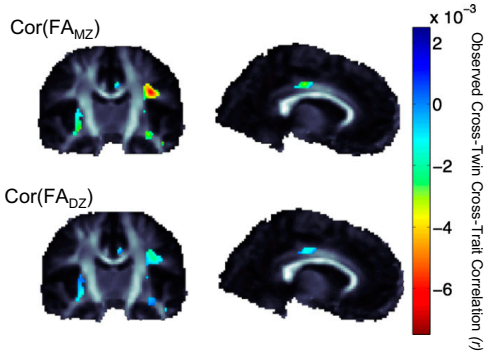

Fig. 3. The magnitude of the observed cross-twin cross-trait (FA and transferrin) correlations are higher in identical than fraternal twin pairs, supporting our hypothesis that partially overlapping sets of genes may explain some of the shared variance in brain structure and transferrin levels. This motivates the use of bivariate ACE modeling to estimate the degree of shared genetic influence.

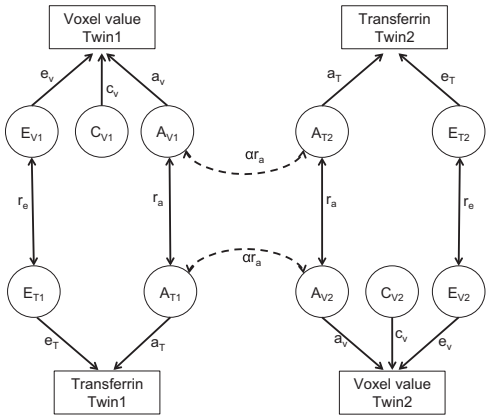

Fig. 4. Path diagram for the best-fitting model of the bivariate association. The models that best fitted the data were the AE model for transferrin and ACE model for the imaging measures. The measures we examined included regional brain volumes and measures of microstructural white matter fiber integrity.

The cross-twin cross-trait correlation was then computed from the best fitting model. Significance of the correlation was determined by removing the *rA* component of the path model as described in *Methods*. The additive genetic determinants of voxel-wise FA measures (Fig. 5) and transferrin showed significant overlap after multiple comparisons correction using the false discovery rate (FDR) procedure (37). Although suggestive, no significant overlap was detected between the additive genetic determinants of transferrin levels and macroscopic structural morphometry as assessed through TBM.

Genetic Associations. After filtering the SNPs in *TF* and *HFE* available in our imputed sample by minor allele frequency (MAF) greater than 0.05, 42 SNPs remained. SNPs chosen for analysis are listed in Table S1, along with their MAF according to the CEU population: Utah residents with Northern and Western European ancestry from the CEPH collection from HapMap. As a result of linkage disequilibrium, the effective number of SNPs tested (38, 39) was 20. When the significant voxels of the cross-twin cross-trait associations were clustered into regions of interest (ROIs), six survived a cluster threshold size of 27 voxels, corresponding to the size of a voxel with all its surrounding neighbors, or a 3 × 3 × 3 cube. These ROIs are shown in Fig. S1. Genetic associations of the 42 (effectively 20) SNPs assessed in these six regions revealed a significant association of the *HFE* rs1799945 SNP (also known as the H63D polymorphism) with the mean FA in the cluster along the left external capsule ($P = 0.00017$). The results of all of the genetic associations per ROI are also listed in Table S1.

Additionally, in the full sample of 565 genotyped subjects with serum transferrin levels available, we found that the H63D minor allele was associated with decreased transferrin levels as expected (*t*-statistic = 1.801, one-tailed $P = 0.0361$).

Post Hoc Voxel-Wise Analysis of *HFE* H63D Missense Polymorphism. In our post hoc analysis, we performed a voxel-wise association of FA with the H63D polymorphism across the entirety of the white matter region. The SNP frequency information for this polymorphism in our sample is available in *SI Methods*. The map of voxel-wise associations of H63D to FA values was found to be

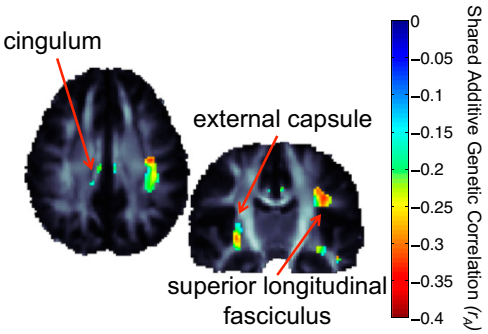

Fig. 5. Significant cross-twin cross-trait correlations for transferrin levels and brain FA. The *P* value controlling the FDR at the 5% level in regions of significant FA-transferrin associations was 0.032. The significant cross-twin cross-trait correlations presented here indicate that partially overlapping sets of genes are associated with transferrin levels and brain FA values in bilateral white matter regions, including the cingulum, external capsule, and superior longitudinal fasciculus. Negative correlations indicate lower anisotropy, perhaps indicating lower levels of myelination with increases in transferrin levels. Positive correlations were not significant.

significant in regions including the external capsule, and portions of the genu of the corpus callosum not initially found to have significant transferrin related associations (Fig. 6).

Discussion

ID, iron overload, and abnormalities in iron concentrations localized to particular structures in the brain have been linked to neurodevelopmental and neurodegenerative disorders.

Fig. 7 shows a schematic illustration relating several biological processes that motivated this study. Both brain structure and the iron transport protein, transferrin, are under strong genetic control, so we used a twin design to find brain regions with genetic determinants in common with transferrin. We were able to establish some previously unknown links between transferrin levels (and associated genes) and brain structure in 615 healthy young adults.

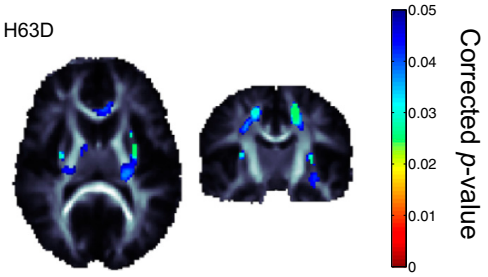

Fig. 6. Corrected *p*-map shows the *HFE* H63D associations with FA voxelwise throughout the white matter. When regressing on the minor allele, there is a positive association between the number of minor alleles and the FA values. Significance was confirmed by enforcing a regional control over the FDR as described by Langers et al. (70) at the 5% level. We adjusted for effects of age and sex to be consistent with the previous tests. Positive correlations were not significant.

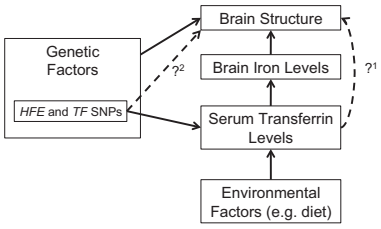

Fig. 7. Several known relationships motivated our study (solid black lines); dashed lines show relationships we wanted to test. Genetic and environmental factors (e.g., diet) affect iron stores in the body; the liver synthesizes more transferrin in response to low iron stores. Our first goal was to relate transferrin levels to brain structure in healthy young adults. Our twin design determined if overlapping sets of genes influence transferrin levels and brain structure, as both are highly heritable. Transferrin levels are genetically modulated mainly through two genes (*HFE* and *TF*); to relate specific variants in transferrin-related genes to brain structure, we determined the additive effect of all variants within these two genes on brain structures that had shown genetic influences in common with transferrin.

Our analysis had three main findings. First, serum transferrin levels, measured during adolescence, were associated with both macro- and microneuroanatomical variations in a regionally selective pattern later, in early adulthood (approximately 9 y after blood was drawn). Second, these associations with white matter integrity were mediated by overlapping sets of genes. This was evident from the cross-twin cross-trait correlations between transferrin levels and white matter anisotropy. Third, we found that the *HFE* H63D polymorphism, well known for its association to iron overload (40, 41), influences both serum transferrin levels and white matter microstructure in the external capsule. This points to a direct link between blood serum related genomic variation and brain structure (Fig. 7, dashed lines).

Iron is important for neural development early in life. In rat brains, iron and transferrin are at extremely high levels, despite low brain transferrin mRNA levels before closure of the blood–brain barrier (42). Even after the barrier develops, serum transferrin levels, which are under high genetic control, influence how much iron is transported to the brain for crucial processes of development, such as myelination. Here we uncovered an association between brain structure in young adults and serum transferrin levels measured during their adolescent years.

By measuring transferrin levels 8 to 12 y before the imaging study, we were interested in knowing whether iron availability in this developmentally crucial period might impact the organization of the brain later in life. Adolescence is a period of high vulnerability to brain insults, and the brain is still very actively developing (43). Transferrin levels, measured before the brain is fully mature, may be especially relevant for the adult brain. Transferrin levels fall with age in children and adolescents, and older adolescents show similar ranges to adults (15, 44). Children have higher transferrin levels than adults, perhaps in response to physiologically low iron stores. By averaging transferrin levels assessed repeatedly at various ages (12, 14, and 16 y of age), we estimated the iron availability to the brain during adolescence. We relied on previous work showing that transferrin measures are stable and can be reliably collected (19), with high sensitivity and specificity, which makes associations easier to detect.

As key components of white matter, oligodendrocytes—the glial cells that produce myelin to insulate axons—stain for iron more than any other cell in the brain (24); these cells are the primary location for iron in the central nervous system (45).

Fig. 1 shows the negative association between serum transferrin levels and the diffusion-based measure of integrity, FA, in

various brain regions, including the external capsule, cingulum, and superior longitudinal fasciculus. As FA can represent the degree of fiber integrity, myelination, or coherence in white matter fibers, the direction of this association is in line with previous reports indicating hypomyelination in cases of ID (36). Our findings of transferrin associations in human white matter tracts are consistent with previous studies of brain iron levels in rats. In a histochemical study of iron staining in the developing rat brain, Connor et al. (46) found major foci of iron staining in the cingulum, superior portions of the internal capsule, and the base of the external capsule.

As shown in Fig. 2, regional brain volume deficits are seen bilaterally in the caudates, the third ventricle, and in the temporoparietal white matter as transferrin levels increase. The caudate is particularly important in cognition, learning, and memory (47); as increased transferrin levels have been implicated in ID, the inverse relation between transferrin levels and caudate volume may indicate underdevelopment of caudates in ID, in line with evidence of poorer cognition in children with ID. If severe enough, a caudate volume reduction related to elevated transferrin levels may explain why certain developmental cognitive deficits are associated with ID. This finding fits with our previous hypothesis that insufficient iron transport to the brain may hinder development of subcortical structures.

Although transferrin levels are low, transferrin in the CSF is fully saturated with iron (48); the regional deficit in the volume of the third ventricle is therefore intriguing, as it may indicate an altered pattern and/or rate of transport for transferrin-bound iron.

Some brain regions were smaller and some larger in people with lower transferrin levels; in fact, there was statistically significant evidence in favor of both effects occurring in different parts of the brain. This pattern of anomalies was somewhat surprising: we expected smaller volumes, not larger ones, in people with low iron (and elevated transferrin) levels. Opposing this, some brain regions involved in neurodegeneration did show lower volumes in those with high iron and low transferrin levels, so iron overload may promote neuronal atrophy in iron-containing structures. The direct association of the volume of these regions to transferrin levels may therefore indicate a future susceptibility to the effects of iron overload and altered transport in these disorders.

Our DTI-based analyses supported a model wherein signs of a less mature or well myelinated brain were found in those with high transferrin levels during adolescence; this may reflect the liver's reaction to sustained periods of lower iron availability. The analysis of brain volumes with TBM gives a more complex picture: in segregated comparisons, there were some brain regions that were larger, and some were smaller in those with high transferrin. This imbalance of structure volumes is similar to that seen in some neurogenetic disorders, in which patterns of abnormally high and low volumes are seen (49, 50). As this was not hypothesized, future independent studies are needed to confirm the localization and direction of these effects.

As indicated by a dashed line in Fig. 7, a way to study the iron pathway's association to brain structure is to determine whether genes influencing transferrin levels also modulate structural variation. Our cross-twin cross-trait genetic analysis revealed that common additive genetic factors influence transferrin concentrations and white matter fiber integrity. Finding neuroanatomical regions whose underlying structure is partially under the same genetic control as transferrin levels can help shed light on the inherited properties of these regions as they develop. Discovering specific iron-associated genetic variants that influence the underlying microstructure in these brain regions could potentially help uncover the neural mechanisms affected by iron transport in the brain. These may lead to downstream genetically mediated impairments.

Specific variants associated with iron mediating proteins in healthy young adults have also been discovered; 40% of the genetic variance in serum transferrin levels is explainable by just a few genetic variants in the *TF* gene (rs3811647, rs1799852, and rs2280673) and the C282Y mutation in the *HFE* gene (35). Additionally, interaction between variants in these two genes has been linked to an increased risk of Alzheimer's disease (51), so the *TF* and *HFE* genes are neurobiologically linked. To comprehensively explore these two genes further and determine any coexisting associations to brain structure, we examined all available variants within these genes in regions where the shared additive genetic component between the two traits, transferrin levels and brain microstructure, was statistically significant. We found the H63D polymorphism within the *HFE* gene is significantly associated with the mean FA of the left external capsule, one of the regions shown to have significant cross-twin cross-trait correlations. The FA of the external capsule has also been shown to be highly heritable (~60%), however, a sex-by-heritability analysis also shows this region is much more heritable in male subjects (28). Intriguingly, genetic factors also explain a higher proportion of the variance for transferrin levels in men than in women (17).

In a recent study of *HFE* and *TF* variants on iron levels and risk for AD, Giambattistelli et al. (52) found that patients with AD with the H63D polymorphism had increased plasma iron and transferrin levels, but this pattern was not found in healthy control subjects with the variant; in fact, a meta-analysis found that the H63D polymorphism may be protective against AD (53). As shown in Table S1, the minor allele at rs1799945 (H63D) showed a positive effect on FA. This is the expected direction of association; as mentioned previously, ID can cause deficits in myelin formation, so it is reasonable that an iron overload allele may play a protective role for myelination during neuronal development of these healthy controls.

Our work here is one of the largest bimodal neuroimaging genetics studies of healthy humans to date. It describes a three-step top-down method to analyze gene effects on the brain. First, we related a heritable serum measure—with known cognitive associations—to specific locations in the brain; second, we used a genetic correlation model to home in on brain regions with evidence of joint genetic determination; and finally, we searched these neuroanatomical locations for variants within genes known to associate with the highly heritable phenotype, serum trans-

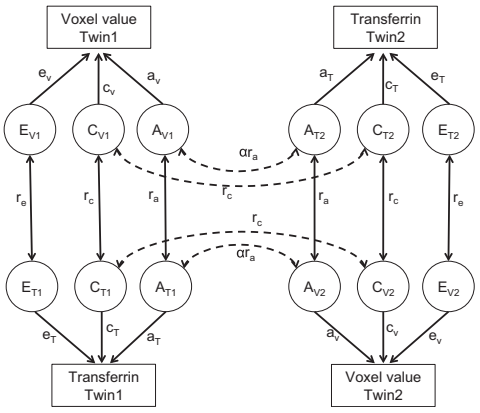

Fig. 8. Path diagram for the full bivariate ACE model.

ferrin. We found localized regions of transferrin association on both the macro- and micro-anatomical scale within the brain. These regions showed additional associations with *HFE* variants, in a direction that is consistent with several previous studies of brain iron and associated proteins. Future analyses may include studying the mechanistic process of transferrin and *HFE* in children with cognitive impairment and in elderly subjects with neurodegenerative diseases.

Several conclusions can be drawn about genetic variations that affect transferrin levels and their effect on brain microstructure. Transferrin levels are influenced by at least two known factors: a shortage of iron, which drives them up, and polymorphisms in the two major transferrin-related genes, *HFE* and *TF*, as shown in Fig. 7. According to a principle known as Mendelian randomization (54), one can examine genes that are known to affect a measure, such as transferrin, to get a sense of the downstream biological effects of other factors that affect transferrin, such as a shortage of dietary iron. We did find that the H63D mutation within the *HFE* gene was related to brain FA, but we did not find an effect on FA of the other common (i.e., MAF > 0.05) SNPs in the *HFE* or *TF* genes, which are known to explain 40% of variation in transferrin levels. A larger sample may be needed to uncover effects of these SNPs, but a more skeptical alternative interpretation may be that some variants known to powerfully affect transferrin may not affect DTI measures at all. At this point, we cannot say conclusively whether polymorphisms in the *TF* gene have any causal role on white matter, although the H63D mutation within the other major transferrin-related gene—*HFE*—was related to brain FA. A qualified interpretation of the available data would suggest that transferrin levels do relate to brain structure, but further work is needed to clarify which of the several known transferrin-related SNPs, other than *HFE* H63D, are contributing to the effect.

Methods

Subject Information. A total of 615 subjects (mean age ± SD, 23.5 ± 2.1 y; 375 women) were included in this study; all subjects had standard structural T1-weighted brain MRI scans and serum iron and transferrin levels measured; 574 also underwent DTI. As part of a reliability analysis, 37 subjects had a duplicate MRI scan taken 3 mo later, and five had a second DTI scan. All subjects were of European ancestry from 350 families. Subjects were recruited as part of a 5-y research project examining healthy young adult Australian twins using structural and functional MRI and DTI with a projected sample size of approximately 1,150 at completion (55). Subjects were screened to exclude cases of pathology known to affect brain structure. No subjects reported a history of significant head injury, a neurological or psychiatric illness, substance abuse or dependence, or had a first-degree relative with a psychiatric disorder. All subjects were right-handed as determined using 12 items from the Annett handedness questionnaire (56). We selected only the paired MZ (T1, n = 107; DTI, n = 95 pairs) and same-sex DZ (T1, n = 65; DTI, n = 59 pairs) twins for the cross-twin cross-trait genetic analysis. The rest of the subjects included 52 (n = 43 DTI) pairs of mixed-sex DZ twins, two sets of fraternal triplets (n = 6 individuals), and 112 (n = 95 DTI) individuals unrelated to anyone else in the study; additional subjects included non-twin siblings or unpaired twins with siblings also in the study in which kinship existed between members. A total of 544 of the subjects with standard MRI scans were genotyped, of whom 509 also had DTI scans available. Study participants gave informed consent; the studies were approved by the institutional ethics committees at the University of Queensland and the University of California, Los Angeles. All images used in this analysis went through, and passed, a rigorous quality control; subjects with anatomical abnormalities, imaging artifacts, and misregistered images were removed from analysis and not included in the subject counts.

Blood was collected from subjects at ages 12, 14, and 16 y. Serum was separated from blood samples and stored at −70 °C until assayed; iron, transferrin, and ferritin were measured by using standard clinical chemistry methods (Roche Diagnostics) on a 917 or Modular P analyzer. Data on serum iron and transferrin levels were extracted from these time points and averaged for use in this analysis.

Establishing Zygosity, Genotyping, and Imputation. Zygosity was established objectively by typing nine independent DNA microsatellite polymorphisms (polymorphism information content > 0.7), by using standard PCR methods and genotyping. Results were cross-checked with blood group (ABO, MNS, and Rh) and phenotypic data (hair, skin, and eye color), giving an overall probability of correct zygosity assignment greater than 99.99%. Genomic DNA samples were analyzed on the Human610-Quad BeadChip (Illumina) according to the manufacturer's protocols (Infinium HD Assay; Super Protocol Guide; Revision A, May 2008). Imputation was performed by mapping the genotyped information to HapMap (release 22, build 36) with Mach software (http://www.sph.umich.edu/csg/abecasis/MACH/index.html).

Image Acquisition. Structural and diffusion-weighted (DW) whole-brain MRI scans were acquired for each subject (4 Tesla Medspec; Bruker). T1-weighted images were acquired with an inversion recovery rapid gradient-echo sequence (inversion/repetition/echo times, 700/1500/3.35 ms; flip angle, 8°; slice thickness, 0.9 mm; 256 × 256 acquisition matrix). DW images were acquired using single-shot echo-planar imaging with a twice-refocused spin echo sequence to reduce eddy current-induced distortions. A 3-min, 30-gradient acquisition was designed to optimize signal-to-noise ratio for diffusion tensor estimation (57). Imaging parameters were repetition/echo times of 6,090/91.7 ms, field of view of 23 cm, and 128 × 128 acquisition matrix. Each 3D volume consisted of 21 axial slices 5 mm thick with a 0.5-mm gap and 1.8 × 1.8 mm^2 in-plane resolution. Thirty images were acquired per subject: three with no diffusion sensitization (i.e., T2-weighted b_0 images) and 27 DW images (b = 1,146 s/mm^2) with gradient directions uniformly distributed on the hemisphere.

Image Preprocessing. Nonbrain regions were automatically removed from each T1-weighted MR image and from a T2-weighted image from the DW image set using FSL software brain extraction tool (58) to enhance coregistration between subjects. All T1-weighted images were corrected for field nonuniformities using FreeSurfer (http://surfer.nmr.mgh.harvard.edu/), linearly aligned [with 9 degrees of freedom (df)] to a common space (59). The raw DW images were corrected for eddy current distortions by using the FSL tool "eddy_correct" (http://fsl.fmrib.ox.ac.uk/fsl/). For each subject, the three eddy-corrected images with no diffusion sensitization were averaged, linearly aligned, and resampled to the subject's corresponding down-sampled T1 image. The average b_0 maps were then elastically registered to the subject's aligned T1-weighted structural scan by using an inverse consistent registration with a mutual information cost function (60) to adjust for any echo-planar–induced susceptibility artifacts.

TBM. TBM is a technique that identifies regional structural differences from the gradients of the deformation fields that align brain images to a common anatomical template. After nonlinearly aligning the full brain of all subjects to their corresponding minimum deformation template (MDT), a separate Jacobian map (i.e., relative volume map) was created for each subject. These Jacobian maps, which share the common space defined by the MDT, help to characterize the local volume differences between one individual and the normal anatomical template. These maps explain the relative expansion and contraction of regions from each individual relative to the template.

Computing Anisotropy and Diffusivity. Under a single-tensor model (61), diffusion of water molecules attenuates the MR signal in direction r, according to the Stejskal–Tanner equation:

$$S_k(\mathbf{r}) = S_0(\mathbf{r})e^{-b_k D_k(\mathbf{r})} \quad [1]$$

Here, $S_0(\mathbf{r})$ is the non-DW baseline intensity in direction r, $D_k(\mathbf{r})$ is the apparent diffusion coefficient, and b_k is a constant depending on the gradient k. Diffusion tensors were computed from the 27-gradient DW images using FSL software (http://fsl.fmrib.ox.ac.uk/fsl/). The FA of diffusion was computed from the tensor eigenvalues (λ_1, λ_2, λ_3) at each voxel. FA is influenced by both axial diffusivity (λ_1; a measure of diffusion along the axonal fibers) and radial diffusivity (the average of λ_2 and λ_3; a measure of diffusion orthogonal to the axonal fibers).

Template Creation and Registration. We created an MDT by using nonlinear fluid registration (62), with the method proposed by Kochunov and colleagues (63, 64). The N 3D vector fields fluidly registering a specific individual to all other N participants were averaged and applied to that subject. This geometrically adjusts the anatomy but preserves the intensities and anatomical features of the template subject.

To create a representative MDT for the TBM analysis, we randomly selected 32 (16 female/16 male) nonrelated participants' T1-weighted images, after down-sampling to be in the same space as the DW imaging and aligning to the Colin template (59), and created two MDTs with 16 subjects (eight female) in each group. For one group, the target was male and the other female. The templates for each group were then averaged to create one representative anatomically centered target. Skull-stripped T1-weighted images for each subject were registered to the final population averaged FA-based MDT by using an inverse consistent 3D elastic warping technique using a mutual information cost function (60).

To create an MDT for DTI analysis, we selected the same 32 participants, yet we used their FA images (calculated after b_0 susceptibility correction) to create the MDT in the exact same manner as the T1-weighted structural scans. FA maps for each of the susceptibility corrected subjects were registered to the final population averaged FA-based MDT by using a 3D elastic warping technique with a mutual information cost function (60). To further align white matter regions of interest, the FA-based MDT and all whole-brain registered FA maps were then thresholded at 0.25, as FA values lower than 0.25 in healthy-appearing white matter may reflect contributions from nonwhite matter. Individual thresholded FA maps were then reregistered to the thresholded MDT in the same way as the whole brain registration. After registration of the FA maps, the FA images were smoothed with a Gaussian filter with an isotropic full-width half maximum of 5 mm).

Random-Effects Regression. The relationships of transferrin to measures of anisotropy and brain morphometry were assessed at each voxel in the brain by using a mixed-effects regression model to account for similarities within families while controlling for the effects of sex and age. To boost power of the association, and reduce random noise brought on by image acquisition, we included duplicate scans for the subjects who had them available. The variable of interest (transferrin), sex, and age were included as fixed effects. Random intercepts were included for each family and subjects to account for relatedness within families as well as the duplicate scans used. The analysis was implemented in the R statistical package (version 2.9.2; http://www.r-project.org/) using the 'nlme' library (65).

As noted earlier, extremely high and extremely low levels of iron can adversely affect the brain, but these observations do not completely imply in which direction the correlation would be in healthy people who maintain their iron levels for the most part in the normal range. As iron overload was not expected in this young, healthy population, mild insufficiencies in iron were considered more likely. This led to a directional hypothesis that poorer brain phenotypes might be found in those with lower chronic levels of iron (as inferred from transferrin measures). However, we considered it also possible, but less plausible, that there might be enough people with very high iron levels to drive the effect in the opposite direction. To allow for this alternative but less likely hypothesis, we ran our analyses with a more conservative searchlight FDR threshold of 0.025, to allow us to reject the null hypothesis in either direction, but distinguish between the alternative hypotheses in different directions. More information may be found in *SI Methods*.

Cross-Twin Cross-Trait Analysis. We used a cross-twin cross-trait analysis (66) to detect common genetic or environmental factors influencing both brain structure (or microstructure) and serum transferrin levels at every voxel within the brain. Covariance matrices for the phenotypes, in this case the voxel-wise structural measure of interest (structural deformation, microstructural anisotropy, or diffusivity) and serum transferrin levels were computed between the MZ twins who share all the same genes, and the DZ twins who share, on average, half of their genetic polymorphisms. These covariance matrices were then entered into a multivariate structural equation model [SEM (67)], using OpenMx software (http://openmx.psyc.virginia.edu/) to fit the relative contributions of additive genetic (A), shared environmental (C), and unshared or unique environmental (E) components to the population variances and covariances of the observed variables. Experimental measurement error is also included in the E component, and is assumed to be independent between twins 1 and 2 (i.e., no correlation).

In multivariate SEM, it is assumed that there are common genetic and environmental factors that affect various phenotypes, as also described in (34). Here we consider bivariate models with two phenotypes, transferrin levels and the brain MRI- or DTI-derived value at each voxel. The common genetic and environmental components of the variance may be estimated from the total population variance by examining the difference between the covariances between the MZ and DZ twins within the same individual (cross-trait within individual) and also between one phenotype in one twin with the other phenotype in the second twin (cross-twin cross-trait). By using this multivariate SEM, we can also obtain the additive genetic and shared environmental influences on the correlations between the two phenotypes, denoted as r_A and r_C, respectively. A path diagram describing the SEM and the connections between the twins is shown in Fig. 8.

The cross-trait within-individual correlation [i.e., the correlation between the voxel value (V) and transferrin (T) in twin 1 or in twin 2] is divided into additive genetic and shared and unique environmental components (e.g., $A_{V,i}$, $C_{V,i}$, and $E_{V,i}$ for voxel value and $A_{T,i}$, $C_{T,i}$, and $E_{T,i}$ for transferrin; $i = 1$ or 2 for twin 1 or 2), and the correlation coefficients between $A_{V,i}$ and $A_{T,i}$, $C_{V,i}$ and $C_{T,i}$, and $E_{V,i}$ and $E_{T,i}$, are denoted by r_a, r_c, and r_e, respectively. The cross-twin cross-trait correlation is shown as $A_{V,i}$ and $A_{T,j}$, and $C_{V,i}$ and $C_{T,j}$ for the voxel value in twin i and the transferrin level in twin j, where $i, j = 1$ or 2, and $i \neq j$. There is no r_e term for $E_{V,i}$ and $E_{T,j}$ because the unique environmental factors between subjects are independent. The covariance across the two phenotypes within the same subject, or separately in the two subjects, is then derived by multiplication of the path coefficients for the closed paths in the path diagram. For example, covariance between the voxel values in twin 1 and the transferrin level in twin 2 is equal to $a_V \cdot r_a \cdot a_T + c_V \cdot r_c \cdot c_T$ for MZ twins, and $a_V \cdot 1/2 r_a \cdot a_T + c_V \cdot r_c \cdot c_T$ for DZ twins. This implies that any excess in cross-twin cross-trait correlation in MZ twins over that in DZ twins is attributed to common genetic factors that affect both voxel values and transferrin levels.

Paths drawn between the same phenotype would be identical to considering a univariate voxel-wise SEM model (27). For A1 and A2, the correlation coefficient is equal to 1 for MZ and 0.5 for DZ twin pairs. The correlation coefficient between C1 and C2 is always 1 from the definition of the shared environment, and E1 and E2 are assumed to be independent and there is no correlation.

In twin studies, it is common to examine whether the observed measures are best modeled by using a combination of additive genetic and shared and unshared environmental factors, or whether only one or two of these factors is sufficient to explain the observed pattern of inter-twin correlations.

If the correlation between the voxel value of the image in one twin and the level of transferrin in the other twin is greater in MZ pairs than in DZ pairs, then, under standard assumptions, the greater correlation may be assumed to be caused by common genetic factors controlling both factors. In the univariate model with a single phenotype, which we denote x, the genetic and environmental contributions in twin j ($j = 1$ or 2) is modeled by defining the following:

$$x_j = a_x A_{xj} + c_x C_{xj} + e_x E_{xj} \quad [2]$$

A, C, and E, respectively, denote the additive genetic and shared and unshared environmental components. Cross-trait correlations between voxel values (v) and serum transferrin (t) level are then derived from the covariance matrix of the following vector:

$$w = (v_1, v_2, t_1, t_2) \quad [3]$$

given by the following 4 × 4 matrix:

$$\mathrm{cov}(w) = \begin{bmatrix} \Phi_{v,v} & \Phi_{t,v} \\ \Phi_{v,t} & \Phi_{t,t} \end{bmatrix} \quad [4]$$

where Φ_{vv} and Φ_{tt} are the 2 × 2 covariance matrices for phenotype v or t between twins 1 and 2, as performed in univariate SEM. Φ_{vt} is the cross-trait covariance matrix, composed of the covariance between the two traits within the different unrelated individuals [$cov(v_1, t_1)$ and $cov(v_2, t_2)$] and the cross-twin cross-trait covariance between the pairs [$cov(v_1, t_2)$ and $cov(v_2, t_1)$], as detailed below:

$$\begin{aligned} \Phi_{v,t} &= \begin{bmatrix} \mathrm{cov}(v_1, t_1) & \mathrm{cov}(v_1, t_2) \\ \mathrm{cov}(v_2, t_1) & \mathrm{cov}(v_2, t_2) \end{bmatrix} \\ &= \begin{bmatrix} r_a a_v a_t + r_c c_v c_t + r_e e_v e_t & \alpha \cdot r_a a_v a_t + r_c c_v c_t \\ \alpha \cdot r_a a_v a_t + r_c c_v c_t & r_a a_v a_t + r_c C_v c_t + r_e e_v e_t \end{bmatrix} \end{aligned} \quad [5]$$

where α is 1 for MZ twins, and 0.5 for DZ twins. r_a, r_c, and r_e are the cross-trait correlation coefficients for A_V and A_T, C_V and C_T, and E_V and E_T, respectively. A higher value of r_a indicates that the two phenotypes are more likely mediated by a common set of genes (34, 68). The path coefficients were estimated by comparing the covariance matrix implied by the model and the sample covariance matrix of the observed variables, using maximum-likelihood fitting to give a χ^2 value. We started from the full set of path coefficients (a_v, c_v, e_v, a_t, c_t, e_t, r_a, r_c, and r_e) and removed one of a_v, c_v a_t, and c_t from the model step by step. Removing a_v or a_t/c_v or c_t also removed r_a/r_c. e_1, e_2, and r_e were always kept in the model to include random noise. A model was considered to better fit the data if the difference in χ^2

values between it and the more comprehensive model at the previous step was not significant. If two models contained the same number of parameters, the model with a smaller χ^2 value was considered better. Model selection ended when the best model was achieved, i.e., when either (*i*) all possible more restricted models were not better than the current model or (*ii*) the current model was the most restricted and contained e_v, e_t, and r_e only. If r_a was included in the best model, the significance of r_a was then determined by comparing the χ^2 values of the best model and its submodel where r_a is 0. To determine the significance of the submodels, or the restricted models, with respect to the full model, we obtain the log-likelihood for the full and the restricted models, denoted by $log(L_f)$ and $log(L_r)$, respectively. Minus two times this difference, or $-2[log(L_r) - log(L_f)]$, is asymptotically distributed approximately as a χ^2 distribution with the df equal to the difference between the df of the two models, and therefore the inverse χ^2 distribution is estimated with these parameters.

SNP Selection. We examined all SNPs within two genes previously shown (35) to affect serum transferrin levels in healthy adults: *TF* and *HFE*. By using HapMap, we searched for SNPs that met our criterion of having an MAF greater than 5%; when matching these SNPs to those with available genotype information in our imputed data, 42 valid SNPs from these genes were available for analysis. We determined significance levels for association tests by first examining the total number of independent tests performed. Linkage disequilibrium among SNPs tested corresponds to correlation between the SNPs, and therefore each test is not completely independent. By first estimating the effective number of independent tests, we can avoid using a significance level too conservative for the number of tests we performed. As a result of linkage disequilibrium, the effective number of SNPs tested (38, 39) was 20.

ROI SNP Association in Significantly Correlated Clusters. In each cluster (>27 voxels to represent a size equivalent to one voxel and all its surrounding neighbors) that was found to have significant cross-twin cross-trait additive genetic associations, we found the average value across all of the voxels in that region and performed univariate associations with all 42 SNPs by using a mixed-model approach controlling for age and sex (emmaX; http://genetics.cs.ucla.edu/emmax/news.html) (69) to account for the familial relatedness between subjects through the use of a kinship matrix describing the approximate proportion of genetic similarities between subjects. A 0 in the kinship matrix represents the relation between unrelated individuals, MZ twins are related by 1 (with identical genomes), and DZ twins and nontwin siblings within the same family by 0.5 (as they share approximately half). Duplicate scans were not used for genetic associations.

Multiple Comparisons Correction. Computing thousands of tests of associations on a voxel-wise level can introduce a high Type I (i.e., false-positive) error rate in neuroimaging studies. To control these errors, we used a searchlight method for FDR correction as described by Langers et al. (70), which ensures a regional control over the FDR in any reported findings. To ensure adequate regionally selective associations with the transferrin levels, we use this searchlight method to correct the associations between the image phenotypes (morphometry or anisotropy) or transferrin. All maps shown are thresholded at the appropriate corrected *P* value after performing searchlight FDR (q = 0.05) to show only regions of significance; uncorrected *P* values are then shown only within these significant regions. To determine the best overall model for the SEM cross-twin cross-trait analysis, we use the standard FDR (37, 71) procedure as opposed to searchlight FDR, as we would like to determine the best overall fit of the SEM model, and not necessarily examine any localized or clustering effects. When examining the significance of the effects of the SNPs regressed on the mean FA value within ROIs with significant cross-twin cross-trait associations, we corrected for multiple comparisons by using the strict Bonferroni correction controlled at the q level of 0.05, at which a threshold for significance was determined by dividing 0.05 by the effective number of SNPs tested (20), and the number of ROIs where these SNPs were each tested previously (5). The Bonferroni threshold for significance was therefore set as follows:

$$q = 0.05/(20 * 6) = 0.00042 \quad [6]$$

Post Hoc Analysis: Voxel-Wise Effect of *HFE* H63D Polymorphism on Fiber Integrity. The number of minor alleles for each subject at *HFE* H63D (rs1799945) was regressed against the FA at each voxel within the white matter, after adjusting for sex and age as before. Family structure was taken into account with mixed-effects modeling (72). To correct for multiple comparisons across voxels, we used a searchlight method to control the FDR regionally (70).

ACKNOWLEDGMENTS. We thank the twins and siblings for their participation. In Brisbane, we thank Marlene Grace and Ann Eldridge for twin recruitment, Aiman Al Najjar and other radiographers for scanning, Kori Johnson for scanning and data transfer, Kerrie McAloney and Daniel Park for research support, and staff in the Molecular Epidemiology Laboratory for serum and DNA sample processing and preparation. This work was supported by National Institute of Child Health and Human Development Grant R01 HD050735, National Health and Medical Research Council (NHMRC; Australia) Grant 486682, Grant T15 LM07356 (to N.J.), the Achievement Rewards for College Scientists Foundation (J.L.S.), National Institute of Mental Health Grant 1F31MH087061 (to J.L.S.), and Australian Research Council Future Fellowship FT0991634 (to G.I.d.Z.). Genotyping was supported by NHMRC Grant 389875. Additional support for algorithm development was provided by National Institutes of Health Grants R01 EB008432, R01 EB008281, and R01 EB007813.

1. CDC (2002) From the Centers for Disease Control and Prevention. Iron deficiency—United States, 1999-2000. *JAMA* 288:2114–2116.
2. Halterman JS, Kaczorowski JM, Aligne CA, Auinger P, Szilagyi PG (2001) Iron deficiency and cognitive achievement among school-aged children and adolescents in the United States. *Pediatrics* 107:1381–1386.
3. Stoltzfus RJ, et al. (2001) Effects of iron supplementation and anthelmintic treatment on motor and language development of preschool children in Zanzibar: Double blind, placebo controlled study. *BMJ* 323:1389–1393.
4. Nelson C, Erikson K, Piñero DJ, Beard JL (1997) In vivo dopamine metabolism is altered in iron-deficient anemic rats. *J Nutr* 127:2282–2288.
5. Bartzokis G, et al. (1994) In vivo evaluation of brain iron in Alzheimer's disease and normal subjects using MRI. *Biol Psychiatry* 35:480–487.
6. Bartzokis G, et al. (1999) MRI evaluation of brain iron in earlier- and later-onset Parkinson's disease and normal subjects. *Magn Reson Imaging* 17:213–222.
7. Jurgens CK, et al. (2010) MRI T2 hypointensities in basal ganglia of premanifest Huntington's disease. *PLoS Curr* 2:RRN1173.
8. Ke Y, Ming Qian Z (2003) Iron misregulation in the brain: A primary cause of neurodegenerative disorders. *Lancet Neurol* 2:246–253.
9. Benarroch EE (2009) Brain iron homeostasis and neurodegenerative disease. *Neurology* 72:1436–1440.
10. Moos T, Morgan EH (2000) Transferrin and transferrin receptor function in brain barrier systems. *Cell Mol Neurobiol* 20:77–95.
11. Das Gupta A, Abbi A (2003) High serum transferrin receptor level in anemia of chronic disorders indicates coexistent iron deficiency. *Am J Hematol* 72:158–161.
12. Chen Q, Connor JR, Beard JL (1995) Brain iron, transferrin and ferritin concentrations are altered in developing iron-deficient rats. *J Nutr* 125:1529–1535.
13. Erikson KM, Pinero DJ, Connor JR, Beard JL (1997) Regional brain iron, ferritin and transferrin concentrations during iron deficiency and iron repletion in developing rats. *J Nutr* 127:2030–2038.
14. Khumalo H, et al. (1998) Serum transferrin receptors are decreased in the presence of iron overload. *Clin Chem* 44:40–44.
15. Suominen P, et al. (2001) Regression-based reference limits for serum transferrin receptor in children 6 months to 16 years of age. *Clin Chem* 47:935–937.
16. Lynch SR, Cook JD (1980) Interaction of vitamin C and iron. *Ann N Y Acad Sci* 355: 32–44.
17. Whitfield JB, et al. (2000) Effects of HFE C282Y and H63D polymorphisms and polygenic background on iron stores in a large community sample of twins. *Am J Hum Genet* 66:1246–1258.
18. Baynes RD (1996) Assessment of iron status. *Clin Biochem* 29:209–215.
19. Ahluwalia N (1998) Diagnostic utility of serum transferrin receptors measurement in assessing iron status. *Nutr Rev* 56:133–141.
20. Zeleniuch-Jacquotte A, et al. (2007) Reliability of serum assays of iron status in postmenopausal women. *Ann Epidemiol* 17:354–358.
21. Pardridge WM, Eisenberg J, Yang J (1987) Human blood-brain barrier transferrin receptor. *Metabolism* 36:892–895.
22. Rouault TA, Zhang DL, Jeong SY (2009) Brain iron homeostasis, the choroid plexus, and localization of iron transport proteins. *Metab Brain Dis* 24:673–684.
23. Zecca L, Youdim MB, Riederer P, Connor JR, Crichton RR (2004) Iron, brain ageing and neurodegenerative disorders. *Nat Rev Neurosci* 5:863–873.
24. Todorich B, Pasquini JM, Garcia CI, Paez PM, Connor JR (2009) Oligodendrocytes and myelination: The role of iron. *Glia* 57:467–478.
25. Aoki S, et al. (1989) Normal deposition of brain iron in childhood and adolescence: MR imaging at 1.5 T. *Radiology* 172:381–385.
26. Frisoni GB, Fox NC, Jack CR, Jr., Scheltens P, Thompson PM (2010) The clinical use of structural MRI in Alzheimer disease. *Nat Rev Neurol* 6:67–77.
27. Jahanshad N, et al. (2010) Genetic influences on brain asymmetry: A DTI study of 374 twins and siblings. *Neuroimage* 52:455–469.
28. Chiang MC, et al. (2011) Genetics of white matter development: A DTI study of 705 twins and their siblings aged 12 to 29. *Neuroimage* 54:2308–2317.

29. Chou YY, et al. (2009) Mapping genetic influences on ventricular structure in twins. *Neuroimage* 44:1312–1323.
30. Thompson PM, et al. (2001) Genetic influences on brain structure. *Nat Neurosci* 4: 1253–1258.
31. Blokland GA, et al. (2008) Quantifying the heritability of task-related brain activation and performance during the N-back working memory task: A twin fMRI study. *Biol Psychol* 79:70–79.
32. Koten JW, Jr., et al. (2009) Genetic contribution to variation in cognitive function: An FMRI study in twins. *Science* 323:1737–1740.
33. Posthuma D, et al. (2002) The association between brain volume and intelligence is of genetic origin. *Nat Neurosci* 5:83–84.
34. Chiang MC, et al. (2009) Genetics of brain fiber architecture and intellectual performance. *J Neurosci* 29:2212–2224.
35. Benyamin B, et al. (2009) Variants in TF and HFE explain approximately 40% of genetic variation in serum-transferrin levels. *Am J Hum Genet* 84:60–65.
36. Connor JR, Menzies SL (1996) Relationship of iron to oligodendrocytes and myelination. *Glia* 17:83–93.
37. Benjamini Y, Hochberg Y (1995) Controlling the false discovery rate - a practical and powerful approach to multiple testing. *J Roy Stat Soc B Met* 57:289–300.
38. Gao X, Starmer J, Martin ER (2008) A multiple testing correction method for genetic association studies using correlated single nucleotide polymorphisms. *Genet Epidemiol* 32:361–369.
39. Gao X, Becker LC, Becker DM, Starmer JD, Province MA (2010) Avoiding the high Bonferroni penalty in genome-wide association studies. *Genet Epidemiol* 34:100–105.
40. Feder JN, et al. (1998) The hemochromatosis gene product complexes with the transferrin receptor and lowers its affinity for ligand binding. *Proc Natl Acad Sci USA* 95:1472–1477.
41. Aguilar-Martinez P, et al. (2001) Variable phenotypic presentation of iron overload in H63D homozygotes: are genetic modifiers the cause? *Gut* 48:836–842.
42. Beard JL, Connor JR, Jones BC (1993) Iron in the brain. *Nutr Rev* 51:157–170.
43. Gogtay N, et al. (2004) Dynamic mapping of human cortical development during childhood through early adulthood. *Proc Natl Acad Sci USA* 101:8174–8179.
44. Virtanen MA, et al. (1999) Higher concentrations of serum transferrin receptor in children than in adults. *Am J Clin Nutr* 69:256–260.
45. Gerber MR, Connor JR (1989) Do oligodendrocytes mediate iron regulation in the human brain? *Ann Neurol* 26:95–98.
46. Connor JR, Pavlick G, Karli D, Menzies SL, Palmer C (1995) A histochemical study of iron-positive cells in the developing rat brain. *J Comp Neurol* 355:111–123.
47. Packard MG, Knowlton BJ (2002) Learning and memory functions of the basal ganglia. *Annu Rev Neurosci* 25:563–593.
48. Moos T, Rosengren Nielsen T, Skjørringe T, Morgan EH (2007) Iron trafficking inside the brain. *J Neurochem* 103:1730–1740.
49. Thompson PM, et al. (2005) Abnormal cortical complexity and thickness profiles mapped in Williams syndrome. *J Neurosci* 25:4146–4158.
50. Lee AD, et al. (2007) 3D pattern of brain abnormalities in Fragile X syndrome visualized using tensor-based morphometry. *Neuroimage* 34:924–938.
51. Lehmann DJ, et al. (2012) Transferrin and HFE genes interact in Alzheimer's disease risk: The Epistasis Project. *Neurobiol Aging* 33:202.e1–202.e13.
52. Giambattistelli F, et al. (2011) Effects of hemochromatosis and transferrin gene mutations on iron dyshomeostasis, liver dysfunction and on the risk of Alzheimer's disease. *Neurobiol Aging,* 10.1016/j.neurobiolaging.2011.03.005.
53. Lin M, et al. (2011) Association between HFE polymorphisms and susceptibility to Alzheimer's disease: A meta-analysis of 22 studies including 4,365 cases and 8,652 controls. *Mol Biol Rep,* 10.1007/s11033-011-1072-z.
54. Davey Smith G, Ebrahim S (2003) 'Mendelian randomization': Can genetic epidemiology contribute to understanding environmental determinants of disease? *Int J Epidemiol* 32:1–22.
55. de Zubicaray GI, et al. (2008) Meeting the challenges of neuroimaging genetics. *Brain Imaging Behav* 2:258–263.
56. Annett M (1970) A classification of hand preference by association analysis. *Br J Psychol* 61:303–321.
57. Jones DK, Horsfield MA, Simmons A (1999) Optimal strategies for measuring diffusion in anisotropic systems by magnetic resonance imaging. *Magn Reson Med* 42:515–525.
58. Smith SM (2002) Fast robust automated brain extraction. *Hum Brain Mapp* 17: 143–155.
59. Holmes CJ, et al. (1998) Enhancement of MR images using registration for signal averaging. *J Comput Assist Tomogr* 22:324–333.
60. Leow A, et al. (2005) Inverse consistent mapping in 3D deformable image registration: its construction and statistical properties. *Inf Process Med Imaging* 19:493–503.
61. Basser PJ, Pierpaoli C (1996) Microstructural and physiological features of tissues elucidated by quantitative-diffusion-tensor MRI. *J Magn Reson B* 111:209–219.
62. Lepore N, et al. (2008) Fast 3D fluid registration of brain magnetic resonance images. *Medical Imaging 2008: Physiology, Function, and Structure from Medical Images* (SPIE, San Diego), Vol 6916, pp 69160Z–69160Z.
63. Kochunov P, et al. (2001) Regional spatial normalization: Toward an optimal target. *J Comput Assist Tomogr* 25:805–816.
64. Kochunov P, et al. (2002) An optimized individual target brain in the Talairach coordinate system. *Neuroimage* 17:922–927.
65. Pinheiro JC, Bates DM (2000) *Mixed-Effects Models in S and S-PLUS* (Springer, New York).
66. Neale MC, Cardon LR; North Atlantic Treaty Organization. Scientific Affairs Division (1992) *Methodology for Genetic Studies of Twins and Families* (Kluwer, Dordrecht, The Netherlands).
67. Rijsdijk FV, Sham PC (2002) Analytic approaches to twin data using structural equation models. *Brief Bioinform* 3:119–133.
68. Lange K, Boehnke M (1983) Extensions to pedigree analysis. IV. Covariance components models for multivariate traits. *Am J Med Genet* 14:513–524.
69. Kang HM, et al. (2010) Variance component model to account for sample structure in genome-wide association studies. *Nat Genet* 42:348–354.
70. Langers DR, Jansen JF, Backes WH (2007) Enhanced signal detection in neuroimaging by means of regional control of the global false discovery rate. *Neuroimage* 38:43–56.
71. Genovese CR, Lazar NA, Nichols T (2002) Thresholding of statistical maps in functional neuroimaging using the false discovery rate. *Neuroimage* 15:870–878.
72. Kang HM, et al. (2008) Efficient control of population structure in model organism association mapping. *Genetics* 178:1709–1723.

4.2 Is iron important in youth to prevent neurodegeneration?

The following section is adapted from:

Thompson PM, **Jahanshad N** (2012). Ironing out neurodegeneration: Is iron intake important during the teenage years? Invited Editorial, Expert Review of Neurotherapeutic. In Press June 2012

Editorial

Ironing out neurodegeneration: is iron intake important during the teenage years?

Expert Rev. Neurother. 12(6), 00–00 (2012)

Paul M Thompson

Author for correspondence:
Laboratory of Neuro Imaging, Department of Neurology, UCLA School of Medicine, Los Angeles, CA 90095, USA and
Department of Psychiatry & Biobehavioral Sciences, Semel Institute for Neuroscience and Human Behavior, UCLA School of Medicine, Los Angeles, CA 90095, USA
Tel.: +1 310 206 2101
Fax: +1 310 206 5518
thompson@loni.ucla.edu

Neda Jahanshad

Laboratory of Neuro Imaging, Department of Neurology, UCLA School of Medicine, Los Angeles, CA 90095, USA and
Medical Imaging Informatics Group, Department of Radiological Sciences, UCLA School of Medicine, Los Angeles, CA 90095, USA

"Iron may be considered a 'double-edged sword': critical for brain development in early life, but a promoter of brain degeneration in old age."

When did you last take an iron supplement? As a dietary supplement, iron has enjoyed varying popularity over the years; for decades, commercials for multivitamins enriched in iron have promised a remedy for 'tired blood'. More recently, however, several studies began to link increasing iron levels as we age with a heightened risk of heart attack and cardiovascular disease [1]; these links remain controversial and are the target of intense research.

A recent study now reports that our iron levels when we are young affect the integrity of the brain years later – differences visible in brain scans [2]. This line of work also establishes new genetic links between iron, brain integrity and a gene that causes the commonest hereditary disease in the world – hemochromatosis. This iron overload disease affects one in every 200–300 people in the USA alone, according to the National Library of Medicine in 2010.

Iron & the brain

Iron is an essential mineral in our daily life; it is a crucial component of hemoglobin, which carries oxygen in our blood from the lungs to the rest of the body. Even in North America and Europe, iron deficiency is still prevalent; it is the commonest nutritional deficiency worldwide and the leading cause of anemia. Abnormally low red blood cell counts can lead to countless complications throughout various organ systems of the body. Iron may be considered a 'double-edged sword': critical for brain development in early life, but a promoter of brain degeneration in old age.

Iron in neurodevelopment & degeneration

Iron enters the brain primarily when a specialized protein – called transferrin – transports it through the blood–brain barrier [3]. Most of the brain's iron is found in oligodendrocytes, which maintain iron homeostasis in the brain. These cells also support myelination, which speeds neuronal transmission [4]. Even after adjusting for brain weight, iron concentrations are lowest at birth and increase throughout life [5], with complex and lasting effects on neurotransmitter systems, cognition and behavior.

"...adequate iron in the diet has been repeatedly linked to better cognition and scholastic achievement. Educational level is one of the most well-documented protective factors against Alzheimer's disease."

Children with iron-deficient diets show poorer cognitive achievement [6]. In school-age children, vitamin and mineral supplements can increase cognitive performance, including nonverbal intelligence [7]. In rural areas where iron deficiency anemia is prevalent, iron supplements have also been shown to boost motor and language capabilities in children [8].

EXPERT REVIEWS

Keywords: Alzheimer's disease • dietary iron • *HFE* gene • myelination • neuroimaging

 10.1586/ERN.12.56 ISSN 1473-7175

As we age, brain iron homeostasis and regulation can be disrupted, making us more vulnerable to a range of neurodegenerative diseases. Neuroimaging methods show abnormally high brain iron concentrations in patients with several neurodegenerative disorders including Alzheimer's disease (AD). High iron concentrations may even cause neuronal death [9]. Brain regions with greatest iron stores include the basal ganglia, hippocampus and substantia nigra, and these show significant atrophy in patients with AD and Parkinson disease, compared with cognitively normal controls. But, why do the higher iron levels that help us in childhood, also promote brain degeneration later in life? A new study suggests these links might be traceable to common variants in our DNA, which affect how iron is used in the body and brain.

Does iron intake affect cognitive reserve?

No study to date has tracked iron intake from childhood into old age (to examine neurodegenerative complications), but adequate iron in the diet has been repeatedly linked to better cognition and scholastic achievement. Educational level is one of the most well-documented protective factors against AD [10]. Iron is critical for myelination, and some argue that myelin itself may increase the brain's resilience to neuropathology later in life, by boosting our 'cognitive reserve' [11].

Iron building a better brain

In our recent study [2], adolescents with lower iron levels had poorer fiber integrity in the brain's white matter. These differences were evident on specialized brain scans that reveal the fine structure of the brain's neural pathways – diffusion tensor images – collected around 9 years after their iron status was assessed. As iron levels fluctuate throughout the day, we measured transferrin levels as a more stable proxy, to assess the long-term availability of iron to the brain. The liver produces more transferrin when iron levels are low, to mobilize what little iron is available. While we were unable to show better cognition in those with higher brain integrity – all our subjects were normal and not iron deficient – the direction of the results was foreshadowed by earlier work in molecular neuroscience. Lower iron levels (higher transferrin) are known to lead to hypomyelination [12]. However, do these results in a cognitively healthy, young population suggest that slight variations in iron levels early on affect the brain's organization? In support of this, we found several regions prone to atrophy in neurodegenerative disorders such as the hippocampi and the midbrain were smaller in those with greater iron stores, but the caudate and basal ganglia regions were larger. The direction of these volumetric associations was mixed and unexpected, suggesting that iron may interact with the trajectory of brain development in complex ways.

Tracing the iron effect to DNA

The people taking part in our study were all twins and most of them had genome-wide scans to assess around half a million variants in their DNA. As we were able to predict one twin's brain integrity from the other twin's iron levels, we knew that some common variation in their shared DNA was affecting both. With genome-wide scans, we set out to trace their brain differences back to a probable cause in the genome – an iron overload gene, called *HFE* (or 'high iron'; 'Fe' in the gene name is based on the chemical symbol for iron). Although dietary intake of iron clearly affects iron levels in the body, iron overload disorder – or hemochromatosis – is the commonest genetic disorder in the world. It arises when the *HFE* gene has a mutation that damages the gene's function and the body's ability to regulate iron.

What is perhaps less known is that approximately one in five of Caucasians carries a variant in the *HFE* gene, the H63D variant (according to the HapMap project). Carriers of this variant have 'genetically high' iron availability; by sorting our subjects into those who had this genetic variant and those who did not, we saw higher brain integrity on brain scans in those with the high-iron variant.

> "Careful attention to dietary iron levels – and how they interact with our genetic predisposition to regulate iron – may help offset iron's role in promoting brain degeneration."

This offers a clue to how this very commonly carried genetic variant affects the brain as well as iron regulation; this variant and a less common mutation in the same gene, *HFE,* have also been associated with neurological disorders, such as sporadic amyotrophic sclerosis [13]. AD patients with the H63D polymorphism have elevated plasma iron and transferrin levels [14], but this pattern is not detectable in healthy controls with the variant, suggesting that *HFE* and plasma iron levels play a role in AD. Currently, it is believed that *HFE* may even have protective implications in AD as reported by a meta-analysis [15].

Iron & gene expression in the brain

So far in our work, we had established a link between brain integrity and a common variant in an iron-regulating gene. Although we are either born with this variant or not, there is some evidence that the expression of other key genes also depends on our iron intake – even, to some extent – on maternal iron intake before we are born.

Neonatal iron deficiency arising from poor maternal diet is known to alter gene expression in the brain. Specifically, in the hippocampus, several AD-related genes (including *Apbb1*, *C1qa*, *Clu*, *App*, *Cst3*, *Fn1* and *Htatip*) show altered expression in iron-deficient rats, relative to iron-sufficient controls. Neonatal iron deficiency may disregulate genes early on, perhaps altering disease risk later [16]. Intriguingly, common genetic variants in Alzheimer's risk genes, including *CLU* [17], have been shown to alter brain integrity in healthy young adults. Remarkably, brain integrity can even be predicted now by genetic profiling of large numbers of people [18].

Clearly, both iron intake, and genetic variants that affect its availability, affect the brain throughout life. Careful attention to dietary iron levels – and how they interact with our genetic predisposition to regulate iron – may help offset iron's role in promoting brain degeneration. Tests of gene-by-environment interactions for

these risk factors, perhaps in larger neuroimaging studies, will shed light on these hypotheses.

Iron-rich foods for thought

Several iron-rich foods, such as spinach, breakfast cereals and fish, may offer sufficient iron for the brain, as well as other nutritional benefits. Folate and omega-3 fatty acids, also present in these foods, have been associated with benefits to the brain and cognitive function, in some but not all studies. Folate, a B vitamin found in high concentrations in spinach and breakfast cereals, can reduce homocysteine levels; those with high homocysteine levels showed reduced brain volumes, in a study of elderly individuals from the Alzheimer's Disease Neuroimaging Initiative (ADNI) [19]. B vitamin supplementation does reduce homocysteine levels in patients with AD, but does not change the rates of cognitive decline [20]. Perhaps this underscores the need for adequate nutrition earlier, before the onset of disease. Additionally, fish consumption is associated with the preservation of brain structure, but healthy dietary factors are hard to isolate in observational studies, as healthy diet tends to be correlated with other health-promoting behaviors. Dietary supplements, in particular, are best taken with medical supervision. Even so, it is plausible that regular consumption of iron-rich foods, starting in childhood, may help to promote a healthy lifestyle and provide nutritional and cognitive benefits beyond those of iron alone.

Financial & competing interests disclosure

The authors have no relevant affiliations or financial involvement with any organization or entity with a financial interest in or financial conflict with the subject matter or materials discussed in the manuscript. This includes employment, consultancies, honoraria, stock ownership or options, expert testimony, grants or patents received or pending, or royalties.

No writing assistance was utilized in the production of this manuscript.

References

1 Sullivan JL. Iron and the genetics of cardiovascular disease. *Circulation* 100(12), 1260–1263 (1999).

2 Jahanshad N, Kohannim O, Hibar DP *et al*. Brain structure in healthy adults is related to serum transferrin and the H63D polymorphism in the *HFE* gene. *Proc. Natl Acad. Sci. USA* 109(14), e851–e859 (2012).

3 Pardridge WM, Eisenberg J, Yang J. Human blood–brain barrier transferrin receptor. *Metab. Clin. Exp.* 36(9), 892–895 (1987).

4 Todorich B, Pasquini JM, Garcia CI, Paez PM, Connor JR. Oligodendrocytes and myelination: the role of iron. *Glia* 57(5), 467–478 (2009).

5 Beard JL, Connor JR, Jones BC. Iron in the brain. *Nutr. Rev.* 51(6), 157–170 (1993).

6 Halterman JS, Kaczorowski JM, Aligne CA, Auinger P, Szilagyi PG. Iron deficiency and cognitive achievement among school-aged children and adolescents in the United States. *Pediatrics* 107(6), 1381–1386 (2001).

7 Benton D, Roberts G. Effect of vitamin and mineral supplementation on intelligence of a sample of schoolchildren. *Lancet* 1(8578), 140–143 (1988).

8 Stoltzfus RJ, Kvalsvig JD, Chwaya HM *et al.* Effects of iron supplementation and anthelmintic treatment on motor and language development of preschool children in Zanzibar: double blind, placebo controlled study. *BMJ* 323(7326), 1389–1393 (2001).

9 Ke Y, Ming Qian Z. Iron misregulation in the brain: a primary cause of neurodegenerative disorders. *Lancet Neurol.* 2(4), 246–253 (2003).

10 Stern Y, Gurland B, Tatemichi TK, Tang MX, Wilder D, Mayeux R. Influence of education and occupation on the incidence of Alzheimer's disease. *JAMA* 271(13), 1004–1010 (1994).

11 Bartzokis G. Age-related myelin breakdown: a developmental model of cognitive decline and Alzheimer's disease. *Neurobiol. Aging* 25(1), 5–18; author reply 49 (2004).

12 Connor JR, Menzies SL. Relationship of iron to oligodendrocytes and myelination. *Glia* 17(2), 83–93 (1996).

13 He X, Lu X, Hu J *et al.* H63D polymorphism in the hemochromatosis gene is associated with sporadic amyotrophic lateral sclerosis in China. *Eur. J. Neurol.* 18(2), 359–361 (2011).

14 Giambattistelli F, Bucossi S, Salustri C *et al*. Effects of hemochromatosis and transferrin gene mutations on iron dyshomeostasis, liver dysfunction and on the risk of Alzheimer's disease. *Neurobiol. Aging* doi:10.1016/j.neurobiolaging.2011.03.005 (2011) (Epub ahead of print).

15 Lin M, Zhao L, Fan J *et al*. Association between *HFE* polymorphisms and susceptibility to Alzheimer's disease: a meta-analysis of 22 studies including 4,365 cases and 8,652 controls. *Mol. Biol. Rep*. 39(3):3089–3095 (2012).

16 Carlson ES, Magid R, Petryk A, Georgieff MK. Iron deficiency alters expression of genes implicated in Alzheimer disease pathogenesis. *Brain Res.* 1237, 75–83 (2008).

17 Braskie MN, Jahanshad N, Stein JL *et al.* Common Alzheimer's disease risk variant within the *CLU* gene affects white matter microstructure in young adults. *J. Neurosci.* 31(18), 6764–6770 (2011).

18 Kohannim O, Jahanshad N, Braskie MN *et al*. Predicting white matter integrity from multiple common genetic variants. *Neuropsychopharmacology* doi:10.1038/npp.2012.49 (2012) (In Press).

19 Rajagopalan P, Hua X, Toga AW, Jack CR Jr, Weiner MW, Thompson PM. Homocysteine effects on brain volumes mapped in 732 elderly individuals. *Neuroreport* 22(8), 391–395 (2011).

20 Aisen PS, Schneider LS, Sano M *et al.*; Alzheimer Disease Cooperative Study. High-dose B vitamin supplementation and cognitive decline in Alzheimer disease: a randomized controlled trial. *JAMA* 300(15), 1774–1783 (2008).

CHAPTER 5

DTI mapping of genes and environment

5.1 Alzheimer's risk gene mapped to white matter

The following section is adapted from:

Braskie MN,* **Jahanshad N***, Stein JL,* Barysheva M, McMahon KL, de Zubicaray GI, Martin NG, Wright MJ, Ringman JM, Toga AW, Thompson PM (2011). Common Alzheimer's disease risk variant within the CLU gene affects white matter microstructure in young adults, Journal of Neuroscience, 2011; 31 (18): 6764-70.

* denotes equal contribution

The Journal of Neuroscience, May 4, 2011 • 31(18):6764–6770

Neurobiology of Disease

Common Alzheimer's Disease Risk Variant within the *CLU* Gene Affects White Matter Microstructure in Young Adults

Meredith N. Braskie,[1]* Neda Jahanshad,[1,2]* Jason L. Stein,[1]* Marina Barysheva,[1] Katie L. McMahon,[4] Greig I. de Zubicaray,[5] Nicholas G. Martin,[6] Margaret J. Wright,[6] John M. Ringman,[3] Arthur W. Toga,[1] and Paul M. Thompson[1]

[1]Laboratory of Neuro Imaging, Department of Neurology, [2]Medical Imaging Informatics, Department of Radiology, and [3]Mary S. Easton Center for Alzheimer's Disease Research, Department of Neurology, University of California, Los Angeles, School of Medicine, Los Angeles, California 90095, [4]Centre of Advanced Imaging and [5]School of Psychology, University of Queensland, Brisbane, Queensland 4072, Australia, and [6]Queensland Institute of Medical Research, Brisbane, Queensland 4029, Australia

There is a strong genetic risk for late-onset Alzheimer's disease (AD), but so far few gene variants have been identified that reliably contribute to that risk. A newly confirmed genetic risk allele C of the clusterin (*CLU*) gene variant rs11136000 is carried by ~88% of Caucasians. The C allele confers a 1.16 greater odds of developing late-onset AD than the T allele. AD patients have reductions in regional white matter integrity. We evaluated whether the *CLU* risk variant was similarly associated with lower white matter integrity in healthy young humans. Evidence of early brain differences would offer a target for intervention decades before symptom onset. We scanned 398 healthy young adults (mean age, 23.6 ± 2.2 years) with diffusion tensor imaging, a variation of magnetic resonance imaging sensitive to white matter integrity in the living brain. We assessed genetic associations using mixed-model regression at each point in the brain to map the profile of these associations with white matter integrity. Each C allele copy of the *CLU* variant was associated with lower fractional anisotropy—a widely accepted measure of white matter integrity—in multiple brain regions, including several known to degenerate in AD. These regions included the splenium of the corpus callosum, the fornix, cingulum, and superior and inferior longitudinal fasciculi in both brain hemispheres. Young healthy carriers of the *CLU* gene risk variant showed a distinct profile of lower white matter integrity that may increase vulnerability to developing AD later in life.

Introduction

Two recent genome-wide association studies identified and replicated an association between risk for Alzheimer's disease (AD) and carrying the C allele of the single nucleotide polymorphism (SNP) rs11136000 in the clusterin (also known as apolipoprotein J) gene (*CLU*-C) (Harold et al., 2009; Lambert et al., 2009). *CLU*-C confers a 1.16 greater odds of developing late-onset AD than the T allele (Bertram et al., 2007). Approximately 36% of Caucasians carry two copies of the risk-conferring allele (Bertram et al., 2007), making this gene of great interest for public health.

Received Nov. 4, 2010; revised Jan. 25, 2011; accepted March 2, 2011.

Author contributions: K.L.M., G.I.d.Z., N.G.M., and M.J.W. collected the data; M.N.B., N.J., J.L.S., M.B., and P.M.T. analyzed the data; and M.N.B., N.J., J.L.S., and P.M.T. wrote the initial manuscript draft. All authors were involved in study design, discussed the results, and revised the manuscript.

This study was supported by the National Institute of Child Health and Human Development (Grant R01 HD050735) and the National Health and Medical Research Council (NHMRC) (Grant 486682), Australia. Genotyping was supported by NHMRC (Grant 389875). Additional support for algorithm development was provided by National Institutes of Health (NIH) R01 Grants EB008432, EB008281, and EB007813. M.N.B. was funded by the NIH (Grant T32 NS048004:05) and University of California, Los Angeles Easton Center for Alzheimer's Disease Research donor funds. N.J. was funded by the NIH/National Library of Medicine (Grant T15 LM07356). J.L.S. was also funded by the ARCS foundation and the National Institute of Mental Health (Grant 1F31MH087061).

*M.N.B., N.J., and J.L.S. contributed equally to the work.

Correspondence should be addressed to Dr. Paul M. Thompson, Laboratory of Neuro Imaging, Department of Neurology, UCLA School of Medicine, 635 Charles Young Drive South, Suite 225, Los Angeles, CA 90095-7334. E-mail: thompson@loni.ucla.edu.

DOI:10.1523/JNEUROSCI.5794-10.2011

 0270-6474/11/316764-07$15.00/0

AD traditionally has been considered a disease marked by neuronal cell loss and widespread gray matter atrophy, but degeneration of myelin in white matter fiber pathways is increasingly considered a key disease component (Braak and Braak, 1996; Hua et al., 2008; Bartzokis, 2009). To evaluate how *CLU*-C affects fiber integrity, we scanned 398 healthy young adults (mean age, 23.6 ± 2.2 years) with diffusion tensor imaging (DTI). DTI is a variant of standard brain magnetic resonance imaging (MRI) that is sensitive to fiber integrity and white matter microstructure. The most widely accepted DTI measure, fractional anisotropy (FA), evaluates the extent to which water diffusion is directionally constrained. Higher FA generally reflects preferential diffusion along more intact, heavily myelinated axons. Demyelination, neurological disease symptoms, and slowed nerve conduction have been associated with lower FA in white matter (Nucifora et al., 2007), suggesting that it may reflect reduced white matter integrity.

White matter pathways deteriorate in AD due to primary effects of impaired myelination and secondary effects of neuronal loss (Brun and Englund, 1986). In several studies of AD and mild cognitive impairment, cognitive impairment has been associated with reduced FA in the corpus callosum, fornix, cingulum, superior longitudinal fasciculus (SLF), and inferior longitudinal fasciculus (ILF) (Liu et al., 2009; Stricker et al., 2009). Additionally, the apolipoprotein E allele ε4 (*APOE4*)—a widely confirmed genetic risk factor for late-onset AD—is associated with lower FA in

the parahippocampal white matter, splenium, and fronto-occipital fasciculus of healthy older subjects (Nierenberg et al., 2005; Persson et al., 2006; Smith et al., 2010).

CLU is a plausible candidate for modulating white matter integrity, as both *CLU* and *APOE* encode apolipoproteins implicated in AD risk. Additionally, clusterin (the gene product) is implicated in lipid transport and membrane recycling (Dati et al., 2007), and in remyelination of nerve fibers in rats (Dati et al., 2007). We hypothesized that young *CLU*-C carriers would show reduced white matter integrity, quantifiable as lower FA in brain regions implicated in AD. Such differences could help to explain why the gene is associated with heightened risk for AD.

It is vital to discover how AD risk variants impact the living brain to better understand disease development and to design interventions for those at risk. Targeting subpopulations most likely to show decline also boosts power for prevention and treatment trials (Kohannim et al., 2010).

Materials and Methods

Subjects and genotype information. DTI scans and genotypes were obtained for 468 right-handed Caucasians recruited as part of a project examining brain structure and white matter integrity in healthy, young adult Australian twins. We excluded 70 subjects for the following reasons: 8 were ancestry outliers; 58 were technically inadequate scans; 3 had ventricle size inconsistent with good health in a young person; and 1 lacked a genotype at rs11136000. Of the remaining 398 subjects (mean age, 23.6 ± 2.2 years; age range, 20–29 years), 92 were monozygotic (MZ) twins, 147 were dizygotic (DZ) twins or triplets, 41 were singleton siblings, and 118 were unrelated individuals. Genomic DNA samples were analyzed on the Human610-Quad BeadChip (Illumina) according to the manufacturer's protocols (Infinium HD Assay; *Super Protocol Guide*, revision A, May 2008). The *CLU* rs11136000 polymorphism was T/T in 68 subjects (17.1%), C/T in 220 subjects (55.3%), and C/C in 110 subjects (27.6%). The frequency for the minor (T) allele (MAF) in unrelated subjects in our sample was 0.40, similar to previous reports in healthy populations of European origin (Harold et al., 2009; Lambert et al., 2009). The genotype distribution in our sample followed Hardy–Weinberg equilibrium using a standard threshold of $p > 0.001$ ($\chi^2_{(1)} = 4.70$, $p = 0.030$). When we calculated the evidence for Hardy–Weinberg equilibrium, the expected proportions of C/C and T/T genotypes compared with observed values differed by small numbers that can be attributed to the effects of random sampling. These differences are unlikely to indicate any ascertainment bias as these subjects were selected only because they are twins or singleton siblings of twins. They were originally recruited for a melanoma study, and the cohort is composed of young adults, meaning that there would not be any disease-related attrition that could adversely impact the allele frequencies for an AD risk allele. We therefore have no good reason to believe that those in the study have a level of AD risk that is different from that of the general Australian population from which our sample was drawn.

Verbal, performance, and full-scale intelligence quotient (IQ) standardized scores were derived from subtest scores of the Multidimensional Aptitude Battery (MAB) (Jackson, 1984), which were available for all but 20 subjects. The MAB is similar to the Wechsler Adult Intelligence Scale (Wechsler, 1981) as it is composed of tests of verbal and performance intelligence. Verbal IQ subtests included assessments of information, arithmetic, and vocabulary. Performance IQ subtests included spatial and object assembly. All subjects provided written, informed consent. The study conformed to the National Statement on Ethical Conduct in Human Research (2007) issued by the National Health and Medical Research Council of Australia and was approved by the Queensland Institute of Medical Research Human Research Ethics Committee.

Image acquisition. T1-weighted images of the brain were acquired with an inversion recovery rapid gradient echo sequence on a 4 Tesla MRI scanner (Medspec, Bruker) [acquisition parameters: inversion time, 700 ms; repetition time (TR), 1500 ms; echo time (TE), 3.35 ms; flip angle = 8°; slice thickness = 0.9 mm; 256 × 256 × 256]. Diffusion-weighted images were acquired using single-shot echo planar imaging (EPI) with a twice-refocused spin echo sequence to reduce eddy-current-induced distortions (TR, 6090 ms; TE, 91.7 ms; field of view, 23 cm; 128 × 128). Each three-dimensional (3D) volume consisted of 55 axial slices (2.0 mm/0 mm gap; 1.79 × 1.79 mm in-plane resolution). We acquired 105 images per subject: 11 with no diffusion sensitization (i.e., T2-weighted b_0 images) and 94 diffusion-weighted (DW) images ($b = 1149$ s/mm^2) with gradient directions evenly distributed on the hemisphere.

DTI preprocessing. We automatically removed nonbrain regions from the T1-weighted MR and DW b_0 images using FSL BET (http://fsl.fmrib.ox.ac.uk/fsl/), then manually refined the brain extraction. All T1-weighted images were linearly aligned to a common space (with a global transform that had 9 degrees of freedom). The raw DW images were corrected for eddy current distortions using the FSL "eddy correct" method (http://fsl.fmrib.ox.ac.uk/fsl/). Individual b_0 images were averaged, linearly aligned, and resampled to their corresponding T1 images. The average b_0 maps were then elastically registered to the individual common space T1-weighted scans using a mutual information cost function (Leow et al., 2005) to control for EPI-induced susceptibility artifacts.

Computing fractional anisotropy. We compared FA values at each voxel across *CLU* genotypes. Diffusion tensors were computed at each voxel using FSL software (http://fsl.fmrib.ox.ac.uk/fsl/). From the tensor eigenvalues (λ_1, λ_2, λ_3), FA was calculated according to the following formula:

$$FA = \sqrt{\frac{3}{2}} \frac{\sqrt{(\lambda_1 - \bar{\lambda})^2 + (\lambda_2 - \bar{\lambda})^2 + (\lambda_3 - \bar{\lambda})^2}}{\sqrt{\lambda_1^2 + \lambda_2^2 + \lambda_3^2}} \in [0,1]$$

$$\bar{\lambda} = \frac{\lambda_1 + \lambda_2 + \lambda_3}{3}.$$

We also analyzed radial diffusivity (D_{rad}) (the average of λ_2 and λ_3) and axial diffusivity (D_{ax}) (λ_1) to clarify the extent to which each might be contributing to the changes in FA.

Template creation and registration. We used nonlinear fluid registration (Lepore et al., 2008) to create a mean deformation target (MDT) from the FA images (calculated after b_0 susceptibility correction) (Jahanshad et al., 2010). Included in the MDT were 32 randomly selected unrelated subjects (16 female/16 male). The N 3D vector fields that fluidly registered a specific individual to all other N subjects were averaged and applied to that subject, preserving the image intensities and anatomical features of the template subject.

Susceptibility-corrected FA maps were registered to the final population-averaged FA-based MDT using a 3D elastic warping technique with a mutual information cost function (Leow et al., 2005). To better align white matter regions of interest, the MDT and all whole-brain registered FA maps were thresholded at 0.25 (excluding contributions from non-white matter). Thresholded FA maps were then re-registered to the thresholded MDT and smoothed with a Gaussian kernel (9 mm full width at half-maximum). In this way, the outlines of the major white matter structures are stable and have been normalized to a very fine degree of matching across subjects, greatly reducing the neuroanatomical variations in these structures across subjects. To ensure that our results were not due to morphometric differences that were not fully corrected by the fluid registration, we additionally performed tissue-specific, smoothing-compensated voxel-based analysis (T-SPOON) (Lee et al., 2009), which reduces that confound.

Statistical analyses. We performed mixed-model regression at each voxel to model family relatedness (Kang et al., 2008). A symmetric $N \times N$ kinship matrix was constructed to describe the relationship of every subject to all others. A kinship matrix coefficient of 1 denoted the relationship of the subjects to themselves or their MZ twin: 0.5 indicated DZ twins and siblings within the same family, and 0 denoted unrelated subjects. Ancestry outliers were removed, so no additional modeling was used in the kinship matrix to adjust for population genetic structure between families. We then used a linear mixed-effects model to estimate the association of each copy of *CLU*-C in the SNP rs11136000 to FA, D_{ax},

J. Neurosci., May 4, 2011 • 31(18):6764 – 6770

and D_{rad} measures at each voxel, controlling for familial relatedness through the kinship matrix, age, and sex.

Our analysis used an additive model that assessed the effect of each risk allele rather than evaluating the effects of *CLU*-C carriers or noncarriers (i.e., we counted the number of adverse alleles and used that number in a regression across the full sample). The *CLU* association with AD initially was discovered using a test for differences in allele frequencies between diagnostic groups. Here we use a quantitative phenotype, so that test cannot be used. However, the additive model we used (vs a recessive or dominant model) is the most powerful for finding genetic effects in a quantitative phenotype. To further investigate the nature of this relationship, we used *post hoc* exploratory tests to evaluate how *CLU* genotype related to FA using models other than the additive model to compare genotype groups, while controlling for age and sex. Specifically, we evaluated C/C versus T, T/T versus C, C/T versus T/T, and C/T versus C/C carrier. This must be considered exploratory testing because we chose the additive model as our primary hypothesis since it is the most powerful model to use if the effects are additive.

To ensure that only white matter was being considered and to reduce the effects of partial voluming, only voxels in which FA > 0.3 in the MDT were considered in the statistical analyses. The *p* value reported is based on the fixed-effect regression coefficient (β parameter) of the additive genetic effect (see Fig. 1). This analysis was performed using Efficient Mixed-Model Association (Kang et al., 2008) (EMMA; http://mouse.cs.ucla.edu/emma/) within the R statistical package (version 2.9.2; http://www.r-project.org/). We used the widely used false discovery rate (FDR) method to control for voxelwise multiple comparisons (Benjamini and Hochberg, 1995). Single-factor ANOVAs were used to evaluate whether genotype groups were different in age, sex, or IQ. We also controlled for age and sex in the full sample, and age, sex, and full IQ in a subsample of 378 subjects for whom IQ values were available.

Results

As shown in Table 1, genotype groups (T/T, C/T, and C/C) were not significantly different in age ($F_{(2, 395)} = 1.30$, $p = 0.27$), verbal IQ ($F_{(2, 375)} = 0.31$, $p = 0.73$), performance IQ ($F_{(2, 375)} = 0.82$, $p = 0.44$), or full-scale IQ ($F_{(2, 375)} = 0.65$, $p = 0.53$), as tested using ANOVAs. Sex was not significantly different between genotype groups, as determined using a χ^2 test ($\chi^2_{(2)} = 0.84$, $p = 0.66$).

White matter integrity was quantified using the widely accepted index FA. In statistical maps based on 398 young adults, each *CLU*-C allele (adjusted for age and sex) was associated with lower FA in frontal, temporal, parietal, occipital, and subcortical white matter (multiple comparisons corrected: critical $p = 0.023$, for an FDR controlled at 5%; minimum $p = 5.9 \times 10^{-7}$; 46.1% of evaluated voxels survived the FDR threshold). Brain regions with lower FA included corticocortical pathways previously demonstrated to have lower FA in AD patients and

Table 1. Subject characteristics by *CLU* rs11136000 genotype in the studied population

	Genotypes		
	T/T	C/T	C/C
Subjects	68	220	110
Sex	24 M, 44 F	77 M, 143 F	44 M, 66 F
Age	23.6 ± 2.3	23.5 ± 2.2	23.9 ± 2.3
No. of IQ test scores	64	208	106
PIQ	112.4 ± 17.0	115.2 ± 15.8	114.0 ± 14.4
VIQ	111.3 ± 10.8	112.2 ± 11.3	112.7 ± 10.0
FIQ	112.8 ± 12.9	114.8 ± 13.1	114.5 ± 11.1

Values are given as the mean ± SD. Sex, age, and IQ scores are not significantly different between genotype groups ($p > 0.05$) using ANOVAs to evaluate group differences in age and IQ, and a χ^2 test to evaluate differences in sex. M, Male; F, female; PIQ, performance IQ; VIQ, verbal IQ; FIQ, full-scale IQ.

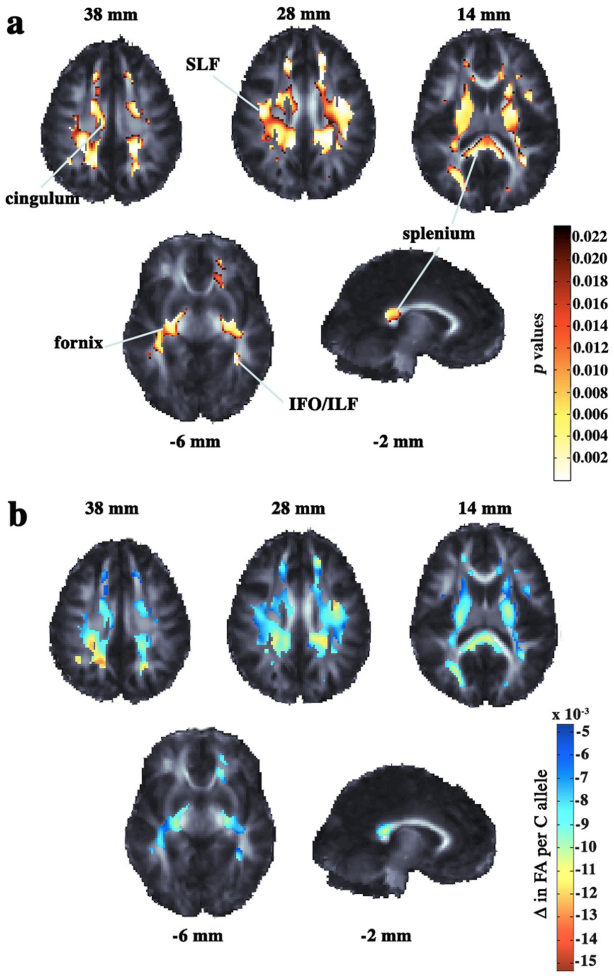

Figure 1. FA association with *CLU*-C displayed on a study-specific FA template. ***a***, Highlighted areas are the *p* values indicating voxels in which *CLU*-C is associated with lower FA after adjusting for age and sex (FDR critical *p* value = 0.023). In ***b***, we show regression coefficients at significant voxels that encompass many regions that degenerate in AD. The left brain hemisphere is displayed on the right. Coordinates listed are for the *Z* (for axial slices) and *X* (for the sagittal slice) directions in ICBM space. SLF and ILF denote the superior and inferior longitudinal fasciculi. IFO is the inferior fronto-occipital fasciculus.

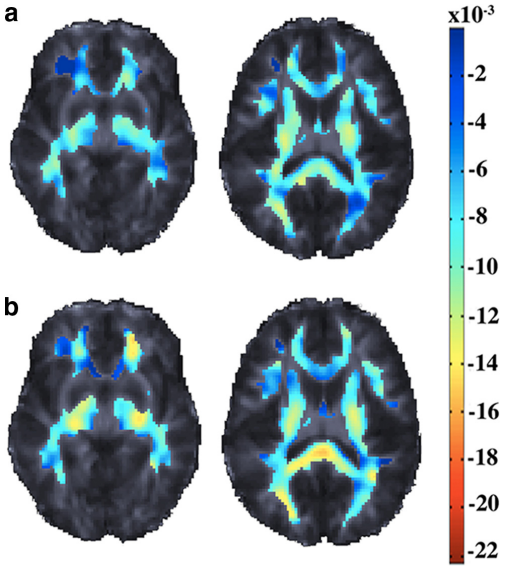

Figure 2. Statistical models. Highlighting represents un-normalized regression coefficients or beta values in all white matter voxels tested. It demonstrates the *CLU*-C association with lower FA (after adjusting for age and sex). ***a***, ***b***, Shown here as *post hoc* explorations are the C/C versus T carrier model (***a***) and the T/T versus C carrier model (***b***). Units are in FA unit difference between groups for these models, while they are in FA units per allele for the additive model (Fig. 1). The per-voxel effect is similar in location using all models, but only the initially hypothesized and most powerful additive model passes FDR correction, as shown in Figure 1 (FDR critical p value = 0.023). The effect appears to depend on the allele dose rather than the presence or absence of a given allele. The left brain hemisphere is displayed on the right.

*APOE*4 carriers. Strongest effects (≥0.01 units FA reduction per risk allele) were found in the splenium, bilateral posterior and anterior corona radiata, bilateral perithalamic tracts, and posterior thalamic radiation, and complex association fibers [left SLF, and ILF/inferior fronto-occipital fasciculus (IFO)]. We also found significant associations bilaterally in peristriatal and periventricular white matter, other callosal fibers (corpus callosum body and genu, and forceps major and minor), limbic tracts (fornix, stria terminalis, and posterior cingulum, including in the parahippocampal white matter), complex association fibers (SLF, ILF/IFO), and tracts of the cerebral peduncles (Fig. 1). Our results remained significant when adjusted for age, sex, and full-scale IQ in the 378 subjects for whom IQ values were available (multiple comparisons corrected: critical $p = 0.028$, for an FDR controlled at 5%; minimum $p = 1.9 \times 10^{-7}$; 56.3% of evaluated voxels survived the FDR threshold).

FA was significantly correlated with *CLU* genotype after FDR correction using the additive model. The additive model outperformed all the other models for comparing genotype categories, and therefore best explains the underlying effect in our sample. Using an uncorrected $p < 0.05$ threshold for illustrative purposes only, we report the following when all subjects were considered: those with a T/T genotype showed regionally greater FA than C carriers in 36% of voxels considered at this liberal statistical threshold (minimum $p = 8.9 \times 10^{-6}$). Those with a C/C genotype showed lower FA than T carriers in 40% of voxels considered at this liberal statistical threshold (minimum $p = 7.0 \times 10^{-5}$) (Fig. 2). When 220 subjects with a C/T genotype were compared with either 110 subjects with a C/C genotype or 68 with a T/T genotype, 14% (minimum $p = 3.6 \times 10^{-4}$) and 10% (minimum $p = 3.6 \times 10^{-5}$) of considered voxels, respectively, were significant at an uncorrected $p < 0.05$ level. Overall, this evidence favors an additive (allele dose-dependent) effect on the white matter.

FA is influenced by both D_{ax} (a measure of diffusion along the axonal fibers) and D_{rad} (a measure of diffusion perpendicular to the axonal fibers). Reduced white matter integrity (as measured by FA) can sometimes be further traced back to greater D_{rad} or lower D_{ax}. To further investigate the reduced FA in *CLU*-C carriers, we examined the correlation of *CLU* genotype with D_{rad} and D_{ax} on a voxelwise basis, while adjusting for age and sex. Each *CLU*-C allele was associated with increased D_{rad} (multiple comparisons corrected: critical $p = 0.022$, for an FDR controlled at 5%; minimum $p = 0.0001$; 44.3% of evaluated voxels survived the FDR threshold) after adjusting for age and sex (Fig. 3). D_{ax} was not significantly associated with *CLU* genotype.

DTI studies have reported lower FA in healthy older *APOE*4+ subjects in the parahippocampal white matter, splenium, and fronto-occipital fasciculus (Nierenberg et al., 2005; Persson et al., 2006; Smith et al., 2010). To determine whether our results were influenced by *APOE* genotypes, we evaluated the effects on DTI FA of a proxy or tag SNP for the *APOE*4 polymorphism rs2075650 within the *TOMM40* gene, because the *APOE*4 polymorphism was not directly genotyped on the chip. The *TOMM40* variant is in moderate linkage disequilibrium with *APOE*4 ($r^2 = 0.48$) (Harold et al., 2009). Our *CLU* results remained significant after adjusting for age, sex, and *TOMM40* genotype (corrected for multiple comparisons; critical $p = 0.026$, for an FDR controlled at 5%; minimum $p = 6.1 \times 10^{-7}$; 51.1% of evaluated voxels survived the FDR threshold). These results confirm that the *CLU*-C effect on FA was not attributable to *TOMM40* genotypes, and hence *APOE*4-associated changes.

Finally, to reduce the likelihood that coregistration errors contributed to our results, we performed an analysis known as T-SPOON (Lee et al., 2009) on our data using individual FA masks thresholded at FA >0.25. We then reran the primary statistical analysis, adjusting for age and sex, and using the same thresholding and spatial smoothing as in the primary analyses. The T-SPOON analysis adjusts for effects at the interfaces of white matter and other tissues. Our results remained significant (corrected for multiple comparisons; critical $p = 0.019$, for an FDR controlled at 5%; minimum $p = 1.2 \times 10^{-5}$; 37.8% of evaluated voxels survived the FDR threshold) in all the same brain regions as our primary analysis. This is in line with expectation, as most of the differences were found far away from any gray matter and reflect differences in the characteristics of white matter in many regions without partial volume of multiple tissue types.

Discussion

We found widespread lower FA in the white matter of healthy young adults who carry a recently identified risk gene for late-onset Alzheimer's disease. Effects occurred in multiple regions, including several known to degenerate in AD. Such regions included the corpus callosum, fornix, cingulum, SLF, and ILF (Liu et al., 2009; Stricker et al., 2009). This suggests that the *CLU*-C related variability found here might create a local vulnerability important for disease onset. These effects are remarkable as they already exist early in life and are associated with a risk gene that is very prevalent (~36% of Caucasians carry two copies of the risk-conferring genetic variant *CLU*-C).

Higher FA does not always imply better neuronal function, and there are neurogenetic syndromes where higher FA in some

brain regions is associated with abnormal function (Hoeft et al., 2007). Accepting these as counterexamples, lower FA is generally a sign of poorer fiber coherence, myelination, and poorer function, as noted in a recent review of DTI studies across many domains of neuropsychiatry (Thomason and Thompson, 2011).

Lower FA may indicate reduced myelin integrity or axonal damage. We found a significant increase in D_{rad} widely throughout the white matter without associated significant decreases in D_{ax}. These results suggest that reduced myelin integrity, rather than axonal degeneration, may be responsible for the lower FA we found in many of these regions (Di Paola et al., 2010). Increased regional D_{rad} has previously been demonstrated in AD patients versus controls (Choi et al., 2005; Stricker et al., 2009; Zhang et al., 2009; Di Paola et al., 2010; Salat et al., 2010) and in healthy *APOE*4+ subjects versus those who do not carry the *APOE*4 allele (Nierenberg et al., 2005). In AD patients, increased D_{rad} has been attributed to degeneration of the myelin sheath (Di Paola et al., 2010), but our demonstration of increased D_{rad} in healthy young *CLU*-C carriers raises the question of whether the increased D_{rad} seen in AD patients in past studies may also stem in part from inadequate myelination that occurs developmentally as a result of genes that increase AD risk. This is not to say that reduced myelin integrity does not play a role in AD, but rather that both developmental differences and age- or disease-related degeneration may contribute to that reduced integrity.

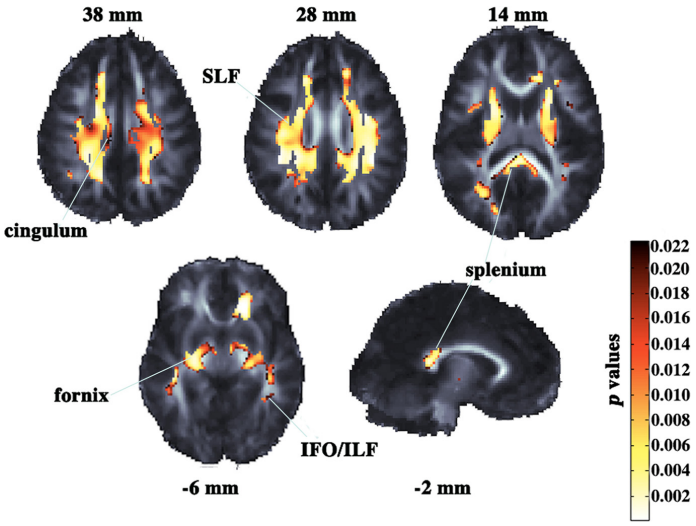

Figure 3. Radial diffusivity. D_{rad} but not D_{ax} showed a significant *CLU* genotype effect after adjusting for age and sex. In highlighted voxels, D_{rad} is significantly greater with each *CLU* allele C (multiple comparisons corrected: critical $p < 0.022$ for an FDR of 5%). The left brain hemisphere is shown on the right.

Genetic risk for reduced FA may increase the risk for later cognitive impairment through developmental insufficiency. A lesser degree of myelination in *CLU*-C carriers may arise during development, which may not translate into poorer cognition in youth as the brain can compensate via redundant functionality. However, when exacerbated by other factors, such as age-related neuronal atrophy, and plaque and tangle burden in AD, reduced myelin integrity could facilitate cognitive impairment. As our study examined how a common AD risk gene affects young adults who have no observable cognitive deficits, it is unlikely that we are seeing the earliest possible signs of AD-associated brain changes. More likely, the reduced fiber integrity represents an early developmental vulnerability that may reduce brain resilience to later AD pathology; in other words, its mechanism of action may not be part of the classic AD pathways that lead to abnormal amyloid plaque and neurofibrillary tangle accumulation in the brain.

Lower FA in late-onset Alzheimer's disease may be promoted by suboptimal amyloid processing in the brain. Amyloid plaques and neurofibrillary tangles—the primary pathological hallmarks of AD—accumulate in the brain decades before symptoms appear. Neurofibrillary tangles are detectable in ~20% of subjects aged 26–35 years (Braak and Braak, 1997), and greater amyloid deposition in healthy elderly subjects is correlated with greater neuropsychological decline over the preceding decade (Resnick et al., 2010). Clusterin is found in amyloid plaques (Calero et al., 1999) and transports soluble β-amyloid (Aβ) across the blood–brain barrier into brain parenchyma (Zlokovic et al., 1996). Aβ then may damage the oligodendrocytes, which generate myelin, as reported *in vitro* (Roth et al., 2005). However, in our young healthy sample, lower FA may reflect variability in lipid processing as the lipid-rich myelin sheath develops; it is unlikely to be evidence of a disease mechanism or a biomarker of AD. Myelin abnormalities and axonal swelling may contribute to synaptic loss and precede amyloid deposition in AD (Bartzokis, 2009). If so, the *CLU* risk variant could increase AD risk in two ways: an early acquired vulnerability paired with suboptimal amyloid processing in later life.

Although the additive model we used assesses evidence for an aggregate risk of carrying increasing numbers of alleles, the associated cellular processes that result in lower FA are not necessarily the primary pathways by which the SNP confers AD risk. Rather, our findings suggest one way in which vulnerability to AD may be increased.

Thus far, only one neuroimaging study has examined brain differences in *CLU*-C carriers (Biffi et al., 2010). That study found that the *CLU* genotypes were not associated with MRI measures. However, in that study structural MRI was used, which is less sensitive than DTI to altered fiber microstructure and myelination. The authors of that study noted that the effects on brain structure of different gene variants that increase AD risk may be specific to particular and disparate aspects of brain structure. This segregation of gene effect on neuroimaging traits can offer important insights into the mechanisms through which the polymorphisms impact AD risk (Biffi et al., 2010).

While 398 subjects would be a small sample on which to identify new genetic risk factors for AD using genome-wide association scanning, it is in fact the largest DTI study to date to examine the effects of Alzheimer's disease genetic risk factors on DTI FA. Prior studies found effects of *APOE*4 on FA in sample sizes that ranged from 29 to 69 (Nierenberg et al., 2005; Persson et al., 2006; Honea et al., 2009; Smith et al., 2010). The effects of familial AD

genes were detected in only 20 adults (Ringman et al., 2007). Admittedly, the odds ratios for those risk factors are greater than for *CLU*. However, our statistical power was boosted not only by our much larger sample size of 398 subjects, but also by our scanning at a stronger field strength (4 T, as opposed to 1.5 or 3 T in the previous studies) and with more diffusion-weighted gradients (94 in our study vs 6 or 12 in previous studies). It is therefore not surprising that we had the power to detect the existing effect.

Although the *CLU* risk variant was a candidate gene, whose effects we set out here to assess, one may also consider the value of making a correction, across studies, for examining multiple AD risk genes. Because of the very strict voxelwise corrections for multiple comparisons required in imaging genetics when using FDR, the rates of false positives (even when examining several hundred SNPs that are not expected to have a significant relationship with the data) remains well below 0.05 (0.2–4.1% for 720 SNPs), as determined empirically (Meyer-Lindenberg et al., 2008). The fact that the *CLU* rs11136000 is a candidate variant chosen a priori based on its relationship to lipid transport and Alzheimer's disease makes it unlikely that our strong results were due to false positives.

We do not yet have available to us a comparably large dataset in which to independently replicate our results. This remains a limitation of our study as genetic studies typically employ very large samples, and, where possible, they replicate effects to avoid the risk of false discoveries. Continued data collection and collaborative efforts that allow for larger sample sizes will remedy this in the future. However, our results remain valuable as a focus for ongoing efforts by our group and others.

Quantitative mapping of structural brain differences in those at genetic risk for AD is crucial for evaluating treatment and prevention strategies. Once identified, brain differences can be monitored to determine how lifestyle choices influence brain health and disease risk. Many lifestyle factors that heighten the risk for dementia—such as exercise and body mass index—have effects on brain structure and the level of brain atrophy (Ho et al., 2010b,c; Raji et al., 2010). Additionally, regular exercise and a healthful diet may reduce the risk of cognitive decline, particularly in those genetically at risk for AD (Rovio et al., 2005; Scarmeas et al., 2009) or those carrying common risk alleles generally associated with brain structure deficits in healthy adults (Ho et al., 2010a). Targeting adults at greatest risk for cognitive deterioration can also improve the power of clinical trials (Kohannim et al., 2010). Future DTI studies of *CLU*-C in those imaged with amyloid- or tangle-sensitive positron emission tomography probes will also help to relate lower white matter integrity to AD pathology as it emerges.

References

Bartzokis G (2009) Alzheimer's disease as homeostatic responses to age-related myelin breakdown. Neurobiol Aging. Advance online publication. Retrieved April 11, 2011. doi:10.1016/j.neurobiolaging.2009.08.007.

Benjamini Y, Hochberg Y (1995) Controlling the false discovery rate- a practical and powerful approach to multiple testing. J R Stat Soc Series B Stat Methodol 57:289–300.

Bertram L, McQueen MB, Mullin K, Blacker D, Tanzi RE (2007) Systematic meta-analyses of Alzheimer disease genetic association studies: the AlzGene database. Nat Genet 39:17–23.

Biffi A, Anderson CD, Desikan RS, Sabuncu M, Cortellini L, Schmansky N, Salat D, Rosand J (2010) Genetic variation and neuroimaging measures in Alzheimer disease. Arch Neurol 67:677–685.

Braak H, Braak E (1996) Development of Alzheimer-related neurofibrillary changes in the neocortex inversely recapitulates cortical myelogenesis. Acta Neuropathol 92:197–201.

Braak H, Braak E (1997) Frequency of stages of Alzheimer-related lesions in different age categories. Neurobiol Aging 18:351–357.

Brun A, Englund E (1986) A white matter disorder in dementia of the Alzheimer type: a pathoanatomical study. Ann Neurol 19:253–262.

Calero M, Tokuda T, Rostagno A, Kumar A, Zlokovic B, Frangione B, Ghiso J (1999) Functional and structural properties of lipid-associated apolipoprotein J (clusterin). Biochem J 344:375–383.

Choi SJ, Lim KO, Monteiro I, Reisberg B (2005) Diffusion tensor imaging of frontal white matter microstructure in early Alzheimer's disease: a preliminary study. J Geriatr Psychiatry Neurol 18:12–19.

Dati G, Quattrini A, Bernasconi L, Malaguti MC, Antonsson B, Nicoletti F, Alliod C, Di Marco R, Sagot Y, Vitte PA, Hiver A, Greco B, Roach A, Zaratin PF (2007) Beneficial effects of r-h-CLU on disease severity in different animal models of peripheral neuropathies. J Neuroimmunol 190:8–17.

Di Paola M, Di Iulio F, Cherubini A, Blundo C, Casini AR, Sancesario G, Passafiume D, Caltagirone C, Spalletta G (2010) When, where, and how the corpus callosum changes in MCI and AD: a multimodal MRI study. Neurology 74:1136–1142.

Harold D, Abraham R, Hollingworth P, Sims R, Gerrish A, Hamshere ML, Pahwa JS, Moskvina V, Dowzell K, Williams A, Jones N, Thomas C, Stretton A, Morgan AR, Lovestone S, Powell J, Proitsi P, Lupton MK, Brayne C, Rubinsztein DC, et al (2009) Genome-wide association study identifies variants at CLU and PICALM associated with Alzheimer's disease. Nat Genet 41:1088–1093.

Ho AJ, Stein JL, Hua X, Lee S, Hibar DP, Leow AD, Dinov ID, Toga AW, Saykin AJ, Shen L, Foroud T, Pankratz N, Huentelman MJ, Craig DW, Gerber JD, Allen AN, Corneveaux JJ, Stephan DA, DeCarli CS, DeChairo BM, et al (2010a) A commonly carried allele of the obesity-related FTO gene is associated with reduced brain volume in the healthy elderly. Proc Natl Acad Sci U S A 107:8404–8409.

Ho AJ, Raji CA, Becker JT, Lopez OL, Kuller LH, Hua X, Dinov ID, Stein JL, Rosano C, Toga AW, Thompson PM (2010b) The effects of physical activity, education, and body mass index on the aging brain. Hum Brain Mapp. Advance online publication. Retrieved April 7, 2011. doi:101002/hbm21113.

Ho AJ, Raji CA, Becker JT, Lopez OL, Kuller LH, Hua X, Lee S, Hibar D, Dinov ID, Stein JL, Jack CR Jr, Weiner MW, Toga AW, Thompson PM, the ADNI Consortium, the CHS Consortium (2010c) Obesity is linked with lower brain volume in 700 AD and MCI patients. Neurobiol Aging 31:1326–1339.

Hoeft F, Barnea-Goraly N, Haas BW, Golarai G, Ng D, Mills D, Korenberg J, Bellugi U, Galaburda A, Reiss AL (2007) More is not always better: increased fractional anisotropy of superior longitudinal fasciculus associated with poor visuospatial abilities in Williams syndrome. J Neurosci 27:11960–11965.

Honea RA, Vidoni E, Harsha A, Burns JM (2009) Impact of APOE on the healthy aging brain: a voxel-based MRI and DTI study. J Alzheimers Dis 18:553–564.

Hua X, Leow AD, Parikshak N, Lee S, Chiang MC, Toga AW, Jack CR Jr, Weiner MW, Thompson PM (2008) Tensor-based morphometry as a neuroimaging biomarker for Alzheimer's disease: an MRI study of 676 AD, MCI, and normal subjects. Neuroimage 43:458–469.

Jackson DN (1984) MAB, multidimensional aptitude battery: manual. Port Hurton, MI: Research Psychologists.

Jahanshad N, Lee AD, Barysheva M, McMahon KL, de Zubicaray GI, Martin NG, Wright MJ, Toga AW, Thompson PM (2010) Genetic influences on brain asymmetry: a DTI study of 374 twins and siblings. Neuroimage 52:455–469.

Kang HM, Zaitlen NA, Wade CM, Kirby A, Heckerman D, Daly MJ, Eskin E (2008) Efficient control of population structure in model organism association mapping. Genetics 178:1709–1723.

Kohannim O, Hua X, Hibar DP, Lee S, Chou YY, Toga AW, Jack CR Jr, Weiner MW, Thompson PM (2010) Boosting power for clinical trials using classifiers based on multiple biomarkers. Neurobiol Aging 31:1429–1442.

Lambert JC, Heath S, Even G, Campion D, Sleegers K, Hiltunen M, Combarros O, Zelenika D, Bullido MJ, Tavernier B, Letenneur L, Bettens K, Berr C, Pasquier F, Fiévet N, Barberger-Gateau P, Engelborghs S, De Deyn P, Mateo I, Franck A, et al (2009) Genome-wide association study identifies variants at CLU and CR1 associated with Alzheimer's disease. Nat Genet 41:1094–1099.

Lee JE, Chung MK, Lazar M, DuBray MB, Kim J, Bigler ED, Lainhart JE, Alexander AL (2009) A study of diffusion tensor imaging by tissue-specific, smoothing-compensated voxel-based analysis. Neuroimage 44:870–883.

Leow A, Huang SC, Geng A, Becker J, Davis S, Toga A, Thompson P (2005) Inverse consistent mapping in 3D deformable image registration: its construction and statistical properties. Inf Process Med Imaging 19:493–503.

Lepore N, Chou YY, Lopez OL, Aizenstein HJ, Becker JT, Toga AW, Thompson PM (2008) Fast 3D fluid registration of brain magnetic resonance images. In: Medical Imaging 2008: Physiology, Function, and Structure from Medical Images. San Diego, USA: SPIE.

Liu Y, Spulber G, Lehtimaki KK, Kononen M, Hallikainen I, Grohn H, Kivipelto M, Hallikainen M, Vanninen R, Soininen H (2009) Diffusion tensor imaging and tract-based spatial statistics in Alzheimer's disease and mild cognitive impairment. Neurobiol Aging. Advance online publication. Retrieved April 11, 2011. doi:10.1016/j.neurobiolaging.2009.10.006.

Meyer-Lindenberg A, Nicodemus KK, Egan MF, Callicott JH, Mattay V, Weinberger DR (2008) False positives in imaging genetics. Neuroimage 40:655–661.

Nierenberg J, Pomara N, Hoptman MJ, Sidtis JJ, Ardekani BA, Lim KO (2005) Abnormal white matter integrity in healthy apolipoprotein E epsilon4 carriers. Neuroreport 16:1369–1372.

Nucifora PG, Verma R, Lee SK, Melhem ER (2007) Diffusion-tensor MR imaging and tractography: exploring brain microstructure and connectivity. Radiology 245:367–384.

Persson J, Lind J, Larsson A, Ingvar M, Cruts M, Van Broeckhoven C, Adolfsson R, Nilsson LG, Nyberg L (2006) Altered brain white matter integrity in healthy carriers of the APOE epsilon4 allele: a risk for AD? Neurology 66:1029–1033.

Raji CA, Ho AJ, Parikshak NN, Becker JT, Lopez OL, Kuller LH, Hua X, Leow AD, Toga AW, Thompson PM (2010) Brain structure and obesity. Hum Brain Mapp 31:353–364.

Resnick SM, Sojkova J, Zhou Y, An Y, Ye W, Holt DP, Dannals RF, Mathis CA, Klunk WE, Ferrucci L, Kraut MA, Wong DF (2010) Longitudinal cognitive decline is associated with fibrillar amyloid-beta measured by [11C]PiB. Neurology 74:807–815.

Ringman JM, O'Neill J, Geschwind D, Medina L, Apostolova LG, Rodriguez Y, Schaffer B, Varpetian A, Tseng B, Ortiz F, Fitten J, Cummings JL, Bartzokis G (2007) Diffusion tensor imaging in preclinical and presymptomatic carriers of familial Alzheimer's disease mutations. Brain 130:1767–1776.

Roth AD, Ramírez G, Alarcón R, Von Bernhardi R (2005) Oligodendrocytes damage in Alzheimer's disease: beta amyloid toxicity and inflammation. Biol Res 38:381–387.

Rovio S, Kåreholt I, Helkala EL, Viitanen M, Winblad B, Tuomilehto J, Soininen H, Nissinen A, Kivipelto M (2005) Leisure-time physical activity at midlife and the risk of dementia and Alzheimer's disease. Lancet Neurol 4:705–711.

Salat DH, Tuch DS, van der Kouwe AJ, Greve DN, Pappu V, Lee SY, Hevelone ND, Zaleta AK, Growdon JH, Corkin S, Fischl B, Rosas HD (2010) White matter pathology isolates the hippocampal formation in Alzheimer's disease. Neurobiol Aging 31:244–256.

Scarmeas N, Luchsinger JA, Schupf N, Brickman AM, Cosentino S, Tang MX, Stern Y (2009) Physical activity, diet, and risk of Alzheimer disease. JAMA 302:627–637.

Smith CD, Chebrolu H, Andersen AH, Powell DA, Lovell MA, Xiong S, Gold BT (2010) White matter diffusion alterations in normal women at risk of Alzheimer's disease. Neurobiol Aging 31:1122–1131.

Stricker NH, Schweinsburg BC, Delano-Wood L, Wierenga CE, Bangen KJ, Haaland KY, Frank LR, Salmon DP, Bondi MW (2009) Decreased white matter integrity in late-myelinating fiber pathways in Alzheimer's disease supports retrogenesis. Neuroimage 45:10–16.

Thomason ME, Thompson PM (2011) Diffusion imaging, white matter and psychopathology. Annu Rev Clin Psychol 7:63–85.

Wechsler D (1981) Wechsler adult intelligence scale-revised. San Antonio, TX: The Psychological Corporation.

Zhang Y, Schuff N, Du AT, Rosen HJ, Kramer JH, Gorno-Tempini ML, Miller BL, Weiner MW (2009) White matter damage in frontotemporal dementia and Alzheimer's disease measured by diffusion MRI. Brain 132:2579–2592.

Zlokovic BV, Martel CL, Matsubara E, McComb JG, Zheng G, McCluskey RT, Frangione B, Ghiso J (1996) Glycoprotein 330/megalin: probable role in receptor-mediated transport of apolipoprotein J alone and in a complex with Alzheimer disease amyloid beta at the blood-brain and blood-cerebrospinal fluid barriers. Proc Natl Acad Sci U S A 93:4229–4234.

5.2 Mapping HIV risk factors to the brain

The following section is adapted from:

Nakamoto BK*; **Jahanshad N***; McMurtray A, Kallianpur KJ, Chow DC, Valcour VG, Paul RH, Thompson PM, Shikuma CM, Cerebrovascular Risk Factors and Brain Microstructural Changes on Diffusion Tensor Images in HIV-infected Individuals. J. Neurovirology In Press

* denotes equal contribution

J. Neurovirol.
DOI 10.1007/s13365-012-0106-1

Cerebrovascular risk factors and brain microstructural abnormalities on diffusion tensor images in HIV-infected individuals

Beau K. Nakamoto · Neda Jahanshad · Aaron McMurtray · Kalpana J. Kallianpur · Dominic C. Chow · Victor G. Valcour · Robert H. Paul · Liron Marotz · Paul M. Thompson · Cecilia M. Shikuma

Received: 31 January 2012 / Revised: 17 April 2012 / Accepted: 23 April 2012

Abstract HIV-associated neurocognitive disorder remains prevalent in HIV-infected individuals despite effective antiretroviral therapy. As these individuals age, comorbid cerebrovascular disease will likely impact cognitive function. Effective tools to study this impact are needed. This study used diffusion tensor imaging (DTI) to characterize brain microstructural changes in HIV-infected individuals with and without cerebrovascular risk factors. Diffusion-weighted MRIs were obtained in 22 HIV-infected subjects aged 50 years or older (mean age=58 years, standard deviation=6 years; 19 males, three females). Tensors were calculated to obtain fractional anisotropy (FA) and mean diffusivity (MD) maps. Statistical comparisons accounting for multiple comparisons were made between groups with and without cerebrovascular risk factors. Abnormal glucose metabolism (i.e., impaired fasting glucose, impaired glucose tolerance, or diabetes mellitus) was associated with significantly higher MD (false discovery rate (FDR) critical p value=0.008) and lower FA (FDR critical p value=0.002) in the caudate and lower FA in the hippocampus (FDR critical p value=0.004). Pearson correlations were performed between DTI measures in the caudate and hippocampus and age- and education-adjusted composite scores of global cognitive function, memory, and psychomotor speed. There were no detectable correlations between the neuroimaging measures and measures of cognition. In summary, we demonstrate that brain microstructural abnormalities are associated with abnormal glucose metabolism in the caudate and hippocampus of HIV-infected individuals. Deep gray matter structures and the hippocampus may be vulnerable in subjects with comorbid abnormal glucose metabolism, but our results should be confirmed in further studies.

Beau K. Nakamoto and Neda Jahanshad contributed equally to this manuscript.

B. K. Nakamoto · K. J. Kallianpur · D. C. Chow · L. Marotz · C. M. Shikuma
University of Hawaii,
Honolulu, HI, USA

B. K. Nakamoto
Straub Clinics and Hospital,
Honolulu, HI, USA

N. Jahanshad · P. M. Thompson
Laboratory of Neuro Imaging, Departments of Neurology and Psychiatry, UCLA School of Medicine,
Los Angeles, CA, USA

A. McMurtray
Ventura County Medical Center,
Ventura, CA, USA

V. G. Valcour
University of California at San Francisco,
San Francisco, CA, USA

R. H. Paul
University of Missouri,
St. Louis, MO, USA

B. K. Nakamoto (✉)
Hawaii Center for AIDS, John A. Burns School of Medicine,
University of Hawaii at Manoa,
3675 Kilauea Ave. Young Bldg 5th Floor,
Honolulu, HI 96816, USA
e-mail: beau_nakamoto@yahoo.com

Published online: 15 May 2012

J. Neurovirol.

Keywords HIV · Cerebrovascular disease · Diffusion tensor imaging

Glossary

Aβ	Amyloid-beta
APOE ε4	Apolipoprotein epsilon 4
ATP-III	Adult Treatment Panel III
BDI-II	Beck Depression Inventory II
cART	Combination antiretroviral therapy
DBP	Diastolic blood pressure
DTI	Diffusion tensor imaging
FA	Fractional anisotropy
FDR	False discovery rate
IDE	Insulin-degrading enzyme
MD	Mean diffusivity
NPZ-3-mem	Age- and education-adjusted composite score of memory
NPZ-3-pm	Age- and education-adjusted composite score of psychomotor speed
NPZ-8	Age- and education-adjusted composite score of global cognitive function
OGTT	2-h oral glucose tolerance test
PET	Positron emission tomography
ROIs	Regions of interest
SBP	Systolic blood pressure
SD	Standard deviation

Introduction

Cerebrovascular risk factors are prevalent in HIV-infected individuals. Several studies show that preexisting cerebrovascular risk factors (e.g., smoking, dyslipidemia, hypertension, and diabetes mellitus) are associated with cognitive impairment (Becker et al. 2009; Wright et al. 2010; Nakamoto et al. 2011).

Ovbiagele and Nath (2011) reported that the incidence of stroke hospitalizations with comorbid HIV infection rose 60 % between 1997 and 2006. In a study of 292 HIV-infected individuals with high CD4 cell counts (median CD4 cell count=536 cells/mm^3) from the Strategies for Management of Antiretroviral Therapy study, patients with preexisting cardiovascular disease had a 6.2-fold higher odds of having cognitive impairment (Wright et al. 2010). Prior cardiovascular disease, hypertension, and hypercholesterolemia were also associated with worse cognitive performance as measured by a composite *z* score of information processing speed, attention, executive, and motor functions (Wright et al. 2010). Analysis of 428 HIV-infected older (≥40) gay and bisexual males from the Multicenter AIDS Cohort Study demonstrated that subclinical atherosclerosis as measured by carotid intima–media thickness was associated with worse psychomotor performance (Becker et al. 2009). The impact of cerebrovascular disease on cognitive function appears to be additive rather than synergistic with HIV infection (Nakamoto et al. 2010).

Infection with HIV is associated with atrophy in the cerebral cortex (e.g., anterior cingulate, insula, and superior frontal, orbitofrontal, parietal, posterior/inferior temporal lobes) (Becker et al. 2011a; Kuper et al. 2011; Kallianpur et al. 2011), deep gray matter (e.g., caudate, putamen) (Becker et al. 2011b), and lower white matter volume (Becker et al. 2011a). The additional impact of cerebrovascular risk factors on brain structure is unclear. One study by Becker et al. (2011a) did not detect an association between brain atrophy and cerebrovascular risk factors.

Diffusion tensor imaging (DTI) is a MRI technique which measures the random motion of water to assess the microstructural integrity of brain tissue. Mean diffusivity (MD) and fractional anisotropy (FA) are two common DTI measures that describe the speed and direction of water diffusion within the brain. MD is a DTI measure of the diffusion speed of water molecules. In constricted regions (e.g., inside cells) where the diffusion of water molecules is slow, MD is low. In unconstricted regions (e.g., inside the ventricles), the diffusion of water molecules is relatively fast, and MD is high. FA is a DTI measure of the directionality of water diffusion. When the diffusion of water molecules is equal in all directions, diffusion is isotropic. The diffusion of water in gray matter is one example of isotropy. When the diffusion of water has directionality, the diffusion is anisotropic. The diffusion of water along axons in the white matter of the brain is one example of anisotropy where the diffusion of water is constrained by the axon's myelin sheath. Higher MD and lower FA values suggest decreased microstructural integrity in the brain.

Several studies, some including HIV-infected populations, have used DTI to study the microstructure of white matter (Basser et al. 1994a, b; Filippi et al. 2001; Pfefferbaum et al. 2007, 2009; Gongvatana et al. 2009, 2011; Chen et al. 2009; Hoare et al. 2011) Little attention has been given to examine the deep gray matter or hippocampal microstructure in the HIV-infected population (Ragin et al. 2005; Chang et al. 2008). These regions of interest (ROIs) are relevant to HIV-infected individuals given the basal ganglia and hippocampus are preferential sites of neuropathology in HIV infection and cerebrovascular disease (Navia et al. 1986; Jellinger 2008; Gorelick and Bowler 2010). DTI can detect subtle microstructural brain changes event when there are no detectable macrostructural changes, such as atrophy, on standard MRI scans in HIV-infected individuals (Filippi

et al. 2001). We hypothesized that cerebrovascular risk factors would be associated with DTI differences.

Methods

Study population This study used data from a parent positron emission tomography (PET) study assessing the impact of the apolipoprotein epsilon 4 (APOE ε4) genotype on cortical metabolism in HIV-infected subjects at least 50 years of age. The PET results were presented elsewhere (McMurtray et al. 2008). Brain MRIs were obtained as an optional procedure in 22 subjects out of 27 subjects who were studied further here. These subjects are the focus of this analysis. The Committee on Human Studies at the University of Hawaii approved the protocol.

Clinical assessment Demographic characteristics collected included age, sex, race/ethnicity, and self-reported years of education. General medical and current medication histories were collected. HIV-relevant characteristics collected included self-reported current and the lowest ever CD4+ lymphocyte cell count and current antiretroviral therapy. Measured biological characteristics included height, weight, waist circumference, blood pressure, plasma HIV RNA, CD4+ lymphocyte cell count, APOE ε4 genotype, fasting lipid profile, directly measured low-density lipoprotein (LDL) cholesterol, and fasting plasma glucose. We evaluated glucose homeostasis with a 2-h oral glucose tolerance test (OGTT).

Hypertension was defined as self-reported diagnosis, use of an antihypertensive medication, or measured systolic blood pressure (SBP) equal to or greater than 140 mmHg or diastolic blood pressure (DBP) equal to or greater than 90 mmHg (U.S. Preventive Services Task Force 2007). We defined diabetes mellitus as self-reported diagnosis, use of diabetes medication, or a fasting plasma glucose greater than 125 mg/dL or 2-h post-challenge glucose greater than or equal to 200 mg/dL (American Diabetes Association 2009). Impaired fasting glucose was defined as a fasting plasma glucose between 100 and 125 mg/dL and impaired glucose tolerance as a 2-h post-challenge glucose between 140 and 199 mg/dL (American Diabetes Association 2009). We classified individuals as having abnormal glucose metabolism if they met criteria for impaired fasting glucose, impaired glucose tolerance, or diabetes mellitus. Elevated LDL cholesterol was defined as a fasting measured LDL cholesterol greater than or equal to 100 mg/dL (Expert Panel on Detection, Evaluation, and Treatment of High Blood Cholesterol in Adults 2002). Elevated triglyceride level was defined as a fasting triglyceride greater than or equal to 150 mg/dL (Expert Panel on Detection, Evaluation, and Treatment of High Blood Cholesterol in Adults 2001). Low high-density lipoprotein (HDL) cholesterol was defined as a fasting HDL cholesterol less than 40 mg/dL in men and less than 50 mg/dL in women (Expert Panel on Detection, Evaluation, and Treatment of High Blood Cholesterol in Adults 2001). Abdominal obesity was defined as a waist circumference in men greater than 102 cm (40 in.) and in women greater than 88 cm (35 in.) (Expert Panel on Detection, Evaluation, and Treatment of High Blood Cholesterol in Adults 2001). Waist circumference was recorded as a measure of abdominal obesity, as possible decreases in hip circumference due to lipodystrophy may make use of waist-to-hip ratio problematic (Brown et al. 2009). Diagnosis of the metabolic syndrome was based on Adult Treatment Panel III (ATP-III) criteria (Expert Panel on Detection, Evaluation, and Treatment of High Blood Cholesterol in Adults 2001). Depressive symptoms were assessed with the Beck Depression Inventory II (BDI-II) (Beck et al. 1961).

Diffusion tensor imaging MRI scans were acquired within 1 month of clinical assessment and neuropsychological testing on the same Philips 3.0-T Achieva scanner equipped with an eight-channel sensitivity encoding head coil. For each subject, structural and diffusion-weighted MRI scans were obtained. Structural MRI included a sagittal T1-weighted image with a three-dimensional turbo field-echo sequence (repetition time/echo time (TR/TE)=6.7/3.1 ms, flip angle 8°, slice thickness 1.2 mm, in-plane resolution 1.0 mm^2; Wright et al. 2010). Diffusion-weighted scans included a single-shot echo planar imaging sequence (24 cm field of view, TR/TE=7,859 ms/80 ms, flip angle 90°, 3.0-mm-thick slices, 0 mm gap, SENSE factor=3.1, maximum slew rate 120 mT/m/ms, gradient amplitude 40 mT/m, 96×95 acquisition matrix, 2.5×2.5 mm^2 in-plane resolution, and a variable number of slices determined by head size). One image with no diffusion sensitization was obtained (i.e., a T2-weighted b_0 image). Diffusion weighting was applied along 15 non-collinear directions evenly distributed over a sphere with a *b*-factor of 1,000 s/mm^2 (Wright et al. 2010) and four signal averages to increase the signal-to-noise ratio. Scan time was 8.6 min.

The diffusion-weighted images were uploaded to the Laboratory of Neuro Imaging at the University of California, Los Angeles. Correction for subject motion inside the scanner and eddy current distortions were performed on the diffusion-weighted images using FSL software (http://fsl.fmrib.ox.ac.uk/fsl/). The correctly aligned images were then used to calculate the tensors from which MD and FA maps were created. Diffusion tensors were computed at each

voxel using FSL software (http://fsl.fmrib.ox.ac.uk/fsl/). From the tensor eigenvalues (λ_1, λ_2, λ_3), FA was calculated according to the formula:

$$\mathrm{FA} = \sqrt{\frac{3}{2}}\frac{\sqrt{(\lambda_1 - <\lambda>)^2 + (\lambda_2 - <\lambda>)^2 + (\lambda_3 - <\lambda>)^2}}{\sqrt{\lambda_1^2 + \lambda_2^2 + \lambda_3^2}} \in [0, 1]$$
$$<\lambda> = \frac{\lambda_1 + \lambda_2 + \lambda_3}{3}!$$

To assess the integrity of all images in the exact same locations, all images were registered to a template image. To preserve high anatomical resolution, a single subject with no anatomical abnormalities and with a high-quality scan was randomly selected as the target for the dataset. All subjects' b_0 images were aligned to the same space using linear registration followed by an elastic inverse consistent mutual information-based nonlinear warping of all subject images to the target (Leow et al. 2005). For each subject, the transformation obtained from the linear registration and deformation field obtained from the nonlinear registration of subject to target b_0 images were then applied to the anisotropy and diffusivity images. Diffusion parameters (MD and FA) were measured voxelwise across the whole brain. Deep gray matter ROIs were manually extracted by the same neuroscientist (N.J.) from the target subject to include the caudate, putamen, globus pallidus, and thalamus. The corpus callosum which included the genu, body, and splenium in toto was also extracted. The mean FA and MD were then computed for each of the subjects, after their scans were registered to the selected target.

Neurocognitive testing The neurocognitive battery tested seven cognitive domains: language (Boston Naming Test), verbal fluency (FAS letter fluency, animal naming), attention/working memory (WAIS-III Digit Span Subtest, WAIS-III Letter–Number Sequencing Subtest), speed of information processing (Trailmaking Test—Part A, California Computerized Assessment Package, WAIS-III Digit Symbol Subtest), executive function (Stroop Interference Test, Trailmaking Test—Part B), verbal and visual learning and memory (Rey Auditory Verbal Learning Test, Rey–Osterrieth Complex Figure Test), and motor skills (Grooved Pegboard Test, Timed Gait). Fasting laboratory measures and OGTT were performed on a different day from neurocognitive testing to minimize bias associated with fasting and the procedure (Lamport et al. 2009). Individual neuropsychological test scores were standardized based on age- and education-adjusted normative data to construct individual z scores (Strauss et al. 2006), and standardized unweighted composite z scores (age- and education-adjusted composite score of global cognitive function (NPZ-8), age- and education-adjusted composite score of memory (NPZ-3-mem), age- and education-adjusted composite score of psychomotor speed (NPZ-3-pm)) were derived by calculating the arithmetic mean of various individual z scores as previously described (Shiramizu et al. 2007). NPZ-8 is a measure of broader cognitive function by including eight tests thought to have specificity in HIV (Schmitt et al. 1988); NPZ-3-mem is a measure of memory; NPZ-3-pm is a measure of psychomotor speed. The composite z scores were defined so that positive values indicate better performance compared with age- and education-adjusted normative values, while negative values indicate poorer performance.

Statistical analysis For DTI analysis, voxelwise statistical comparisons were made on diffusion parameters (MD and FA) between groups on spatially normalized and geometrically registered DTI-based diffusivity (MD) and anisotropy (FA) images in the whole brain. Additional ROIs were outlined on the template subjects and used as ROIs for which mean FA and MD values were compared across subjects. These ROIs include the corpus callosum, caudate, putamen, globus pallidus, and thalamus. Student's t tests were performed to compare the mean FA or MD values based on the presence or absence of each cerebrovascular risk factor (e.g., hypertension, abnormal glucose metabolism, metabolic syndrome, elevated total cholesterol, elevated LDL, past or present smoking history, and at least one APOE ε4 allele). Multiple comparison correction for the voxelwise tests was conducted using the false discovery rate (FDR) (Benjamini and Hochberg 1995). The cumulative distribution of p values was obtained in regions of high anisotropy (FA>0.3 for the group average) and plotted against the null distribution of p values where no significant differences (FDR controlling p value≤0.05) were detected on a voxelwise level. FDR was performed across the whole brain, corpus callosum, and four deep gray matter ROI for each cerebrovascular risk factor assessed. Pearson product–moment correlations were obtained between MD and FA values in the statistically significant ROI and composite measures of neurocognitive performance (e.g., NPZ-8, NPZ-3-mem, NPZ-3-pm).

For clinical data, statistical analyses were performed with SAS 9.1 (Cary, NC, USA). Means, standard deviations, and proportions were calculated for baseline characteristics. The null hypothesis was that there was no association between neurocognitive composite scores and traditional cerebrovascular risk factors. NPZ-8, NPZ-3-mem, and NPZ-3-pm were used as dependent variables in three different linear regression models. Independent variables included age, current CD4+ count, self-reported lowest ever CD4+ count, SBP, DBP, LDL cholesterol, triglyceride, and HDL cholesterol as continuous variables and treatment with a protease inhibitor, abnormal glucose metabolism, and the presence of at least one APOE ε4 allele as categorical (present or absent)

J. Neurovirol.

variables. Forward selection was used, and independent variables with p values less than or equal to 0.20 were included in the final regression model. A p value$\leq$0.05 was considered statistically significant.

Results

Subject characteristics The mean (standard deviation, SD) age of the sample was 58 (6) years (Table 1). All but one subject was on combination antiretroviral therapy (cART), and 20 of 21 were on the same cART regimen for 12 months. A minority (four of 22, 18 %) was treated with a protease inhibitor-based cART. All had current CD4+ counts >200 cells/μL. A majority (18 of 22, 82 %) had undetectable viral loads. The mean self-reported lowest ever CD4+ count was 210 cells/μL (SD 171 cells/μL). Subjects with a history of central nervous system opportunistic infection, seizures, head trauma with a loss of consciousness or cognitive sequelae, active psychosis, uncontrolled major affective disorders, and current substance abuse or dependence as defined by the *Diagnostic Statistical Manual of Mental Disorders* (American Psychiatric Association 2000) had been excluded from the parent study (McMurtray et al. 2008) from which these data were obtained.

Nine subjects had impaired fasting glucose or impaired glucose tolerance with one of these nine treated with metformin. Four subjects had diabetes mellitus among whom three were treated with either an oral antihyperglycemic or insulin, and the fourth subject was not on treatment. The rates of other cerebrovascular risk factors were high with seven meeting the definition of the metabolic syndrome as defined by ATP-III criteria (Expert Panel on Detection, Evaluation, and Treatment of High Blood Cholesterol in Adults 2001). Nine subjects had at least one APOE ε4 allele, and on average, these individuals were older (mean age=62, SD=7 versus 56, SD=5 years; p=0.03). However, there were no significant differences between the subjects with and without at least one APOE ε4 allele in mean SBP, DBP, fasting LDL, fasting triglycerides, fasting HDL, BMI, waist circumference, or proportion with abnormal glucose metabolism, or metabolic syndrome. The mean BDI-II score was 7 (SD, 4). No subjects had severe depression based on BDI-II.

Diffusion tensor imaging Microstructural differences (i.e., higher MD, lower FA) were noted in the caudate and hippocampus of subjects with abnormal glucose metabolism in post hoc analysis (Table 2; Fig. 1). No hyperintensities were noted in the deep gray matter structures or hippocampus on visual inspection of T2-weighted sequences nor significant differences in the frequencies of individuals with a history of stimulant abuse between those with and without abnormal glucose metabolism (p=0.25) to explain these results. We were unable to determine if there was an increased effect size in DTI measures between individuals with impaired fasting glucose/impaired glucose tolerance versus diabetes mellitus due to the small sample size. No statistically significant correlations were found between MD and FA in the caudate and hippocampus and neurocognitive composite scores (i.e., NPZ-8, NPZ-3-mem, and NPZ-3-pm) by unadjusted Pearson correlation. There was a trend toward an inverse correlation between hippocampal MD and global cognitive function (NPZ-8; r=−0.4381, p=0.07). No significant relationships were seen in MD and FA in the white matter (i.e., whole brain, corpus callosum), putamen, globus pallidus, or thalamus and other cerebrovascular risk factors (i.e., hypertension, metabolic syndrome, elevated total cholesterol, elevated LDL, past or present smoking history, and at least one APOE ε4 allele).

Neurocognitive testing Age, abnormal glucose metabolism, metabolic syndrome, tobacco use, and the presence of at least one APOE ε4 allele met our criteria for inclusion using forward selection ($p\leq$0.20) in the final multivariate analysis. Age (β=−0.05; p=0.02), abnormal glucose metabolism (β=0.92; p<0.01), metabolic syndrome (β=−0.81; p<0.01), tobacco use (β=−0.51; p=0.03), and the presence of at least one APOE ε4 allele (β=−0.81; p<0.01) were significantly associated with the composite measure of global cognitive function (NPZ-8). There were no significant associations of these variables with composite measures of memory (NPZ-3-mem) and psychomotor speed (NPZ-3-pm).

Discussion

This cross-sectional study used DTI to examine the microstructural differences associated with cerebrovascular risk factors in HIV-infected subjects aged 50 years and older. Our findings suggest that subtle microstructural brain abnormalities are noted in the caudate and hippocampus in subjects with comorbid impairment in glucose metabolism.

In our study, only individuals with abnormal glucose metabolism but not other cerebrovascular risk factors were associated with microstructural differences in the caudate and hippocampus. More specifically, we found no differences by hypertension, dyslipidemia, smoking, or by APOE ε4 status. The differences demonstrated by impaired glucose metabolism were significant even when corrected for multiple comparisons. It is intriguing that differences were not found in other cerebrovascular risk factors which may be a result of the small sample size but also raises the possibility that the microstructural changes associated with abnormal glucose metabolism may not be mediated through atherosclerosis. For example, chronic hyperglycemia and hyperinsulinemia stimulate the

Table 1 Demographic and clinical characteristics of subjects

	N=22
Mean age, years (SD; range)	58 (6; 50–73)
% male	86 (19/22)
% non-Hispanic white	77 (17/22)
% Hispanic white	5 (1/22)
% Asian	9 (2/22)
% Native American	5 (1/22)
% Native Hawaiian	5 (1/22)
Mean years of education (SD; range)	16 (2; 12–20)
HIV-associated parameters	
Mean years HIV-positive (SD; range)	17 (2–26)
% on HAART	95 (21/22)
% on protease inhibitor	18 (4/22)
% with current CD4+ count >200 cells/μL	100 (22/22)
% with undetectable HIV RNA viral load (<50 copies/mL)	82 (18/22)
Mean self-reported lowest ever CD4 count, cells/μL (SD; range)	210 (171; 1–450)
% with history of prior stimulant use	64 (14/22)
Cerebrovascular risk factors	
Mean body mass index, kg/m (Wright et al. 2010) (SD)	24 (3)
% with abdominal obesity[a]	0 (0/22)
Mean waist circumference, cm (SD, range)	91 (7; 76–102)
% with impaired glucose tolerance	41 (9/22)
% with adult-onset diabetes mellitus	18 (4/22)
% with hypertension	45 (10/22)50
Mean SBP, mmHg (SD, range)	126 (18; 99–159)
Mean DBP, mmHg (SD, range)	74 (10; 52–89)
% with fasting LDL≥100 mg/dL	50 (11/22)
Mean fasting LDL, mg/dL (SD, range)	112 (44; 52–226)
% with fasting triglycerides ≥150 mg/dL	36 (8/22)
Mean fasting triglycerides, mg/dL (SD, range)	169 (128; 36–341)
% with fasting HDL cholesterol <40 mg/dL in men or <50 mg/dL in women	64 (14/22)
Mean fasting HDL cholesterol, mg/dL (SD; range)	40 (19; 18–110)
% with metabolic syndrome	32 (7/22)
% with past or present smoking history	45 (10/22)
Mean pack years (SD, range)	19 (11; 1–30)
% with at least one APOE ε4 allele	40 (9/22)
% with white matter hyperintensities on MRI	36 (8/22)
Mean Beck Depression Inventory score (SD, range)	7 (4, 1–15)

APOE ε4 allele apolipoprotein epsilon 4 allele, *DBP* diastolic blood pressure, *HAART* highly active antiretroviral therapy, *MI* myocardial infarction, *SBP* systolic blood pressure, *SD* standard deviation

[a]Abdominal obesity was defined as a waist circumference in men greater than 102 cm (40 in.) and in women greater than 88 cm (35 in.) (Detection et al. 2001)

formation of advanced glucosylated end-products, which can lead to overproduction of reactive oxygen species and resultant brain damage from oxidative stress (S Roriz-Filho et al. 2009). Alternatively, insulin-degrading enzyme (IDE) is the main clearance mechanism amyloid-beta (Aβ), and since IDE is more selective for insulin than Aβ, hyperinsulinemia may result in reduced neurotoxic Aβ clearance (S Roriz-Filho et al. 2009). Finally, hyperglycemia and hyperinsulinemia may also disrupt brain microstructure by inducing tau hyperphosphorylation (S Roriz-Filho et al. 2009). The increased diffusion (i.e., MD) and disorganization (i.e., FA) of water molecules in the caudate and hippocampus may be associated with increased edema from ischemia or inflammation associated with any of these possible mechanisms (Assaf and Pasternak 2008). Although past stimulant abuse has been associated with reduced microstructural integrity in the basal ganglia and hippocampus (Thames et al. 2011), there were no differences in frequency of past stimulant abuse between individuals with and without impaired glucose intolerance/diabetes in our study.

Abnormal glucose metabolism is highly prevalent in the HIV-infected population particularly as HIV-infected individuals live longer and prolonged exposure to cART increases the

Table 2 Association of vascular risk factors and DTI parameters

	Abnormal glucose metabolism[a]			Hypertension			Dyslipidemia		
	Present	Absent	FDR critical *p* value	Present	Absent	FDR critical *p* value	Present	Absent	FDR critical *p* value
Caudate MD	1.33 (0.65)	1.14 (0.54)	0.008	1.32 (0.63)	1.19 (0.58)	NS	1.31 (0.63)	1.20 (0.58)	NS
Caudate FA	0.19 (0.10)	0.21 (0.11)	0.002	0.20 (0.10)	0.21 (0.11)	NS	0.19 (0.10)	0.21 (0.12)	NS
Hippocampus MD	1.16 (0.27)	1.01 (0.20)	NS	1.15 (0.27)	1.05 (0.23)	NS	1.15 (0.26)	1.05 (0.23)	NS
Hippocampus FA	0.16 (0.08)	0.19 (0.09)	0.004	0.17 (0.08)	0.18 (0.09)	NS	0.17 (0.08)	0.18 (0.09)	NS
Thalamus MD	1.01 (0.47)	0.92 (0.36)	NS	1.02 (0.51)	0.93 (0.35)	NS	1.02 (0.47)	0.93 (0.39)	NS
Thalamus FA	0.29 (0.10)	0.29 (0.09)	NS	0.30 (0.10)	0.29 (0.09)	NS	0.28 (0.09)	0.30 (0.09)	NS
Putamen MD	0.75 (0.7)	0.75 (0.06)	NS	0.76 (0.06)	0.74 (0.07)	NS	0.76 (0.06)	0.74 (0.07)	NS
Putamen FA	0.25 (0.07)	0.22 (0.07)	NS	0.24 (0.07)	0.25 (0.07)	NS	0.24 (0.08)	0.24 (0.06)	NS
Globus pallidus MD	0.70 (0.14)	0.65 (0.15)	NS	0.69 (0.14)	0.66 (0.15)	NS	0.70 (0.14)	0.65 (0.15)	NS
Globus pallidus FA	0.37 (0.09)	0.41 (0.09)	NS	0.38 (0.08)	0.39 (0.09)	NS	0.37 (0.09)	0.40 (0.08)	NS
Corpus callosum MD	0.90 (0.17)	0.90 (0.03)	NS	1.02 (0.19)	0.91 (0.03)	NS	1.01 (0.19)	0.91 (0.03)	NS
Corpus callosum FA	0.42 (0.05)	0.44 (0.03)	NS	0.41 (0.05)	0.45 (0.02)	NS	0.43 (0.05)	0.44 (0.02)	NS
Frontal lobe WM MD	1.09 (0.32)	1.02 (0.29)	NS	1.10 (0.32)	1.01 (0.29)	NS	1.10 (0.33)	1.02 (0.28)	NS
Frontal lobe WM FA	0.20 (0.11)	0.20 (0.12)	NS	0.20 (0.11)	0.20 (0.12)	NS	0.20 (0.11)	0.20 (0.12)	NS
Parietal lobe WM MD	1.02 (0.36)	0.96 (0.33)	NS	1.02 (0.37)	0.96 (0.33)	NS	1.02 (0.36)	0.97 (0.33)	NS
Parietal lobe WM FA	0.20 (0.13)	0.21 (0.13)	NS	0.20 (0.12)	0.21 (0.13)	NS	0.20 (0.13)	0.21 (0.13)	NS
Temporal lobe WM MD	1.00 (0.35)	0.92 (0.31)	NS	1.00 (0.36)	0.93 (0.31)	NS	1.00 (0.35)	0.93 (0.32)	NS
Temporal lobe WM FA	0.18 (0.08)	0.19 (0.09)	NS	0.18 (0.08)	0.19 (0.09)	NS	0.18 (0.09)	0.19 (0.09)	NS
Occipital lobe WM MD	0.96 (0.26)	0.89 (0.23)	NS	0.95 (0.27)	0.91 (0.23)	NS	0.95 (0.26)	0.91 (0.24)	NS
Occipital lobe WM FA	0.17 (0.08)	0.18 (0.09)	NS	0.17 (0.08)	0.17 (0.09)	NS	0.17 (0.08)	0.17 (0.09)	NS
	Past or current tobacco use			Metabolic syndrome			At least one APOE ε4 allele present		
	Present	Absent	FDR critical *p* value	Present	Absent	FDR critical *p* value	Present	Absent	FDR critical *p* value
Caudate MD	1.25 (0.59)	1.26 (0.61)	NS	1.33 (0.65)	1.22 (0.58)	NS	1.25 (0.60)	1.26 (0.60)	NS
Caudate FA	0.20 (0.11)	0.20 (0.10)	NS	0.20 (0.10)	0.20 (0.11)	NS	0.21 (0.11)	0.19 (0.10)	NS
Hippocampus MD	1.10 (0.24)	1.10 (0.24)	NS	1.16 (0.28)	1.07 (0.23)	NS	1.11 (0.26)	1.09 (0.24)	NS
Hippocampus FA	0.18 (0.08)	0.17 (0.08)	NS	0.16 (0.08)	0.18 (0.08)	NS	0.17 (0.08)	0.17 (0.08)	NS
Thalamus MD	0.98 (0.43)	0.97 (0.42)	NS	0.99 (0.46)	0.97 (0.41)	NS	0.98 (0.45)	0.97 (0.41)	NS
Thalamus FA	0.29 (0.09)	0.30 (0.09)	NS	0.30 (0.10)	0.29 (0.09)	NS	0.30 (0.10)	0.29 (0.09)	NS
Putamen MD	0.76 (0.06)	0.74 (0.06)	NS	0.75 (0.08)	0.75 (0.06)	NS	0.76 (0.06)	0.74 (0.06)	NS
Putamen FA	0.23 (0.07)	0.25 (0.07)	NS	0.26 (0.07)	0.23 (0.07)	NS	0.23 (0.07)	0.25 (0.07)	NS
Globus pallidus MD	0.67 (0.16)	0.69 (0.13)	NS	0.69 (0.15)	0.67 (0.14)	NS	0.70 (0.13)	0.66 (0.15)	NS
Globus pallidus FA	0.39 (0.10)	0.38 (0.08)	NS	0.39 (0.08)	0.39 (0.09)	NS	0.37 (0.08)	0.40 (0.09)	NS
Corpus callosum MD	0.96 (0.14)	0.96 (0.15)	NS	0.99 (0.19)	0.94 (0.12)	NS	0.96 (0.15)	0.96 (0.14)	NS
Corpus callosum FA	0.43 (0.05)	0.43 (0.03)	NS	0.43 (0.04)	0.43 (0.04)	NS	0.42 (0.05)	0.44 (0.04)	NS
Frontal lobe WM MD	1.05 (0.30)	1.07 (0.32)	NS	1.08 (0.33)	1.05 (0.29)	NS	1.07 (0.32)	1.05 (0.30)	NS

Table 2 (continued)

Frontal lobe WM FA	0.20 (0.12)	0.20 (0.11)	NS	0.20 (0.12)	0.20 (0.11)	NS	0.20 (0.11)	0.20 (0.12)	NS	
Parietal lobe WM MD	0.98 (0.34)	1.00 (0.35)	NS	1.01 (0.37)	0.99 (0.34)	NS	1.00 (0.36)	0.99 (0.34)	NS	
Parietal lobe WM FA	0.20 (0.13)	0.21 (0.13)	NS	0.20 (0.13)	0.20 (0.13)	NS	0.20 (0.13)	0.20 (0.13)	NS	
Temporal lobe WM MD	0.96 (0.33)	0.97 (0.34)	NS	1.00 (0.37)	0.95 (0.32)	NS	0.97 (0.34)	0.96 (0.33)	NS	
Temporal lobe WM FA	0.19 (0.09)	0.19 (0.09)	NS	0.18 (0.09)	0.19 (0.09)	NS	0.19 (0.09)	0.18 (0.09)	NS	
Occipital lobe WM MD	0.92 (0.25)	0.94 (0.25)	NS	0.96 (0.27)	0.92 (0.24)	NS	0.93 (0.26)	0.93 (0.24)	NS	
Occipital lobe WM FA	0.17 (0.08)	0.17 (0.08)	NS	0.17 (0.08)	0.17 (0.08)	NS	0.17 (0.08)	0.17 (0.08)	NS	

MD values are expressed as 10^{-3}

[a] Abnormal glucose metabolism is defined as impaired fasting glucose, impaired glucose intolerance, or diabetes mellitus

risk of hyperinsulinemia, impaired fasting glucose, impaired glucose tolerance, and ultimately diabetes mellitus (Brown et al. 2005; Justman et al. 2003; Tien et al. 2008). Our DTI findings suggesting altered tissue integrity are supported by studies that have demonstrated insulin resistance and diabetes mellitus to be associated with cognitive dysfunction in HIV-infected individuals (Valcour et al. 2005, 2006, 2012).

Our study may have been underpowered to detect significant correlations between DTI parameters and other cerebrovascular risk factors, such as hypertension and hyperlipidemia. Furthermore, our study did not have a HIV-seronegative control group. Nevertheless, although our sample size was relatively small and we cannot exclude a spurious finding associated with post hoc analysis, significant differences were found in the caudate and hippocampus on DTI in our cohort of older HIV-infected subjects with abnormal glucose metabolism. This may illustrate the sensitivity of DTI to detect potential influences of abnormal glucose metabolism on brain microstructure. In summary, DTI can detect microstructural changes associated with abnormal glucose metabolism in the caudate and hippocampus of HIV-infected individuals, but

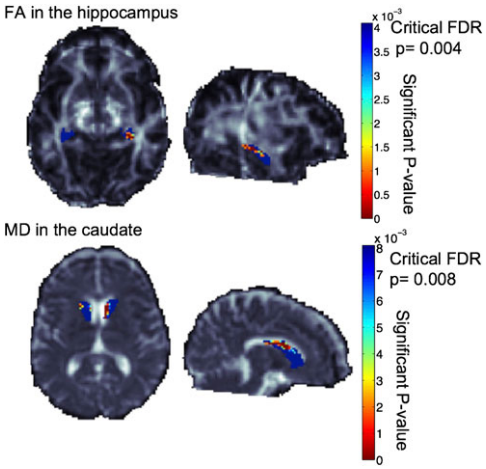

Fig. 1 *Top panel* shows the hippocampal segmentation over the FA image. Voxelwise associations of FA within the hippocampus revealed a significant association with impaired glucose intolerance/diabetes mellitus. *Bottom panel* shows the caudate segmentation over the MD image. Voxelwise associations of MD within the caudate revealed a significant association with impaired glucose intolerance/diabetes mellitus. More significant voxels are colored *reddish yellow*. Voxels that did not pass the false discovery rate (*FDR*) correction for multiple tests are colored *blue*. The FDR critical *p* values are 0.004 and 0.008, respectively. Note that the higher the FDR critical *p* values (i.e., the closer to 0.05), the greater the association. Images are shown in radiological convention, and the sagittal images are of the left hemisphere. *FA* fractional anisotropy, *FDR* false discovery rate, *MD* mean diffusivity

further studies are warranted to determine if this finding is reproducible.

Acknowledgments BKN, KJK, DCC, and CMS are funded in part by research grants P20RR011091, U54NS43049, and U54RR026136. NJ and PT are funded in part by R01 EB008432 and EB 007813, and R01 AG040060 and a UCLA Medical Informatics Fellowship (NJ).

References

American Diabetes Association (2009) Standards of medical care in diabetes—2009. Diabetes Care 32(Suppl 1):S13–S61

American Psychiatric Association (2000) Diagnostic and statistical manual of mental disorders, 4th edn. American Psychiatric Association, Washington, DC

Assaf Y, Pasternak O (2008) Diffusion tensor imaging (DTI)-based white matter mapping in brain research: a review. J Mol Neurosci 34:51–61

Basser PJ, Mattiello J, LeBihan D (1994a) MR diffusion tensor spectroscopy and imaging. Biophys J 66:259–267

Basser PJ, Mattiello J, LeBihan D (1994b) Estimation of the effective self-diffusion tensor from the NMR spin echo. J Magn Reson 103:247–254

Beck AT, Ward CH, Mendelson M, Mock J, Erbaugh J (1961) An inventory for measuring depression. Arch Gen Psychiatry 4:561–571

Becker JT, Kingsley L, Mullen J et al (2009) Vascular risk factors, HIV serostatus, and cognitive dysfunction in gay and bisexual men. Neurology 73:1292–1299

Becker JT, Maruca V, Kingsley LA et al (2011a) Factors affecting brain structure in men with HIV disease in the post-HAART era. Neuroradiology 54:113–121

Becker JT, Sanders J, Madsen SK et al (2011b) Subcortical brain atrophy persists even in HAART-regulated HIV disease. Brain Imag Behav 5:77–85

Benjamini Y, Hochberg Y (1995) Controlling the false discovery rate: a practical and powerful approach to multiple testing. J R Biostatis Soc 57:289–300

Brown TT, Cole SR, Li X et al (2005) Antiretroviral therapy and the prevalence and incidence of diabetes mellitus in the multicenter AIDS cohort study. Arch Intern Med 165:1179–1184

Brown TT, Xu X, John M et al (2009) Fat distribution and longitudinal anthropometric changes in HIV-infected men with and without clinical evidence of lipodystrophy and HIV-uninfected controls: a substudy of the Multicenter AIDS Cohort Study. AIDS Res Ther 6:8

Chang L, Wong V, Nakama H et al (2008) Greater than age-related changes in brain diffusion of HIV patients after 1 year. J Neuroimmune Pharmacol 3:265–274

Chen Y, An H, Zhu H et al (2009) White matter abnormalities revealed by diffusion tensor imaging in non-demented and demented HIV+ patients. NeuroImage 47:1154–1162

Expert Panel on Detection, Evaluation, and Treatment of High Blood Cholesterol in Adults (2001) Executive summary of The Third Report of The National Cholesterol Education Program (NCEP) Expert Panel on Detection, Evaluation, And Treatment of High Blood Cholesterol In Adults (Adult Treatment Panel III). JAMA 285:2486–2497

Expert Panel on Detection, Evaluation, and Treatment of High Blood Cholesterol in Adults (2002) Third Report of the National Cholesterol Education Program (NCEP) Expert Panel on Detection, Evaluation, and Treatment of High Blood Cholesterol in Adults (Adult Treatment Panel III) final report. Circulation 106:3143–3421

Filippi CG, Ulug AM, Ryan E, Ferrando SJ, van Gorp W (2001) Diffusion tensor imaging of patients with HIV and normal-appearing white matter on MR images of the brain. Ajnr 22:277–283

Gongvatana A, Schweinsburg BC, Taylor MJ et al (2009) White matter tract injury and cognitive impairment in human immunodeficiency virus-infected individuals. J Neurovirol 15:187–195

Gongvatana A, Cohen RA, Correia S et al (2011) Clinical contributors to cerebral white matter integrity in HIV-infected individuals. J Neurovirol 17:477–486

Gorelick PB, Bowler JV (2010) Advances in vascular cognitive impairment. Stroke; J Cereb Circ 41:e93–e98

Hoare J, Fouche JP, Spottiswoode B et al (2011) White-matter damage in clade C HIV-positive subjects: a diffusion tensor imaging study. J Neuropsychiatry Clin Neurosci 23:308–315

Jellinger KA (2008) Morphologic diagnosis of "vascular dementia"—a critical update. J Neurol Sci 270:1–12

Justman JE, Benning L, Danoff A et al (2003) Protease inhibitor use and the incidence of diabetes mellitus in a large cohort of HIV-infected women. J Acquir Immune Defic Syndr 32:298–302

Kallianpur KJ, Kirk GR, Sailasuta N et al (2011) Regional cortical thinning associated with detectable levels of HIV DNA. Cereb Cortex. doi:10.1093/cercor/bhr285

Kuper M, Rabe K, Esser S et al (2011) Structural gray and white matter changes in patients with HIV. J Neurol 258:1066–1075

Lamport DJ, Lawton CL, Mansfield MW, Dye L (2009) Impairments in glucose tolerance can have a negative impact on cognitive function: a systematic research review. Neurosci Biobehav Rev 33:394–413

Leow A, Huang SC, Geng A et al (2005) Inverse consistent mapping in 3D deformable image registration: its construction and statistical properties. Inf Process Med Imaging 19:493–503

McMurtray A, Kwee S, Grace T, Shikuma C (2008) Changes in cerebral glucose metabolism associated with the presence of the apolipoprotein E4 allele in older HIV seropositive individuals. In: 11th RCMI International Symposium on Health Disparities, 2008, Honolulu, Hawaii

Nakamoto BK, Jahanshad N, Kallianpur K, Shikuma C, Valcour VG, Thompson PM (2010) Impact of ApoE and cerebrovascular risk factors on brain structure and cognition in HIV in the HAART era. In: CROI, 2010 February 16–19, San Francisco, CA

Nakamoto BK, Valcour VG, Kallianpur K et al (2011) Impact of cerebrovascular disease on cognitive function in HIV-infected patients. J Acquir Immune Defic Syndr 57:e66–e68

Navia BA, Cho ES, Petito CK, Price RW (1986) The AIDS dementia complex: II. Neuropathology. Ann Neurol 19:525–535

Ovbiagele B, Nath A (2011) Increasing incidence of ischemic stroke in patients with HIV infection. Neurology 76:444–450

Pfefferbaum A, Rosenbloom MJ, Adalsteinsson E, Sullivan EV (2007) Diffusion tensor imaging with quantitative fibre tracking in HIV infection and alcoholism comorbidity: synergistic white matter damage. Brain 130:48–64

Pfefferbaum A, Rosenbloom MJ, Rohlfing T, Kemper CA, Deresinski S, Sullivan EV (2009) Frontostriatal fiber bundle compromise in HIV infection without dementia. AIDS (London, England) 23:1977–1985

Ragin AB, Wu Y, Storey P, Cohen BA, Edelman RR, Epstein LG (2005) Diffusion tensor imaging of subcortical brain injury in patients infected with human immunodeficiency virus. J Neurovirol 11:292–298

S Roriz-Filho J, Sa-Roriz TM, Rosset I et al (2009) (Pre)diabetes, brain aging, and cognition. Biochim Biophys Acta 1792:432–443

Schmitt FA, Bigley JW, McKinnis R, Logue PE, Evans RW, Drucker JL (1988) Neuropsychological outcome of zidovudine (AZT)

treatment of patients with AIDS and AIDS-related complex. N Engl J Med 319:1573–1578

Shiramizu B, Paul R, Williams A et al (2007) HIV proviral DNA associated with decreased neuropsychological function. J Neuropsychiatry Clin Neurosci 19:157–163

Strauss E, Sherman EMS, Spreen O (2006) A compendium of neuropsychological tests: administration, norms, and commentary, 3rd edn. Oxford University Press, New York

Thames AD, Foley JM, Panos SE et al (2011) Past stimulant abuse is associated with reduced basal ganglia and hippocampal integrity in older HIV+ adults. A Diffusion Tensor Imaging Study 2:129–134

Tien PC, Schneider MF, Cole SR et al (2008) Antiretroviral therapy exposure and insulin resistance in the Women's Interagency HIV study. J Acquir Immune Defic Syndr 49:369–376

U.S. Preventive Services Task Force (2007) Screening for high blood pressure: U.S. Preventive Services Task Force reaffirmation recommendation statement. Ann Intern Med 147:783–786

Valcour VG, Shikuma CM, Shiramizu BT et al (2005) Diabetes, insulin resistance, and dementia among HIV-1-infected patients. J Acquir Immune Defic Syndr 38:31–36

Valcour VG, Sacktor NC, Paul RH et al (2006) Insulin resistance is associated with cognition among HIV-1-infected patients: the Hawaii Aging With HIV cohort. J Acquir Immune Defic Syndr 43:405–410

Valcour V, Maki P, Bacchetti P et al (2012) Insulin resistance and cognition among HIV-infected and HIV-uninfected adult women: The Women's Interagency HIV Study. AIDS Res Hum Retroviruses 28(5):447–53

Wright EJ, Grund B, Robertson K et al (2010) Cardiovascular risk factors associated with lower baseline cognitive performance in HIV-positive persons. Neurology 75:864–873

CHAPTER 6

Human brain connectivity

6.1 Mapping sex differences

The following section is adapted from:

Jahanshad N, Aganj I, Lenglet C, Jin Y, Joshi A, Barysheva M, McMahon KL, de Zubicaray GI, Martin NG, Wright MJ, Toga AW, Sapiro G, Thompson PM (2011). High angular resolution diffusion imaging (HARDI) tractography in 234 young adults reveals greater frontal lobe connectivity in women, International Symposium of Biomedical Imaging (ISBI) 2011.

SEX DIFFERENCES IN THE HUMAN CONNECTOME: 4-TESLA HIGH ANGULAR RESOLUTION DIFFUSION IMAGING (HARDI) TRACTOGRAPHY IN 234 YOUNG ADULT TWINS

Neda Jahanshad[1], Iman Aganj[2], Christophe Lenglet[3,2], Anand Joshi[1], Yan Jin[1], Marina Barysheva[1], Katie L. McMahon[4], Greig I. de Zubicaray[5], Nicholas G. Martin[6], Margaret J. Wright[5,6], Arthur W. Toga[1], Guillermo Sapiro[2], Paul M. Thompson[1]

[1]Laboratory of Neuro Imaging, Department of Neurology, UCLA School of Medicine, Los Angeles, CA
[2]Department of Electrical and Computer Engineering, University of Minnesota, Minneapolis, MN
[3]Center for Magnetic Resonance Research, University of Minnesota Medical School, Minneapolis, MN
[4]University of Queensland, Centre for Advanced Imaging, Brisbane, Australia
[5]University of Queensland, School of Psychology, Brisbane, Australia
[6]Queensland Institute of Medical Research, Brisbane, Australia

ABSTRACT

Cortical connectivity is associated with cognitive and behavioral traits that are thought to vary between sexes. Using high-angular resolution diffusion imaging at 4 Tesla, we scanned 234 young adult twins and siblings (mean age: 23.4 ± 2.0 SD years) with 94 diffusion-encoding directions. We applied a novel Hough transform method to extract fiber tracts throughout the entire brain, based on fields of constant solid angle orientation distribution functions (ODFs). Cortical surfaces were generated from each subject's 3D T1-weighted structural MRI scan, and tracts were aligned to the anatomy. Network analysis revealed the proportions of fibers interconnecting 5 key subregions of the frontal cortex, including connections between hemispheres. We found significant sex differences (147 women/87 men) in the proportions of fibers connecting contralateral superior frontal cortices. Interhemispheric connectivity was greater in women, in line with long-standing theories of hemispheric specialization. These findings may be relevant for ongoing studies of the human connectome.

Index Terms— tractography, high angular resolution diffusion imaging (HARDI), network analysis, inter-hemispheric connectivity, human connectome

1. INTRODUCTION

The organization of white matter fiber pathways connecting the two cerebral hemispheres is of great interest when studying normal development as well as neurological and psychiatric disorders such as Alzheimer's disease [1] and schizophrenia [2].

Differences in cortical connectivity between men and women may also contribute to reported sex differences in traits such as linguistic processing [3] and general cognition [4]. Both of these measures have been associated with connectivity metrics in women but not in men [3,4]. Tractography studies based on diffusion tensor imaging have also been applied to subdivide the inter-hemispheric fibers of the corpus callosum into functionally organized sectors or tracts, based on the cortical regions that the fibers interconnect [5]. Chao et al. [6] used high angular resolution diffusion imaging (HARDI) to derive tracts, and studied interhemispheric connections passing through the corpus callosum to parcellate its structure.

In a small sample of 5 subjects, Hagmann et al. [7] showed network connectivity maps for fibers connecting cortical regions within and across hemispheres using high-resolution tractography based on diffusion spectrum imaging (DSI). In their study, the majority of connections were found to be between regions within rather than across hemispheres.

Here we used a novel HARDI tractography algorithm based on the Hough transform [8] to extract tracts throughout the entire brain. In a large cohort of 234 young healthy subjects scanned with HARDI, we seeded voxels with a probability proportional to the fractional anisotropy (FA) measured at each voxel, derived (for simplicity) from the single-tensor model of diffusion. We then examined the interhemispheric connection matrix, and its statistical variation in 36 monozygotic (MZ) and 28 same-sex dizygotic (DZ) twin pairs. We set out to discover genetic influences and any sex differences in the population of connectivity matrices.

The human frontal lobes mediate or influence a broad variety of behaviors. These include executive function, working memory, problem solving, judgment, motor planning, speech production, impulse control, and some aspects of social behavior. The frontal lobe is also heavily interconnected. Many voxels contain white matter fiber mixings and crossings. These fiber crossings may not be correctly captured by tractography methods based on the single-tensor diffusion model, so higher order modeling of the diffusion propagator with HARDI becomes advantageous. Using the entire set of 234 subjects, we examined sex differences in the extent of interhemispheric fiber connectivity between cortical regions in the frontal lobes. As aberrant connectivity is implicated in various brain disorders, sex differences in connectivity may also be important to recognize, in ongoing projects to map the human connectome.

2. METHODS

2.1. Subject Demographics and Image Acquisition

As part of a large-scale imaging genetics initiative focusing on twins [9], we scanned 234 young adults (147 women/87 men; mean age: 23.4 ± 2.0 SD years) with 4T HARDI and standard T1-weighted structural MRI. To examine genetic and environmental influences on brain connectivity, the participants were all twin subjects and their siblings from 131 families. All MR images were collected using a 4 Tesla Bruker Medspec MRI scanner (Bruker Medical, Ettingen, Germany), with a transverse electromagnetic (TEM) headcoil, at the Center for Magnetic Resonance (University of Queensland, Australia). T1-weighted images were acquired with

978-1-4244-4128-0/11/$25.00 ©2011 IEEE

an inversion recovery rapid gradient echo sequence (TI/TR/TE = 700/1500/3.35 ms; flip angle=8°; slice thickness = 0.9 mm, with a 256^3 acquisition matrix). Diffusion-weighted images were acquired using single-shot echo planar imaging with a twice-refocused spin echo sequence to reduce eddy-current induced distortions. Imaging parameters were: TR/TE 6090/91.7 ms, 23 cm FOV, with a 128×128 acquisition matrix. Each 3D volume consisted of 55 2-mm thick axial slices with no gap, and a 1.79×1.79 mm^2 in-plane resolution. We acquired 105 images per subject: 11 with no diffusion sensitization (i.e., T2-weighted b_0 images) and 94 diffusion-weighted (DW) images (b = 1159 s/mm^2) with gradient directions evenly distributed on the hemisphere, as is required for unbiased directional sampling of the diffusion propagator. Scan time was 14.2 minutes.

2.2. DWI preprocessing, cortical surface extractions and registrations

Non-brain regions were automatically removed from each T1-weighted MRI scan, and from a T2-weighted image from the DWI set using the FSL tool "BET" (http://fsl.fmrib.ox.ac.uk/fsl/). A trained neuroanatomical expert manually edited the T1-weighted scans to further refine the brain extraction. All T1-weighted images were linearly aligned using FSL (with 9 DOF) to a common space [10] with 1mm isotropic voxels and a 220×220×220 voxel matrix. Raw diffusion-weighted images were corrected for eddy current distortions using the FSL tool, "eddy_correct" (http://fsl.fmrib.ox.ac.uk/fsl/). For each subject, the 11 eddy-corrected images with no diffusion sensitization were averaged, linearly aligned and resampled to a downsampled version of their corresponding T1 image (110×110×110, 2×2×2mm). Averaged b_0 maps were elastically registered to the structural scan using a mutual information cost function [11] to compensate for EPI-induced susceptibility artifacts.

Table 1: List of the cortical labels extracted from FreeSurfer [11]; label 1 was reserved for non-cortical surfaces.

1	Banks of the superior temporal sulcus	19	*Pars orbitalis*
2	Caudal anterior cingulate	20	*Pars triangularis*
3	Caudal middle frontal	21	Peri-calcarine
4	Corpus callosum	22	Postcentral
5	Cuneus	23	Posterior cingulate
6	Entorhinal	24	Pre-central
7	Fusiform	25	Precuneus
8	Inferior parietal	26	Rostral anterior cingulate
9	Inferior temporal	27	Rostral middle frontal
10	Isthmus of the cingulate	28	Superior frontal
11	Lateral occipital	29	Superior parietal
12	Lateral orbitofrontal	30	Superior temporal
13	Lingual	31	Supra-marginal
14	Medial orbitofrontal	32	Frontal pole
15	Middle temporal	33	Temporal pole
16	Parahippocampal	34	Transverse temporal
17	Paracentral	35	Insula
18	*Pars opercularis*		

35 cortical labels per hemisphere (**Table 1**) were automatically extracted from all aligned T1-weighted structural MRI scans using FreeSurfer (http://surfer.nmr.mgh.harvard.edu/) [12]. As a linear registration is performed within the software, the resulting T1-weighted images and cortical models were aligned to the original T1 input image space and down-sampled using nearest neighbor interpolation (to avoid intermixing of labels) to the space of the DWIs. To ensure tracts would intersect cortical labeled boundaries, labels were dilated with an isotropic box kernel of 5 voxels.

2.3. HARDI tractography

The transformation matrix from the linear alignment of the mean b_0 image to the T1-weighted volume was applied to each of the 94 gradient directions to properly re-orient the orientation distribution functions (ODFs). At each HARDI voxel, ODFs were computed using the normalized and dimensionless ODF estimator, derived for QBI in [13]. Contrary to prior methods, this approach considers the Jacobian factor r^2 to compute the constant solid angle (CSA) ODF:

$$\underset{\text{in CSA-QBI}}{ODF}(\hat{u}) \approx \frac{1}{4\pi} + \frac{1}{16\pi^2}\,\mathrm{FRT}\left\{\nabla_b^2 \ln\left(-\ln\frac{S(\hat{u})}{S_0}\right)\right\}$$

Here $S(\hat{u})$ is the diffusion signal, and S_0 is the baseline image. FRT is the Funk-Radon transform and ∇_b^2 is the Laplace-Beltrami operator. We used this ODF reconstruction scheme as it is mathematically more accurate and also outperforms the original QBI definition [14], e.g., it improves the resolution of multiple fiber orientations [13]. With this set of ODFs, we performed HARDI tractography on the linearly aligned sets of DWI volumes.

Tractography was performed by probabilistically seeding voxels with a prior probability based on the fractional anisotropy (FA) value derived from the single-tensor model [15]. All curves passing through a seed point receive a score estimating the probability of the existence of the fiber, computed from the ODFs. We used a voting process provided by the Hough transform to determine the best fitting curves through each point. Further details of the method may be found in [8].

Elastic deformations obtained from the EPI distortion correction, mapping the average b_0 image to the T1-weighted image, were then applied to the tract's 3D coordinates. As this was a study of inter-hemispheric connectivity, tracts with fewer than 15 points were filtered out. Each subject's dataset contained 2000-4000 useable fibers (3D curves).

2.4. *N*x*N* frontal lobe connectivity analysis

For each subject, a full 70×70 connectivity matrix was created. Each element described the estimated proportion of the total number of fibers, in that subject, connecting each of the labels in one hemisphere to those in the other hemisphere. If more than 5% of subjects had no fibers connecting the regions, then the connection was considered invalid and was not included in the analysis.

To further focus our analyses, 5 cortical regions of interest (ROIs) were selected from the frontal lobes in each hemisphere. These regions included: (1) the caudal middle frontal, (2) lateral orbito- frontal, (3) rostral anterior cingulate, (4) superior frontal, and (5) insular, cortical surface labels. **Figure 1** shows these 5 ROIs in one representative subject. A 10×10 normalized connectivity matrix was created for each subject. This encodes the proportion of the total number of fibers, in that subject, connecting each of the 5 ROIs in one hemisphere to each other as well as across hemispheres.

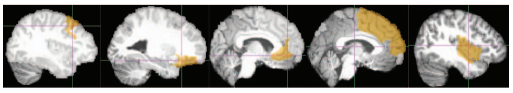

Figure 1: Hemispheric frontal lobe regions of interest included, from left to right: (1) the caudal middle frontal, (2) lateral orbito-frontal, (3) rostral anterior cingulate, (4) superior frontal, and (5) insular, cortical surface labels.

Similarities may arise in the tractography maps as individuals in the same family are related; therefore, we used a random-effects regression analysis to group the subjects by family. A random intercept was included for each family. The analysis was performed covarying for the effect of age. Sex (coded as 1 - male and 2 - female) was regressed on each valid matrix connection.

To obtain an accurate estimate of sex differences in brain connectivity, a nonparametric test was performed using 5,000 random permutations of the sex of each individual and repeating the regression. Constraints were applied to ensure that all monozygotic twin pairs remained of the same sex, in the randomly permuted sex assignments. As such, the permutation test was valid and sensitive to genetic differences other than sex differences. The analysis was implemented using the 'nlme' library, in the R statistical package (version 2.9.2; http://www.r-project.org/) [16].

2.5. Falconer's heritability analysis

Falconer's heritability analysis was performed using a subset of the population— 36 (25F) monozygotic twin pairs, and 28 (19F) same-sex dizygotic twin pairs. The heritability of each valid connection was then determined according to Falconer's heritability estimate [17]: $h^2=2(rMZ - rDZ)$. Here, *rMZ* and *rDZ* denote the intraclass correlation (ICC) coefficients for monozygotic and dizygotic twins; heritability denotes the proportion of the observed variation that is attributable to genetic differences among individuals. To assess the significance of the measures of familial resemblance, the false discovery rate (FDR) was controlled at q=0.05 for p-values corresponding to the observed MZ twin correlations.

3. RESULTS

Figure 2 shows the full map of the dilated cortical surface labels of one subject's left hemisphere overlaid on top of their T1-weighted image. The EPI-corrected map of the fiber density is also directly overlaid to show that the DWI-derived fibers are accurately registered to the structural scan.

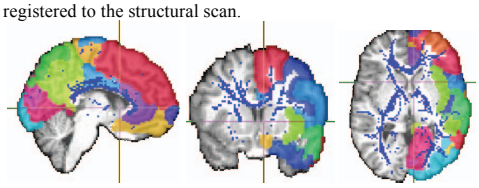

Figure 2: Cortical surface labels from a representative subject's left hemisphere are overlaid on sections from the same subject's 3D T1-weighted image. The EPI-corrected map of the fiber density is also overlaid. This shows that the DWI-derived fibers are accurately registered to the structural scan.

The proportion of fibers that form the full hemispheric cortical connectivity matrix, averaged across all subjects in the study, is plotted in **Figure 3.** In agreement with [7], most connections were found to be within the same hemisphere. 4 valid interhemispheric connections were observed: (1) between the right and left precuneus (2) the right precuneus and the left isthmus of the cingulate, (3) the left precuneus and the right isthmus of the cingulate, and (4) the left and right posterior cingulate. On average, about 15% of the inter-hemispheric fibers connect the left and right precuneus regions of the cortex (region 25). In these estimates, we note a minor bias that fiber selection was weighted toward seed voxels with high FA, but was not biased towards any one region, unless it had higher FA in aggregate.

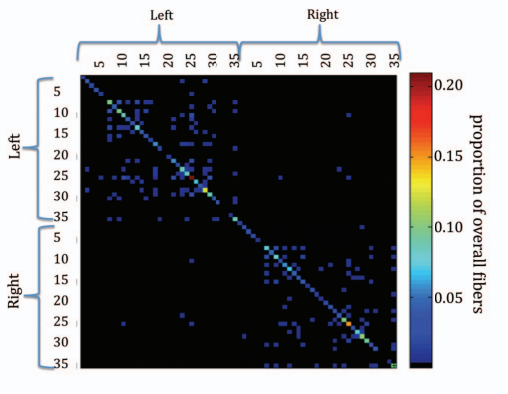

Figure 3: Averaged across all 234 subjects, here we show the proportion of fibers that form the full inter-hemispheric cortical connectivity matrix. In agreement with [7], most connections are within the same hemisphere. On average, about 15% of the fibers traced here interconnect both the left (label number 25) and right (label number 60) precuneus regions of the cortex, and 10% the insula (labels 35 and 70).

After Bonferroni correction for the statistical tests conducted on consistently identified connections within the frontal lobe, significant ($p < 0.0033$) sex differences were found in the inter-hemispheric connectivity of the superior frontal cortices, with women showing higher connectivity than men. Men had a significantly higher proportion of connections within the right lateral orbito-frontal cortex and more fibers interconnecting this region with the ipsilateral insula. Permutation corrected p-values are shown in **Figure 4.**

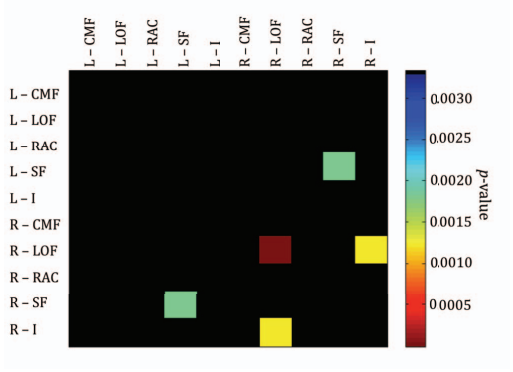

Figure 4: Significant ($p < 0.0033$) sex differences were found in the inter-hemispheric connectivity of the superior frontal cortices, with women showing higher connectivity. Men had a significantly higher proportion of connections within the right lateral orbito-frontal cortex and more fibers interconnecting this region with the ipsilateral insula.

A cumulative distribution plot of the significance of the MZ and DZ correlations is shown in **Figure 5** highlighting the significance in the correlations between the monozygotic pairs as opposed to the dizygotic twins within the valid connections (where at least 95% of all subjects had tracts), providing strong evidence for heritability. Falconer's heritability estimates are displayed for these consistently found connections, in **Figure 6**. The most heritable fiber counts were those in the left precuneus, fibers connecting the cortical regions of the left peri-calcarine and fusiform gyri, and those of the left cuneus and precuneus, also showed moderate heritability (10-12%). When the analysis was limited to only female twin pairs, very high heritability (73%) was found for the fibers interconnecting the left insula with the left superior temporal regions. No other connections were found to be heritable in the female subpopulation. Analysis restricted to men was not performed due to the limited number of male-only twin pairs in each group (11 MZ pairs, 9 DZ pairs).

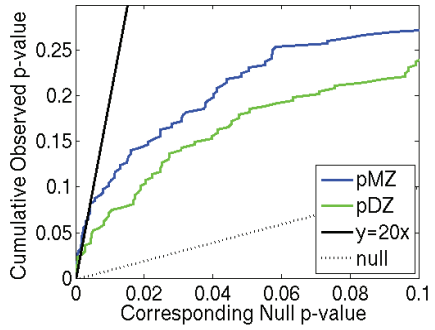

Figure 5: Cumulative distribution plots of the intraclass correlation probabilities within each group of twins. As expected for genetically influenced traits, correlation effects are greater for monozygotic twins than dizygotic twins. This suggests the presence of genetic influences on cortical connectivity that can be further analyzed by modeling heritability.

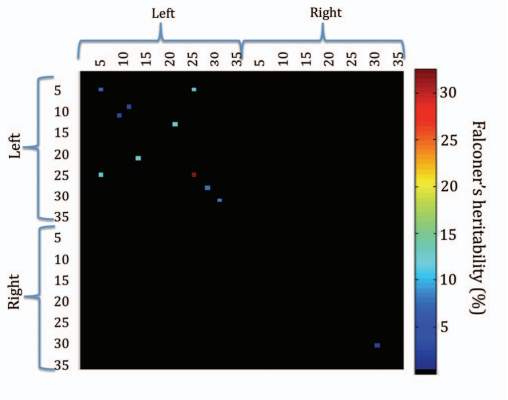

Figure 6: The heritability matrix is shown. Color values in the cells show the heritability coefficient for each valid (consistently found) connection. The heritability matrix shows regions of significant heritability in the left hemisphere, with highest levels (~32%) for the fiber counts of the left precuneus. Fibers connecting cortical regions of the left peri-calcarine and fusiform gyri, and those of the left cuneus and precuneus, also showed moderate heritability (10-12%).

4. DISCUSSION

In this study, we used 94-direction high-angular resolution images (HARDI) in 234 individuals at 4 Tesla, to trace fiber tracts throughout the entire brain. We used a novel orientation distribution function (ODF) based tractography method to account for crossing fibers, allowing valid pursuit of the diffusion propagator where fibers mix or cross. Cortical labels were extracted automatically from co-registered surface models, and the proportion of interhemispheric connections was further studied, using statistical analysis of the connectivity matrices.

In our heritability analysis for cortical fiber connectivity, we observed moderate (33%) levels of heritability for the fiber proportions innervating the left precuneus in the full group. However, when the analysis was limited to only female twin pairs, high heritability (73%) was found in the fibers interconnecting the left insula with the left superior temporal regions. When larger samples are available, we will be able to assess interactions between sex and heritability, and model environmental sources of variance using structural equation models.

The frontal lobe has a high proportion of voxels containing white matter fibers that mix or cross. This leads to fiber incoherence and partial volume effects in the large voxels typical of diffusion-weighted images. Tracts in these regions are challenging to trace accurately using the standard single-tensor model. The principal direction of the tensor can be misleading when fibers mix or cross in the same voxel, so here we used a full ODF model of the HARDI signal, to better capture fiber trajectories. The use of higher magnetic fields with smaller voxel sizes might lead to further improvements.

The human frontal lobe is critical for mediating executive function, self-control, and speech. As there is also some evidence for sex-dependent functioning, we examined sex differences in the intra- and inter-hemispheric circuitry of 5 key frontal lobe cortical regions using ODF-based whole-brain HARDI tractography. In line with some theories of hemispheric specialization and sex differences [18-20], we were able to find significant sex differences in the white matter fiber counts. Women had a greater proportion of connections between left and right superior frontal cortices. They also had fewer fibers overall within the right lateral orbito-frontal region. We previously found sex differences in the geometric complexity of these cortical regions, using fractal dimension analysis, in a separate cohort [21].

In this study, we did not normalize the fiber counts to account for differences in the sizes of the cortical regions within the brain and across subjects. It is at least logically possible that a greater proportion of fibers will be present in subjects with larger brains than others. Brains may also scale allometrically, e.g., according to a logarithmic power law. An overall larger brain does not necessarily mean that the size of each cortical region is proportionately scaled up by the same multiplicative factor. The dependency of connectivity on brain size may be a topic of future investigation.

This pilot connectivity study is limited by the relatively small number of tracts traced in these subjects, but the sample size is still very large for a 4T HARDI study (N=234). While these tracts were probabilistically seeded in regions of high anisotropy, ensuring a high probability of finding the major tracts, future studies including more tracts will allow conclusions to be made regarding connectivity in regions that were discarded in this analysis due to lack of sufficient fibers across the entire population.

REFERENCES

[1] M. Thomason and P. Thompson, "Diffusion Imaging, White Matter and Psychopathology," *Annual Review of Clinical Psychology*. in press, Oct. 2010.
[2] M. Kubicki, *et al.*, "Reduced interhemispheric connectivity in schizophrenia-tractography based segmentation of the corpus callosum," *Schizophr Res,* vol. 106, pp. 125-31, Dec 2008.
[3] T. Bitan, *et al.*, "Bidirectional connectivity between hemispheres occurs at multiple levels in language processing but depends on sex," *J Neurosci,* vol. 30, pp. 11576-85, Sep 1 2010.
[4] C. Davatzikos and S. M. Resnick, "Sex differences in anatomic measures of interhemispheric connectivity: correlations with cognition in women but not men," *Cereb Cortex,* vol. 8, pp. 635-40, Oct-Nov 1998.
[5] H. J. Park, *et al.*, "Corpus callosal connection mapping using cortical gray matter parcellation and DT-MRI," *Hum Brain Mapp,* vol. 29, pp. 503-16, May 2008.
[6] Y. P. Chao, *et al.*, "Probabilistic topography of human corpus callosum using cytoarchitectural parcellation and high angular resolution diffusion imaging tractography," *Hum Brain Mapp,* vol. 30, pp. 3172-87, Oct 2009.
[7] P. Hagmann, *et al.*, "Mapping the structural core of human cerebral cortex," *PLoS Biol,* vol. 6, p. e159, Jul 1 2008.
[8] I. Aganj, *et al.*, "A Hough transform global probabilistic approach to multiple-subject diffusion MRI tractography," Medical Image Analysis, *in press* 2011.
[9] G. I. de Zubicaray, *et al.*, "Meeting the Challenges of Neuroimaging Genetics," *Brain Imaging Behav,* vol. 2, pp. 258-263, Dec 1 2008.
[10] C. J. Holmes, *et al.*, "Enhancement of MR images using registration for signal averaging," *J Comput Assist Tomogr,* vol. 22, pp. 324-33, Mar-Apr 1998.
[11] A. Leow, *et al.*, "Inverse consistent mapping in 3D deformable image registration: its construction and statistical properties," *Inf Process Med Imaging,* vol. 19, pp. 493-503, 2005.
[12] B. Fischl, *et al.*, "Automatically parcellating the human cerebral cortex," *Cereb Cortex,* vol. 14, pp. 11-22, Jan 2004.
[13] I. Aganj, *et al.*, "Reconstruction of the orientation distribution function in single- and multiple-shell q-ball imaging within constant solid angle," *Magn Reson Med,* vol. 64, pp. 554-66, Aug 2010.
[14] D. S. Tuch, "Q-ball imaging," *Magn Reson Med,* vol. 52, pp. 1358-72, Dec 2004.
[15] P. J. Basser and C. Pierpaoli, "Microstructural and physiological features of tissues elucidated by quantitative-diffusion-tensor MRI," *J Magn Reson B,* vol. 111, pp. 209-19, Jun 1996.
[16] J. C. Pinheiro and D. M. Bates, *Mixed-effects models in S and S-PLUS*. New York: Springer, 2000.
[17] A. M. O. Veale, "Introduction to Quantitative Genetics - Falconer,Ds," *The Royal Statistical Society Series C-Applied Statistics,* vol. 9, pp. 202-203, 1960.
[18] J. B. Hellige, "Hemispheric asymmetry," *Annu Rev Psychol,* vol. 41, pp. 55-80, 1990.
[19] N. Geschwind and A. M. Galaburda, "Cerebral lateralization. Biological mechanisms, associations, and pathology: I. A hypothesis and a program for research," *Arch Neurol,* vol. 42, pp. 428-59, May 1985.
[20] D. Kimura, *Sex and cognition*. Cambridge, Mass.: MIT Press, 1999.
[21] E. Luders, *et al.*, "Gender differences in cortical complexity," *Nat Neurosci,* vol. 7, pp. 799-800, Aug 2004.

ACKNOWLEDGMENTS

This work was supported by NIH grant R01 HD050735 and the National Health and Medical Research Council, Australia, grant NHMRC 496682. Additional support was provided by grants R01 EB008281, P41 RR013642, P41 RR008079, P30 NS057091, R01 EB008432, the University of Minnesota Institute for Translational Neuroscience and NLM T15 LM07356.

6.2 Genetics of the connectome

The following section is adapted from:

Jahanshad N, Hibar DP, Ryles A, McMahon KL, de Zubicaray GI, Martin NG, Wright MJ, Toga AW, and Thompson PM (2012). Discovery of genes that affect the human brain connectivity: A genome-wide analysis of the connectome. International Symposium of Biomedical Imaging (ISBI) Barcelona, Spain, May 2-5 2012.

DISCOVERY OF GENES THAT AFFECT HUMAN BRAIN CONNECTIVITY: A GENOME-WIDE ANALYSIS OF THE CONNECTOME

Neda Jahanshad[1], Derrek P. Hibar[1], April Ryles[1], Arthur W. Toga[1], Katie L. McMahon[2], Greig I. de Zubicaray[3], Narelle K. Hansell[4], Grant W. Montgomery[4], Nicholas G. Martin[4], Margaret J. Wright[4], and Paul M. Thompson[1]

[1]Laboratory of Neuro Imaging, Department of Neurology, UCLA School of Medicine, Los Angeles, CA
[2]University of Queensland, Centre for Advanced Imaging, Brisbane, Australia
[3]University of Queensland, School of Psychology, Brisbane, Australia
[4]Queensland Institute of Medical Research, Brisbane, Australia

ABSTRACT

Human brain connectivity is disrupted in a wide range of disorders – from Alzheimer's disease to autism – but little is known about which specific genes affect it. Here we conducted a genome-wide association for connectivity matrices that capture information on the density of fiber connections between 70 brain regions. We scanned a large twin cohort (N=366) with 4-Tesla high angular resolution diffusion imaging (105-gradient HARDI). Using whole brain HARDI tractography, we extracted a relatively sparse 70x70 matrix representing fiber density between all pairs of cortical regions automatically labeled in co-registered anatomical scans. Additive genetic factors accounted for 1-58% of the variance in connectivity between 90 (of 122) tested nodes. We discovered genome-wide significant associations between variants and connectivity. GWAS permutations at various levels of heritability, and split-sample replication, validated our genetic findings. The resulting genes may offer new leads for mechanisms influencing aberrant connectivity and neurodegeneration.

Index Terms— genetics, high angular resolution diffusion imaging (HARDI), cortical surfaces, twin modeling, human connectome

1. INTRODUCTION

The human brain is a complex network of structural and functional interconnections, with diverse regions activated during functional tasks. Advanced diffusion imaging methods, which track the diffuson of water along the brain's axons, can reveal dense microstructural fiber bundles connecting anatomically distinct cortical and subcortical regions. Such connections are remodeled throughout development [1] and deteriorate in diseases such as Alzheimer's disease [2]. While initial investigations have examined the degree of genetic involvement in functional connectivity, genetic contributions to the brain's structural connectivity, i.e. the proportions and densities of axonal fibers connecting cortical subregions, have yet to be explored.

The degree of genetic influence on a particular trait can be determined by studying twins. Twin studies have long been used to determine the heritability (proportion of variance explainable by genetic variation) of human traits. Some studies have begun to estimate the heritability of DTI-derived measures of fiber integrity and its asymmetry as well as other neuroimaging measures [3-6]. Proportions of variance due to genes versus environment can be inferred by fitting structural equation models (SEMs) to data from different types of twins--monozygotic (MZ) twins share all their genes while dizygotic (DZ) twins share, on average, half.

In a large family cohort comprised of 366 individuals from 223 families, we used high angular resolution diffusion imaging (HARDI) at high magnetic field (4 Tesla) along with anatomical MRI to delineate cortical regions into areas of known structure and functionality [7]. We also mapped out white matter fiber pathways using high angular-resolution HARDI tractography. In this work, we define connectivity as the proportion of total fibers traced in the brain that intersect a specific pair of cortical regions – this may include connections within or between hemispheres. The connectivities of all pairs of regions are compiled into symmetric matrices, in which each matrix element (x,y) is the proportion of fibers connecting brain regions x and y.

To determine the genetic influences contributing to the density of each cortical connection, we fitted a SEM to connectivity matrices extracted from 46 pairs of MZ and 64 pairs of DZ twins. If a connection was significantly influenced by genetic factors, we followed through with a genome-wide association test to identify specific genetic variants associated with the proportion of fiber densities at that connection. The sample was split in half to allow replication of discovered associations in non-overlapping samples.

2. METHODS

2.1. Subjects and Image Acquisition

Subjects included 92 young adult monozygotic (MZ) twins (46 pairs) and 128 dizygotic (DZ) twins (64 pairs) along with 146 non-twin siblings and unpaired twins with caucasian ancestry. In total, images from 366 right-handed young adults (mean age: 23.5 years, SD 2.0) were included, from a 5-year research project examining healthy young adult twins with MRI and DTI [8]. Genomic DNA was analyzed on the Human610-Quad BeadChip (Illumina) according to the manufacturers protocols (Infinium HD Assay; Super Protocol Guide; Rev. A, May 2008).

Anatomical and 105-gradient (11 b_0, 94 direction) high angular resolution diffusion imaging (HARDI) whole-brain MRI scans were acquired on a high magnetic field (4T) Bruker Medspec MRI scanner. T1-weighted images were acquired with an inversion recovery rapid gradient echo sequence. For imaging parameters, please see [4].

2.2. A/C/E Heritability Analysis of Connectivity

NxN structural connectivity matrices were created as in [9] with a pipeline shown in **Fig 1A.** A covariance matrix S_g was obtained for every matrix element in the connection matrix within the pairs for each of the two types of twins (identical or fraternal). A structural equation model (SEM) was then fitted to compare the

978-1-4577-1858-8/12/$26.00 ©2012 IEEE

observed and expected covariances (under different degrees of heritability) to estimate the proportion of the variance attributable to additive genetic (A), shared environmental (C) and unique environmental (E) components of variance [10]: $Z = Aa + Cc + Ee$. *Z* can be any quantitative phenotypic trait, in this case the fiber count proportion at a particular matrix element. *A*, *C*, and *E* are latent (unobserved) variables and *a*, *c*, *e* are each parameter's weights determined by optimizing *S* via full information maximum likelihood estimation (FIML). The variance components combine to create the total observed inter-individual variance, and sum to 1: $a^2 + c^2 + e^2 = 1$. This SEM uses FIML: $FIML_g = N_g \left\{ \ln|S_g| - \ln|\Sigma_g| + tr\left(S_g \Sigma_g^{-1}\right) - 2m \right\}$ with a χ^2 null distribution to estimate genetic versus environmental contributions to the observed variance, where *m* is the number of twin pairs per group (49 for MZ and 65 for DZ), S_g is the observed covariance matrix for each twin group *g*, and Σ_g is the expected covariance matrix for group *g,* with α=1 for the MZ group and α=0.5 for DZ, as MZ twins share all their genes while dizygotic (DZ) twins share, on average, half: $\Sigma_g = \begin{bmatrix} a^2 + c^2 + e^2 & \alpha a^2 + c^2 \\ \alpha a^2 + c^2 & a^2 + c^2 + e^2 \end{bmatrix}$

In SEM, the χ^2 goodness of fit measure determines a *p*-value for all specified regions of interest (elements of the matrix) where the test was performed. This value indicates that the model is a good fit to the data if $p>0.05$ (this is the opposite of the usual convention that rejects models or hypotheses). To determine the significance of the the A or C factors, the χ^2 goodness-of-fit values of the model are compared to those for a model excluding that factor (i.e., to a C/E model to determine the significance of the additional A factor; A/E model to determine the significance of C), giving: $p(A) = \chi^{2^{-1}}_{DF}\left[\chi^2(ACE) - \chi^2(CE)\right]$, where $\chi^2_{1DF^{-1}}$ denotes the inverse of the cumulative distribution function for a chi-squared distributed variable with one degree of freedom. *p(C)* is computed analogously. In this case, low *p*-values express significant improvements when adding a factor. This is consistent with the more standard convention for *p*-values, and allows us to assess the resulting uncorrected *p*-value maps using the false discovery rate (FDR) method [11].

OpenMX software [12] was implemented in R (http://www.r-project.org/) for calculating the A/C/E parameters. The covariates sex, age, and total brain volume (TBV) were added to the model, and 95% CIs for the A term were computed.

2.3. Genome-wide associations across the matrix

Genome-wide associations were performed at each of the 90 valid (out of 122) matrix elements (after filtering out connections which are not heritable ($a^2 < 0.01$) or not present in at least 95% of the subjects) using *emmaX* - a mixed model approach - controlling for age, sex, and TBV [13]. Connections with a heritability estimate of < 1% were excluded to limit the search region to connections where we can estimate some degree of genetic interation. EmmaX accounts for the familial relatedness between subjects through the use of a kinship matrix describing the genetic similarities between all pairs of subjects. Analysis was limited to those single nucleotide polymorphisms (SNPs) with a minor allele frequency (MAF) greater than 0.1. 428,287 SNPs were tested.

2.4. Establishing significance thresholds

A significance threshold of $7x10^{-9}$ was established for genome-wide significance for reasons described below. We determined significance levels for association tests by first estimating the total number of independent tests performed. Linkage disequilibrium (LD) leads to correlation among the 428,287 SNPs and when two genotyped SNPs are in high LD, each test is not completely independent. By first estimating the effective number of independent tests we can avoid using an unduly conservative significance criterion. Due to linkage disequilibrium, the effective number (M_{eff}) of SNPs tested [14] was 214,578. The same logic can also be applied to the matrix elements tested. Clearly an off-diagonal element is not independent of the entries in the same row and column. For a matrix element, C(*x*,*y*), representing the total proportions of fibers connecting cortical regions *x* and *y*, this value is not fully independent of matrix elements (*x*,*x*) and (*y*,*y*) corresponding to the total proportions of tracts crossing each cortical region *x* and *y*, respectively. While a total of 90 connections were evaluated, 33 of those connections lie on the diagonal corresponding to different regions on the cortex and might be expected to be independent components (although not necessarily), while off diagonal elements are clearly dependent on two regions. Similarly, a principal components analysis of the 90 matrix elements using information from the twins in the A/C/E model reveals that 29 components are sufficient to explain 95% of the variance in the sample. A Bonferroni correction on the number of independent samples would be 0.05/(33*214,578)= $7.06x10^{-9}$ or 0.05/(29*214,578)= $8.04x10^{-9}$, respectively. We chose the more conservative $7x10^{-9}$ as our threshold for genome-wide significance, which we show is acceptable through extensive permutations to find the null distribution of association statistics. Other GWA-studies of multiple traits have used the false discovery rate (FDR) procedure to find the appropriate correction threshold for one analysis across the genome [15]. For comparison, we performed a similar analysis using FDR on the *p*-values obtained from the 90 traits to obtain a correction threshold of $7.58x10^{-9}$ for the full cohort GWAS.

2.5. Modeling null distributions for GWAS

At each of the 90 accepted nodes in the connectivity matrix, a GWAS was performed for the 220 twins used in the A/C/E structural equation model. To determine any potential differences in the null distributions with respect to the degree of the additive genetic component, GWAS was performed 1000 times on permuted matrices. When conducting these permutations, each subject's covariates (age, sex, and TBV) remained true to its source, while the matrix elements were permuted in a manner that ensured preservation of family structure. Values for MZ twin pairs were only permuted with each other, while the DZ twin pairs were permuted separately. Within each permutation, within-twin pair rearrangements were also allowed to maximize permutations.

2.6. Split-sample GWAS

While all families are participants in the same study, each family is genetically unique, so we were able to split our large sample into two unique subgroups in order to provide a genetically independent sample for replicating the effect of any suggestive genetic variants on brain structural connectivity. A schematic workflow, of the processing and statistical pipeline, is presented in **Fig 1B.** The groups were split according to unique subject identification numbers. All members of the same family were assigned to the

same group. No significant differences were seen between groups with respect to sex ($p = 0.91$) or TBV ($p = 0.06$). As the study was deliberately designed to sample young adults in the narrow age-range 21-30, although mean differences were minimal, there was a significant difference in age as calculated through a two-sided t-test of the populations ($p = 1.2\text{x}10^{-18}$; mean Group 1 = 24.4; mean Group 2 = 22.6).

3. RESULTS

Fig. 2 shows regions for which the A/C/E model was found to fit the data well and $a^2 > 1\%$ as well as CDF plots of describing the significance of ACE, and sub-models with respect to the E model.
Fig 3 shows the null distribution of GWA statistics at 10 connections with increasing levels of heritability. We note in general that when preserving the family structure, as is done in this case, the choice of more highly heritable connections tended to produce permutations with on average lower p-values. Across all 1000 permutations of the 10 connections, 251 SNPs had a p-value falling below the $7\text{x}10^{-9}$ genome-wide significance threshold, which suggests that the expected number of false positives over all 90 regions in the group is on average is 90x0.0251 = 2.26 (where we found 4).
Our GWAS of the connectivity in Group 1 showed a genome-wide significant ($p = 3.23\text{x}10^{-9}$) association within the *SPON1* gene. The contribution of this variant was then assessed in Group 2 at the same node. The association was replicated in the second group to again show significant ($p = 0.0021$) reductions (un-standardized slope of regression, $\beta_{Group1} = -0.0022$, $\beta_{Group2} = -0.0015$) in the white matter fiber density for connections between the left posterior cingulate and the left superior parietal lobe.

For exploratory purposes, we combined the two groups to perform a GWAS at all 90 nodes as before. With 331 genotyped subjects (out of 366 subjects overall with matrices computed), the statistical power for genetic association is greatly increased; however, we are no longer able to provide a sample for replication. 4 SNPs were found to be significant: 3 in *SPON1* and one in *DLGAP2*. A stronger association for the *SPON1* variants is presented in the full group for the same connection, with an additional variant in the *DLGAP2* gene showing significant associations with the proportion of fibers connecting the right superior parietal lobe and the right post-central region of the cortex. Manhattan plots for the 2 nodes where variants reached genome-wide significance are presented in **Fig 5**.

4. DISCUSSION

In this study, we used 94-direction HARDI in 366 individuals at 4 Tesla, to trace fiber tracts throughout the entire brain using an orientation distribution function (ODF) based tractography method [16]. We used automatically extracted cortical labels to compute cortical connectivity matrices based on the proportion of fiber counts. Expanding on a twin design, we conducted the first-ever genetic and genome-wide association analysis of the connectivity matrices.

The nodes where genome-wide significant associations were discovered include the connections between the left superior parietal lobe and the left posterior cingulate (*SPON1*) and those between the right superior parietal lobe and the right post-central cortex (*DLGAP2*). Through our A/C/E analysis, we were able to attribute 7.1% and 38.6% of the observed variance in these two connections, respectively, to additive genetic components. Our previous analysis as demonstrated the reliability of these matrices [17]. Variants found in this study may have particular significance to genetic mechanisms underlying physiological pathways, rather than affecting the global white matter fiber density. Corrections for performing a genome-wide search (and tests across each element of the *NxN* matrix) are also highlighted in this study.

REFERENCES

[1]D. D. Jolles, *et al.*, "A comprehensive study of whole-brain functional connectivity in children and young adults," *Cereb Cortex,* vol. 21, pp. 385-91, Feb 2011.
[2]M. E. Thomason and P. M. Thompson, "Diffusion imaging, white matter, and psychopathology," *Annu Rev Clin Psychol,* vol. 7, pp. 63-85, Apr 2011.
[3]M. C. Chiang, *et al.*, "Genetics of brain fiber architecture and intellectual performance," *J Neurosci,* vol. 29, pp. 2212-24, 2009.
[4]N. Jahanshad, *et al.*, "Genetic influences on brain asymmetry: a DTI study of 374 twins and siblings," *Neuroimage,* vol. 52, pp. 455-69, Aug 15 2010.
[5]P. M. Thompson, *et al.*, "Genetic influences on brain structure," *Nat Neurosci,* vol. 4, pp. 1253-8, Dec 2001.
[6]P. Kochunov, *et al.*, "Genetics of microstructure of cerebral white matter using diffusion tensor imaging," *Neuroimage,* vol. 53, pp. 1109-16, Nov 15 2010.
[7]R. S. Desikan, *et al.*, "An automated labeling system for subdividing the human cerebral cortex on MRI scans into gyral based regions of interest," *Neuroimage,* vol. 31, pp. 968-80, 2006.
[8]G. I. de Zubicaray, *et al.*, "Meeting the Challenges of Neuroimaging Genetics," *Brain Imaging Behav,* vol. 2, pp. 258-263, Dec 1 2008.
[9]N. Jahanshad, *et al.*, "Sex differences in the Human Connectome: 4-Tesla high angular resolution diffusion tensor imaging (HARDI) tractography in 234 young adult twins," presented at the ISBI, Chicago, IL, 2011.
[10]F. V. Rijsdijk and P. C. Sham, "Analytic approaches to twin data using structural equation models," *Brief Bioinform,* vol. 3, pp. 119-33, Jun 2002.
[11]Y. Benjamini and Y. Hochberg, "Controlling the False Discovery Rate - a Practical and Powerful Approach to Multiple Testing," *Journal of the Royal Statistical Society Series B-Methodological,* vol. 57, pp. 289-300, 1995.
[12]S. Boker, *et al.*, "OpenMx: An Open Source Extended Structural Equation Modeling Framework," *Psychometrika,* vol. 76, pp. 306-317, Apr 2011.
[13]H. M. Kang, *et al.*, "Variance component model to account for sample structure in genome-wide association studies," *Nat Genet,* vol. 42, pp. 348-54, Apr 2010.
[14]X. Gao, *et al.*, "Avoiding the high Bonferroni penalty in genome-wide association studies," *Genet Epidemiol,* vol. 34, pp. 100-5, Jan 2010.
[15]C. Sabatti, *et al.*, "Genome-wide association analysis of metabolic traits in a birth cohort from a founder population," *Nat Genet,* vol. 41, pp. 35-46, Jan 2009.
[16]I. Aganj, *et al.*, "A Hough transform global probabilistic approach to multiple-subject diffusion MRI tractography," *Med Image Anal,* vol. 15, pp. 414-25, Aug 2011.
[17]N. Jahanshad, *et al.*, "4-Tesla High Angular Resolution Diffusion Tractography Analysis of the Human Connectome in 234 Subjects: Sex Differences and EPI Distortions Effects," in *ISMRM* Montréal, Canada, 2011.

ACKNOWLEDGMENTS

This work was supported by NIH grant R01 HD050735 and NHMRC (Australia) grant 496682, R01 EB008281, and P41 RR013642, and NLM T15 LM07356.

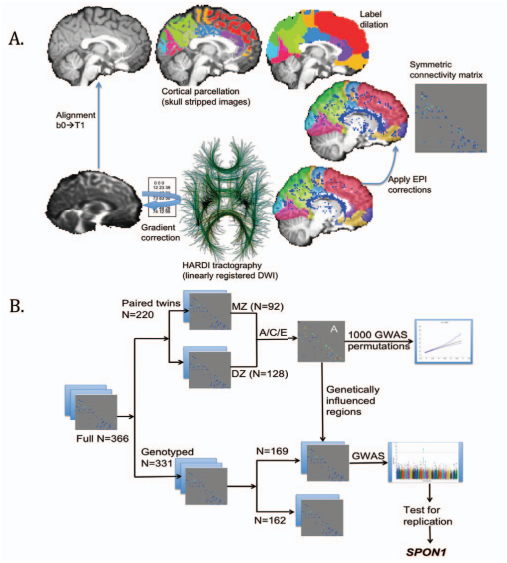

Figure 1- a) NxN connectivity matrix design workflow; b) workflow for genetic association analysis in independent non-overlapping samples (for split-sample replication of genetic hits).

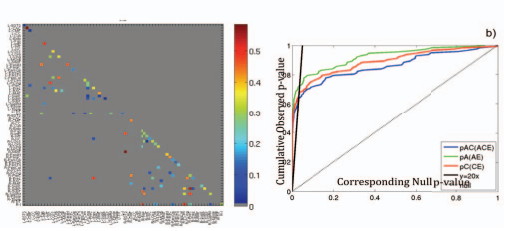

Figure 2- Genetic analysis of a sample of 46 monozygotic twin pairs and 64 dizygotic twin pairs, through the A/C/E structural equation model, breaks down the observed variance in structural neural connectivity into variance components describing the contribution of additive genetic effects (A), shared environmental effects (C), and unique individual variance or measurement error (E). For nodes where the A/C/E model fits the data well, the value of a^2 is shown for each node in *a*). Regions are only displayed if a^2 was higher than 1%. We show through cumulative distribution function (CDF) plots, *b*), that the A/C/E model significantly improves upon the E model (the model derived if we assume the entire brain network is attributable to unique environmental attributes); the A/E and C/E models each fit better than the E model.

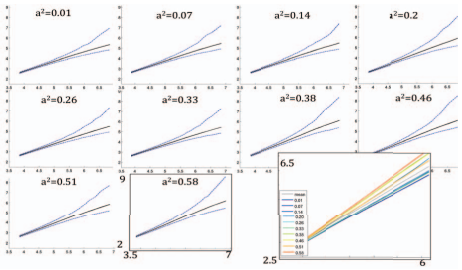

Figure 3 – At connections with increasing levels of heritability, from 1% to 58% (a-j), 1000 GWASs were conducted on permutations of the twin NxN matrices used for the A/C/E heritability analysis. The –log10 of the lowest 1000 p-values of each permutation are plotted against the –log10 expected ordered p-values for the same number of tests. The solid black line represents the mean of the ordered p-values, while the dashed blue lines represent the 0.025 and 0.975 point-wise quantiles of the ordered *p*-values. The mean of the ordered *p*-values of all the 10 plots (solid black line in each), are plotted together in k) against the –log10 expected ordered *p*-values. –log10 *p*-values tend to be higher as heritability of the trait is increased, suggesting the benefits of pre-screening connections for heritability, before running GWAS.

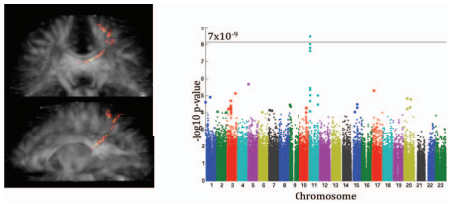

Figure 4 – A genome-wide significant association to connectivity was found in Group 1 ($N_{discovery}$=169) and replicated in an independent sample, Group 2 ($N_{replication}$=162). The association was found for the density of connections between the left posterior cingulate and the left superior parietal lobe, shown in a). The Manhattan plot of the GWAS of this connection is shown in b). The threshold for significance was set to $7x10^{-9}$ (see text for justification).

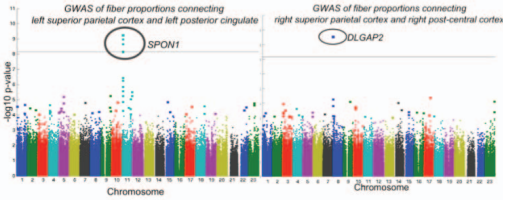

Figure 5 - In the full group (N=331), we conducted a GWAS at every connection, leading to two genetic loci reaching genome-wide significance ($p < 7x10^{-9}$) at two connections. Manhattan plots are shown for the a) connection between the L superior parietal cortex and the L posterior cingulate where variants in *SPON1* were significant, b) connection between the R superior parietal cortex and R post-central cortex, where *DLGAP2* was found to have genome-wide significant associations.

CHAPTER 7

Future works

The work presented in this dissertation lends itself to further studies, with biologically pressing questions that can be explored for answers. In this section, several lines of work drawn from material presented including connectomics, gene-by-environment interactions, and replicating and improving power for genetic studies are described. Most of this work is already in progress.

7.1 Connectivity measures as biomarkers

7.1.1 The connectome as an endophenotype for disease

Brain connectivity is derailed in Alzheimer's disease (AD), autism, and related disorders, making it urgent to screen the human genome for common variants affecting brain networks. Here we adapted genome-wide association scans (GWAS) to screen the anatomical connectivity matrix for genetic effects. We scanned 331 Caucasian twins and siblings with high-field, high-angular resolution diffusion imaging. Parcellations of the cortex and whole-brain tractography were used to compile matrices counting white matter connections between $70x70$ cortical regions. Using a twin design, we screened 500,000 genetic variants at all heritable connections; a statistical threshold corrected for searching over the entire connectome and genome. At this strict threshold, a single intragenic locus at 11p15.2 associated with fiber density in one connection - between the left superior parietal and posterior cingulate cortices. This genes protein product modulates amyloid-beta precursor protein (APP) cleavage, and interacts with receptors for ApoE, the most widely accepted AD genetic risk factor. As such, we mapped our top variant across 738 elderly Caucasians scans from the Alzheimer's Disease

Neuroimaging Initiative to screen for structural variations associated with the variant. Carriers of more major alleles showed enlarged ventricles, excess temporal lobe CSF, and had lower gray matter volume in the superior parietal cortex. This variant was associated with dementia severity assessed via the Clinical Dementia Rating (p=0.017) and AD diagnosis in ADNI (p=0.036). We find a nominal significant association to disease status, hence proving the endophenotype concept.

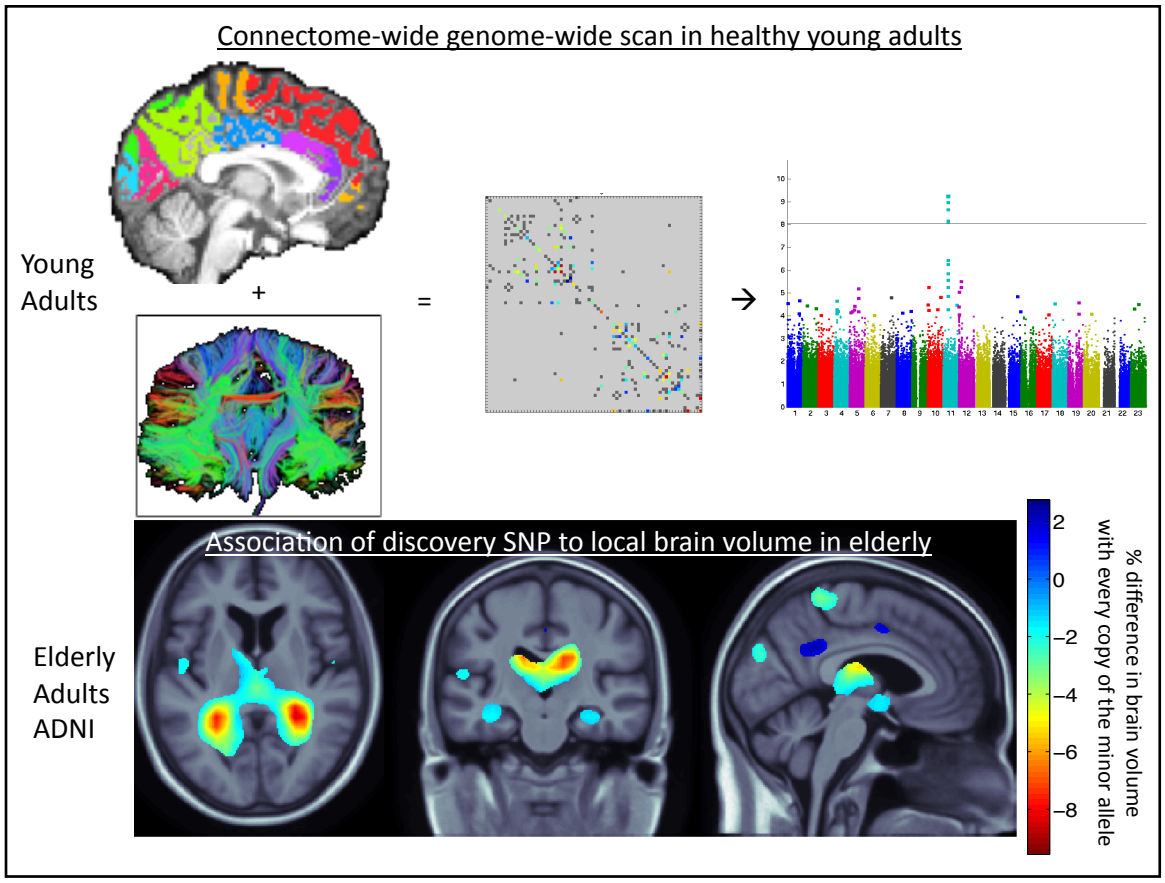

Figure 7.1: Intragenic variants at 11p15.2 were found through a GWAS of the healthy young human connectome. As the protein product of this gene has been previously shown to interact in the amyloid-beta precursor protein (APP) pathway, an unbias search of the elderly brain in ADNI finds significant anatomical variations in carriers of the top variant as compared to non-carriers.

7.1.2 Biomarkers for disease progression

Expanding on our discovery, we will set out to determine if measures obtained from the connectivity matrices can serve as biomarkers for disease progression. As the Alzheimer's Disease Neuroimaging Initiative (ADNI) recently launched a second phase of the study to incorporate diffusion tensor imaging, an initial investigation was set out to determine whether connectivity measures at an initial time point could predict neuroanatomical changes in follow up scans. Using generalized network theory measures on the connectome, we find suggestive evidence that these measures may be able to predict anatomical changes in follow up scans. Structural brain networks are modeled as graphs where nodes designate elements (i.e., brain regions) that are linked by edges representing physical connections. Abnormal small-world architecture in large-scale brain networks has been found in AD patients, with increased clustering and shortest paths linking individual regions, implying a less optimal topological organization (He *et al.* , 2008). Smallworldness is a measure of topological organization defined as being between a random and an organized network; it is composed of two measures obtainable from the – characteristic path length (CPL) and mean clustering coefficient (MCC). CPL is an average measure of the minimum number of edges necessary to get from one node to another in a network (i.e. average minimum path length and MCC is a measure of how many neighbors of a given node are also connected to each other, relative to the total possible number of connections in the network (Rubinov & Sporns, 2010). While the ratio of these two (each with respect to randomized networks) constitutes smallworldness, the individual values analyzed jointly may be more informative. As far as we know, small-world global network measures, such as CPL and MCC, have not yet been used to predict anatomical disruption in AD. This hypothesis was tested and recently presented in the following from which we adapt Figure 7.2:

> Nir T*, **Jahanshad N***, Jack Jr CR, Weiner MW, Toga AW, Thompson PM and the Alzheimers Disease Neuroimaging Initiative (ADNI) (2012). Small world network measures predict white matter degeneration in patients with early-stage mild cognitive impairment, International Symposium of Biomedical Imag-

ing (ISBI) Barcelona, Spain, May 2-5 2012.

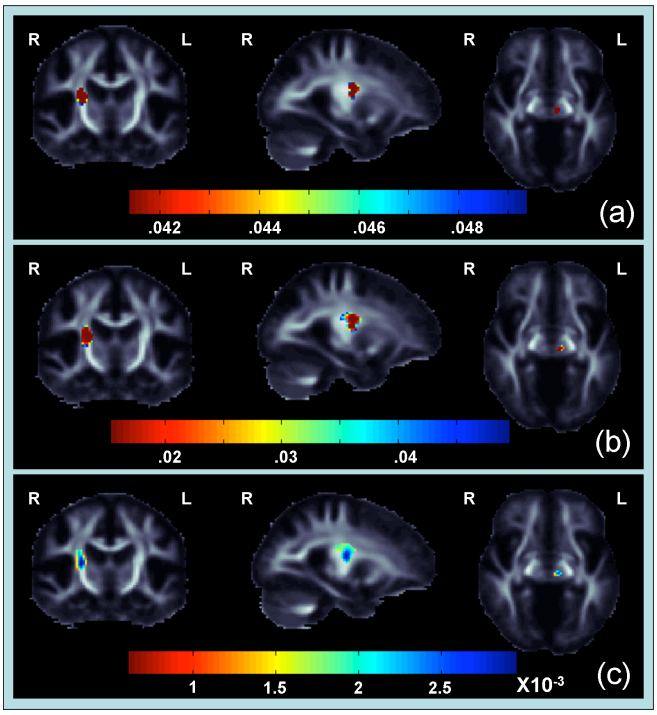

Figure 7.2: (a) These p-maps show regions where CPL and MCC are joint predictors of FA differences (corrected $p < .05$) (b) These p-maps show regions where MCC is significantly associated with change in FA (corrected $p < .05$) (c) These maps show Beta-values (non-normalized slope of the regression) within regions where MCC has a significantly positive correlation with changes in FA.

Results in the small group of 19 presented here are encouraging and we are currently expanding our analysis as more and more patients are coming in for follow up scans to include more measures indicitive of degeneration in a growing dataset.

7.1.3 Defining new biomarkers

We aim to extend methods presented to find ways of discovering biologically meaningful representations from networks. For example, while CPL is a standard measure calculated from measures, no true path length measure exists to estimate distances lengths of pathways between cortical regions. When used for brain network analysis, the physical distance

between cortical regions may also be relevant, as (among other factors) it may affect how vulnerable the connection is to lesions, trauma, or degenerative processes. In this work, we use HARDI tractography to map fibers in the brain connecting various cortical regions. We created maps of the proportions of fibers that interconnect various cortical regions within and across hemispheres and calculate an optimal path between cortical regions based on the fiber counts.

For each subject, a full 70x70 connectivity matrix was created as in Chapter 6. Each element described the proportion of the total number of fibers in the brain connecting each of the labels; diagonal elements of the matrix describe the total number of fibers passing through a certain cortical region of interest. If more than 5% of subjects had no fibers in a matrix element, then the connection was considered invalid, or insufficiently consistent in its incidence in the population, and was not included in the analysis. For each connection across two nodes that was considered valid across the full healthy population (200 different connections were present in 95% of the population), a fiber density image was created. This image consists of a voxelwise mapping of the fibers intersecting the two regions, where a count of fibers crossing each voxel was made.

All voxels in each person's 3D fiber density map were then considered as nodes in a graph; and each node in the graph is considered to be connected to 26 nodes (3D neighboring voxels) by undirected edges. Note that now we are considering adjacency in the 3D image, not the 2D matrix of cortical connections. Each edge was weighted inversely by the sum of the fiber densities at each of the two voxels on the edge, and the weight was inversely proportional to the Euclidean distance from the center of one voxel to the other. As the edge weights correspond to edge costs for our shortest path detection method, a connection between a pair of voxels that each had a high fiber density was assigned to a lower weight, or lower cost. Suppose voxels i and j are voxelwise neighbors with integer fiber counts (densities) d_i and d_j respectively, and Euclidean distance between their centers is $dist_{i,j} = \sqrt{(x_i - x_j)^2 + (y_i - y_j)^2 + (z_i - z_j)^2}$. Then we defined the edge weight as $w_{i,j} = \frac{dist_{i,j}}{d_i + d_j}$. As most voxels in the density image are not immediate neighbors of each other (the region is generally a elongated path several voxels wide), the path graph can be represented by a

sparse matrix.

We found a path through the graph from one cortical connection to the other, by following nodes that minimize the weight using Dijkstra's algorithm (Dijkstra, 1959). Dijkstra's algorithm is a graph search method to find the shortest discrete path from a source node to every other node while minimizing the weight of the edges and has been previously applied for tractography (Zalesky, 2008). To find the shortest path, Dijkstra's algorithm requires the graph to have specified start and end nodes. As the cortical segmentation spans a large region with several voxels, the centroid of each region was selected as a representative termination point. Therefore, all connections starting or ending at that cortical segmentation would ideally be made through the centroid. However, as the fibers would not necessarily be expected to cross at the exact point of the centroid, and would often be outside the path, the Euclidean distance was calculated from the centroid to all other voxels in the fiber density map (that comprise the graph) to find the closest representative point. As such, for each connection, a unique start or end point for a particular cortical ROI can be expected, as not all fibers connecting Cortical ROI 1 to 2 will necessarily cross Cortical ROI 1 in the same location as those fibers crossing Cortical ROI 1 and 3.

Dijkstra's algorithm will then find the path, once the start and end nodes are specified. It first assigns a distance value to every node in the graph, zero for the start node and infinity for the rest. The algorithm sets the start point to be the current node and all marks all others as unvisited. The current nodes distance to its unvisited neighbors is calculated; if that distance is smaller then the neighbors existing distance value, it is replaced. The method will mark the current node as visited and the current nodes distance is final, meaning the distance from the start node to itself will remain zero. The new current node will be selected as any unvisited node and the algorithm will continue exploring nodes until the destination node is visited, resulting in a path to this node that minimizes the distance. The algorithm will be incapable of finding a connection between the two nodes if the graph structure is such that there are no edges from the subgraph containing the start node with the subgraph containing the end node. Due to discretization of fibers into voxels, it is possible that the density image would not show a continuous path, but piecewise sections of fibers instead,

as shown in 2D in Figure 7.3. To account for this possibility, and to avoid having tracts that do not start and end in different cortical regions, a 3D box is created spanning from the start point in one cortical region to the end point in the other. After the start and end points have been computed, this box is then artificially labeled with a uniform fractional fiber density count (0.01) to allow for a continuous path between different cortical regions to be connected, albeit at a high cost. Additionally, all voxels of the path were dilated (and given the small density count). This helps to ensure a continual path such that Dijkstra's algorithm can find a set of voxel locations in to create a representative path connecting the start and end regions.

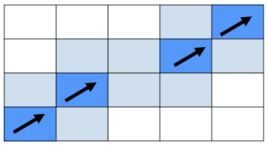

Figure 7.3: Discretization of a fiber into a set of voxels in the image (here in 2D, but the 3D case is used) may leave a piecewise path (dark blue) rather than a continuous one. Voxels are dilated (light blue) to ensure a continual path exists.

Once the optimal path has been calculated based on the weights, the length of the path is computed by summing the distances from the center of the neighboring voxel points along the path, starting from the start point, following the path, and ending at the end point in the other cortical region. Alternative approaches might use tensor-derived measures such as FA as weights, or other scalar measures not making full use of the HARDI data. Once all the path lengths have been calculated from all valid cortical connections to the next, an observed path length connectivity matrix can be computed Figure 7.4 Instead of each element representing the fiber density between the connections, the physical length of fibers connecting the regions is approximated.

In Figure 7.5 a single path with start and end points is visualized.

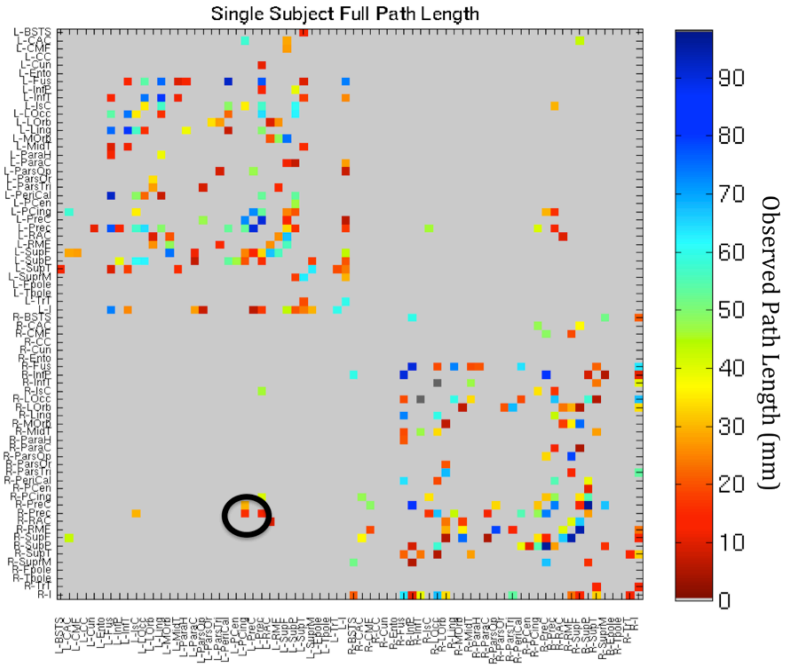

Figure 7.4: Connectivity map of the path length estimates for a single subject. All path lengths correspond to mm between one cortical centroid to the other. The path was defined using Dijkstra's shortest path on voxels weighted by the density of fibers passing through them.

7.2 ENIGMA-DTI

The Enhancing Neuro-Imaging Genetics through Meta Analysis (ENIGMA) Project was initialized in late 2009 in an effort to prove neuroimaging markers can serve as relavent traits for discovering genetic markers of interest.

> *A number of groups around the world are now conducting brain imaging studies of normal individuals with MRI, DTI, and fMRI, and also obtaining (or planning to obtain) genomewide association scanning (GWAS) data. The best return on our research investments will come from combining our data to achieve the large samples (thousands of subjects) necessary to detect the modest gene effect sizes that we now know are the rule rather the exception for complex traits.*
> http://enigma.loni.ucla.edu/

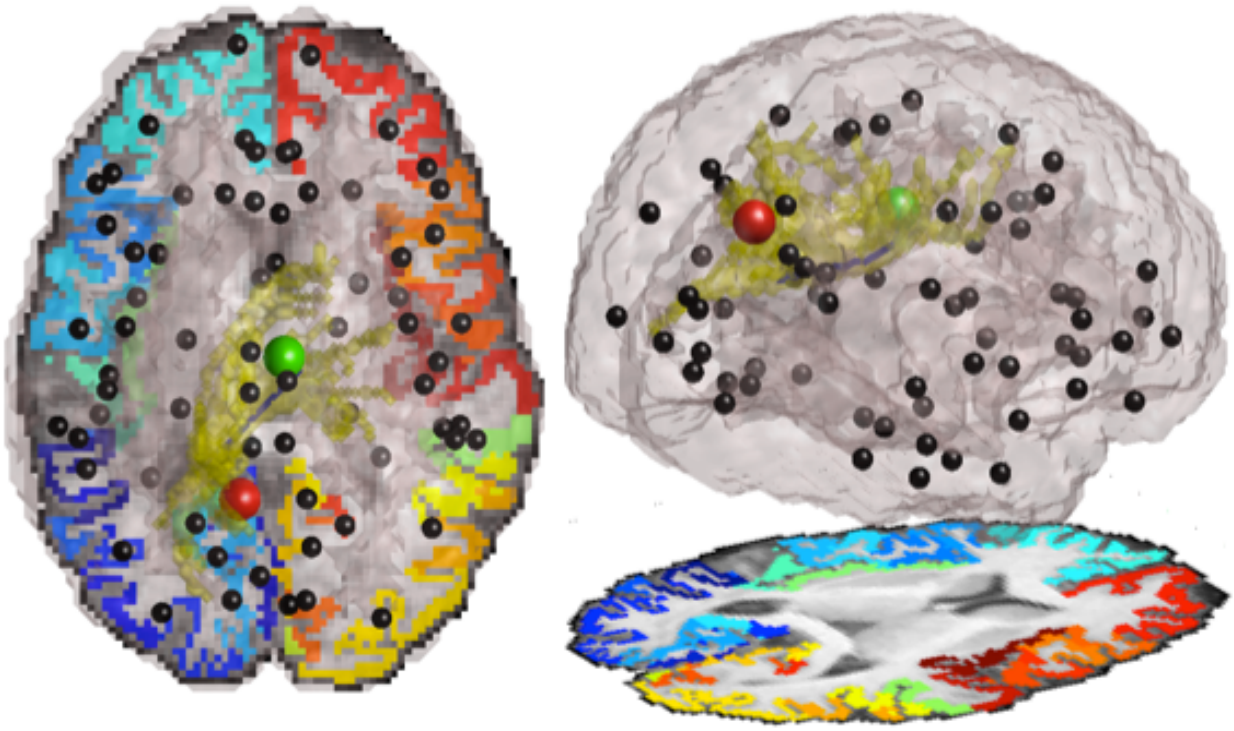

Figure 7.5: The observed path (blue line) constitutes a skeletonized path from the left precuneus to the right posterior cingulate. The yellow colors show the density of all fibers drawn from tractography connecting the two regions. Red and green spheres indicate the start and end points.

The pilot project for ENIGMA (Stein *et al.* , 2012) was based on using hippocampal volume and intracranial volume as phenotypes for genetic search. As this project was a success, efforts continue to explore other neuroanatomical structures and imaging modalities. A vast number of behavior traits, psychiatric disorders, diseases and types of neurodegeneration – all with complex genetic characteristics – have been made with white matter microstructure, perhaps more so than with hippocampal volume. In this sense, the quest to search the white matter microstructure for genetic influence becomes a global priority. We will subsequently lead a multinational effort to combine DTI and GWAS data across multiple institutions for exploring the genetic potential of DTI meta analysis.

7.2.1 Working group

However, due to the high variability of DTI based measures and high dependence of DTI obtained anisotropy measures on imaging protocol as described in Chapter 2, an intial investigation must be put into place to identify stable, reliable, and heritable measures from the DTI scans before developing protocols for global use. The integrity of the brain's white matter can serve as an important endophenotype, and several genetic associations have already been established. However, as described in Chapter 2, measures derived from DTI, such as fractional anisotropy, can vary substantially depending on variables in the imaging acquisition protocols such as the image voxel size, number of directional gradients used, scanner magnetic field strength, and the ratio of the number of directional images to those with no diffusion sensitization. We therefore need an initial investigation into the genomic stability of scans and are therefore forming a DTI working group for phenotype harmonization to determine several measures computed from DTI images to serve as possible phenotypes to pool together for multi-site genetic analyses. This working group is a methods development group to identify heritable, and reproducible, measures from diffusion images and ways to model or account for intersite differences in these phenotypes.

Currently approximately 2000 scans from 4 international sites (see Table 7.1 for a list of sites) are being used for phenotype harmonization. The group is currently testing various processing methods, initial phenotypes, and establishing quality control procedures that will be able to be applied to large datasets. Results from an initial investigation are promissing and are being presented at the Organization for Human Brain Mapping in June 2012.

> Kochunov P., **Jahanshad N**, Thompson PM, Sprooten E, McIntosh A, Deary I, Bastin ME, Toga AW, McMahon KL, de Zubicaray GI, Martin NG, Wright MJ, Hong E. Carless M, Curran J, Dyer T, Olvera R, Duggirala R, Blangero J, Glahn D. Genome-wide association of full brain white matter integrity from the ENIGMA DTI working group. Organization for Human Brain Mapping (OHBM 2012), Beijing, China, June 10-14, 2012.

ENIGMA DTI Working group website

7.2.2 Global expansion

Efforts from the working group will result in an easy-to-implement DTI protocol for all interested ENIGMA sites to use for future meta-analysis in 2012. Already, several groups have expressed interest in joining these efforts and the expected number of members is expected to greatly increase.

Group	N with DTI + GWAS	Personnel	in Working group?
QTIM	600	Thompson/Jahanshad	Yes
GOBS	700	Glahn/Kochunov	Yes
LBC1936	700	Deary/Bastin	Yes
BFS	200	McIntosh/Sprooten	Yes
UMCU	200	Hulshoff Pol/Mandl	May 2012
UMD	500	Hong/Stein	No
NAPLS	600	Cannon	No
MAS/OATS	??	Sachdev	No
BIG	600	Franke/Zwiers	No

Table 7.1: Groups interested in joining ENIGMA DTI to date

7.3 LONI Pipeline updates

As our imaging genetics work expands, more and more tools will be developed to parellize analyses. We will continue to use the LONI pipeline infrastructure to build tools for these processes. Tools will continue to be shared for use by other group members online here: http://users.loni.ucla.edu/~njahansh/Pipelines.htm

Bibliography

Aganj, I., Lenglet, C., Jahanshad, N., Yacoub, E., Harel, N., Thompson, P. M., & Sapiro, G. 2011. A Hough transform global probabilistic approach to multiple-subject diffusion MRI tractography. *Med Image Anal*, **15**(4), 414–25.

Alexander, A. L., Hasan, K. M., Lazar, M., Tsuruda, J. S., & Parker, D. L. 2001. Analysis of partial volume effects in diffusion-tensor MRI. *Magn Reson Med*, **45**(5), 770–80.

Assemlal, H. E., Tschumperle, D., Brun, L., & Siddiqi, K. 2011. Recent advances in diffusion MRI modeling: Angular and radial reconstruction. *Med Image Anal*, **15**(4), 369–96.

Bartzokis, G., Sultzer, D., Mintz, J., Holt, L. E., Marx, P., Phelan, C. K., & Marder, S. R. 1994. In vivo evaluation of brain iron in Alzheimer's disease and normal subjects using MRI. *Biol Psychiatry*, **35**(7), 480–7.

Bartzokis, G., Cummings, J. L., Markham, C. H., Marmarelis, P. Z., Treciokas, L. J., Tishler, T. A., Marder, S. R., & Mintz, J. 1999. MRI evaluation of brain iron in earlier- and later-onset Parkinson's disease and normal subjects. *Magn Reson Imaging*, **17**(2), 213–22.

Basser, P. J., & Pierpaoli, C. 1996. Microstructural and physiological features of tissues elucidated by quantitative-diffusion-tensor MRI. *J Magn Reson B*, **111**(3), 209–19.

Beaton, A. A. 1997. The relation of planum temporale asymmetry and morphology of the corpus callosum to handedness, gender, and dyslexia: a review of the evidence. *Brain Lang*, **60**(2), 255–322.

Beaulieu, C. 2002. The basis of anisotropic water diffusion in the nervous system - a technical review. *NMR Biomed*, **15**(7-8), 435–55.

Benarroch, E. E. 2009. Brain iron homeostasis and neurodegenerative disease. *Neurology*, **72**(16), 1436–40.

Braskie, M. N., Jahanshad, N., Stein, J. L., Barysheva, M., Johnson, K., McMahon, K. L., de Zubicaray, G. I., Martin, N. G., Wright, M. J., Ringman, J. M., Toga, A. W., &

Thompson, P. M. 2012. Relationship of a Variant in the NTRK1 Gene to White Matter Microstructure in Young Adults. *J Neurosci*, **32**(17), 5964–5972.

Brown, J. A., Terashima, K. H., Burggren, A. C., Ercoli, L. M., Miller, K. J., Small, G. W., & Bookheimer, S. Y. 2011. Brain network local interconnectivity loss in aging APOE-4 allele carriers. *Proc Natl Acad Sci U S A*.

Brun, C. C., Lepore, N., Pennec, X., Lee, A. D., Barysheva, M., Madsen, S. K., Avedissian, C., Chou, Y. Y., de Zubicaray, G. I., McMahon, K. L., Wright, M. J., Toga, A. W., & Thompson, P. M. 2009. Mapping the regional influence of genetics on brain structure variability–a tensor-based morphometry study. *Neuroimage*, **48**(1), 37–49.

CDC. 2002. From the Centers for Disease Control and Prevention. Iron deficiency–United States, 1999-2000. *JAMA*, **288**(17), 2114–6.

Chiang, M. C., Dutton, R. A., Hayashi, K. M., Lopez, O. L., Aizenstein, H. J., Toga, A. W., Becker, J. T., & Thompson, P. M. 2007. 3D pattern of brain atrophy in HIV/AIDS visualized using tensor-based morphometry. *Neuroimage*, **34**(1), 44–60.

Chou, Y. Y., Lepore, N., Chiang, M. C., Avedissian, C., Barysheva, M., McMahon, K. L., de Zubicaray, G. I., Meredith, M., Wright, M. J., Toga, A. W., & Thompson, P. M. 2009. Mapping genetic influences on ventricular structure in twins. *Neuroimage*, **44**(4), 1312–23.

Crow, T. J. 1990. Schizophrenia as a genetic encephalopathy. *Recenti Prog Med*, **81**(11), 738–45.

Desikan, R. S., Segonne, F., Fischl, B., Quinn, B. T., Dickerson, B. C., Blacker, D., Buckner, R. L., Dale, A. M., Maguire, R. P., Hyman, B. T., Albert, M. S., & Killiany, R. J. 2006. An automated labeling system for subdividing the human cerebral cortex on MRI scans into gyral based regions of interest. *Neuroimage*, **31**(3), 968–80.

Dijkstra, E.W. 1959. A note on two problems in connexion with graphs. *Numerische mathematik*, **1**(1), 269–271.

Duarte-Carvajalino, J. M., Jahanshad, N., Lenglet, C., McMahon, K. L., de Zubicaray, G. I., Martin, N. G., Wright, M. J., Thompson, P. M., & Sapiro, G. 2012. Hierarchical topological network analysis of anatomical human brain connectivity and differences related to sex and kinship. *Neuroimage*, **59**(4), 3784–804.

Eckert, M. A., Galaburda, A. M., Karchemskiy, A., Liang, A., Thompson, P., Dutton, R. A., Lee, A. D., Bellugi, U., Korenberg, J. R., Mills, D., Rose, F. E., & Reiss, A. L. 2006. Anomalous sylvian fissure morphology in Williams syndrome. *Neuroimage*, **33**(1), 39–45.

Gong, G., Rosa-Neto, P., Carbonell, F., Chen, Z. J., He, Y., & Evans, A. C. 2009. Age- and gender-related differences in the cortical anatomical network. *J Neurosci*, **29**(50), 15684–93.

Gottesman, II, & Gould, T. D. 2003. The endophenotype concept in psychiatry: etymology and strategic intentions. *Am J Psychiatry*, **160**(4), 636–45.

Halterman, J. S., Kaczorowski, J. M., Aligne, C. A., Auinger, P., & Szilagyi, P. G. 2001. Iron deficiency and cognitive achievement among school-aged children and adolescents in the United States. *Pediatrics*, **107**(6), 1381–6.

Hamilton, L. S., Narr, K. L., Luders, E., Szeszko, P. R., Thompson, P. M., Bilder, R. M., & Toga, A. W. 2007. Asymmetries of cortical thickness: effects of handedness, sex, and schizophrenia. *Neuroreport*, **18**(14), 1427–31.

He, Y., Chen, Z., & Evans, A. 2008. Structural insights into aberrant topological patterns of large-scale cortical networks in Alzheimer's disease. *J Neurosci*, **28**(18), 4756–66.

Hulshoff Pol, H. E., Schnack, H. G., Posthuma, D., Mandl, R. C., Baare, W. F., van Oel, C., van Haren, N. E., Collins, D. L., Evans, A. C., Amunts, K., Burgel, U., Zilles, K., de Geus, E., Boomsma, D. I., & Kahn, R. S. 2006. Genetic contributions to human brain morphology and intelligence. *J Neurosci*, **26**(40), 10235–42.

Jahanshad, N., Lee, A. D., Barysheva, M., McMahon, K. L., de Zubicaray, G. I., Martin, N. G., Wright, M. J., Toga, A. W., & Thompson, P. M. 2010. Genetic influences on brain asymmetry: a DTI study of 374 twins and siblings. *Neuroimage*, **52**(2), 455–69.

Jahanshad, Neda, Aganj, Iman, Lenglet, Christophe, Joshi, Anand, Jin, Yan, Barysheva, Marina, McMahon, Katie L., Zubicaray, Greig I. de, Martin, Nicholas G., Wright, Margaret J., Toga, Arthur W., Sapiro, Guillermo, & Thompson, Paul M. 2011. *Sex differences in the Human Connectome: 4-Tesla high angular resolution diffusion tensor imaging (HARDI) tractography in 234 young adult twins.*

Jurgens, C. K., Jasinschi, R., Ekin, A., Witjes-Ane, M. N., Middelkoop, H., van der Grond, J., & Roos, R. 2010. MRI T2 Hypointensities in basal ganglia of premanifest Huntington's disease. *PLoS Curr*, **2**.

Ke, Y., & Ming Qian, Z. 2003. Iron misregulation in the brain: a primary cause of neurodegenerative disorders. *Lancet Neurol*, **2**(4), 246–53.

Klingberg, T., Hedehus, M., Temple, E., Salz, T., Gabrieli, J. D., Moseley, M. E., & Poldrack, R. A. 2000. Microstructure of temporo-parietal white matter as a basis for reading ability: evidence from diffusion tensor magnetic resonance imaging. *Neuron*, **25**(2), 493–500.

Kochunov, P., Glahn, D. C., Lancaster, J. L., Winkler, A. M., Smith, S., Thompson, P. M., Almasy, L., Duggirala, R., Fox, P. T., & Blangero, J. 2010. Genetics of microstructure of cerebral white matter using diffusion tensor imaging. *Neuroimage*, **53**(3), 1109–16.

Koziol, J. A., Wagner, S., Sobel, D. F., Feng, A. C., & Adams, H. P. 2005. Asymmetries in the spatial distributions of enhancing lesions and black holes in relapsing-remitting MS. *J Clin Neurosci*, **12**(8), 895–901.

Kriegeskorte, N., Lindquist, M. A., Nichols, T. E., Poldrack, R. A., & Vul, E. 2010. Everything you never wanted to know about circular analysis, but were afraid to ask. *J Cereb Blood Flow Metab*, **30**(9), 1551–7.

Landman, B. A., Farrell, J. A., Jones, C. K., Smith, S. A., Prince, J. L., & Mori, S. 2007. Effects of diffusion weighting schemes on the reproducibility of DTI-derived fractional anisotropy, mean diffusivity, and principal eigenvector measurements at 1.5T. *Neuroimage*, **36**(4), 1123–38.

Lenglet, C., Campbell, J. S., Descoteaux, M., Haro, G., Savadjiev, P., Wassermann, D., Anwander, A., Deriche, R., Pike, G. B., Sapiro, G., Siddiqi, K., & Thompson, P. M. 2009. Mathematical methods for diffusion MRI processing. *Neuroimage*, **45**(1 Suppl), S111–22.

Luders, E., Thompson, P. M., & Toga, A. W. 2010. The development of the corpus callosum in the healthy human brain. *J Neurosci*, **30**(33), 10985–90.

Muhlau, M., Weindl, A., Wohlschlager, A. M., Gaser, C., Stadtler, M., Valet, M., Zimmer, C., Kassubek, J., & Peinemann, A. 2007. Voxel-based morphometry indicates relative preservation of the limbic prefrontal cortex in early Huntington disease. *J Neural Transm*, **114**(3), 367–72.

Narr, K. L., Bilder, R. M., Luders, E., Thompson, P. M., Woods, R. P., Robinson, D., Szeszko, P. R., Dimtcheva, T., Gurbani, M., & Toga, A. W. 2007. Asymmetries of cortical shape: Effects of handedness, sex and schizophrenia. *Neuroimage*, **34**(3), 939–48.

Nelson, C., Erikson, K., Pinero, D. J., & Beard, J. L. 1997. In vivo dopamine metabolism is altered in iron-deficient anemic rats. *J Nutr*, **127**(12), 2282–8.

Pardridge, W. M., Eisenberg, J., & Yang, J. 1987. Human blood-brain barrier transferrin receptor. *Metabolism*, **36**(9), 892–5.

Pender, M. P. 2011. The essential role of Epstein-Barr virus in the pathogenesis of multiple sclerosis. *Neuroscientist*, **17**(4), 351–67.

Raine, A., Lencz, T., Taylor, K., Hellige, J. B., Bihrle, S., Lacasse, L., Lee, M., Ishikawa, S., & Colletti, P. 2003. Corpus callosum abnormalities in psychopathic antisocial individuals. *Arch Gen Psychiatry*, **60**(11), 1134–42.

Raji, Cyrus, Ericson, Kirk, Lopez, Oscar, Kuller, Lewis, Michael, Gach H., Thompson, Paul, Riverol, Mario, & Becker, James. 2011. Regular Fish Consumption Is Associated with Larger Gray Matter Volumes and Reduced Risk for Cognitive Decline in the Cardiovascular Health Study. *In: Radiological Society of North America*. Chicago, IL: Radiological Society of North America.

Rubinov, M., & Sporns, O. 2010. Complex network measures of brain connectivity: uses and interpretations. *Neuroimage*, **52**(3), 1059–69.

Sowell, E. R., Thompson, P. M., Peterson, B. S., Mattson, S. N., Welcome, S. E., Henkenius, A. L., Riley, E. P., Jernigan, T. L., & Toga, A. W. 2002. Mapping cortical gray matter asymmetry patterns in adolescents with heavy prenatal alcohol exposure. *Neuroimage*, **17**(4), 1807–19.

Stein, J. L., Medland, S. E., Vasquez, A. A., Hibar, D. P., Senstad, R. E., Winkler, A. M., Toro, R., Appel, K., Bartecek, R., Bergmann, O., Bernard, M., Brown, A. A., Cannon, D. M., Chakravarty, M. M., Christoforou, A., Domin, M., Grimm, O., Hollinshead, M., Holmes, A. J., Homuth, G., Hottenga, J. J., Langan, C., Lopez, L. M., Hansell, N. K., Hwang, K. S., Kim, S., Laje, G., Lee, P. H., Liu, X., Loth, E., Lourdusamy, A., Mattingsdal, M., Mohnke, S., Maniega, S. M., Nho, K., Nugent, A. C., O'Brien, C., Papmeyer, M., Putz, B., Ramasamy, A., Rasmussen, J., Rijpkema, M., Risacher, S. L., Roddey, J. C., Rose, E. J., Ryten, M., Shen, L., Sprooten, E., Strengman, E., Teumer, A., Trabzuni, D., Turner, J., van Eijk, K., van Erp, T. G., van Tol, M. J., Wittfeld, K., Wolf, C., Woudstra, S., Aleman, A., Alhusaini, S., Almasy, L., Binder, E. B., Brohawn, D. G., Cantor, R. M., Carless, M. A., Corvin, A., Czisch, M., Curran, J. E., Davies, G., de Almeida, M. A., Delanty, N., Depondt, C., Duggirala, R., Dyer, T. D., Erk, S., Fagerness, J., Fox, P. T., Freimer, N. B., Gill, M., Goring, H. H., Hagler, D. J., Hoehn, D., Holsboer, F., Hoogman, M., Hosten, N., Jahanshad, N., Johnson, M. P., Kasperaviciute, D., Kent, J. W., Jr., Kochunov, P., Lancaster, J. L., Lawrie, S. M., Liewald, D. C., Mandl, R., Matarin, M., Mattheisen, M., Meisenzahl, E., Melle, I., Moses, E. K., Muhleisen, T. W., Nauck, M., Nothen, M. M., Olvera, R. L., Pandolfo, M., Pike, G. B., Puls, R., Reinvang, I., Renteria,

M. E., Rietschel, M., Roffman, J. L., Royle, N. A., Rujescu, D., Savitz, J., Schnack, H. G., Schnell, K., Seiferth, N., Smith, C., Steen, V. M., Hernandez, M. C. Valdes, den Heuvel, M. Van, van der Wee, N. J., Haren, N. E. Van, Veltman, J. A., Volzke, H., Walker, R., Westlye, L. T., Whelan, C. D., Agartz, I., Boomsma, D. I., Cavalleri, G. L., Dale, A. M., Djurovic, S., Drevets, W. C., Hagoort, P., Hall, J., Heinz, A., Jack, C. R., Jr., Foroud, T. M., Hellard, S. Le, Macciardi, F., Montgomery, G. W., Poline, J. B., Porteous, D. J., Sisodiya, S. M., Starr, J. M., Sussmann, J., Toga, A. W., Veltman, D. J., Walter, H., Weiner, M. W., Bis, J. C., Ikram, M. A., Smith, A. V., Gudnason, V., Tzourio, C., Vernooij, M. W., Launer, L. J., Decarli, C., Seshadri, S., Andreassen, O. A., Apostolova, L. G., Bastin, M. E., Blangero, J., Brunner, H. G., Buckner, R. L., Cichon, S., Coppola, G., de Zubicaray, G. I., Deary, I. J., Donohoe, G., de Geus, E. J., Espeseth, T., Fernandez, G., Glahn, D. C., Grabe, H. J., Hardy, J., Pol, H. E. Hulshoff, Jenkinson, M., Kahn, R. S., McDonald, C., McIntosh, A. M., McMahon, F. J., McMahon, K. L., Meyer-Lindenberg, A., Morris, D. W., Muller-Myhsok, B., Nichols, T. E., Ophoff, R. A., Paus, T., Pausova, Z., Penninx, B. W., Potkin, S. G., Samann, P. G., Saykin, A. J., Schumann, G., Smoller, J. W., Wardlaw, J. M., Weale, M. E., Martin, N. G., Franke, B., Wright, M. J., & Thompson, P. M. 2012. Identification of common variants associated with human hippocampal and intracranial volumes. *Nat Genet*.

Stern, Y., Gurland, B., Tatemichi, T. K., Tang, M. X., Wilder, D., & Mayeux, R. 1994. Influence of education and occupation on the incidence of Alzheimer's disease. *JAMA*, **271**(13), 1004–10.

Thompson, P. M., Moussai, J., Zohoori, S., Goldkorn, A., Khan, A. A., Mega, M. S., Small, G. W., Cummings, J. L., & Toga, A. W. 1998. Cortical variability and asymmetry in normal aging and Alzheimer's disease. *Cereb Cortex*, **8**(6), 492–509.

Thompson, P. M., Giedd, J. N., Woods, R. P., MacDonald, D., Evans, A. C., & Toga, A. W. 2000. Growth patterns in the developing brain detected by using continuum mechanical tensor maps. *Nature*, **404**(6774), 190–3.

Thompson, P. M., Mega, M. S., Woods, R. P., Zoumalan, C. I., Lindshield, C. J., Blanton,

R. E., Moussai, J., Holmes, C. J., Cummings, J. L., & Toga, A. W. 2001a. Cortical change in Alzheimer's disease detected with a disease-specific population-based brain atlas. *Cereb Cortex*, **11**(1), 1–16.

Thompson, P. M., Cannon, T. D., Narr, K. L., van Erp, T., Poutanen, V. P., Huttunen, M., Lonnqvist, J., Standertskjold-Nordenstam, C. G., Kaprio, J., Khaledy, M., Dail, R., Zoumalan, C. I., & Toga, A. W. 2001b. Genetic influences on brain structure. *Nat Neurosci*, **4**(12), 1253–8.

Thompson, P. M., Vidal, C., Giedd, J. N., Gochman, P., Blumenthal, J., Nicolson, R., Toga, A. W., & Rapoport, J. L. 2001c. Mapping adolescent brain change reveals dynamic wave of accelerated gray matter loss in very early-onset schizophrenia. *Proc Natl Acad Sci U S A*, **98**(20), 11650–5.

Thompson, P. M., Hayashi, K. M., de Zubicaray, G., Janke, A. L., Rose, S. E., Semple, J., Herman, D., Hong, M. S., Dittmer, S. S., Doddrell, D. M., & Toga, A. W. 2003. Dynamics of gray matter loss in Alzheimer's disease. *J Neurosci*, **23**(3), 994–1005.

Thompson, P. M., Lee, A. D., Dutton, R. A., Geaga, J. A., Hayashi, K. M., Eckert, M. A., Bellugi, U., Galaburda, A. M., Korenberg, J. R., Mills, D. L., Toga, A. W., & Reiss, A. L. 2005a. Abnormal cortical complexity and thickness profiles mapped in Williams syndrome. *J Neurosci*, **25**(16), 4146–58.

Thompson, P. M., Dutton, R. A., Hayashi, K. M., Toga, A. W., Lopez, O. L., Aizenstein, H. J., & Becker, J. T. 2005b. Thinning of the cerebral cortex visualized in HIV/AIDS reflects CD4+ T lymphocyte decline. *Proc Natl Acad Sci U S A*, **102**(43), 15647–52.

Thompson, P. M., Dutton, R. A., Hayashi, K. M., Lu, A., Lee, S. E., Lee, J. Y., Lopez, O. L., Aizenstein, H. J., Toga, A. W., & Becker, J. T. 2006. 3D mapping of ventricular and corpus callosum abnormalities in HIV/AIDS. *Neuroimage*, **31**(1), 12–23.

Thompson, Paul M., Narr, Katherine L., Blanton, Rebecca E., & Toga, Arthur W. 2002. Mapping structural alterations of the corpus callosum during brain development and de-

generation. *In:* Zaidel, Eran, & Iacoboni, Marco (eds), *Proceedings of the NATO ASI on the Corpus Callosum*. Kluwer Academic Press.

Tournier, J. D., Mori, S., & Leemans, A. 2011. Diffusion tensor imaging and beyond. *Magn Reson Med*, **65**(6), 1532–56.

Tuch, D. S., Reese, T. G., Wiegell, M. R., Makris, N., Belliveau, J. W., & Wedeen, V. J. 2002. High angular resolution diffusion imaging reveals intravoxel white matter fiber heterogeneity. *Magn Reson Med*, **48**(4), 577–82.

Vidal, C. N., Nicolson, R., DeVito, T. J., Hayashi, K. M., Geaga, J. A., Drost, D. J., Williamson, P. C., Rajakumar, N., Sui, Y., Dutton, R. A., Toga, A. W., & Thompson, P. M. 2006. Mapping corpus callosum deficits in autism: an index of aberrant cortical connectivity. *Biol Psychiatry*, **60**(3), 218–25.

Wedeen, V. J., Rosene, D. L., Wang, R., Dai, G., Mortazavi, F., Hagmann, P., Kaas, J. H., & Tseng, W. Y. 2012. The geometric structure of the brain fiber pathways. *Science*, **335**(6076), 1628–34.

Wen, W., Zhu, W., He, Y., Kochan, N. A., Reppermund, S., Slavin, M. J., Brodaty, H., Crawford, J., Xia, A., & Sachdev, P. 2011. Discrete neuroanatomical networks are associated with specific cognitive abilities in old age. *J Neurosci*, **31**(4), 1204–12.

Zalesky, A. 2008. DT-MRI fiber tracking: a shortest paths approach. *IEEE Trans Med Imaging*, **27**(10), 1458–71.

Zhan, L., Leow, A. D., Jahanshad, N., Chiang, M. C., Barysheva, M., Lee, A. D., Toga, A. W., McMahon, K. L., de Zubicaray, G. I., Wright, M. J., & Thompson, P. M. 2010. How does angular resolution affect diffusion imaging measures? *Neuroimage*, **49**(2), 1357–71.